Experimental and CFD investigation of the solidification of blood plasma using heat pipe based cryo-freezer storage system

A thesis submitted for the degree of Doctor of Philosophy (PhD)

By

Amisha Chauhan

Department of Mechanical, Aerospace and Civil Engineering
College of Engineering, Design and Physical Sciences
Brunel University London

February 2020

Abstract

The methods of cryo-preservation are one of the most diverse applications of technology with multiple applications and different levels of scalability. The technology surrounding cryo-preservation is currently separated into two categories, indirect and direct freezing. Typically, indirect freezing is associated with air blast freezing which is associated to ineffective freezing times. The application of direct freezing commonly uses a cryogenic fluid to rapidly preserve products, but the technology is hazardous to operate due to the handling and the asphyxiation risk. The need for a safe but efficient technology within the cryo-preservation market is evident, which can utilise the thermal capacity of cryogenic fluids without the associated risks. To address this need, the aim of this study presents the application of heat pipe technology in a retrofitted cryogenic freezer to preserve a blood plasma simulant. A novel heat pipe was developed and installed in a retrofitted liquid nitrogen batch freezer and examined in this thesis, in comparison to an injection-based system. The developed heat pipe system consisted of two tube bundles connected by a bottom header. The condenser section of the heat pipe is located in the annulus of a cooling coil containing liquid nitrogen

The thermal performance and freezing capabilities were investigated experimentally in both freezer schematics to preserve a blood plasma simulant consisting of water and glycerol. Both freezer prototypes were further simulated via CFD to determine any thermal discrepancies. Both freezer prototypes were discussed at a multitude of set points and fan rotations. It was observed that the addition of the heat pipe greatly influenced the temperature distribution across the freezing chamber. The associated change in the solidification pattern was investigated experimentally and via CFD simulations. The visualisation for the solidification process was conducted by defining the change of fluid properties in relation to the applied boundary conditions. The results were analysed by a mean average percentage error, which compared the numerical accuracy of the solidification model to validate the experimental results. The outcome reflected a good agreement between the model and the experiment.

The outcomes from this research have been published in international journals and conferences. The remainder of the research work is being prepared for publication.

Publications

Published Papers

Jouhara H, Chauhan A, Nannou T, Almahmoud S, Delpech B, Wrobel LC. Heat pipe based systems - Advances and applications. Energy 2017;128:729–54. doi:10.1016/j.energy.2017.04.028.

Celades I, Gomar S, Romero F, Chauhan A, Delpech B, Jouhara H. Acid emissions monitoring needs in ceramic tile industry: Challenges derived from new policy trends 2017;22. doi:10.1051/e3sconf/20172200026.

Jouhara H, Almahmoud S, Chauhan A, Delpech B, Bianchi G, Tassou SA, et al. Experimental and theoretical investigation of a flat heat pipe heat exchanger for waste heat recovery in the steel industry. Energy 2017;141:1928–39. doi:https://doi.org/10.1016/j.energy.2017.10.142.

Jouhara H, Almahmoud S, Chauhan A, Delpech B, Bianchi G, Tassou SA, et al. Experimental and theoretical investigation of a flat heat pipe heat exchanger for waste heat recovery in the steel industry. Energy 2017;141:1928–39. doi:10.1016/j.energy.2017.10.142.

Jouhara H, Khordehgah N, Almahmoud S, Delpech B, Chauhan A, Tassou SA. Waste heat recovery technologies and applications. Therm Sci Eng Prog 2018;6:268–89. doi:https://doi.org/10.1016/j.tsep.2018.04.017.

Delpech B, Milani M, Montorsi L, Boscardin D, Chauhan A, Almahmoud S, et al. Energy efficiency enhancement and waste heat recovery in industrial processes by means of the heat pipe technology: Case of the ceramic industry. Energy 2018;158:656–65. doi:10.1016/j.energy.2018.06.041.

Chauhan A, Trembley J, Wrobel LC, Jouhara H. Experimental and CFD validation of the thermal performance of a cryogenic batch freezer with the effect of loading. Energy 2019;171:77–94. doi:10.1016/J.ENERGY.2018.12.149.

Brough D, Mezquita A, Ferrer S, Segarra C, Chauhan A, Almahmoud S, et al. An experimental study and computational validation of waste heat recovery from a lab scale ceramic kiln using a vertical multi-pass heat pipe heat exchanger. Energy 2020;208. doi:10.1016/j.energy.2020.118325.

Conference Papers

Jouhara, H. Mesquita-Marti, A. Ferrando, S. Ferrera, C. Chauhan, A. Almahmoud, S. Gibbs A. Experimental Investigation on a Vertical Multipass heat pipe heat exchanger applied within the ceramic industry. 2nd Int Conf Adv Energy Syst Environ Eng Confernence Proc 2019.

Chauhan, A. Jouhara H. CFD Performance Of An Industrial Sized Multipass Heat Pipe Heat Exchangers (HPHE). 11th Int Conf Sustain Energy Environ Prot Conf Proc 2018. **Award Won For Best Presentation**

Jouhara, H. Delpech, B. Almahmoud, S. Chauhan, A. Boocock, M. Wrobel, L. Carrau,I. Carrau F. Heat pipe based heat exchanger for clean yerba mate drying process. 10th Int Conf Sustain Energy Environ Prot Conf Proc 2017.

Almahmoud, S. Delpech, B. Chauhan, A. Serey, N, Jouhara H. Experimental and theoretical investigation on heat pipe shell and tube heat exchanger. 1st Int Conf Adv Energy Syst Environ Eng Confernence Proc 2017.
Chauhan, A. Almahmoud, S. Jouhara H. CFD MODELLING OF A MULTIPASS HEAT PIPE BASED HEAT EXCHANGER. Proc SEEP2017 2017.

Chauhan A, Herrmann J, Nannou T, Trembley J, Wrobel L, Jouhara H. CFD model of a lab scale cryogenic batch freezer with the investigation of varying effects on the heat transfer coefficient 2017;123:256–64. doi:10.1016/j.egypro.2017.07.260.

Acknowledgements

Firstly, I would like to express my thanks and gratitude towards my supervisor Professor Hussam Jouhara. Firstly, I would like to thank him for this wisdom and guidance throughout the PhD process. Secondly, I would like to thank him for the countless opportunities to expand my repertoire of applicable engineering and life skills ranging from research opportunities to my career development. Lastly, I would like to thank him for his mentorship throughout the past three years.

I would like to thank Jon Trembley from AirProducts PLC for the continuous industrial support and advice. I would like to thank him for the countless research opportunities he has provided throughout the past three years.

I would like to express my gratitude towards Professor Luiz Wrobel, whose support, knowledge and suggestions has been invaluable. I would like to thank him for his advice and his patience.

I would like to thank my friend and colleague Dr. Sulaiman Almahmoud for his on-going support and advice for any technical difficulties.

I would like to thank my friend and colleague Bertrand Delpech, for his on-going support and advice during my experimental validation and progress through this PhD process.

I would like to thank my friend and colleague Lujean Ahmad, for her support and friendship. I would like to thank her for always making time to listen during the difficulties of my research.

I would like to extend my gratitude towards the researchers within Professor Jouharas' research group, whose friendship and comedic quips improved the PhD experience.

Lastly, I would like to thank my parents, friends and extended family for their emotional support, I would like to thank them for their words of encouragement and motivation during this difficult time.

Table of Contents

List of Figures

List of Tables

Nomenclature

Symbol		
A	Area	m^2
a	Thermal diffusivity	m^2/s
a,b,c,n	Solidification constants	-
c	Specific heat	J/kg.K
cp	Specific heat	J/(kg.°C)
D	Thickness	m
D	Diffusivity coefficient	m^2/s
G	Temperature gradient	°C
g	Gravity	-
H	Total enthalpy	kJ/kg
h	Heat transfer coefficient	$W/m^2.K$
I	Identity tensor	-
k	Thermal conductivity	W/m.K
k	Neuman parameter	-
k	Permeability	m^2
L	Latent heat	J/kg
L	Length	M
m	Mass	kg
Nu	Nusselt number	-
P	Pressure	Pa
Pr	Prandtl number	-
q	Heat flux	W/m^2
R	Thermal conductivity difference between both phases	W/m.K
R	Specific constant	kJ/ Kg. K
Re	Reynolds number	-
S	Source term	-
st	Stefan number	-
T	Temperature	K
T	Pure shear tensor	-
t	Time	s
v	Phase change time parameter	m/s
W	Work	kJ

X	Interface position	m

Subscripts

1	Solid
2	Liquid phase
a	Adiabatic
ac	Axial conduction
b	Boiling
C	Condenser
c	Condensation
co	Outer condenser wall
con	Conduction
crit	Maximum
e	Excess time
e	Conductive
E	Evaporator
eo	Outer evaporator wall
f	Frictional
f	Freezing point
f	Film
film	Liquid film
g	Generated
g	Gas
hp	Heat pipe
in	Inner radius
in	Interface (Liquid vapour)
∞	Free stream
L	Liquid (WF)
l	Length
m	Matching
m	Nusselt number constant
m	Initialisation point (Fluent)
mol	Molar
n	Nusselt number constant
nb	Nucleate boiling
o	Initial

Subscripts

o	Initial condition
Out	Outer radius
ref	Reference
S	Surface
solid	Solid
t	Total
v	Vapour (WF)
w	Wall
x	Interface

Greek Symbols

α	Phase fraction	
β	Thermal penetration depth parameter	
β	Thermal expansion coefficient	
Δ	Velocity divergence	1/s
Δ	Difference	-
δ	Thermal penetration depth	m
λ	Phase change parameter	-
μ	Dynamic viscosity	Kg/m.s
ρ	Density	kg/m^3
σ	Stress tensor	N/m^2
γ	Phase change depth parameter	

Chapter 1 : Introduction

The motivation for this study is based on the development and application of a cryogenic thermosyphon retrofitted inside a cryogenic injection freezer. The initial application of the cryogenic freezer is for the preservation of blood plasma, but the use of liquid nitrogen within the health service is not recommended due to its high costs. The thermal advantages of liquid nitrogen are highly noted in the literature, but the substance carries multiple safety risks such as asphyxiation. The operation of an injection-based system is also popular in the literature with the freezing process being well accepted. The research will investigate the freezing of blood plasma and other simulants using a heat pipe-based cryopreservation technique. The modelling technique has been used in latent heat storage systems and casting processes but has not been previously applied to the visualisation and application of cryopreservation. The modelling accounts for the solidification of blood plasma in a simple single bag schematic but can also be applied to an array of loading configurations. The results of the multiphase model will highlight the potential for its application within multiple cryopreservation technologies to visualise the change in solidification with different preservation technologies.

1.1 General Background

The principle of cryopreservation is a vast subject ranging from food processing to the preservation of mammalian cells. The application of cryopreservation dates back to 1842, with the preservation of produce with water and brine mixtures. The developments led to the usage of cryogenic fluids in the 1920s, with the application being for preservation of fish. The operation is based on air blasting produce to instantly freeze it for transportation to its destination. The flash freezing process commonly occurred within the Arctic and the produce was shipped to the country of choice where it was thawed and consumed [1]. The subsequent mass production freezing techniques expanded to production of plate freezers and immersion freezing. The development was included the development of cryogenic heat exchangers to improve the performance of commercialised cryogenic freezers, this includes the development of cryogenic heat pipes used for cooling. [2–4] The development of heat exchangers within cryopreservation has been widely debated with the new heat pipe technology reflecting the most effective heat exchangers. The general operation of a heat pipe is carried out as a vacuumed tube with a small amount of working fluid inside. A heat source is applied to the evaporator section, which causes a boiling phenomenon inside the tube. The vapour formed travels upwards to the condenser section containing a cooler stream which condenses the fluid. The condensate returns to liquid form and travels back to the evaporator with the

assistance of a wick or gravity as shown in Figure 2-7, and further explained in chapter 2. The operation of the two phase process within a heat pipe is constant operation allowing for it to be a passive structure with super conductive properties and minimal maintenance [5].

The development of new technologies allowed the freezing profiles and characterisation of multiple samples ranging from biological fluids to vegetables [6–8]. The developed technologies highlighted studies reflecting the importance of freezing time in relation to crystallisation and product quality. The optimisation and development of the technology has been investigated by Computational Fluid Dynamics (CFD) simulations allowing the mapping of velocity profiles, highlighting the forced convection within a system [9].The velocity and thermal distribution around a freezing chamber have highlighted the potential of large-scale freezing systems allowing for small samples to large carcasses [10]. Similarly, the application and development of CFD simulations has allowed for the optimisation of a thermally even preservation regime. Thermal variations within a sample have proved to be a hinderance, with significant variations leading to high levels of crystallisation resulting in cell death, making biological substances unsuitable for application or consumption. The visualisation of thermal variance provided by CFD simulation allows for the characterisation and ease of identification of potential crystallisation zones, which can deteriorate the product quality alongside the phase change process from water to ice.

The development of refrigeration and cryopreservation includes the discovery and production of Chlorofluorocarbon (CFC) refrigerants [11]. The discovery allowed multiple pathways and alternatives of freezing technologies and soon became commercialised in domestic appliances. The application of cold air soon became phased out in favour of refrigerant-based systems. The introduction of refrigerants provided heat pipes with a new inert working fluid with flexibility, chemical stability and numerous material compatibilities between the refrigerant and heat pipe wall material acting as a casing material. The application of refrigerants within heat pipes is a widely researched topic, with boiling regime simulated effectively by CFD models [12]. The applications of cooling heat pipes include refrigeration and HVAC appliances. The modern development of heat pipe and cooling technologies is in increasing demand, but the application of refrigerants is dwindling. The Kyoto protocol has limited the production and application of CFC-based refrigerants due to the global warming potential of the substance [13]. The development of low temperature heat pipes including cryogenic heat pipes has been investigated in the form of pulsating and loop heat pipes, allowing the investigation of cryogenic elemental fluids such as helium and hydrogen to reach near absolute temperatures [14]. The application of such temperature ranges does not exist

commercially but highlight the potential for preservation of substances requiring long-term preservation.

1.2 Research Gap

The amount of clinical work in this area is vast, highlighting the importance of cryopreservation with rapid freezing times and minimal amounts of cellular damage. The implementation of direct contact is a frequently applied technology but contains a high contamination risk and is technologically dated. The development of new age freezing technology such as isobaric is still far from commercial applications, with systems being limited to lab scale with a significant number of variables to be defined before commercialisation. Both traditional and new technologies highlight the need for a safe, replicable and scalable method suitable for mass production and implementation. The application of a remote cooling cryogenic heat pipe offers a safe and reliable operation. The present research work highlights the use of heat pipe technology to remotely cool blood plasma with the aid of forced convection within a batch freezer schematic. The amount of numerical simulations is vast with multiple heat pipe heat exchanger CFD applications being available in many fields, including challenging media and high temperature ranges. Similarly, low temperature applications are still limited to experimental applications but the potential to combine heat pipe technology with cryogenic preservation of biological substances has not yet been explored. The current research project highlights the solidification process of blood plasma within a heat pipe-based preservation system.

The visualisation of multiphase processes exists from both liquids, to vapour and liquid to solid. Multiple applications involving multiphase problems have been assumed to be of a single state with the alteration of the thermal conductivity of the conjugate material, including the preservation of aqueous substances used in the food processing industries. The visualisation of the preservation process commonly exists within the modelling of liquid metals and the modelling of latent heat storage systems. The visualisation allows the identification of geometrical changes due to contraction during the casting process. The assumptions during the CFD simulation allow for the solidification to occur on a single state model assuming that the material properties stay constant, with the coexistence of both phases proving to be increasing in complexity and computational instability. Estimations have been quantified to visualise the identification process, but they do not allow a significant visualisation of the mushy zone or crystallisation points.

A limited amount of solidification CFD simulations exists as full transport simulations in both latent heat storage and metal casting. The process of solidification has not been expanded to the visualisation of biological substances.

There is a large gap highlighting the lack of CFD simulations reflecting the solidification process in biological substances where the freezing process is crucial to the preservation of the sample. The research will contain an experimental element which will be used to validate the heat pipe based cryogenic freezer and the solidification of the blood plasma simulant. The validation methods will allow a proof of concept for a novel heat pipe design, and the solidification rate of a blood plasma simulant as defined in Chapter 4. The validation of both experimental works will be conducted via computational fluid dynamics (CFD), the simulations will be carried out with the following objectives:

1. Development of a CFD heat and mass transfer model allowing for phase change to account for solidification from conductive and convective processes on the plasma simulant
2. Subsequent solidification modelling on blood plasma to investigate its solidification properties
3. Accurate modelling of mushy zone interface during solidification process
4. Investigate the solidification rate by testing different boundary layer conditions, to reflect the load position within the freezer
5. Define changes in physical properties using User Defined Functions (UDFs), as these changes have not been previously included in the solidification model.
6. Model the solidification process with the consideration of forced convection and conduction experienced during the preservation process.
7. Model and experimentally investigate the development of a retrofitted heat pipe based cryogenic freezer to preserve a blood plasma simulant, in comparison to a liquid nitrogen injection freezer.

Figure 1-1 shows the overall research scope framework to achieve the listed research objectives. To address the research gap, the scope can be split into two branches: the development of the solidification model and the development of the heat pipe based freezer. The first branch showing the solidification model signifies two sub objectives: developing the CFD model and the associated experimental studies. The combination of these allows for a successful validation and achieving the solidification part of the research scope. The second branch signifies the development and characterisation of a retrofitted heat pipe based freezer. The second branch has been split into two sub-branches which include the CFD analysis and

the associated validation to achieve the second half of the research gap. The achievement of both branches indicates the completion of objectives and the research scope.

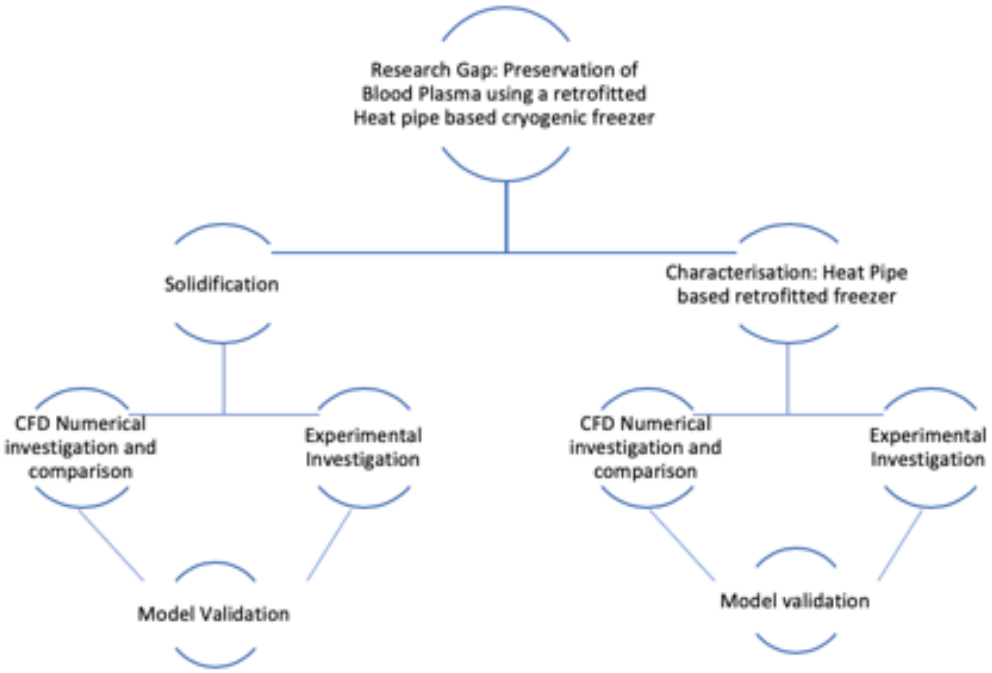

Figure 1-1: Research scope framework

1.3 Thesis scope

The thesis consists of seven chapters defining the research work and the relevant validation methods. The initial chapter includes a general overview of cryogenic preservation, with the focus on the main aims of the research alongside the identified research gap.

The contents of chapter 2 explore the current applications of cryogenic preservation, highlighting the state of the art of the technology and the current innovations with cryogenic heat pipes. The review of cryogenic heat pipes includes the operation of basic thermosyphons and a brief explanation of wicked heat pipes. The various compositions of applicable cryogenic heat pipes in relation to working fluid and shell compatibility are reviewed. The review highlights the depleting availability of working fluids due to the discontinuation of refrigerants, and the complex extraction and rarity of elemental gases.

Chapter 3 defines the heat transfer mechanisms during the phase change process from liquid to solid. The chapter primarily focuses on the definition and growth of ice crystals during the freezing process from conductive and convective processes, with the main focus on the blood

plasma simulant. The heat transfer mechanism during the phase change process will be defined and validated in chapters 5 and 6, respectively.

Chapter 4 outlines the procedure and design method used to develop the novel heat pipe installed within the freezing chamber. The chapter focuses on the composition of the heat pipe and the functionality within the freezing chamber, and the use of liquid nitrogen without direct injection.

Chapter 5 outlines the experimental procedure used to carry out the investigation of the cryogenic heat pipe system. The heat pipe is based on a wickless design, with the main investigation being the thermal effect of the plasma with the implementation of the heat pipe. A set of experiments has been conducted on the proof of concept to characterise the performance of the heat pipe and the methods used to validate the phase change process of the plasma.

Chapter 6 focuses on the CFD theory and validation of the plasma bags. The bags will be investigated in a single bag schematic to outline the preservation process. The traditional method of modelling solidification is via the pull velocities defining the volume change during solidification. The chapter investigates the of modelling solidification with the change in plasma density during the freezing process. This chapter highlights the simulation results with flow visualisation of the plasma simulator phase change from solid to liquid. The CFD model is validated using the experimental techniques discussed in chapter 4.

Chapter 7 combines heat pipe technology and blood plasma preservation methods. The chapter defines the retrofitting of a liquid nitrogen injection freezer with a cryogenic heat pipe. The initial blast freezer acts as a baseline and comparative point of an operational aspect for subsequent heat pipe prototypes. The chapter defines the development of the concept to safely freeze and store blood plasma simulators. The development of each prototype involves the test results alongside the simulation results and the characterisation of the thermal performance of the system.

Chapter 8 concludes the thesis with the discussion of outcomes from the research project, and future recommendations regarding the use of heat pipes for cryopreservation, advances in CFD modelling and the yet undiscovered applications of cryogenic heat pipes

Chapter 2 : Cryopreservation Methods

In order to understand the cellular discrepancies associated with commercialised freezing, it is important to understand the current technology available. The available technologies highlighted in this chapter reflect the importance of freezing rates, preservation quality and heat transfer coefficients, discussed in more detail in chapter 3 and 6.

2.1 Plate freezing

The operation of plate freezers is based on a hollowed out rectangular shelf containing a cooling loop which circulates internally a cryogenic fluid or refrigerant. The product is placed in between two flat plates, where they are cooled beyond the freezing point of the subject. The operation of a plate freezer is based on a feedback system installed within the plates, with a series of probes monitoring the temperature of the plate. The probes indicate the wall temperature of the slab at the point where the product freezes. The technique itself has been investigated within multiple industries, ranging from blood preservation to food packaging.

Goyal et al [15] investigated the implementation of plate freezers within fish preservation samples. The samples are arranged on the base plate of the freezer where fillets were preserved within the system. The freezing rate highlighted a nearly isothermal operation with minimal physical and cellular defects. The investigation stresses that the operation is only applicable to flat objects within the tolerances of 32mm to 100mm, with a flat surface on both sides to ensure maximum contact. The application is unsuitable for curved or uneven surfaces due to the lack of contact, which can lead to improper freezing and unwanted crystallisation. The investigation discussed the preservation of an entire fish but, due to the irregular shape, preservation via plate freezing was not recommended. Creed and James [16] investigated one of the first innovations of plate freezing methods to the preservation of pork livers. The studies showed an effective freezing rate, but the accelerated freezing rate reflected cold burn on the produce. The implementation of plate freezers reflects the versatility of the technology, allowing for small lab scale systems to optimise the development of large systems with various amounts of shelf configurations.

Dopazo and Seara [17] investigated the potential for carbon dioxide as a refrigerant by using the expelled latent heat during evaporation. The system reached approximately -55°C, with the main product being frozen consisting of rectangular blocks of water. The implementation of plate freezers faces multiple issues from a mechanical aspect and a biological aspect. Regarding the mechanical aspect, the implementation of plate freezers is an economically

friendly option, being a mass-produced system. The commercially available systems can be manipulated to the desired footprint size, allowing for a quick solution for time dependent freezing issues. On a biological level, the implementation of plate freezers eliminates the risk of cross-contamination between the product and the refrigerant fluid. The use of plate freezers is limited only to flat objects such as rectangular food blocks or malleable packages such as blood plasma bags. The operation of the plate freezer is typically applied in batch processes due to the extremely prolonged down time for the defrost cycle. Figure 2-1 highlights a method currently used for blood plasma preservation. The bags are loaded in a single layer where a single probe is located in one shelf to determine if the product is frozen. The system exists as an off-the-shelf unit, but the lack of sensors within the system has led to a mushy zone in a number of products which are neither liquid nor solid. The variation in product temperature can lead to irregular product quality, which is crucial when preserving blood plasma.

Figure 2-1: Plate Freezer used for Preservation of Blood Plasma

2.2 Immersion Freezing

Immersion freezing is one of the most frequently used freezing techniques. The process involves submerging a product inside a cryogenic fluid tank, either through direct contact with a bio-compatible fluid or in a protective sleeve. The high heat transfer coefficient of the refrigerant allows rapid freezing with minimal amounts of crystallisation, which is ideal for food preservation with regards to cell quality. The application of this technology has progressed by the addition of ultrasound assistance. The implementation of ultrasound prevents the formation of bubbles and cavities on the surface of the product, as the sound waves disrupt the flow field by allowing for additional turbulence and overall improving the heat transfer and accelerating the freezing process. The studies involving ultrasonic freezing methods allows the manipulation of ice crystals, allowing for longer preservation of the sample.

Zhang et al [18] implemented ultrasonic assisted immersion freezing on a pig carcass. The study compared immersion freezing and air blast freezing with ultrasound assisted immersion freezing. The results reflected a shorter phase transition time during the total freezing time, allowing for limited crystallisation due to the increased forced convection during the process. The test was conducted with increasing ultrasound intensities, reflecting a significant decrease in freezing time until a point where the thermal conductivity of the moisture within the matter increased, prolonging the freezing time. In comparison to unassisted immersion freezing, the presence of large ice crystal formation is vast, with the main implementation being the investigation of moisture rich samples such as fruit and vegetables. Liang et al [19], investigated the quality of litchi fruits during immersion freezing. The study was compared to air blast freezing, with the investigation of the change in microstructure and ice crystal production. The freezing technique was conducted with a biocompatible substance which was a mixture of water, alcohol, glycol and sodium chloride. With the litchi fruit itself being an existing moisture rich food, the formation of ice crystals significantly reduced when preserved via immersion freezing. The results reflect a rapid freezing rate, with the difference in freezing times being six times shorter than with air freezing injectors. The selected immersion freezing study used an alternative fluid to liquid carbon dioxide, but it is worth noting that the litchi fruit was preserved within a nylon composite bag which was previously water treated. The effect of water treatment is applied to prevent the darkening of fruit and moisture loss, to prevent litchi fruit extend past the pre-treatments. The immersion fluid mixture is based on humectants, which play a key part in retaining the moisture within the fruit and in the success of this specific application. The use of humectants has also been applied in the preservation of strawberries, another moisture rich fruit.

Galetto et al [20] investigated the potential of immersion freezing of strawberries using a calcium chloride suspension. The basis of the suspension is used to increase the structural integrity of produce. The fruits were pre-treated in a pectin solution to prevent the softening of the fruit by increasing its viscosity to a more gelatinous phase. Both tests, with and without pre-treatment during immersion freezing, showed minimal difference in the firmness of the fruit. The application of immersion freezing highlights a flexible system, with the range of fluids available being adaptable to the requirements of the samples. The selection of fluid and pre-treatment is the basis of immersion freezing success, with the freezing process improving the sample quality by the manipulation of chemical properties. Immersion freezing has been applied to the preservation of blood plasma. The plasma is stored within blood bags and placed within an immersion freezing unit as shown in Figure 2-2. The figure highlights blood bags being placed within wallets arranged in a baffle configuration to maximise the available heat transfer area. The technology assures frozen plasma, but the risk of cross-contamination is high. Due to stringent rules within national blood banks, the contamination of the label is strictly prohibited. The technology poses a high risk if the plasma collection bag is compromised.

Figure 2-2 Immersion Freezer used for Blood Plasma Storage

2.3 Injection Freezing

Injection freezing involves the utilisation of a cryogenic fluid sprayed continuously during the freezing process. The process of injection freezing is regularly used in large food processing units requiring mass production as shown in Figure 2-3. The application of injection freezing employs liquefied versions of nitrogen and carbon dioxide.

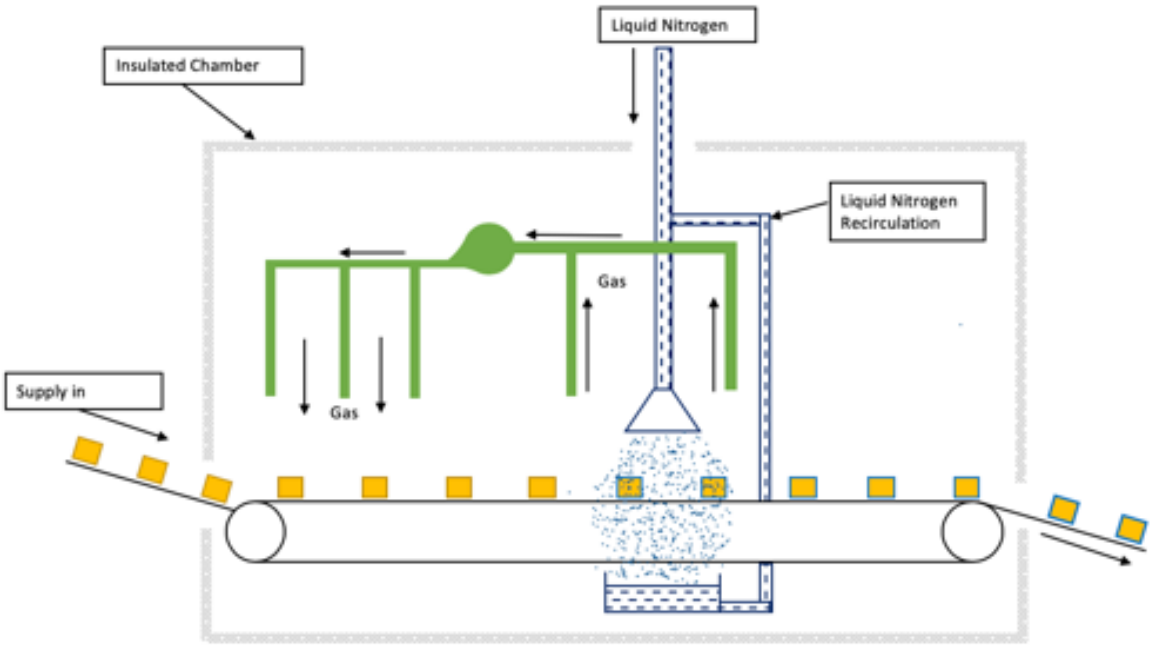

Figure 2-3: Schematic of Injection Freezer Operation

The process of injection freezing can exist in multiple forms such as a tunnel and a chamber format, but both methods allow for continuous freezing operations. The use of cryogenic freezing has allowed the flexibility of freezing any item of any compatible size to the system. The system has been implemented to the preservation of dates. Alhamdan et al [21] investigated the preservation of fresh date with a cryogenic freezing process. The elasticity of the fruit reduced when preserved using slow freezers in comparison to a liquid nitrogen-based cryogenic freezer. The use of slow freezers increased the rate of crystallisation due to the prolonged freezing time, thus deteriorating the product quality. Agnelli and Mascheroni [22] evaluated the quality of cryogenically frozen produce. The study highlighted the effects of each freezing method in relation to product quality with moisture rich and dry produce. The technology involved a pre-treatment with liquid nitrogen before being processed through a tunnel freezer. Various moisture level produce such as chicken, mushrooms and strawberries were processed through the two-step process to highlight aesthetic and textural changes alongside changes to moisture levels. The samples were equalised to ensure identical dimensions and mass and entered the cycle for equal periods of time. The results reflect the

selected samples darkening due to the change in the formation of ice crystals, with an increase in surface hardness. The application of tunnel freezing exists within the food industry due to its quick-freezing rates and potential for constant production. Gonçalves and Ribeiro [23] investigated the implications of an injection-based system on the processing of raw shellfish with a phosphate-based treatment to minimise drip loss. The use of an injection freezer has been used in conjunction with an air blast freezer before it reaches a storage facility. The addition of a preservative highlights the improved drip loss experienced during the freezing process without the hardening of product experienced during cryogenic freezing. The performance of impinging cryogenic freezers has been widely analysed. The capabilities of cryogenic freezers and injection systems are some of the most effective ways of rapidly freezing produce and samples. One of the similarities between the studies described is the scalability and usage of each system. The studies all highlight the implementation of injection-based systems within the food industry where mass production Is required. Studies involving injection-based systems for cryopreservation are limited due to the continuous belt operation of the freezer [24].

The process of injection-based systems has been widely noted in the literature for both numerical and experimental studies. Chauhan et al [9] investigated the thermal distribution around a lab scale batch freezer. The study was conducted experimentally and through numerical simulations. The study highlights the application of a liquid nitrogen injection-based batch freezer in the preservation of blood plasma simulants. The apparatus involved a freezing chamber equipped with liquid nitrogen injectors, with the addition of loading shelves. The results highlighted effective freezing times, the parallel CFD simulations related to the process showed a relatively even heat transfer, although the plasma bags located closest to the injectors presented a significantly higher heat transfer coefficient which could lead to an altered crystallisation rate. The study offers a novel application for existing freezing methods optimised for the cryopreservation of blood plasma. Typically, food industry grade freezers are inapplicable due to the mass production of food, whereas the preservation of blood plasma is commonly processed in batches due to the prior stabilisation periods.

2.4 Air Blast Freezing

The principle behind air blast freezing is the cooling of a product with cold air jets or streams of precooled air as shown in Figure 2-4.

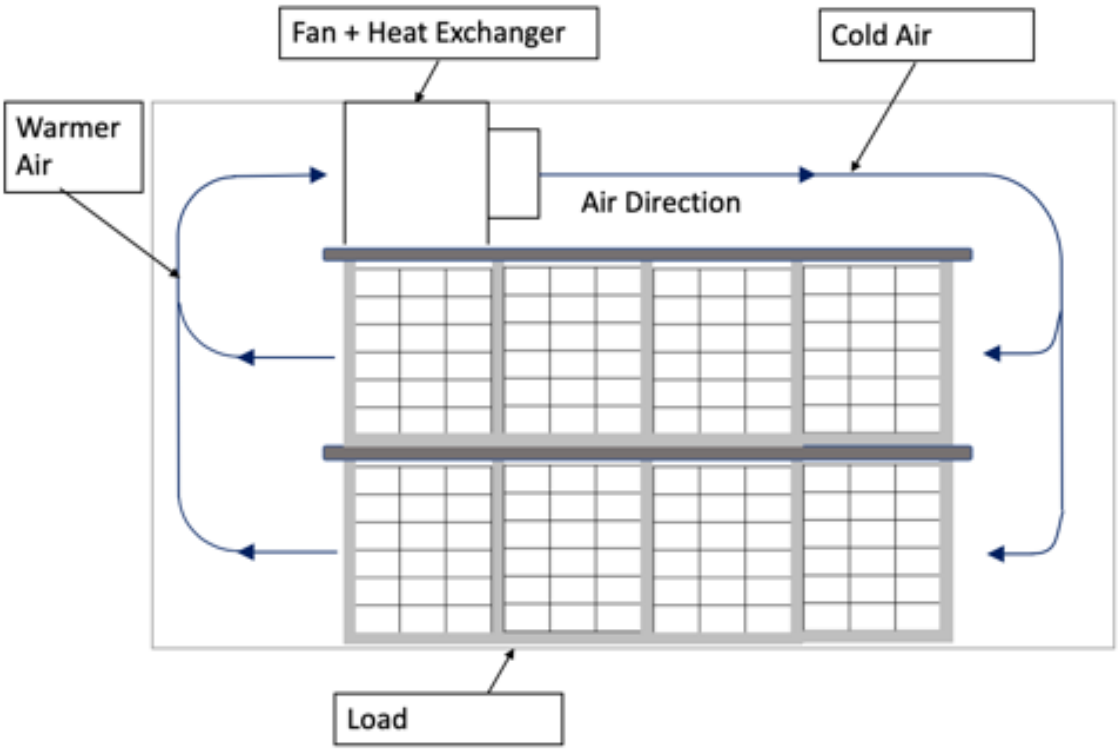

Figure 2-4: Schematic of Air Blast Freezer Operation.

The application of air-cooling acts as a benchmark comparison for other freezing technologies. Air freezing has been applied in multiple industries ranging from vegetables to meat carcasses. Sun et al [25] investigated the performance of air freezing comparatively against other freezing techniques, such as immersion freezing, in relation to ice crystal size whilst preserving carp. The samples were pre-cooled as a preservation step, and then placed into the respective freezing chamber and immersion pool and frozen within a specified time period. The results demonstrated that the level of ice crystal formation is higher in air freezing in comparison to immersion freezing. The physiological effect of air freezing has been investigated on a molecular level with the preservation of probiotic bacteria. Volkert et al [26] states the cellular damage that can occur at low and high freezing rates, allowing an optimum performance of air blast freezing. The study on the effects of air blast freezing with regards to crystallisation has been developed with turbot fillets, with air freezing reflecting smaller but frequent ice crystals within the sample regardless of the preparation method. The implementation of air blast freezing seems questionable based on the thermal performance of the system. Chourot et al [2] investigated the economic model for freezing techniques. The study compares the viability of all three technologies in a case study where equal operating times and load conditions are assumed. The study highlights immersion freezing as the most cost-effective option whereas cryo-mechanical is the most expensive. With the progress and

results in immersion freezing technology being rapidly enhanced, the addition of air blast freezing seems questionable.

Gazda [27] defined the potential of a hybrid system which utilises both air and a cryogenic refrigeration system. The proposed system contains multiple operations which, when combined, allows less fluctuations in air temperature and also the enhancement of freezing when reaching -30°C. The system offers a greater versatility compared to plate freezing, which is size limited. A combination of both technologies causes a sharp decline in temperature, which does not allow cells to readjust to the air temperature and contribute to cellular damage and the reproduction of bacteria. The combination of blast freezing, and cryogenic cooling allows the advantages of forced convection with the freezing benefits of cryogenic fluids. The operation of the blast freezer is variable, allowing the option to increase the level of forced convection, which can be useful as moisture-rich products require a rapid freezing time to prevent deterioration.

Air blast technologies have been applied experimentally and numerically to constant production units. Dima et al [28] investigated the cryopreservation of marine shellfish . The study was primarily focused on the experimental and numerical simulation of the preservation of crab meats, ranging from claws to meat packages. The experiment consisted of the recirculation of cold air on the crab produce to effectively freeze the produce, and a combination of experiments was conducted in conjunction with a numerical model to predict the freezing regime. Unlike traditional numerical models, the developed model allowed the consideration of minerals and the exoskeleton. The model effectively predicted the freezing performance when the sample entered the air blast system. The implementation of such validated models highlights a new potential of air blast freezing by allowing the prediction of freezing rates for a previously unpredictable substance. The determination of heat transfer coefficients for air blast-based systems has been widely studied by Becker and Fricke [29]. The research highlights an analytical method used to determine the heat transfer coefficient for complex shapes with air blast cooling. Unlike cryogenic quick freezers, the freezing profile of an air blast system has a relatively low Biot number which leads to a thermal variation, which has contributed to the low use of air blast systems within cryopreservation. The definition of heat transfer coefficients has led to improvements within the system.

Reno et al [30] defined the energy consumption and heat transfer coefficients for the preservation of guava pulp stored in vats and large barrels. The preservation of guava pulp vats was optimised using isothermal contour plots. The results highlighted the improved recirculation, with the adjustment of storage from vats to drums being the most influential. The

implementation of vats highlighted an increasing isothermal profile but, due to the sheer capacity, both freezing time and energy consumption was poor. The study reflected the success of smaller rectangular batches where both freezing times and energy consumption is beneficial. From this overview of air blast systems, it is evident that air blast technology is applied in the food industry. Although multiple technological and numerical breakthroughs have been made, the technology still risks inefficient freezing times which may not be enough to reduce the metabolic rate of cells to prevent deterioration

2.5 Electromagnetic Freezing

The development of commercial electromagnetic freezing is a relatively new technology with key innovations occurring within the past few decades. The principle follows a basic freezing process but with the introduction of static and oscillating electromagnetic waves. Electrodes are attached to the sample and a current is passed through as shown in Figure 2-5

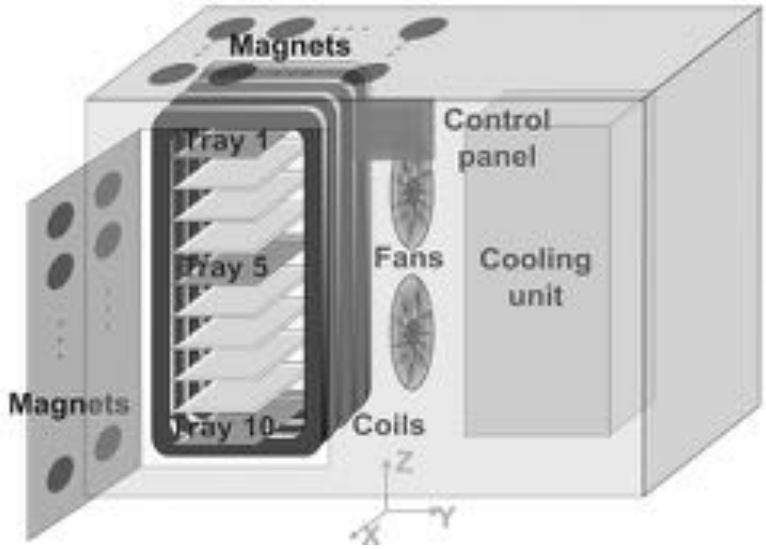

Figure 2-5:General Schematic of an Electromagnetic Freezer [31]

The electrodes' role is to create predictable sites of nucleation in comparison to spontaneous locations. The implementation of flat electrodes can cause some issues with regards to electrolysis within the sample, which can alter the product quality. A similar issue within liquids occurs when gaseous bubbles are produced as a result of electrolysis and chemical reactions between the probe and the substance. The studies regarding electromagnetic freezing allowed the development of controlled nucleation, allowing the product to stay at a subcooled temperature whilst remaining unfrozen, acting as an ideal development for food chillers. The manipulation and prolonged supercooled stage results in a shorter freezing time with the development of smaller ice crystals, with biological tests showing minimal difference between fresh produce.

Otero et al [32] investigated electromagnetic freezing on crab sticks to reduce the formation of ice crystallisation and the damage caused to produce. The test was conducted in comparison to air freezing and non-electromagnetic freezing. The tests were conducted at a low frequency to determine the effectiveness of the system. The results from the low frequencies reflect a prolonged phase change point, allowing the production of ice crystals and thus reducing the quality of the product. Electromagnetic freezing has been as a primary form to be used in the cryopreservation of brains. The utilisation of electromagnetic fields within cryopreservation has been hotly contested, with a significant number of unknowns such as the rate and alteration of nucleation. The change in volume experienced by water during the freezing process is widely noticed and linked to the risk of cell injury due to ruptured membranes. The risk of cell injury is a key parameter for the preservation of biological substances; when applied within an electromagnetic field, the alteration and change in rate of nucleation, experienced by biological samples is an unknown, with no prospect or prediction on the freezing pattern/ time for each preservation sample. The study conducted by Kobayashi and Kirschvink [33] highlights the applicability and change in nucleation for the preservation of livers containing an electromagnetic precipitate. The study was based on organs containing natural precipitates as a result of a lifetime with environmental factors, with the preservation with a low range electromagnetic freezing regime. The premise behind the technology highlights the further disturbance of the nucleation points, allowing for a prolonged subcooling time. The results reflected no major difference in subcooling time due to the reduced amount of electromagnetic precipitate and the magnetic field applied. One of the parameters of the study is the potential variation in precipitate throughout different samples, which may contribute to the nucleation points for each sample.

An investigation of electromagnetic waves and the subsequent nucleation was conducted by Dalvi-Isfahan et al [34]. The study highlights the importance of the electrode probes used, highlighting that the roughness of the surface will inhibit the nucleation process and crystal growth with unknown effects due to the varying surface roughness. Depending on the water concentration of the produce, the effects of electromagnetic freezing can accelerate nucleation and cause cavitation, which can subsequently lead to a secondary nucleation. The process of secondary nucleation is caused by vibration experienced by molecules, which leads to electromagnetic heating during crystal formation which melts sections of the formation. The process of secondary nucleation significantly changes the freezing profile of a substance, leading to irregularities within the product such as irregular ice crystal formation. The application of electromagnetic freezing has been investigated by Kaku et al [35] with periodontal ligaments for the application of tooth banking. The application involved the long-term storage of pre-treated periodontal ligaments for subsequent transplantation. The study

was compared against a traditional air blast system at a range of electromagnetic frequencies. The results highlighted an improved freezing time with the addition of electromagnetic frequency with minimal presence of irregular nucleation patterns. The use of the cryoprotectant prevented intercellular ice crystals, maintaining the integrity of the preserved sample. Although cryoprotectants are widely used, they are highly toxic which poses the question of whether such samples can be re-transplanted.

Both low oscillating electromagnetic frequencies and air freezing proved to offer similar freezing rates in comparison to static magnetic fields. The development around electromagnetic freezing offers industries the potential to freeze produce effectively with minimal cellular damage, but its widescale implementation is yet to be explored. Variables such as probe material, probe dimensions, biological compatibility, effect of additives and design patents are yet to be defined before large scale implementation.

2.6 Isochoric Freezing

Recent technologies allowing the development of systems to preserve produce at sub-freezing temperatures whilst minimising cellular damage due to ice crystal formation are quickly progressing. These new age freezing technologies allow for the development of isochoric freezing. The principle behind the technology is to lower the product into a chamber filled with a fluid that is in an osmotic equilibrium with the product, minimising the risk of dry-out on a cellular level as shown in Figure 2-6.

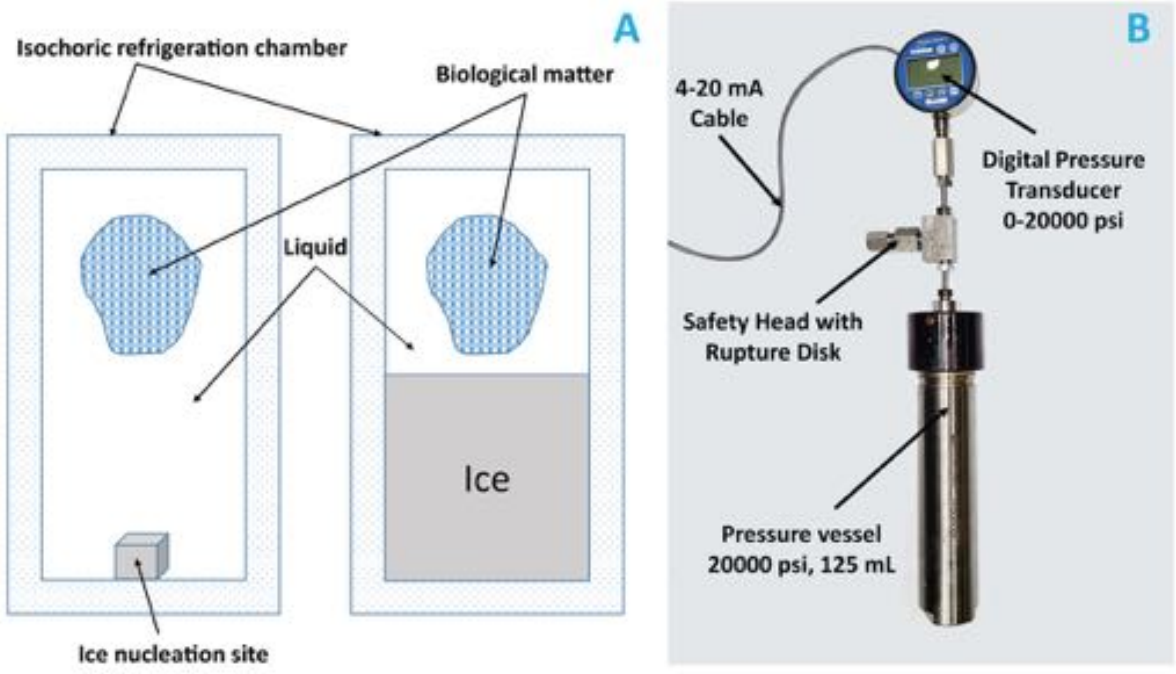

Figure 2-6: Schematic of Isochoric Operation [36]

The chamber temperature is reduced to the freezing point of the product, where ice crystals will begin to form. The ice formation will increase the pressure within the chamber until an equilibrium is reached between the ice and chamber fluid. The premise of the technology follows Le Chateliers relationship between the declined production of ice crystals within high pressure vessels. Sainz et al [37] investigated the implementation of isochoric freezing for the preservation of cherries. The samples were regulated prior to freezing by being placed within an ice bath before being placed within the isochoric chamber. The chamber reached a stable pressure of 29.5 MPa and remained at a constant pressure. The results reflected that a significant amount of cell damage occurred with the decrease in antioxidant levels when tested, which may be due to a high hydrostatic pressure during testing. Isochoric freezing has been deemed to be a progression of cell and organ preservation, with recent developments of the preservation of mammalian cells. Preciado and Rubinsky [6] investigated the potential of isochoric freezing on canine kidney epithelial cells suspended within a phosphate solution. The premise of the study is based on the lack of ice crystals occurring, eliminating the risk of cellular damage and cell death. The results highlighted only 0.075% of dead cells, with the majority alive at an atmospheric controlled pressure. The results also highlighted an increase in cell death with an increase in pressure up to 205MPa. Most studies involve the addition of a cryoprotectant to maximise the cellular preservation of the system.

Nastase et al [38] investigated the preservation of fish with isobaric freezing systems without cryoprotectants, with the main concern being cellular dehydration. The results demonstrated minimal change in cell damage with minimal dehydration effects. The system reflects the real-life aspect of the system without the addition of time intensive treatment processes. The key variable in isochoric freezing has been its application to biological samples—in particular the preservation of rat hearts. The study conducted by Wan et al [39] included an entire heart; presenting a novel application where traditional samples are commonly samples of tissue. The heart was placed within a chamber filled with a mixture of glycol and water. Prior to freezing, the sample was treated with an intracellular solution acting as a cryoprotectant to prolong the metabolic rate and thus prevent deterioration of the heart tissue. The chamber itself was precooled to 4°C before the heart was loaded into the system, and then sealed and preserved at -4°C to -8°C at a varying pressure. The results reflect the decline in muscle integrity in relation to the reduction in temperature when applied with a flow field to investigate the effectiveness of atrial muscles. The results also highlight the significant influence freezing techniques have in relation to the lack of application of biological cells post freezing. The samples reflected an increased hardness as expected, but the microscopic cellular damage highlighted disruptive cells used for ventricular action. Such cells can be preserved with an array of cryoprotectants, but this is unsuitable in this case due to the toxicity factor when

transferred back into an integrated pre-existing circulatory system. The study highlights an interesting aspect regarding the applicability and compatibility for transplants. Previous studies conducted by Takahashi et al [40] used a similar technique to preserve rat livers, the progression of freezing-thawing and re-transplanting highlighted a significant amount of cellular damage with livers preserved at -4°C. The progression from freezing to transplantation poses an interesting and potentially problematic development. The re-transplantation of rat livers back into recipients was successful but caused subsequent organ failure. The potential for cryopreservation for complex organs exists with successful subcooling operations, but the cell injury associated with the preservation of complex organs remains an unviable option.

2.7 Cryogenic Heat Pipes

2.7.1 Heat pipe operation

2.7.1.1 Thermosyphon Operation (Gravity Assisted)

The configuration of a heat pipe consists of a hollow hermetically sealed pipe containing a small amount of working fluid as shown in Figure 2-7. The structure is split into three sections: the evaporator, condenser and an adiabatic section. The hollow chamber exists as a void to allow a phase change process occurring within the pipe. The simplest form exists as a gravity assisted operation where the condenser is located above the evaporator. In scenarios where the pipe geometry is complex or when the condenser is below the evaporator, a wick may be added.

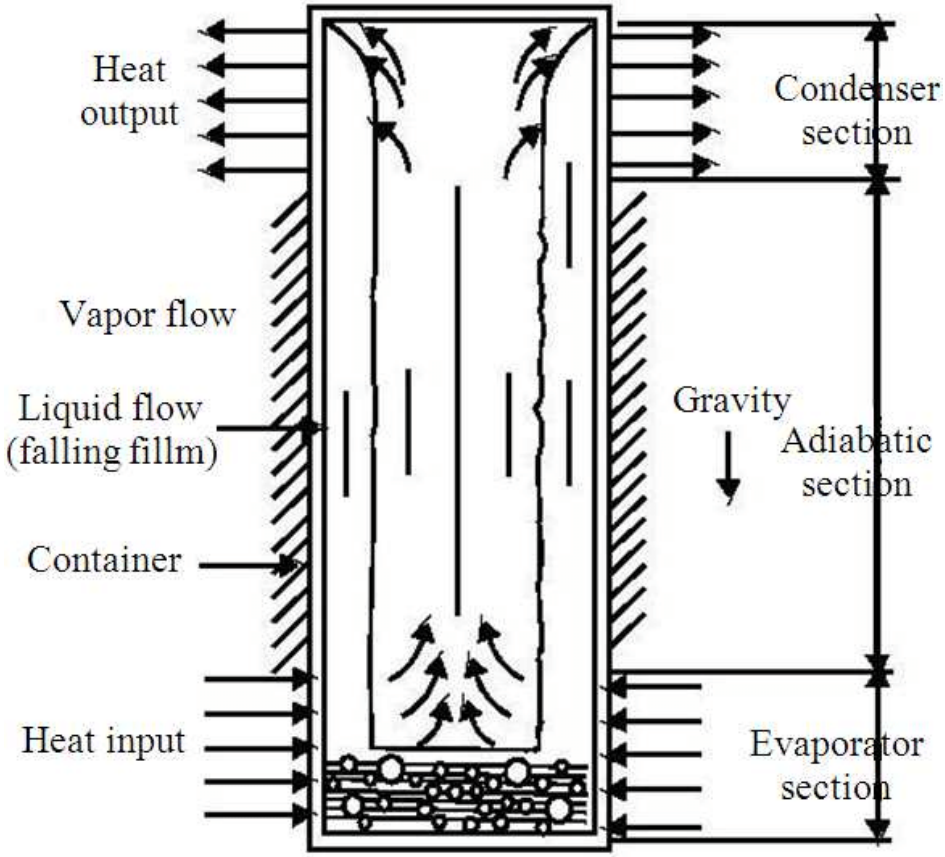

Figure 2-7: Schematic Highlighting the Thermosyphon Operation [41]

The heat pipe is filled with a compatible working fluid, and a flow stream is applied where the working fluid can reach the saturation temperature for the phase change cycle to begin and continue. When a heat source is applied to the evaporative section, the working fluid is heated until boiling occurs. The working fluid will vaporise, the pressure difference between the two phases causes the vapour to rise to the condenser section. The vapour releases the latent

heat to the condenser flow stream and returns to a liquid state. The liquid returns to the liquid pool in the evaporator via a wick or by gravity. The two-phase cycle is continuously in operation with uninterrupted evaporation and condensation.

2.7.1.2 Wicked Heat Pipes

The operational processes of gravity-assisted and wicked heat pipes are similar and rely on the same two-phase changes to transport heat to the cold stream of the condenser section. The main difference between thermosyphons and wicked heat pipes is the mechanism through which the condensate returns to the evaporator. Thermosyphons rely on gravity to return the condensate to the evaporator whereas wicked heat pipes rely on a wick as the evaporator is located above the condenser. Wick structures are a common addition to complex heat pipe design, including those involved in anti-gravity applications as shown in Figure 2-8 [42]. The application of wicks provides flexibility to heat pipe design by allowing infinite design possibilities. The selection of wick types is vast, but the selection is significantly dependent on the porosity, thermal conductivity and the minimal capillary radius.

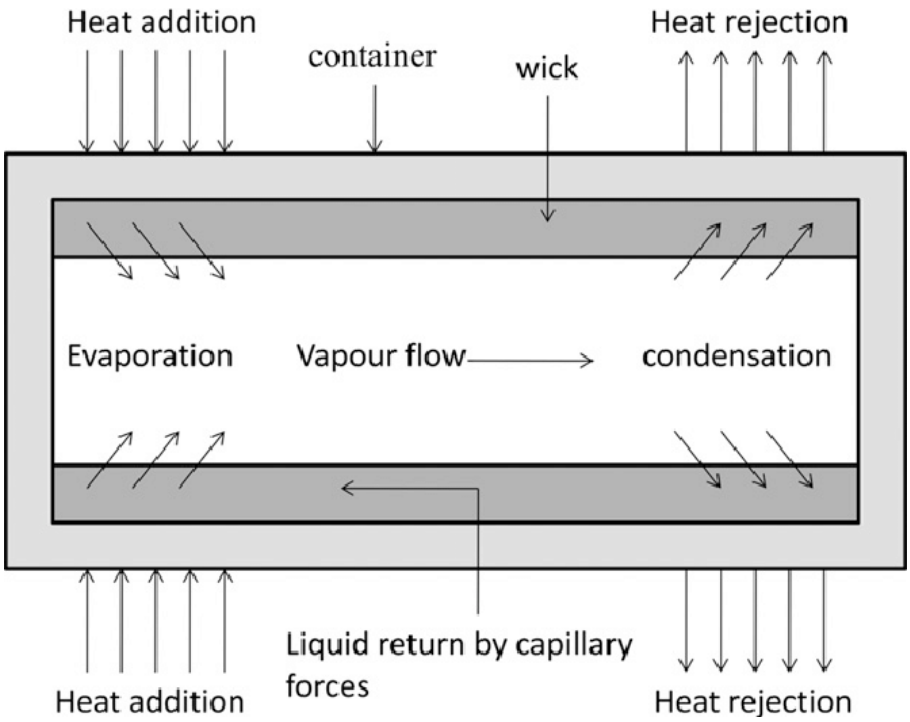

Figure 2-8 Schematic highlighting the operation of a wicked heat pipe

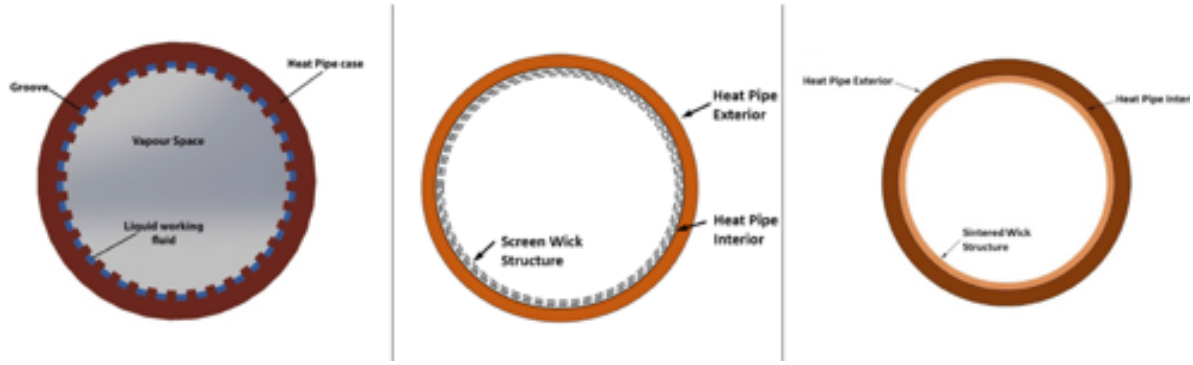

Figure 2-9: Selection of wicks used in wicked heat pipes (a) grooved wick (b) screen mesh (c) sintered wick

The most common types of wicks are sintered, grooved and screen mesh as shown in Figure 2-9a-c [43]. For cryogenic applications, the operation of loop heat pipes is highly dependent on wicks. Wicks within loop heat pipes are usually applied through the compensation chamber forming part of the evaporator system, to ensure that there is always working fluid in the compensation chamber section of the loop heat pipe to prevent dry out.

2.7.2 Compatible shell material

The operation and thermal performance of the heat pipe is dependent on multiple variables, including the shell material of the pipe. The material properties play a key role from both a thermal aspect and from a mechanical aspect. The casing material needs to have a high thermal conductivity to optimise the system, but also to be mechanically strong. Typically, the casing is constructed from metal, but recent developments have indicated a rise of flexible silicone casing materials. The casing material needs to be compatible with the working fluid to prevent the formation of non-condensable gases or chemical reactions, which could hinder the heat pipe performance.

2.7.3 Working Fluid Selection

The availability of working fluids for heat pipe technology is endless, with the working fluid spectrum ranging from 1000°C liquid metals to -268.9°C cryogenic liquids such as helium. The selection of an appropriate working fluid is crucial to the operation of the heat pipe, with each fluid having a specific set of operating temperatures. The combination of working fluid and shell material must be compatible as chemical reactions can occur at the interface of both materials, leading to the production of non-condensable gases (NCG) which will hinder the thermal performance of the heat pipe by being swept to the condenser section whilst in operation, lowering the wall temperature of the condenser.

The determination of the heat pipe is widely based on the operational range of the working fluid. The selection of working fluid is also dependent on multiple factors such as:

- Operational limits
- Optimum vapour pressure
- Chemical stability
- Wettability
- Compatibility between fluid and shell material
- High latent heat

The characterisation of working fluids in cold applications can be sub-categorised as two entities: cryogenic and low temperature. The category of low temperature is based on fluids operating up to -70°C. Cryogenic heat pipes operate at -70°C and below with an organic working fluid such as ammonia, but other working fluids can be used such as methanol due to the short carbon chain. The selection of working fluids shown in section 2.7.3.1 reflects categorised working fluids. Ideally, the preferred working fluid is water due to stability and economic viability, but due to the temperature range the applicability within cryogenic heat pipes is non-existent. Typically, the most common working fluid is a refrigerant such as R410a or R134a, combined with copper or steel. Other working fluids include Nobel gases, Alkanes, alcohols and organic compounds.

2.7.3.1 Low temperature working fluids.

Refrigerants

The application of refrigerants as a working fluid within heat pipes seems like a good choice due to the inert chemical properties and versatility between multiple shell materials. The implementation of the Montreal protocol outlawed the use of refrigerants containing chlorofluorocarbons (CFC) due the associated environmental effects and the contribution towards the depletion of the ozone layer. The protocol has resulted in multiple stable refrigerants phased out, such as: R22, R11, R21, R113 (CFC based), which has led to a need to develop alternative refrigerants with a lower global warming potential. Table 2-1 highlights the currently available refrigerants which can be used as a working fluid.

The result from the restriction of refrigerants has significantly shrunk the available refrigerant based working fluids, with the choice being Hydrochlorofluorocarbons (HCFC). The prospects for refrigerants are bleak with a complete halt to production and import of HCFC in 2030. Refrigerants have been applied within multiple industries such as HVAC and within

wraparound loop heat pipes (WLHP) for cooling systems within hot and humid climates. The use of WLHP was initially investigated in energy efficient and air handling units. The investigation was conducted by Jouhara and Meskimmon [44], and highlights a heat pipe-based HVAC system, the operation of which is primarily based on a loop heat pipe charged with R134a. The system consists of a hot air stream entering the system at the evaporator section. The latent heat of the stream is absorbed causing boiling of the fluid within the pipe. The difference between both vapour and liquid phases allows the vapour to travel to the condenser, where the condensate is returned to the liquid state and back to the evaporator. Most WLHP systems contain a cooling coil which can be wrapped around the condenser to maximise the surface area and the cooling potential of the system whilst providing a dehumidification process. The application of WLHP within HVAC was further developed by Jouhara and Meskimmon [45], allowing the system to replace the refrigerant by water. The study highlights the operation of the system with two configurations: a chiller and a heater, where both variations were conducted at similar inlet velocities, with identical operating conditions.

The comparison between both working fluids highlighted an overall increase in effectiveness for the water charged system. The restriction of refrigerants highlights the obvious needs and requirements for a new age in refrigerants or alternative working fluids. Developments have been progressing to replace R134a with newer refrigerants such as HFO1234ze, R1234yf and R1234ze. The development of such refrigerants is designed to have a low to almost zero global warming potential, whilst harnessing the same thermophysical properties as traditional refrigerants. The replacement of R134a with HFO1234ze within refrigeration systems has been developed by Aprea et al [46], which highlights the new age of refrigerants from a cost effective, environmental and energy efficient standpoint but is extremely dependent on atmospheric conditions. The substance possesses a significant risk of flammability when in warm and humid conditions. For the application of WLHP, the implementation of HFO1234ze as the working fluid could be an alternative due to the hermetically sealed structure but presents a significant risk should the structure be compromised. R1234yf has been applied in a small power refrigeration system in a comparative study with R134a. Gomez and Cascales [47] investigated the GWP of alternative refrigerants within a small power refrigeration system to identify the potential of new age refrigerants. The study consisted of two loops - a refrigeration loop and a water loop, which is linked to a number of auxiliary units used to either heat or pre-cool the water stream to test the capabilities of the refrigeration loop. Both refrigerants were tested at a multitude of flow rates, and the results highlighted a direct relation between the flow rate of the refrigerant and the efficiency of the refrigeration loop. Although both refrigerants promise effective heat transfer rates, there was a sizable difference of 26%

when R134a was replaced by R1234yf. To achieve the same efficiency of an R134a loop, the mass flow rate was drastically increased which resulted in a drastic increase in power consumption. The applicability of new age refrigerants within heat pipes seems positive due to the existing thermal capacity.

Fluid	Symbol	Normal Boiling Temperature	Critical Temperature	Latent Heat of Vaporisation (LHV)	Useful Range	Compatible Casing Materials
Units		°C	°C	(kJ/kg)	°C	
Freon R410a	CH_2F_2, CHF_2CF_3	-48.5	72.8	256.7	-100 to 35	Stainless Steel
Freon R134a	CH_2FCF_3	-27	101	215.9	-75 to 50	Stainless Steel
Freon R113	$CCLF_2CCLF_2$	47.6	214	13.2	-36 to 214	Copper Ferritic Steels Stainless Steel Polymers
Freon 408a	CHF_2CF_3, CH_3CF_3, $CHCIF_2$	-44.4	83.3		-82 to 48	Stainless Steel

Table 2-1: Refrigerants working fluids thermophysical properties [43,48]

Alkanes

Organic alkane chains as working fluids are used in low temperature applications. The use of alkanes has been increasing in popularity due to the large amount of versatility with the available casing materials. Alkanes are relatively stable working fluids with a minimal global warming depletion effect but carry other significant risks such as flammability. The flammability of alkanes is the downfall of their implementation as a special permit is needed for the charging of alkane working fluids. Due to this special requirement, its widescale application is non-existent.

Fluid	Symbol	Normal Boiling Temperature	Critical Temperature	Latent Heat of Vaporisation (LHV)	Useful Range	Compatible Casing Materials
Units	°C	°C	°C	(kJ/kg)	°C	
Propane	C_3H_8	-42	96.8	428	-85 to 57	Aluminium Copper Ferritic Steels Stainless Steel Polymers
Pentane	C_5H_{12}	36.1	196.7	367.3	-20 to 120	Aluminium Polymers
Heptane	C_7H_{16}	98.3	266.8	318	-91 to 267	Aluminium Polymers

Table 2-2: Alkanes working fluid thermophysical properties [43,48]

Alcohols

The usage of alcohols within heat pipes covers a vast temperature range, with alcohols such as methanol ranging from -98°C to 239°C allowing their application to low and mid-range temperature zones. The application of methanol was investigated by Barrak et al [49] within an oscillating heat pipe. The study was based on a comparative analysis against other low temperature working fluids such as aqueous methanol. The study involved a methanol PHP within a ventilation system offering cooling and dehumidification. The heat pipe was constructed from copper and charged with aqueous methanol with a 50% filling ratio. The study highlighted a beneficial dehumidification performance without the need for a cooling coil due to the smaller plugs formed from the mixture. The addition of alcohol to water within heat pipes alters the latent heat of vaporisation, which also lowers the boiling point of the substance. When the mixture is applied within the evaporator, the bubbles produced are significantly smaller in comparison to pure methanol. The smaller vapour plug tends to be more buoyant allowing for a quick progression to the condenser, the accelerated process leading to a higher rate of heat transfer.

Fluid	Symbol	Normal Boiling Temperature	Critical Temperature	Latent Heat of Vaporisation (LHV)	Useful Range	Compatible Casing Materials
Units	°C	°C	(kJ/kg)	°C	°C	
Ethanol	C_2H_6O	78.35	241	837	0 to 130	Aluminium Copper Stainless Steel Ferritic Steels Elastomers
Methanol	CH_3OH	64.6	239	1100	-98 to 239	Copper Ferritic Steels Stainless Steel Elastomers Polymers

Table 2-3: Alcohols working fluid thermophysical properties [43,48]

Organic Agents

Organic agents cover one of the widest useful ranges, from low temperatures of -95°C to high temperatures of 350°C, as shown in Table 2-4 The application of organic agents ranges across multiple heat pipe styles, ranging from simple thermosyphon heat pipe heat exchangers for low grade waste heat recovery to refrigeration cycles. Jouhara et al [50] developed heat pipe-based refrigeration shelves charged with ammonia. The development was used for the application of food preservation where food products were placed on the shelves and cooled simultaneously. The premise behind the innovative technology is based on a gravity-assisted thermosyphon where the food products are frozen via three different heat transfer mechanisms. The refrigeration system uses conduction due to the contact of the food to the food block, convection and radiation from the upper refrigeration shelf. The research presents a comparative study with conventional refrigeration shelves where the thermal variation was investigated. The results from the study highlight an isothermal performance due to the attributes of the heat pipe with an even product temperature. A key parameter of the study is the acidity of the food samples which highlights the increased

metabolic rate and the rancidity of the produce. Overall, the heat pipe-based shelves showed a minor change of 0.1 in the product pH levels.

The use of organic fluids has been compared against compounds such as ethanol. The study conducted by Hao et al [51] highlights the application and comparison of a polytetrafluoroethylene (Polymer) pulsating heat pipe charged with water, ethanol and acetone. The study was conducted for an array of filling ratios and with a variable heat load condition. Both evaporator and condenser were wrapped around heating and cooling blocks, respectively, to represent a heat load and a heat sink. Importantly, the evaporator block allowed a variable heat load ranging from 70W to 300W. As experienced with pulsating heat pipes, a high filling ratio can lead to the lack of pressure differentials between both phases, which leads to a decline in oscillations. The lack of oscillations was evident in this research when all three configurations with a 70% filling ratio were applied, when the system experienced a delayed start up. The difference in operation between the three working fluids has highlighted that acetone charged PHP experienced a higher level of oscillations due to a lower capillary resistance. The lack of resistance allowed the acetone liquid slugs to increase in velocity, improving the overall heat transfer of the system. Similar results with a water charged system showed dry out at a 50% filling ratio.

Fluid	Symbol	Normal Boiling Temperature	Critical Temperature	Latent Heat of Vapourisation (LHV)	Useful Range	Compatible Casing Materials
Units	°C	°C	°C	(kJ/kg)	°C	
Ammonia	NH_3	-33.34	132.4	1369.5	-65 to 100	Aluminium Ferritic Steels Stainless Steel Elastomers Polymers
Acetone	C_3H_6O	56.1	235	538.4	0 to 120	Stainless steel Copper Ferritic Steel

						Stainless Steel Polymers
Toluene	C_7H_8	110.6	320	351	-95 to 350	Aluminium Copper Ferritic Steels Stainless Steel Polymers

Table 2-4: Organic compound fluids thermophysical properties [43,48]

2.7.3.2 Cryogenic Working Fluids

Elemental gases

Elemental gases as working fluids form a part of the cryogenic working fluid spectrum. Elemental fluids have been applied in non-gravity applications, from the cooling of satellites and telescopes to the cooling of particle detectors. The implementation of cryogenic heat pipes has been investigated and applied in a cooling system at the CERN research facility. The study presented by Pereria et al [4] highlights the utilisation of loop heat pipes (LHP) to effectively cool particle detectors in an initial lab scale scenario. The LHP was investigated with both krypton and argon working fluids with a copper shell material. The system schematic exists as a serpentine-shaped pipe connected to a working fluid chamber; to ensure that the operation is independent from the environmental conditions, the system was housed within an evacuated vessel. During the operation, the LHP effectively transfers heat allowing for a considerable temperature difference between the evaporator and the condenser sections, without the risk of dry out—previously observed in other LHP. The comparison between krypton and argon was performed with a change of inclination angles ranging from 0° to 90°, and the overall results highlighted the decline in performance as the system reached 90°. When the LHP reached 75°, the liquid condensate fails to reach the evaporator section, which led to the saturation of wicks and the compensation chamber and a significant decline in performance. The operational difference between both working fluids highlighted the superior performance of krypton of 25W at 75°, with argon providing 10W.

The application of cryogenic working fluids within loop heat pipes has experienced a level of dry out which is a significant limiter in the performance of the heat pipe. The physical operation of cryogenic loop heat pipes often features auxiliary loops due to the failure to start during initial conditions. The characterisation of failure has been widely researched, Guo et al [52]

investigated the operational failure of a neon-based loop heat pipe. The experimental set up highlights a simplistic loop heat pipe design connected to a cryocooler acting as a heat sink and a primary evaporator acting as the heat source. The system is similarly housed within a vacuum chamber to eliminate any ambient convective effects. The overall results highlighted a successful start-up with a dramatic temperature decline in the condenser temperature once the minimum wettability requirement of the wick was achieved. The success of the operation was hindered once a heat load was applied, showing a failure to start up due to a number of reasons, ranging from irregularity in condenser temperature leading to the solidification of the working fluid within the condenser which blocks the operation of the heat pipe. Similarly, the failure could be due to the limited liquid fraction to the evaporator, allowing for a significantly reduced operation and incapability to handle the thermal load. Phenomena such as impurities within the gas were investigated, tested with and without a heat load, showing significant level of dry-out due to a condenser blockage. The studies highlighted the potential for cryogenic fluids, but the operation is highly dependent on the heat load requirements which can lead to the failure of the system. Other working fluids such as helium have also been used in cryogenic cooling systems and experimental studies requiring conditions close to absolute zero. Table 2-5 highlights the available working fluids used in cryogenic heat pipes.

Fluid	Symbol	Normal Boiling Temperature	Critical Temperature	Latent Heat of Vapourisation (LHV) (kJ/kg)	Useful Range	Compatible Casing Material
Units	°C	°C	°C	(kJ/kg)	°C	
Helium	He	−268.9	−267.95	21	-271 to -269.1	Aluminium Copper Ferritic Steels Stainless Steel Sillicone Elastomers
Hydrogen	H_2	-252.87	−239.95	461	-259 to -242	Aluminium Copper Ferritic Steels

						Stainless Steel Polymers
Nitrogen	N_2	-195.8	-146.9	199	-203 to -170	Aluminium Copper Ferritic Steels Stainless Steel Elastomers Polymers
Neon	Ne	-246.08	−228.75	86.3	-246 to -236	Aluminium Copper Ferritic Steels Stainless Steel
Argon	Ar	-185.8	-122.3	162.3	-190 to -122	Aluminium Copper Ferritic Steels Stainless Steel Elastomers Polymers
Oxygen	O_2	-182.9	−118.6	213	-200 to -154	Aluminium Stainless steel
Krypton	Kr	-153.2	-63.8	107.5	-157 to -64	Aluminium Copper Ferritic Steels Stainless Steel
Xenon	Xe	-108.1	16.6	96.3	-112 to 17	Aluminium Copper

						Ferritic Steels Stainless Steel

Table 2-5: Elemental liquid thermophysical properties [43,48]

Compounds

Similarly, compounds are also classified as cryogenic working fluids. The application of compound fluid based cryogenic heat pipes has been investigated regarding the applicability within loop heat pipes. The existing studies regarding loop heat pipes have frequently used elemental working fluids with minimal research regarding their application. Guo et al [53] investigated the implications of a methane-based loop heat pipe, and concluded that methane was widely beneficial due to its existing applications within regenerative cooling systems. The research highlighted the development of a methane-charged stainless-steel cryogenic loop heat pipe for application within the space industry. The system adopts a compact design with coiled condensers linked to a heat sink. The system itself contains both liquid and vapour lines linked to a gas reservoir to ensure minimum wettability of the wick is achieved. To simulate a thermal load, an electrical heater was installed on the evaporator line. During the initial start-up of the loop heat pipe, the operation highlights a delay due to the prolonged time to cool down the condenser section, which led to flooding of the compensation chamber. The operation of the LHP managed to be functional until a heat load of 1W was applied, which led to an irrecoverable failure.

Similarly, an ethane charged heat pipe has been applied in a mid-low temperature range within a pulsating heat pipe, with the operation behaving differently compared to the LHP. The investigation conducted by Chen et al [54] highlights the implications of an ethane-based pulsating heat pipe tested with multiple filling ratios at an inclination of 45°. The filling ratio comparative study ranges from 22% to 60% at a constant inclination angle. The initial tests with a low fill ratio showed a sufficient production of vapour but an insufficient formation of liquid slugs which led to dry out. Similarly, the results at a higher fill ratio showed a reduction in the number of bubbles and in the pressure, differential needed between both phases, which is vital as it allows the liquid slug to move through the system. The lack of perturbation at a high filling ratio highlighted a decline in heat pipe performance. The study that the optimum operation achieved -90°C, with a filling ratio of 30%. Compounds are beneficial working fluids, with the potential to be developed into cryogenic systems. In comparison to elemental fluids,

the latent heat of vaporisation (LHV) of compounds is considerably higher compared to the elemental working fluids highlighted in Table 2-6. The LHV plays a key role in the success of cryogenic heat pipes—a higher LHV value requires a significant amount of energy to initiate the phase change process, with a better heat transfer of latent heat due to the absorption of energy during start up.

Fluid	Symbol	Normal Boiling Temperature	Critical Temperature	Latent Heat of Vapourisation (LHV)	Useful Range	Compatible Casing material
Units	°C	°C	°C	(kJ/kg)	°C	
Methane	C_3H_8	-161.7	-82.5	510.8	-182 to -113	Aluminium Copper Ferritic Steels Stainless Steel
Ethane	C_2H_6	-88.5	32.4	489.4	-123 to -33	Aluminium Copper Ferritic Steels Stainless Steel

Table 2-6: Compound liquid thermophysical properties [43,48]

Nanofluids

Working fluids are not limited to refrigerants and elemental compounds. Recent developments of nanofluids as working fluids allow a new age of potential working fluids. Nanofluids have shown to have enhanced heat transfer capability due to the metallic particles suspended within the fluid. The development and implementation of nanofluids produced an improved performance of the heat pipe but also allowed the identification of major setbacks. Sarafraz et al [55] discovered the presence of fouling within the chamber walls of a thermosyphon, reducing the condenser temperature. Gupta et al [56] investigated the application of nanofluids within wicked heat pipes but fouling occurred within the wick with trapped metallic elements.

The continuous operation led to the failure of the heat pipe due to the change in porosity in the wick and further inabilities to transport the fluid. The use of nanofluids has been widely contested as working fluids—with a large need for development to overcome wall deposits.

2.7.4 Development of Cryogenic Heat Pipes

2.7.4.1 Gravity assisted

A thermosyphon is gravity assisted with a phase change occurring within the pipe as defined previously in section 2.7.1 The operation of the thermosyphon relies on gravity to return the condensate to the evaporator section. A gravity assisted thermosyphon can operate at a multitude of angles as long as the condenser is located above the evaporator. The development of low temperature and cryogenic heat pipes has been investigated with multiple working fluids and operations from both experimental and computational perspectives. Long and Zhang [57] investigated the operation of a cryogenic thermosyphon at different fill ratios and inclinations. The system exists as a single copper thermosyphon charged with nitrogen. The condenser section is linked to a reservoir tank filled with liquid nitrogen. To simulate a heat load, the evaporator was attached to a heating wire. The problematic condition of the test is the lack of control to normalise the evaporator temperature, as the results show a consistent fluctuation as a result of constant on and off operations, leading to an unsteady heat transfer rate and fluctuating condenser temperature. When the filling ratio was increased, the unsteady evaporator temperature led to significant increases which led to the dry-out of the thermosyphon at high filling ratios.

The authors also developed a system of a single heat pipe charged with liquid helium encased with a copper shell [58]. Similarly, to the nitrogen charged heat pipe, the evaporator contains a heated wire to simulate a heat load. The condenser system contains a cryocooler which acts as a heat sink. Unlike the nitrogen configuration, the system contains two radiation shields to minimise radiative effects. The initial tests highlighted a minimum radiative effect of 1W during the start up. A relationship was defined between the filling ratio and the risk of dry out, with dry out occurring at 0.7W at 100% filling ratio. Helium is an optimum working fluid, often used to create conditions close to absolute zero. Cryogenic heat pipes and cooling systems have been applied at CERN for the cooling of particle colliders. The loop is cooled by liquid helium, although storage and containment of helium is extremely difficult. The application of helium within a thermosyphon could be problematic for leakages allowing for an altered filling ratio. The application of other cryogenic fluids such as liquid nitrogen has been investigated by Bolozdynya et al [59]. The premise of the test was based on a copper thermosyphon, with an electrical heater wire applied on the evaporator. The condenser heat sink exists as a liquid

nitrogen cooled head. The test is primarily based on the filling ratio and the subsequent cooling rate, with the addition of a heat load. The operation highlighted a poor cooling rate of 0.6 K/min when the filling ratio is 32%, whereas a smaller filling ratio of 6.5% showed a cooling rate at 3K/min under identical test conditions.

2.6.4.2 Loop Heat pipe

A loop heat pipe (LHP) is based on a closed loop circuit containing both liquid and vapour phases simultaneously. The operation of a loop heat pipe begins with a compensation chamber containing the working fluid and a wick structure to ensure working fluid is always in the fluid chamber of the heat pipe. A section of a loop heat pipe from the compensation chamber houses an evaporator section, where a heat input is supplied. The vapour travels through the adiabatic section of the LHP to the condenser section. The condenser transforms the vapour back into liquid, which travels back to the fluid chamber. Loop heat pipes are widely applied within cryogenics. Bai et al [60] investigated cryogenic loop heat pipes charged with nitrogen for the cooling of space exploration devices. The heat pipe employs the same principle highlighted in Figure 2-10, with the addition of secondary auxiliary loops. The secondary loops contain additional evaporator and condenser sections to start the supercritical operation of the LHP. In the study, an electrical heater was used as a thermal load to the auxiliary evaporator and the main evaporator.

Similar applications for space technologies have used loop heat pipes. Guo et al [53] investigated a methane-based cryogenic LHP for thermal regulation within an infrared detection system, which was tested in conditions such as the performance under supercritical conditions and its heat transport capacity. The research demonstrates an innovative compact system with a wick structure integrated within both evaporator and compensation chambers, eliminating the risk of dry-out. The condenser exists as a primary and secondary coil which is wrapped around a cryocooler acting as a heat sink. The supercritical operation highlights the function of the heat pipe with an ambient temperature. The start-up function highlighted a successful operation, allowing the evaporator to drop the operating range of the working fluid, although once a heat load was applied, the performance dropped leading to the failure of the system.

Multiple studies regarding cryogenic loop heat pipes demonstrate their potential of dry out and failure of supercritical start up. The selection of the working fluid has been investigated by Yan et al [61] to determine the optimum working fluid for cryogenic loop heat pipes. The test was initially conducted with liquid nitrogen at different filling ratios and filling pressures. The system

contains both a primary and secondary evaporation loops, where the secondary evaporator loop is connected to a reservoir tank. One of the main problems with traditional closed loop heat pipes is the difficulty to maintain a constant level of working fluid within the compensation chamber. The improvements within the study accounted for another chamber to ensure that dry out and heat pipe failure is mitigated. The second loop reduces the risk of failure during supercritical conditions. The secondary loop circulates fluid through the system whilst the evaporator can reach a suitable operating range for the working fluid. The relationship between the secondary loop and the filling ratio was widely discussed in the study. Due the improved circulation of fluid, the need for excess fluid only hindered the performance of the heat pipe, leading to an increase in saturation pressure. The change in fill pressure with constant fill ratio highlighted an increase in saturation pressure, which led to an increase in resistance and a decrease in heat pipe performance.

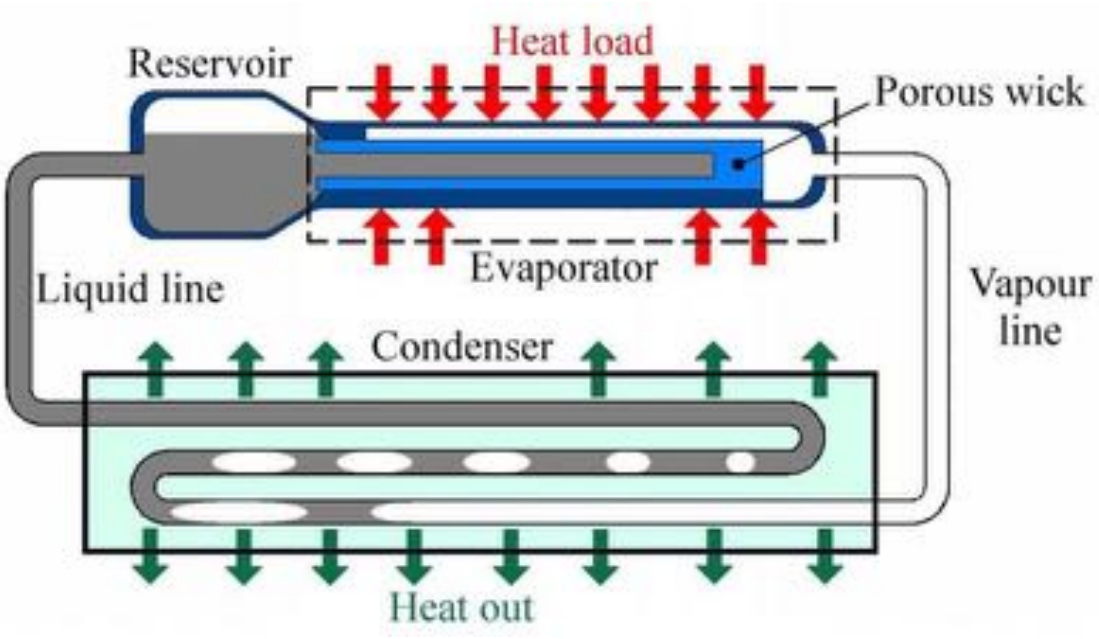

Figure 2-10: Schematic of Loop heat pipe operation [62]

2.6.4.3 Pulsating/ Oscillating Heat Pipe

A pulsating heat pipe (PHP) is a closed loop circuit that relies on variations of both vapour bubbles and liquid slugs within the system. The temperature and pressure differential between the evaporator and condenser sections creates a pulsating motion, allowing the liquid slug to pass through the system as shown in Figure 2-11 [63].

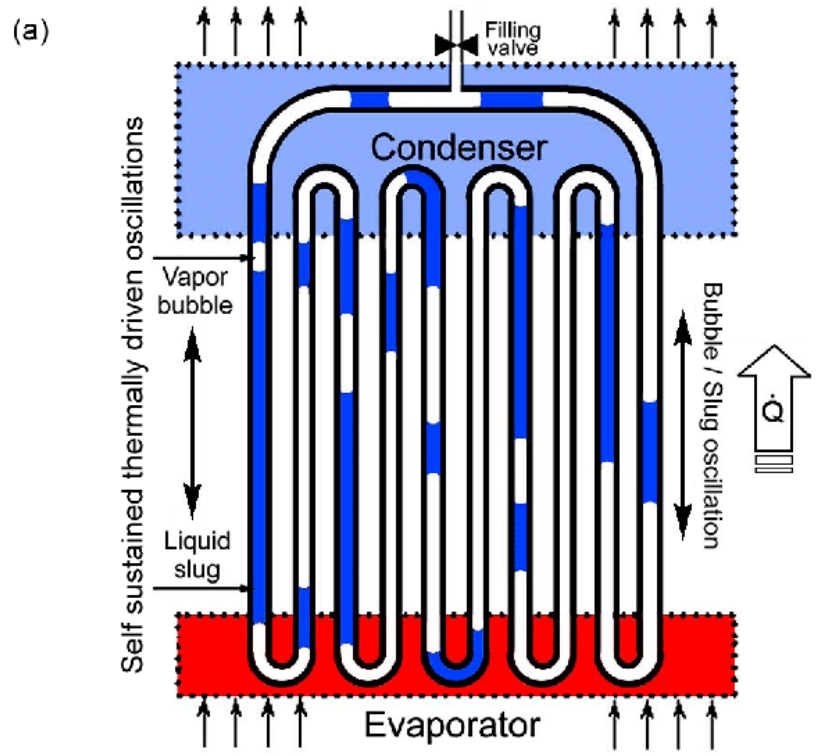

Figure 2-11: Schematic of Pulsating heat pipe

The system typically exists without a wick, making it a viable option for cryogenic heat pipes, but the system performance is highly dependent on the number of turns. Liang et al [64] investigated the performance of an oscillating heat pipe charged with neon as the working fluid. The system operated from room temperature to the critical point of the working fluid, to investigate the cool down period of the heat pipe. A heat load was applied to the evaporator, whereas a cooling plate was fixed onto the condenser section. The system showed its performance is dependent on the rate of liquid neon entering the system, as the cooling rate took 9 hours from 223K to 31K. It is worth noting that the system experienced significant pressure changes indicating dry out, which also occurred in other pulsating heat pipes when charged with a cryogenic fluid. The effects of dry out were experienced by Li et al [65]. The study investigated the operation of a pulsating heat pipe charged with liquid nitrogen. The evaporator section was connected to a heating wire wrapped around the breadth of the system; the electrical input of the heater was increased accordingly to observe the thermal performance. The PHP was charged with liquid nitrogen with an increase in evaporator temperature. The increase in evaporator temperature led to the dry out of the pulsating heat pipe. Xu et al [14] investigated a pulsating heat pipe charged with helium for ultrafast cooling applications. A cryocooler was attached to the condenser, whereas a heater wire was used for the evaporator to apply a heat load to the system. A pre-cool function was applied to allow the pulsating heat pipe to reach the desired operation temperature. The helium PHP allowed

the cooling down from room temperature to 7K in 8 hours. The configuration was placed vertically, highlighting the effect of gravity allowing the fluid to reach the evaporative system and surpass the operating temperature. The test was conducted horizontally but no major impact was noted. The variation and configuration play a key role in the operation, with the number of turns increasing the resistance of the system. Stevens et al [49] investigated different variations of pulsating heat pipes with a selection of working fluids. The study involved six pulsating heat pipes charged with butane and refrigerant R134a. A heater was applied through the evaporator section, with a coolant stream passing through the condenser. The location of the heater and cooler varied with a single or double contact with a variable power supply. The six PHP were tested with both contact positions and electrical loads. The results demonstrated the improved performance of a double contact evaporator for an increasing power input. Similarly, the effects of horizontal and vertical positions were investigated with the effects of thermal resistance, with the results reflecting an improved and reliable vertical operation, in comparison to the horizontal during repeated results.

2.8 Heat Transfer Theory

2.8.1 Forced Convection

The characterisation of convective forces can be determined by the Reynolds number defined as:

$$Re = \frac{\rho v D}{\mu} \qquad 2\text{-}1$$

where *D* denotes the hydraulic diameter, v (m/s) is the flow velocity and ρ (kg/m^3) is the density of the fluid and μ indicates the viscosity of the fluid (N.s/m^2). The implementation of non-dimensional numbers allows boundary conditions to correlate within one function. The definition of the Reynolds numbers allows the characterisation of flows, where flows beyond 10^5 are considered to be turbulent. The Reynolds number can also be used to define the Nusselt number. The Nusselt number is a non-dimensional number to characterise the relation between convection and conduction as a function of the Reynolds and Prandtl numbers defined in equation 2-2

$$Nu = f(Re, Pr) \qquad 2\text{-}2$$

The determination of a convective heat transfer coefficient can be calculated through the Nusselt number as:

$$Nu = \frac{hl}{k} \qquad 2\text{-}3$$

$$h = \frac{Nu.k}{l} \qquad 2\text{-}4$$

where h denotes the heat transfer coefficient, l the characteristic length and k is the thermal conductivity of the fluid. The definition of the Nusselt number depends on a multitude of factors including the Reynolds number and Prandtl limits[66]. Table 2-7 presents suitable applicable correlations for the Nusselt number.

Churchill and Bernstein [67]	$$Nu = 0.3 + \frac{0.62Re^{\frac{1}{2}}Pr^{\frac{1}{3}}}{\left[1+(0.4/\mathrm{Pr})^{\frac{2}{3}}\right]^{\frac{2}{3}}}\left[1+\left(\frac{Re}{282\,000}\right)^{\frac{5}{8}}\right]^{-\frac{4}{5}}$$ When Re>400,00	2-5
Churchill and Bernstein [67]	$$Nu = 0.3 + \frac{0.62Re^{\frac{1}{2}}Pr^{\frac{1}{3}}}{\left[1+(0.4/\mathrm{Pr})^{\frac{2}{3}}\right]^{\frac{1}{4}}}\left[1+\left(\frac{Re}{282\,000}\right)^{\frac{1}{2}}\right]$$ When 10,000 < Re < 400,000	2-6
Hilpert [68]	$$Nu = C\ Re^{m}Pr^{\frac{1}{3}}$$ where the constants can be defined as:	2-7
Flores and Mascheroni [69]	$$Nu = 0.3526\ Re^{0.64}$$ 20,000 < Re < 70,000	2-8
Tocci [81]	$$Nu = 0.363\ Re^{0.64}Pr^{\frac{1}{3}}$$ 10,000 < Re < 70,000	2-9

Re	c	m
0.4 - 4	0.989	0.33
4 - 40	0.911	0.385
40 - 4000	0.683	0.466
4000 – 40,000	0.193	0.618
40,000 – 400,000	0.027	0.805

Table 2-7: Nusselt Number approximations

2.8.2 Conduction

The effect of solidification is mainly based on a conduction process, where the natural convection terms are often omitted. Figure 2-12 highlights the resistance diagram highlighting the conductive resistances [66].

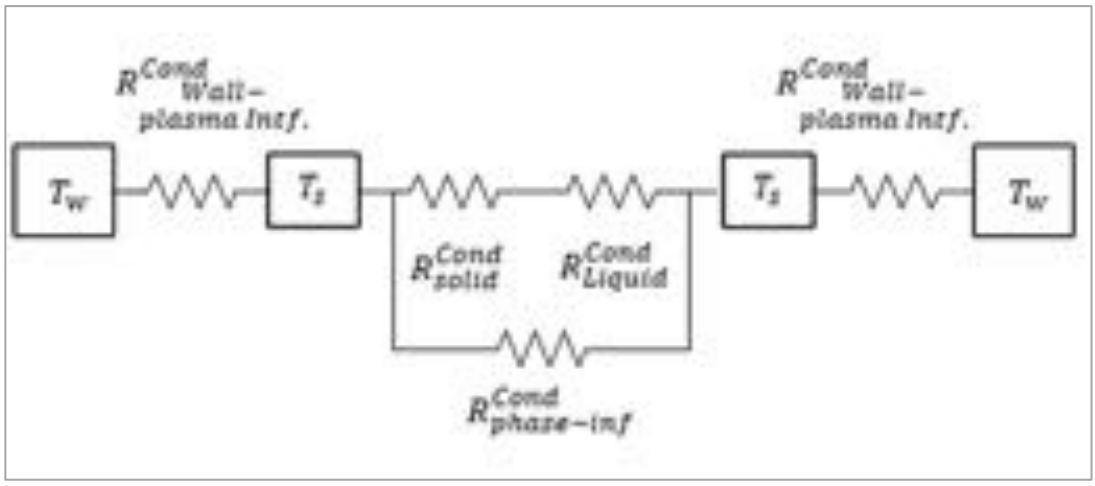

Figure 2-12: Conduction thermal resistance diagram

One of the key resistances defined in Figure 2-12 is the definition of the solid-liquid interface, which needs to account for the temperature jump between both phases. Equation 2-10 highlights the resistance across the liquid-solid interface [70].

$$R^{Cond}_{phase-inf} = \frac{\Delta T_{sol-liq}}{q} \quad 2\text{-}10$$

The conduction across plasma bag to the plasma simulant labelled as $R^{Cond}_{wall-plasma\ Intf}$ can be defined as:

$$R^{Cond}_{wall-plasma} = \frac{L}{k_1 A} \quad 2\text{-}11$$

The conduction across each phase can be defined as:

$$R^{Cond}_{solid} = \frac{L_2}{k_2 A} \quad 2\text{-}12$$

$$R^{Cond}_{liquid} = \frac{L_3}{k_3 A} \quad 2\text{-}13$$

2.9 Heat Pipe Theory

As defined in section 2.7, the operation of any heat pipe system is reliant on the constant boiling and condensation processes within the pipe. The boiling phenomenon occurs when the temperature in the evaporator wall section, in contact with the working fluid, exceeds the saturation temperature of the working fluid. The interaction between the wall and the fluid causes the adjacent working fluid to boil. Other types of boiling regimes include nucleate boiling, transition boiling and film boiling.

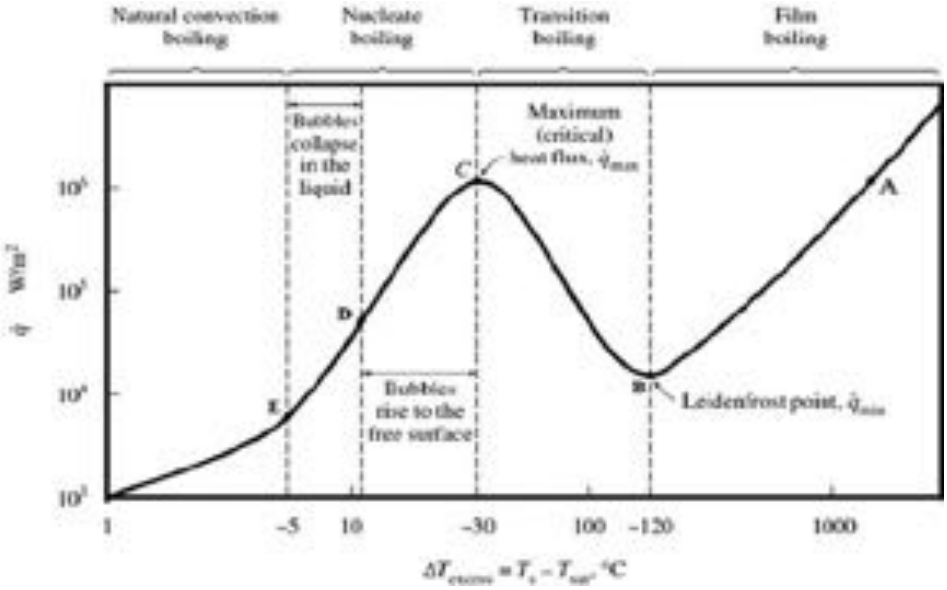

Figure 2-13: Water Boiling Graph at 1 Atmosphere (General Boiling Schematic) [71]

2.9.1 Boiling regimes

2.9.1.1 Nucleate Boiling

Nucleate boiling occurs when the wall temperature adjacent to the working fluid is above the saturation temperature of the working fluid. Typically, nucleate boiling occurs in the two-phase operation within the heat pipe. Nucleate boiling often transitions from natural convection boiling, resulting in the formation of bubbles within the working fluid. These bubbles soon collapse within the liquid (subcooled nucleate boiling). As the heat flux increases, the thermophysical properties of bubbles and liquid pool allow the vapour bubbles to break free from the surface. Eventually, the boiling regime will reach a critical heat flux (saturated nucleate boiling). An example boiling curve is shown in Figure 2-13 showing the progression from natural convection boiling to the maximum critical heat flux as a result of an increase in excess temperature.

The investigations and research in nucleate boiling within heat pipes have allowed the definition of multiple conditions for controlled nucleate boiling to occur. As the heat flux is a

variable, this results in an altered boiling regime and associated heat transfer rate. By understanding the boiling phenomena for an array of conditions, the design of a thermosyphon can be improved to its maximum efficiency. Table 2-8 shows an array of boiling correlations used in heat pipes.

Title	Eq.	
Nishiwaka [72]	2-14	$h_{nb} = 12.7 \left(\frac{R_{mol} T_{crit} {p_{crit}}^2}{M_{mol}}\right)^{\frac{1}{10}} \times F_N(P^*) \times {q''}_{nb}^{\frac{4}{5}} \times \left(8R_p/R_{p0}\right)^{\left(1-\frac{P^*}{5}\right)}$ $F_N(P^*) = P^{*0.23}(1-0.99P^*)^{0.9}$
Developed for the use of refrigerants		
Stephan and Abdelsalam [73]	2-15	$h_{nb} = 4.82 \frac{k_l}{D_d} \times X_1^{0.624} X_3^{0.374} X_4^{0.329} X_5^{0.257} X_7^{0.117}$ $4 \times 10^{-3} \leq P^* \leq 0.97$ and $\theta = 1°$ (For Cryogenic Fluids) --- $h_{nb} = 207 \frac{k_l}{D_d} \times X_1^{0.745} X_5^{0.581} X_6^{0.533}$ $3 \times 10^{-3} \leq P^* \leq 0.78$ and $\theta = 35°$ (For Refrigerants)
Developed for the use of refrigerants and cryogenic fluids		
Kutateladze [74]	2-16	$h_{nb} = 0.44 {Pr_l}^{0.35} \left(\frac{k_l}{L_b}\right) \left(\frac{\rho_l}{\rho_l - \rho_v} \frac{P \times 10^{-4}}{{\rho_v}^{gi} lv \mu l} {q''}_{nb}\right)^{0.7}$ Where, $L_b = \left[\frac{\sigma}{g(\rho_l - \rho_v)}\right]^{1/2}$
Danilova [75]	2-17	$h_{nb} = C \left(\frac{R_a}{R_{a0}}\right)^{0.12} (0.14 + 2.2P^*) {q''}_{nb}^{0.67}$
Developed for the use of refrigerants		
Rohsenow [76]	2-18	$h_{nb} = \frac{q^{\frac{2}{3}}}{C_{sf} h_{fg} \left\{\frac{1}{h_{fg} \mu_l} \left(\frac{\sigma}{g[\rho_l - \rho_v]}\right)^{\frac{1}{2}}\right\}^{0.33} Pr_l^n}$ Condition
Frequently used for boiling situations.		

Table 2-8: Correlations for nucleate boiling related to the scope of this research

2.9.1.2 Transition and Film Boiling

The point past the critical heat flux is defined by a zone called transition boiling. As the temperature of the fluid increases, layers of vapour pockets form on the heated wall of the evaporator. The vapour layer acts as a film which increases the resistance of boiling due to its insulation properties. The result is a sharp drop in heat flux, and the boiling regime containing properties of film and nucleate boiling. The increase in wall temperature results in film boiling, where a stable vapour film exists on the surface. At this point, the heat flux is at a minimum point, which is also called the Leidenfrost point shown in Figure 2-13 . The heat transfer between the solid and liquid interface is now replaced by the heat transfer from the interface of a vapour phase.

2.9.2 Condensation

During the operation of a heat pipe, the vapour phase moves towards the condenser section of the heat pipe. Due to the lower condenser wall temperature, the vapour condensates and the fluid is returned back to the evaporator section. The return of the condensate may happen in two different forms, film-wise and dropwise condensation. Film-wise condensation primarily occurs when the condensate flow is a film flow, typically in a laminar flow regime. Typically, the initial point of where condensation occurs is the thinnest section of the condensate. As the condensate flows back down to the evaporator, the thickness of the film condensate increases as shown in Figure 2-14a. Table 2-9 highlights frequently used correlations to determine the heat transfer coefficient for liquid film condensation. The second type of condensation that may occur is called dropwise condensation. The development of dropwise condensation happens when droplets begin to form in the condenser walls as shown in Figure 2-14b. The formation of dropwise condensation and film condensation is dependent on the temperature difference between the condenser wall and the evaporate temperature. Typically, dropwise condensation occurs when the temperature difference between the vapour and condenser wall is small [77].

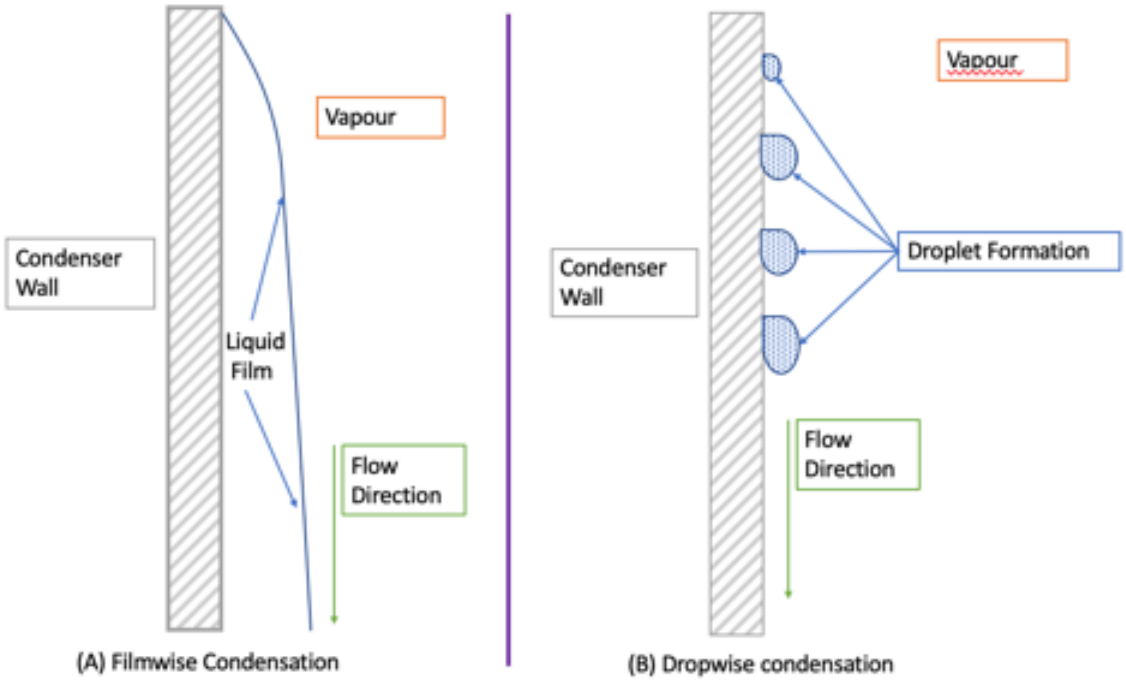

Figure 2-14: Schematic of Condensation (A) Filmwise Condensation (B) Dropwise Condensation

Title	Eq.	
Nusselt [78]	2-19	$h_{film} = 0.943\left[\frac{\rho_l(\rho_l-\rho_v)g i_{lv}^* k_f^3}{l_c \mu_l (T_{sat}-T_w)}\right]^{\frac{1}{4}}$ Typically used for laminar flow conditions where conditions must satisfy: 0< Re <30
Nusselt (Rohsenow Correction) [79]	2-20	$i_{lv}^* = i_{lv} + 0.68C_{pl}(T_{sat}-T_w)$ For non-linear temperature distribution. $i_{lv}^* = i_{lv} + 3/8C_{pl}(T_{sat}-T_w)$ For subcooled condensate
Jouhara et al [80]	2-21	$h_{ci} = 0.85Re_f^{0.1}\exp\left(0.000067\frac{\rho_l}{\rho_v}-0.14\right)\times h_{film}$

Table 2-9: Table of common condensation correlations

2.10: Chapter Summary

The chapter presents the state of the art from both a cryopreservation aspect and a low temperature heat pipe aspect. The chapter identifies a clear gap in the research with the lack of applicable technologies suited towards a batch freezing process. Similarly, the chapter highlights the gap of technologies that are being phased out, and a lack of commercially ready

cryopreservation technologies. The addition of the heat pipe sections addresses the existing use of heat pipes within the cryogenic temperature spectrum and provides a foundation for the technology developed and described in Chapter 4.

Chapter 3. : Solidification Theory

This chapter mainly focuses on the process of solidification to explain the phenomenon of solidification within a plasma bag. The chapter builds a foundation on solidification theory which is further applicable to Chapter 6.

3.1 Solidification Theory

The process of solidification allows the co-existence of two different phases due to the presence of an intermediary phase acting as an interface, called a mushy zone. The location of the mushy zone exists as a variable which is dependent on the rate of phase change within a plasma bag. The interface between both phases acts as a key component in the temperature distribution between phases. The interaction between both phases in the mushy zone allows for the presence of an intermediary zone, which can alter the thermal distribution. The intermediary zone is considered as a zero-thickness interface where the chemical composition is a mix of the properties of both zones.

The interface between both phases is a moving boundary where the latent heat is dispelled during the solidification process. During this process, heat is transferred mostly by conduction between the phases, the result being the presence of a thermal boundary layer. The presence of the interface and its relation to the freezing schematic are heavily interlinked. Studies by Estrada et al [81] highlighted the risks associated with fast freezing processes, the thermal inconsistencies present in the microstructures and the risk of inconsistent freezing patterns. These inconsistencies are further exaggerated when investigating binary solutions, which contain a level of solute due to the mixed nature of the substance. The solute contains a level of impurities, which is either diffused away from the interface or integrated within the interface structure. The position of the solute is dependent on its solubility within the mixture, where solutes with low solubility than the solid are rejected. The rejected solutes are diffused away from the interface.

As the physics of the problem is mathematically described by partial differential equations, many unknowns appear when modelling more realistic scenarios. One of the most popular methods of solution is the Neumann method, which considers that the position of the phase change interface is directly proportional to the square root of time. An error function is then defined to satisfy the original governing equations. Alternatively, the problem can be defined as a Stefan problem, which is able to determine the ratio between latent heat and sensible heat.

Methods of analysis for solidification problems exist in two forms; a classical model where the temperature is treated as the main variable, with energy equations defined in each phase and solved independently. The production of different energy equations is based on defining both enthalpy and temperature terms as variables. The second form of analysis is called the enthalpy method, where the interface between the liquid and solid phases is not taken into consideration. The latter is not as commonly used as discussed by Smith et al [82] and Voller et al [83] due to deficiencies within the model regarding inaccuracies for the phase depths. The classical method is based on the Neumann problem where the rate of solidification is determined by the change in time.

The solidification thermal map exists in many forms, with the rate of solidification being highly dependent on the boundary conditions applied. The schematic depicted in Figure 3-1 highlights the thermal resistances of a single plasma bag on a wire mesh shelf, which adds a level of resistance. Figure 3-2 highlights the temperature distribution with the effect of the shelf acting as a further resistance, where T_f and T_s denote the phase change temperature and the surface temperature respectively.

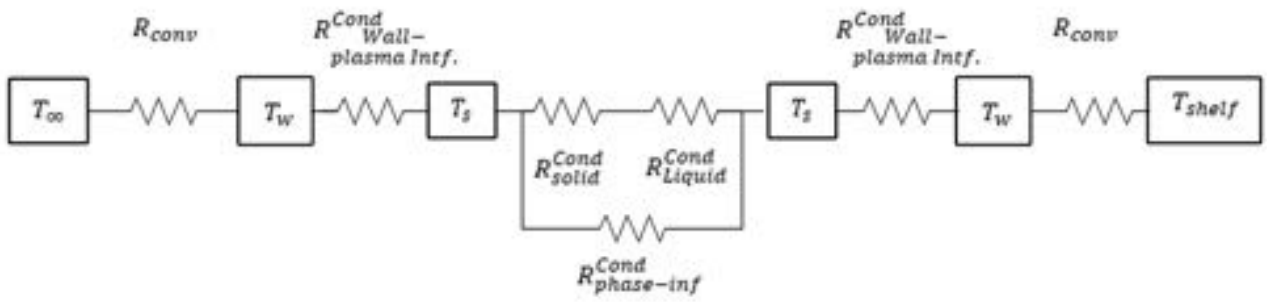

Figure 3-1: Example resistance diagram for solidification

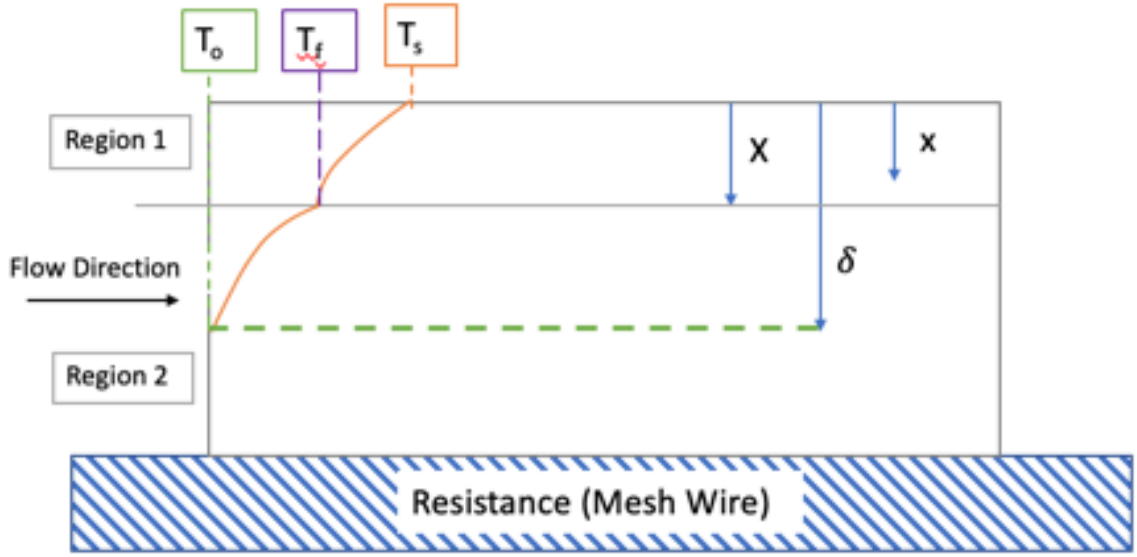

Figure 3-2: Thermal Map

The areas of solidification in a finite dimension have been investigated, where the product temperature is different to the external boundary conditions applied. Equation 3-1 is the diffusion equation which governs the transient heat conduction problem for the solid phase. Equation 3-2 defines the initial conditions of the problem, while Equations 3-3 and 3-4 define the boundary conditions at the external boundary x=0 and at the interface between the two phases [82,84,85].

$$\frac{\partial^2 T_1}{\partial x^2} = \frac{1}{\alpha_1}\frac{\partial T_1}{\partial t} \qquad 3\text{-}1$$

$$T_1(0,t) = T_s \qquad 3\text{-}2$$

$$-k_1\frac{\partial T}{\partial x} = \overline{H_o}(T_{x=0} - T_\infty) \qquad 3\text{-}3$$

$$-k_1\frac{\partial T}{\partial x} = \rho L_f\frac{d\varepsilon}{dt} + \overline{H_e}(T_1 - T_f) \qquad 3\text{-}4$$

The variables in the above equations are denoted as follows:

T_1 = temperature of the solid (K)

T_s = surface temperature (K)

k_1 = thermal conductivity of the solid (W/m.K)

α_1 = thermal diffusivity of the solid (m^2/s)

H_o = convective heat transfer coefficient (W/m^2. K)

T_x = Initial interface temperature (K)

T_∞ = temperature of the surrounding fluid (K)

Equation 3-4 states that the movement of the interface depends on the thickness of the mushy zone, defined as a function of time. The symbols used in this equation are defined as follows:

$\frac{d\varepsilon}{dt}$ = rate of solidification

L_f = latent heat per unit volume (J/kg)

H_e = conductive heat transfer coefficient at the initial position of the interface (W/m^2.K)

T_f = freezing point of the fluid (K)

t = time (s)

As it can be assumed that the position of the interface (X) is a function of time, the temperature of both liquid and solid phases at their interface is equal to the phase change temperature:

$$T_1(X,t) = T_2(X,t) = T_f \qquad 3\text{-}5$$

$$\frac{\partial^2 T_2}{\partial x^2} = \frac{1}{\alpha_2}\frac{\partial T_2}{\partial t} \qquad 3\text{-}6$$

$$T_2(x,0) = T_o \qquad 3\text{-}7$$

where the following terms denote:

T_2 = temperature of the fluid (K)

T_o = initial temperature of the fluid (K)

$$\frac{\partial T_2(D,t)}{\partial x} = 0 \qquad 3\text{-}8$$

with D = thickness of the plasma bag (mm)

Due to the thermal resistance and assuming a thermal penetration depth, a new definition of boundary conditions is as follows:

$$\frac{\partial T_2(\partial, t)}{\partial x} = 0 \tag{3-9}$$

$$T_2(\partial, t) = T_o \tag{3-10}$$

$$-k_1 \frac{\partial T_1(X, t)}{\partial x} + k_2 \frac{\partial T_2(X, t)}{\partial x} = -\rho_1 \ell \frac{dX}{dt} \tag{3-11}$$

The position of the interface (X) is defined as follows:

$$X = 2\sqrt{\alpha_1 t} \tag{3-12}$$

where the following terms denote:

$X = \text{Phase change interface position}$

A heat balance integral applied to the liquid phase is given by:

$$\frac{d}{dt}\int_X^\delta T_2 \, dx = T_o \frac{d\delta}{dt} + T_f \frac{dX}{dt} + \alpha_2 \frac{\delta T_2(X, t)}{\partial X} = 0 \tag{3-13}$$

If equations 3-8 - 3-10 are applied and a polynomial temperature function for the fluid region is assumed, the temperature in the fluid phase can be given by:

$$T_2 = T_o - \left(T_o - T_f\right)\left(\frac{\delta - x}{\delta - X}\right)^4 \tag{3-14}$$

The temperature of the fluid phase considers the temperature difference between the fluid phase and the boundary conditions. As the phase change interface is a function of the change in temperature, the relation between the thermal penetration depth and the boundary condition layer must be defined. The position of the interface in relation to the thermal penetration depth must be considered.

The thermal penetration depth δ is assumed to be:

$$\delta = 2\beta\sqrt{\alpha_1 t} \tag{3-15}$$

in which β is the thermal penetration depth parameter.

Equations 3-13- 3-15 can be reduced to:

$$\beta - \gamma = \frac{5}{2}\left[-\gamma + \sqrt{\gamma^2 + 8\frac{\alpha_2}{5}}\right] \quad 3\text{-}16$$

By applying the initial boundary condition given by equation 3-11, the following equation can be obtained.

$$\frac{e^{-\gamma^2}}{\operatorname{erf}\gamma} - \frac{2(T_o - T_f)k_2\sqrt{\pi}}{(T_f - T_s)k_1(\beta - \gamma)} = \frac{\ell\gamma\sqrt{n}}{c_1(T_f - T_s)} \quad 3\text{-}17$$

where the following terms denote:

$n = \text{interface constant}$

$c_1 = \text{specific heat of phase 1}$ (J/kg.K)

$n = X/(2\sqrt{\alpha t})$

The error function can be calculated approximately as given by Carslaw and Jaeger [86] as follows:

$$\operatorname{erf}\eta = \frac{2}{\sqrt{n}}\int_o^n e^{-\beta^2} d\beta \quad 3\text{-}18$$

As the solidification process continues, the thermal penetration depth will reach the maximum position. When this occurs, the following assumptions can be applied $\delta = D$ and $X = D$. The time when this occurs can be defined by:

$$t_1 = \frac{D^2}{4\alpha_1\beta^2} \quad 3\text{-}19$$

$$t_2 = \frac{D^2}{4\alpha_1\gamma^2} \quad 3\text{-}20$$

The wall temperature T_w can be estimated, by assuming: $t_1 < t < t_2$:

$$T_2(x,t) = T_w - (T_w - T_f)\left(\frac{D - x}{D - X}\right)^4 \quad 3\text{-}21$$

$$T_{w=}T_2(D,t) \quad 3\text{-}22$$

when $t_1 < t < t_2$

Equation 3-23 defines the temperature of the interface between the wire mesh shelf and the plasma simulant, under the condition $t_1 < t < t_2$. If we apply a heat balance process to the

liquid phase, a differential equation can be produced to define the transient condition for the change in wall temperature.

$$(D-X)\frac{d}{dt}(T_w - T_f) + \left(\frac{5\alpha^2}{D-X} - \frac{dD}{dt}\right)(T_w - T_f) = 0 \quad \text{3-23}$$

Equation 3-23. can be re-arranged and solved as equation 3-24, where the conditions remain as $t_1 < t < t_2$

$$\frac{T_2(D,t) - T_f}{T_o - T_f} = \left(\frac{a}{b}\right)^{-(1+c)} e^{c\left(\frac{1}{b}-\frac{1}{a}\right)} \quad \text{3-24}$$

The constants: a, b, c can be defined as:

$$a = 1 - 2\gamma\frac{\sqrt{\alpha_1 t}}{D} \quad \text{3-25}$$

$$b = 1 - \frac{\gamma}{\beta} \quad \text{3-26}$$

$$c = \frac{5}{2}\gamma^2\frac{\alpha_2}{\alpha_1} \quad \text{3-27}$$

This condition suggests that the temperature of the product exceeds the time constraints given, assuming that the product exists as an entirely single frozen phase. To define the rate of phase change, Dewynne and Hill [87] investigated the rate of phase change, where the initial boundary conditions are different from the phase change temperature. Equation 3-28 defines the change in phase change position with the change in initial boundary conditions.

$$\frac{\Delta^2}{2} \leq \frac{\alpha_1 S_t t}{D^2} \leq \frac{\Delta^2}{2}(2-\Delta)\left[1 + \left(\frac{1}{3} + a_{12}\phi\right)S_t\right] \quad \text{3-28}$$

The following terms denote:

$\Delta =$ velocity divergence, which is a function of heat dissipation (1/s)

$S_t =$ Stefan number

where:

$$\Delta = \frac{X}{D} \quad \text{3-29}$$

The freezing time of the product is a function of the Neumann parameter, defined by

$$t_f = t_e + \frac{D^2}{4\alpha_1\kappa^2} \quad \text{3-30}$$

$T_o = T_f$, where t_e defines the excess time after a complete freeze, in the presence of just a single phase.

$$t_e = \left[1 - \left(\frac{\lambda}{\kappa}\right)^2\right] t_m \quad \text{3-31}$$

where the terms are denoted by:

$c = \text{phase change parameter}$

$\kappa = \text{Neumann parameter}$

Note that:

$$\lambda = \sqrt{2/S_t} \quad \text{3-32}$$

where the matching time t_m can be defined as:

$$t_m = \frac{D^2}{4\alpha_1 \upsilon^2} \quad \text{3-33}$$

where D defines the diffusivity coefficient, α defines the thermal diffusivity in the frozen region denoted by the subscripts, and υ denotes the total phase change time parameter.

3.1.1 Energy Equation

The energy equation throughout the phase change is defined by the two different phases and the intermediate phase change interface. The energy equation for both aspects of the solidification process assumes that the liquid phase is not in motion in relation to the solid phase, where all the velocities are zero. Unlike the generic energy equation, the terms highlighting the dissipation and pressure terms have been omitted. The energy equation transforms into:

$$div\left(\bar{k}.grad\ T\right) + q_r + q_g = \rho C_p \frac{\partial T}{\partial t} \quad \text{3-34}$$

If we assume that the other methods of heat transfer are treated as a boundary condition, the equation can be reduced to:

$$\frac{\partial}{\partial x}\left(k_x \frac{\partial T}{\partial x}\right) + \frac{\partial}{\partial y}\left(k_y \frac{\partial T}{\partial x}\right) + \frac{\partial}{\partial z}\left(k_z \frac{\partial T}{\partial x}\right) + q_g = \rho C_p \frac{\partial T}{\partial t} \quad \text{3-35}$$

The assumptions mean that the solidification process will mainly be conduction based. If the chemical properties of the fluid remain constant during the solidification process, the equation can be reduced to:

$$\nabla^2 T + \frac{q_g}{k} = \frac{1}{\alpha}\frac{\partial T}{\partial t} \qquad 3\text{-}36$$

where the following terms denote:

$q_g = \text{Generated Energy}$

The thermal diffusivity is represented by:

$$\alpha = \frac{k}{\rho C} \qquad 3\text{-}37$$

Further derivations and modifications of the energy equation in relation to the multiphase model used can be found in Chapter 5.

Solid Liquid Interface

The definition of the conservation of energy at the point of phase change is applied to the volume in a given time interval is;

$$(q_1 - q_2)\,\Delta t + q\Delta t - W = \Delta E \qquad 3\text{-}38$$

The term represented as $(q_1 - q_2)$ defines the heat transfer via conduction, whereas q represents the influence of other heat transfer methods. W highlights the work in relation to the volume change. The energy balance at the interface can be determined by:

$$\left(-k_1 \frac{\partial T_1}{\partial x} + k_2 \frac{\partial T_2}{\partial x}\right) A\Delta t + p\, A\Delta X \left(1 - \frac{\rho_1}{\rho_2}\right) + q\, A\Delta T = m\left(h_f - h_i\right) \qquad 3\text{-}39$$

Equation 3-40 highlights the energy balance phase change, which highlights the enthalpy change from the solid to liquid phase denoted by $m\left(h_f - h_i\right)$. Where ℓ As the interface experiences an enthalpy change from liquid to solid defined by:

$$-k_1 \frac{\partial T_1}{\partial x} + k_2 \frac{\partial T_2}{\partial x} + p\left(1 - \frac{\rho_1}{\rho_2}\right)\frac{dX}{dt} + q = -\rho_1 \ell \frac{dX}{dt} \qquad 3\text{-}40$$

Equation 3-40 denotes the change in enthalpy, the equation assumes the interface to be moving in a positive direction in space coordinates. Depending on the direction of the solidification process, the signs can be reversed.

3.1.2 Momentum and Continuity

The definition of momentum and continuity exist as the default value where the momentum equation is given by Newton's second law defined in equation

$$\sum F = ma \tag{3-41}$$

where f denotes body or surface forces related to the stress tensor σ. The stress tensor for a Newtonian fluid is defined as:

$$\tilde{\sigma} = -p\tilde{I} + \tilde{T} \tag{3-42}$$

where the stress tensor is a function of pressure denoted by p, $\tilde{I}$ is the identity tensor and $\tilde{T}$ representing the pure shear tensor. Further alterations of the momentum and continuity can be found in Chapter 5

3.1.3 Heat Transfer Coefficient

For the determination of the heat transfer coefficient at the interface between the solid and fluid phases, a number of assumptions needs to be made, typically that the heat capacity of the solid will be negligible due to the latent heat of solidification.

3.1.4 Numerical assumptions and advances in technology

The modelling of solidification processes has commonly been carried out in the metallurgy industry for casting processes, to determine phenomena such as shrinkage and thermo-mechanical analysis. The process of solidification has been discussed in various studies with two main types of solidification depending on the level of bulk. Typically, the prediction of nucleation is erratic and unpredictable, as it depends on the amount of impurities within a substance. The level of impurities highlights the potential for random nucleation points which can make the interface between solid and fluid phases unstable, where the system is no longer in equilibrium. Dendrites begin to form on a microscopic level, with tree-like structures forming at the interface. The formation of dendrites can occur under two conditions, the first being growth occurring when the latent heat is dissipated through the liquid phase from the interface from an undercooled melt. Typically, with an undercooled melt, the growth direction is parallel to the heat flow. The second is the conditions where solidification occurs when the latent heat is dissipated through the solid. The modelling complexities associated with dendrite growth is are complex due to unknowns associated with the modelling of the interface including the shape and depth of the interface. Zhao et al [88] investigated modelling of dendrites by associating the dendrite radius inversely proportional to the tip velocity. The formation of dendrites is dependent on the interface temperature and the kinetic motion of the interface,

both key parameters for solidification. The research presents a quasi-stationary mathematical model from an undercooled melt. The author highlights the instability of modelling dendrite growth as any disruptions can cause the dendrite formation to branch. Whereas approximations and linear assumptions lead to robust but inaccurate results. The research proposed a boundary element method (BEM) numerical model which is based on the calculation of each node point at the interface. The calculation allows the determination of the surface tension with given temperature boundary conditions. The growth rate at each node is calculated under a time step regime. The results highlight a successful visualisation of dendrite growth allowing for a symmetric growth rate, with accurate representation of dendrite formation along a channel with minimal errors. The modelling of moving interfaces has been investigated by Zerroukat and Wrobel [89], through Finite Difference (FD), Finite Element (FE) and Boundary Element (BE). The authors highlight the use of BE as a preferred modelling technique due to the accuracy in relation to cost effectiveness. The research describes the development of a boundary element-based method to solve a moving boundary problem with multiple moving boundaries. The study applies a set of assumptions which allows the interface to be tracked simultaneously between two phases. The solving regime allows an iterative process where the velocity and interface location are extrapolated from previous time steps. The results obtained from the study demonstrates a good agreement in predicting the velocity and the energy balance throughout the domain. The tracking of the interface has also been conducted using BEM formulations. The study conducted by Delima-Silva and Wrobel [90] developed a formulation for tracking a moving interface with a one-dimensional model. The initial condition utilises the phase change temperature for melting to occur, where the boundary condition defines the temperature to be diffused across the solid to account for the latent heat of melting. The direction of the interface was defined as a direction normal to the phase change boundary, which is recomputed after each timestep. The formulation was tested on an array of one-dimensional models which highlights a good convergence between all one-dimensional models. The research highlights the advantages of BEM modelling where a mesh is required at the boundaries which can be solved, eliminating the need to construct a whole domain. The modelling of interfaces has been widely studied, from both an experimental and numerical perspective highlighting an important development in predicting the thermal and physical properties of the interface.

The solidification process adds a complexity to the modelling, with the convection providing a mixing element which can skew results of numerical models due to the approximations made. The variables within numerical models, such as variable food properties, packaging, air gaps, etc., all play a significant influence in the freezing profile. The change in profile subsequently means a change in diffusion, affecting the rate of conduction [91]. The use of predictive

solidification models within food freezing systems was investigated by Moraga et al [92]. The basis of the research demonstrated the rate of conduction during solidification in a food freezer based on natural convection. The cooling aspect of the freezer was represented by the walls being simultaneously cooled. The research describes the development of a two-dimensional model based on independent variables to model conduction within solidification. The model itself allows the solidification process to be defined by the change in specific heat. Unlike traditional numerical modelling, the developed model allows the replacement of convective terms by conduction terms. The model accounts for a pre-existing solid structure which considers the available liquid fraction. The model assumes that the physical properties remain constant during the phase change, with the mass transfer omitted. The reflected results highlight the change in temperature rather than the definition of the interface and fraction of all phases.

Typically, CFD simulations of solidification processes have also been applied for the solidification of phase change materials (PCM), where the key parameters are the rate of heat transfer, solidification rate and the associated energy stored. The modelling of a PCM considers the volume and liquid fractions, with the analysis of phase change models. The methodology for modelling PCMs may be applied in the two traditional forms defined in section 3.1.

3.2 Chapter summary

This chapter has outlined the solidification model in relation to a plasma bag, the chapter provides a foundation for the solidification phenomenon simulated in chapter 6.

Chapter 4 : Heat Pipe Design

This chapter will mainly focus on the development of the novel heat pipe system. The chapter begins with the identification of the specification to provide a base point into the design. The chapter further explains the thermal resistance analogy used to develop heat pipe tube bundles. The chapter will justify the tube bundle spacing in relation to the freezing chamber size. The outcome of this chapter highlights the development of novel heat pipe installed within a retrofitted cryogenic freezer.

4.1 Specification

The design of a HPHE is primarily based on the effectiveness model. The model is based on a set of dimensionless numbers determining the number of transfer units (ε-NTU) between the evaporator and condenser. The model considers a multitude of factors such as the effectiveness of a single pipe, the heat capacity ratio between the incoming streams, the working fluids and the tube bundle. The selection of using the ε-NTU eliminates the need to characterise both incoming and exhaust streams, and only accounting for the performance of the heat pipe tube bundle, allowing for greater flexibility in design.

The design of a HPHE operation needs to be defined. Table 4-1 highlights the key parameters for the heat exchanger design.

Condition	Value	Unit
Nitrogen average specific heat capacity	1.04	J/Kg.K
Nitrogen Inlet Temperature	-196°C	°C
Nitrogen Outlet Temperature	Variable (Gaseous form)	°C
Available Chamber Space	65 x 50 x 50	cm

Table 4-1: Design Conditions

The design of a heat pipe typically can be done through electrical analogy. The electrical analogy is based on the resistance experienced by the heat flow during the operation of a heat pipe. Figure 4-1 highlights the electrical resistance schematic for a single heat pipe [93].

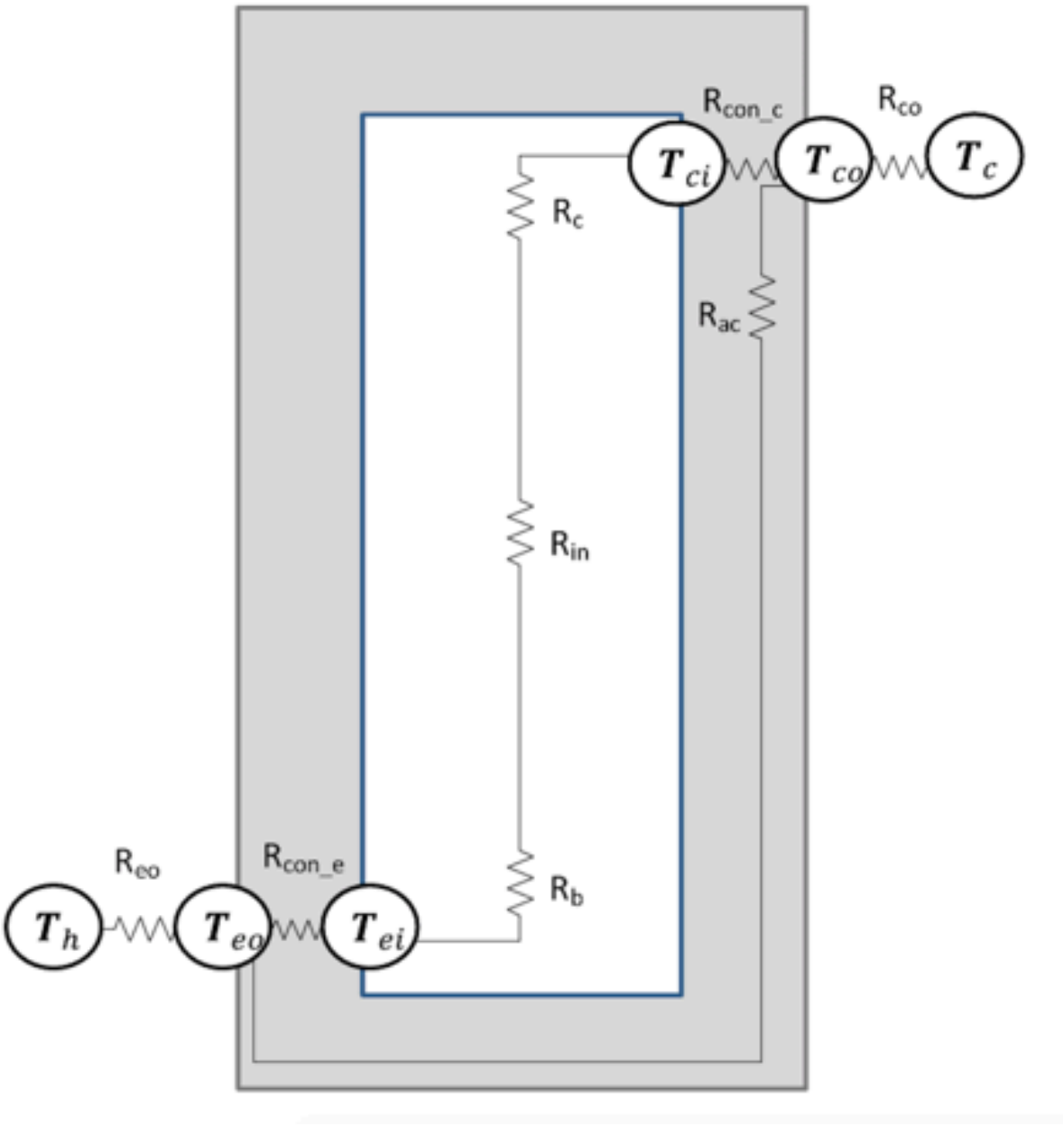

Figure 4-1: Single heat pipe thermal resistance diagram

The labelled resistances can be defined as:

R_{eo}: Convective thermal resistance in the evaporator section

R_{con_e}: Conduction thermal resistance of the evaporator wall

R_b: Thermal resistance from boiling

R_{in}: Thermal resistance experienced due to the pressure difference between the two phases.

R_c: Thermal resistance from condensation

R_{con_c}: Conduction resistance across the wall of the condenser section.

R_{co}: Thermal resistance (convection) from the outside wall of the heat pipe.

R_{ac}: Thermal resistance from axial conduction across the thermosyphon

The denoted terms can be summed to determine the total thermal resistance highlighted in equation 4-1

$$R_T = R_{eo} + R_{con\_e} + R_b + R_{in} + R_c + R_{con\_c} \quad 4\text{-}1$$

4.4.1. Conduction (Thermosyphon Walls)

The initial heat flow begins at the point where the warm fluid is in contact with the heat pipe walls. The heat transfer from the hot stream to the heat pipe walls is via conduction. The resistance can be determined by:

$$R_{con} = \frac{ln(R_{out}/R_{in})}{2\pi kl} \quad 4\text{-}2$$

where the following terms denote:

k: Thermal conductivity (W/m.K)

l: length of pipe, in contact with the incoming hot stream (m)

R_{out}/R_{in}: Difference between outer and inner radius (m)

Equation 4-2 applies to both condenser and evaporator sections where the main variables will be the temperatures of the condenser and evaporator sections, the tube lengths in contact with the fluid streams and the change in conductivity [93].

4.4.2 Convection (External)

Convective terms from the heat pipe are defined as the fluid flowing externally around the pipe, prior to conduction. The following equations show the convective terms for the evaporator and condenser sections [93].

$$R_{eo} = \frac{1}{h_{eo}A_e} \quad 4\text{-}3$$

$$R_{co} = \frac{1}{h_{co}A_c} \quad 4\text{-}4$$

The following terms in equation 4-3 and 4-4 denote:

h: Heat transfer coefficient (W/m^2.K)

A: Surface area (m^2)

k: Thermal conductivity of the fluid (W/m.K)

4.4.3 Resistance (Between two phases)

The resistance R_{in} at the interface denotes the decrease in vapour pressure due to the pressure difference between liquid and vapour phases. Equation 4-5 highlights the resistance at the interface between both phases [93].

$$R_{in} = \frac{8R_g\mu_v{T_v}^2}{\pi{h_{fg}}^2 P_v\rho_v}\left[\frac{(L_e + L_c)/2 + L_a}{{r_i}^4}\right] \quad 4\text{-}5$$

where the following terms denote:

R_g : Specific gas constant (J/Kg. K)

h_{fg}: Latent heat of vaporisation (Working fluid)

L: Characteristic length, where subscripts a, c and e indicate adiabatic, condenser and evaporator, respectively. (m)

T_v: Temperature (Vapour) (K)

P_v: Pressure (Vapour) (Pa)

μ_v: Dynamic viscosity (Vapour) (kg/ms)

ρ_v: Density (Vapour) (kg/m^3)

4.4.4 Boiling Resistance

When the heat pipe is in the operation window, the working fluid within the pipe begins to boil, and then it vaporises and flows towards the condenser section [93]. Equation 4-6 highlights the resistance denoted as R_b:

$$R_b = \frac{1}{h_b A_{ew}} \quad 4\text{-}6$$

where:

A_{ew}: Surface area of evaporator section (m^2)

h_b: Heat transfer coefficient of boiling (W/m^2.K)

Equation 4-6 can be modified to account for nucleate and falling film boiling, while the heat transfer coefficient can be determined by Table 2-8

4.4.5 Condensation resistance

Figure 4-1 highlights the resistance in the condenser section, defined by:

$$R_c = \frac{1}{h_c . A_c} \quad \text{4-7}$$

where the following terms denote:

A_c: The total surface area of the condenser section (m^2)

h_c: Condensation heat transfer coefficient ($W/m^2.K$), which can be obtained from the selection of correlations defined in Table 2-9

The heat transfer through the heat pipe can be calculated by the following equation:

$$Q_{hp} = \frac{T_{eo} - T_{co}}{R_t} \quad \text{4-8}$$

4.4.6 Heat pipe heat exchanger

The proposed heat pipe defined in Chapter 4 is a set of two tube bundles consisting of 8 pipes on each side. which are considered to be connected in parallel. Figure 4-2 shows the schematic where heat pipes are connected in parallel. We can define the resistances of tubes connected in parallel as [93]:

$$\frac{1}{R_t} = \frac{1}{R_{hp1}} + \frac{1}{R_{hp2}} + \cdots \frac{1}{R_{hpn}} \quad \text{4-9}$$

where n denotes the number of heat pipes connected in parallel.

If we assume that each heat pipe has a similar thermal resistance, Equation 4-9 can be rewritten as:

$$R_t = \frac{R_{hp}}{n} \quad \text{4-10}$$

where n represents the number of heat pipes.

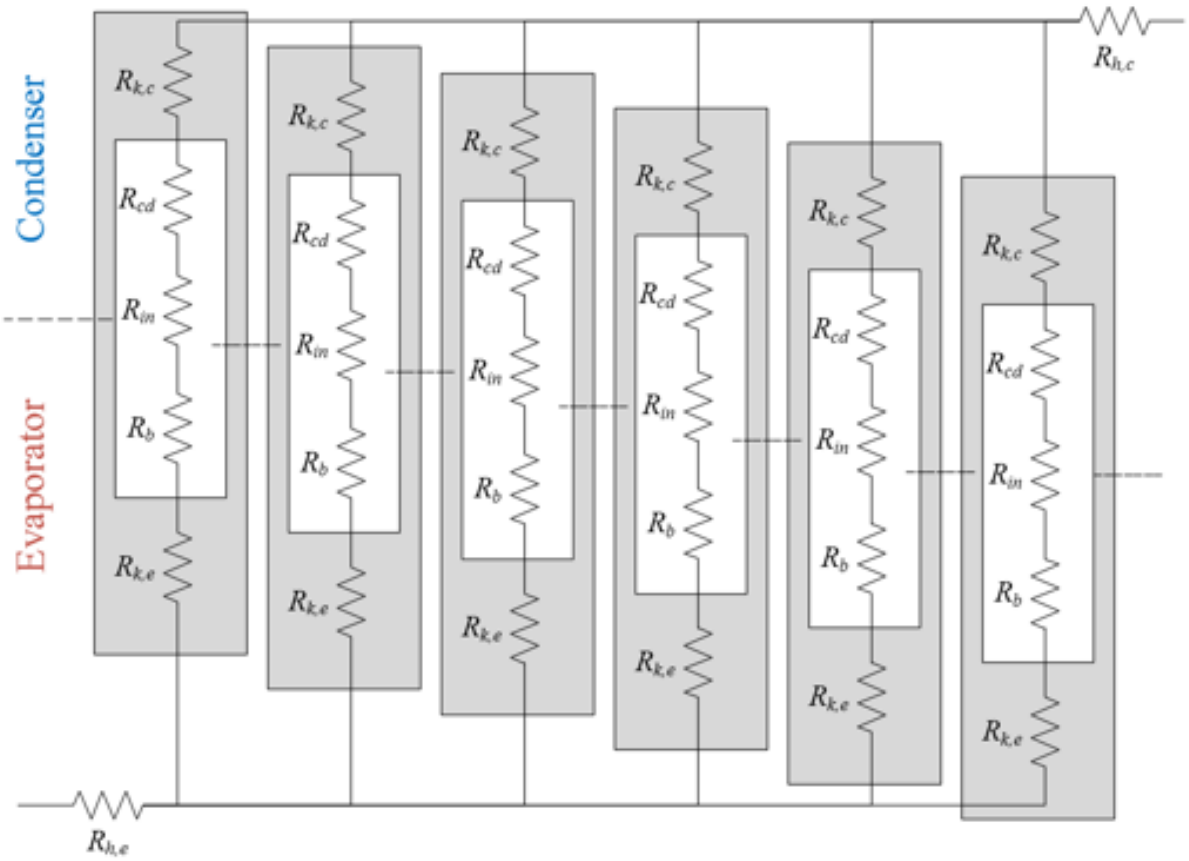

Figure 4-2: Heat pipe heat exchanger resistance

4.4.7 Log mean temperature difference (LMTD)

There are two different ways of modelling heat pipes, the log mean temperature difference (LMTD), and the effectiveness (ε-NTU) method. Both methods use the thermal analogy to analyse the HPHE. The LMTD model is mainly representative of the thermal difference across the condenser and evaporator sections, where the entire heat transfer coefficient of the HPHE system can be determined. The models offer the allocation of inlet temperatures, flow rates and overall heat transfer coefficient. If some parameters are unknown, an iterative process can be used. The main difficulty of the LMTD method is the prediction of outlet temperatures, which is the ε-NTU advantage. The ε-NTU allows an accurate prediction of outlet conditions. As the operation of the experiment (Chapter 5) allows control of the exhaust, the LMTD method will be discussed next [93,94]:.

The premise of the LMTD method is based on the following equation:

$$LMTD = \left(\frac{(\Delta T_1 - \Delta T_2)}{\ln\left(\frac{\Delta T_1}{\Delta T_2}\right)} \right) \quad 4\text{-}11$$

where:

$$\Delta T_1 = T_{hot,i} - T_{cold,i} \quad \text{4-12}$$

$$\Delta T_2 = T_{hot,o} - T_{cold,o}$$

(For co- current arrangement)

$$\Delta T_1 = T_{hot,i} - T_{cold,o} \quad \text{4-13}$$

$$\Delta T_2 = T_{hot,o} - T_{cold,i}$$

(For counter current arrangement)

For the design defined in section 3.2.1.7, a counter flow operation has been applied.

The heat transfer rate can be derived from the LMTD, defined in equation 4-14

$$Q_t = U_t S_t . LMTD \quad \text{4-14}$$

The following terms denote:

U_t: Overall heat transfer coefficient

S_t: Total heat transfer area

LMTD: Log Mean Temperature difference (Equation 4-11)

Note: the summation of $U_t S_t$ is inversely proportional to the total thermal conductance of the heat exchanger.

4.4.8 Pipe Arrangement

The arrangement of the heat pipes can be organised in either a staggered or an aligned configuration, depending on the required performance of the heat exchanger. Typically, the heat transfer determined by the flow over one tube can be defined as: $Nu_D = Const\ (Re_D)^m (Pr)^n$, which can also be defined for tube bundles. The key parameter for optimising the arrangement of tube bundles is the heat transfer coefficient, where the rate of heat transfer is dependent on the Reynolds number. Typically, the design of the tube bundles is based on a reference velocity, which can determine the Reynolds number. The flow over the bundle can be defined by the flow of the free area around each pipe and the distance around surrounding pipes. Figure 4-3a highlights an inline pipe arrangement. S_l denotes the longitudinal pitch, St is the transverse pitch, and At is the minimum flow area, which can be calculate by S_t-D. Figure 4-3b shows an arrangement of staggered tubes. The minimum free flow area follows a similar relationship to an inline schematic between adjacent tubes [95]. If

the available flow area is small, the conditions are: $\sqrt{(S_t/2)^2 + {S_l}^2} < (S_t + D)/2$ between diagonal tubes. The maximum velocity can be defined by: $(S_t/2)/\left(\sqrt{{S_l}^2 + (S_t/2)^2} - D\right)$.

Zukaushas [96] developed a set of correlations to determine the heat transfer from tube bundles, which is dependent on the respective Reynolds number, Prandtl number and number of rows. Equations 4-15 and 4-16 highlight the Nusselt number for a turbulent regime.

$$Nu_D = 0.022 {Re_D}^{0.84} Pr^{0.36} \left(\frac{Pr}{Pr_s}\right)^{0.25} \quad 4\text{-}15$$

where Pr>1

$$Nu_D = 0.019 {Re_D}^{0.84} \quad 4\text{-}16$$

where Pr=0.7

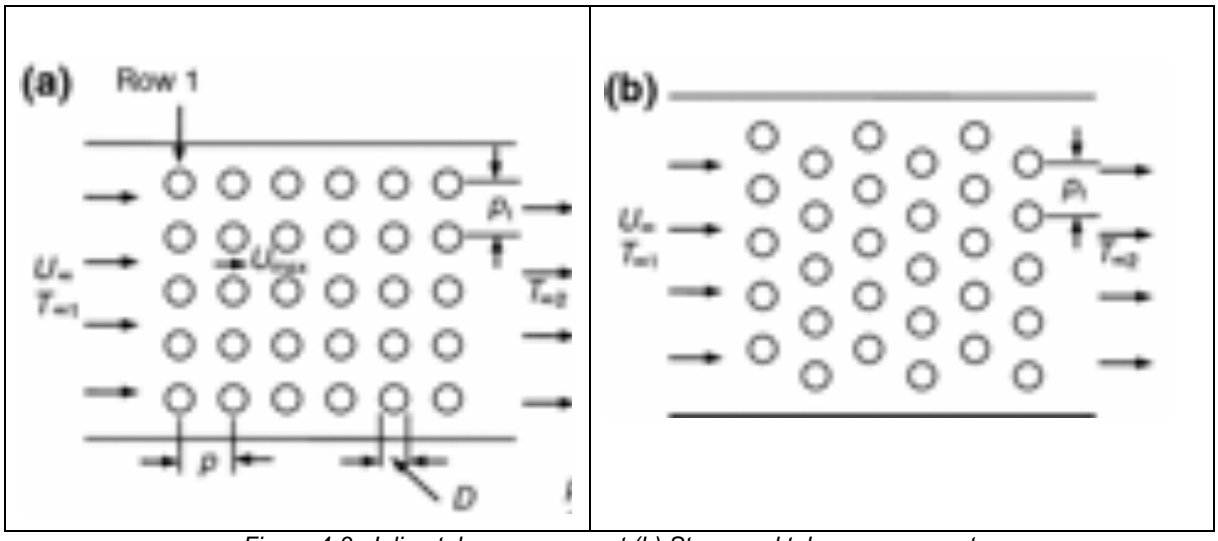

Figure 4-3a Inline tube arrangement (b) Staggered tube arrangement

Given the above arrangement of staggered tubes, the designed heat pipe can be defined in Table 4-2.

Parameter	Length (mm)
S_t	30.5
S_l	34
A_t	21.3
S_d	13.9
A_d	13.9

Table 4-2: Staggered tube arrangement characteristics

4.4.9 Developed Heat pipe

4.4.9.1.Specification

Figure 4-4 and Figure 4-5 display the developed heat pipe system. The heat pipe features two copper tube bundles consisting of 8 tubes connected by a bottom header, and a connector pipe. Both tube bundles are connected by a single condenser section, where the condenser section features a helical cooling coil. The selection of a helical coil was chosen to increase the surface area in contact with the condenser resulting in an increased heat transfer rate. The details of the helical coil are further defined in Section 4.4.9.2.

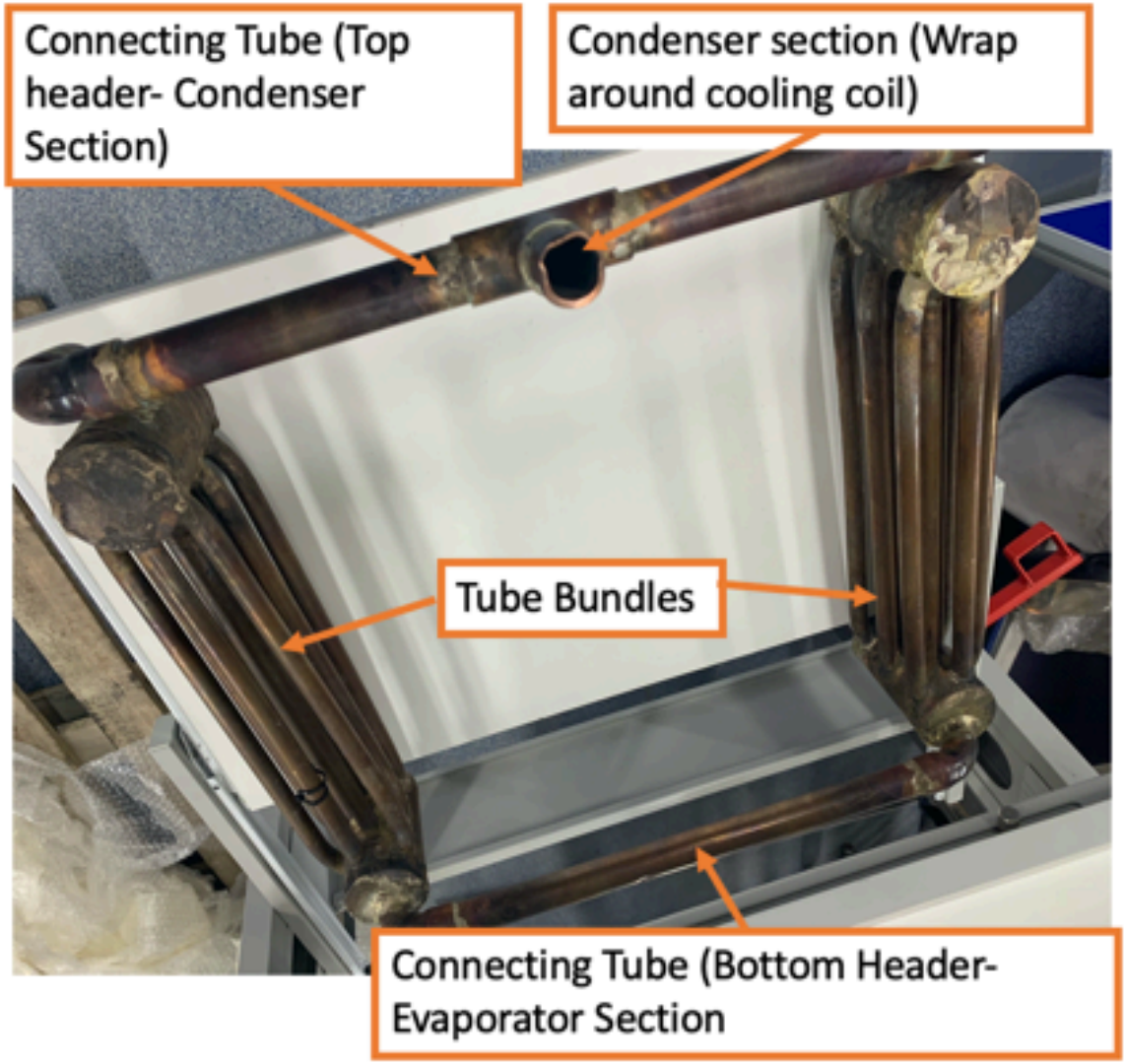

Figure 4-4: Designed Heat pipe

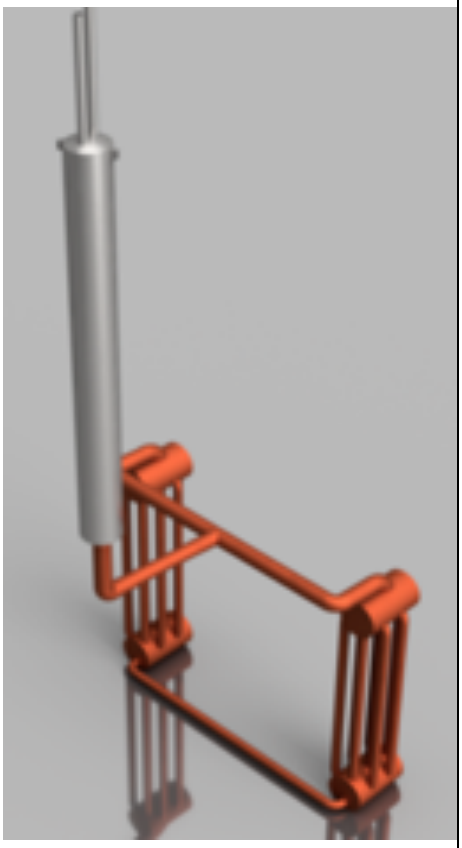

(a)

(b)

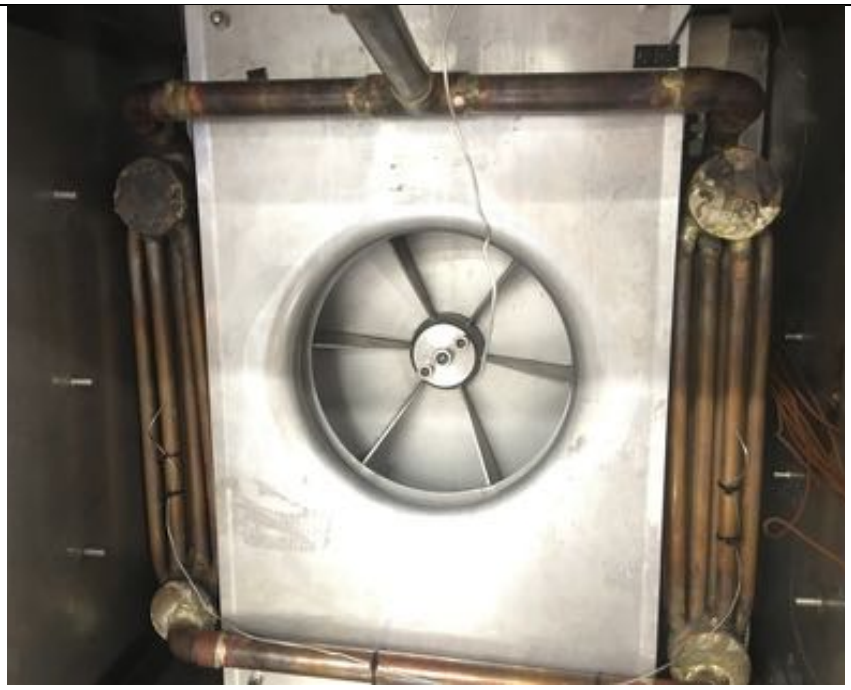

(c)

Figure 4-5: Designed Heat pipe System (a) Rendered Design (b) modified batch freezer (c) Installed heat pipe

4.4.9.2 Cooling Coil

Figure 4-6 shows the operation of the installed heat pipe. The heat pipe is constructed from copper containing R134a, which encapsulates the vapour phase. The condenser section is a helical coil wrapped around a tube length to condense the working fluid, where liquid nitrogen vaporises as the working fluid releases its latent heat to the cold stream. The gaseous nitrogen stream is subsequently exhausted to the atmosphere.

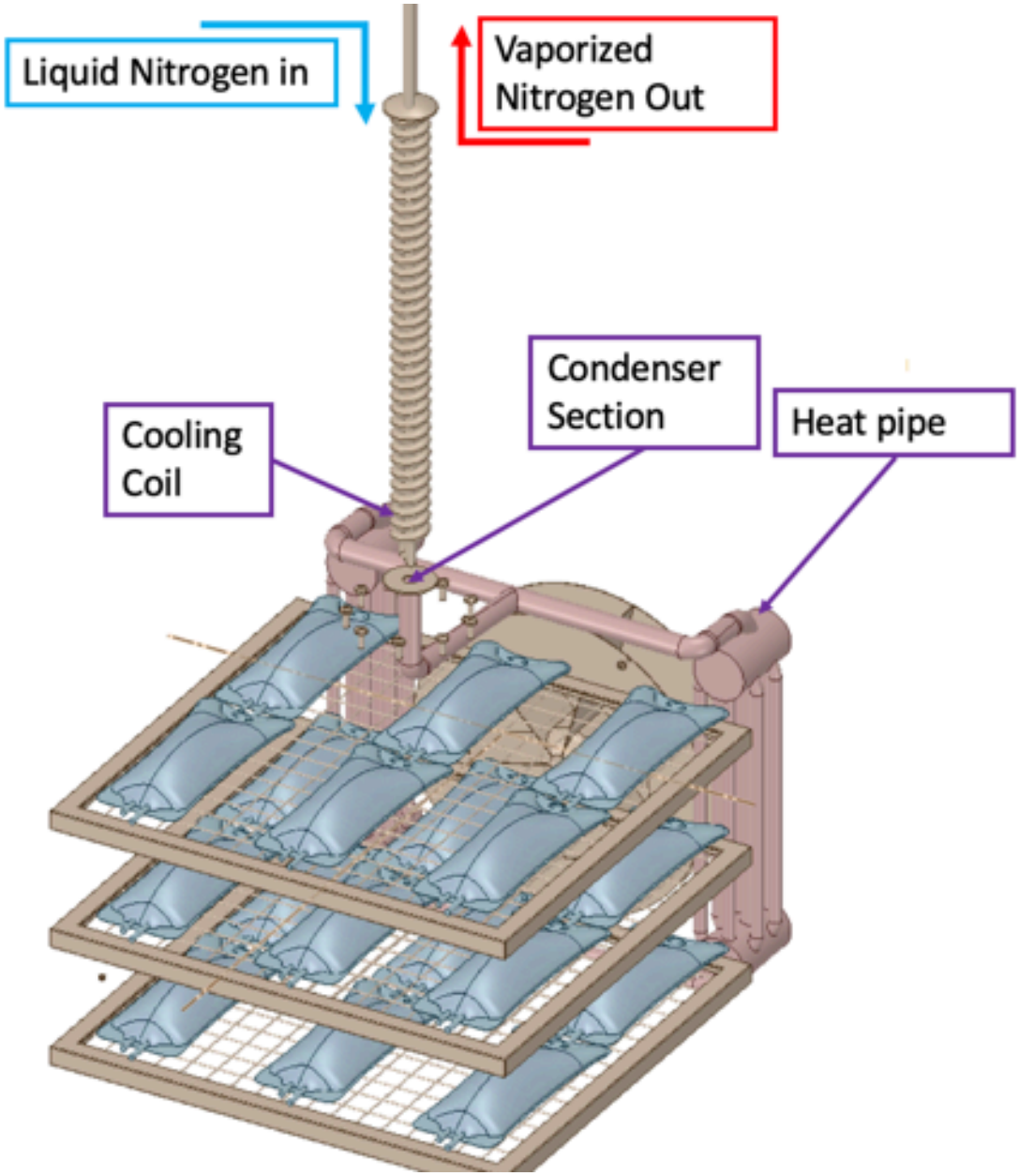

Figure 4-6: Cooling Coil

4.4.9.3 Thermal Conductivity

For the validation of the HPHE, assumptions are made to account for its super conducting properties. To mimic this behaviour, a set of thermal conductivities is applied. The axial conduction rate highlighted in Figure 4-2 can be applied. The axial conduction can be defined as:

$$R_t = \frac{1}{kA} \qquad 4\text{-}17$$

where the terms denote:

R_t: Total thermal resistance

L: Length of thermosyphon

A: Cross sectional area

k: Effective thermal conductivity

Equation 4-17 can be re-arranged to:

$$k = \frac{L}{R_t A} \qquad 4\text{-}18$$

4.2 Chapter Summary

The chapter defines the development of the novel heat pipe which was subsequently installed in a freezing chamber. The chapter highlights the successful design of the tube bundles with the given parameters to optimise the heat transfer rate.

Chapter 5 : Experimental Procedure

In this chapter, a series of types of experimental apparatus were developed and constructed to validate the solidification of the plasma simulant and the development of thermosyphon based cryogenic freezers. Subsequent experimental testing is divided into two main sections: the testing and validation of the solidification of a blood plasma simulant and the testing and validation of the thermosyphon cryo-freezer. The results of the experimental measurements will be used to assess the reliability and accuracy of the CFD simulations for both the solidification of the plasma bag presented in chapter 6, and the development of the heat pipe based cryogenic freezing systems presented in chapter 7.

The experimental procedure and configuration for both the baseline model and the proof of concept (POC) remain identical to observe the change in thermal distribution between an impingement and a retrofitted heat pipe version. Subsequent developments adopted an optimised monitoring system.

5.1 Mechanical Design

The mechanical configuration of components of the prototype and the heat pipe model remains identical, with the only change being an increase in data modules. Figure 5-1, shows the configuration of both systems with the associated section references providing an in-depth explanation into the component.

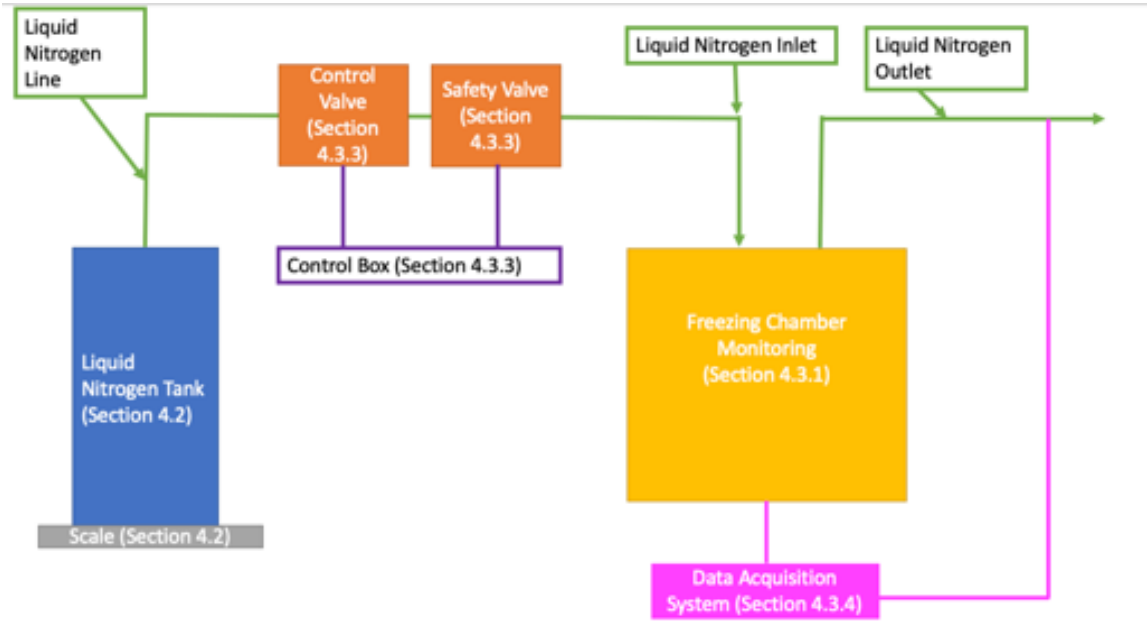

Figure 5-1: Experiment Layout

5.1.1. Cyrogenic Freezer: Liquid nitrogen injection

The development of the system is based on an injection-based system highlighted in Figure 5-2. The cryogenic freezer shown in Figure 5-2, allows the preservation of blood plasma to be processed in batches, to limit the amount of cell degradation. The cryogenic injection freezer presented within this chapter emulates the capacity and processing time within the blood processing facility. The retrofitting of this system allows the direct comparison between an injection and a heat pipe based freezer. The overall loading configuration exists as three removable cross-hatched loading shelves where plasma bags can be loaded and unloaded as highlighted in Figure 5-2. The injectors are located on either side of the chamber, adjacent to the separation plate and the fan as shown in Figure 5-2. The main operation of the system is based on an internal control loop to maintain the set air temperature. Figure 5-3a highlights the probe used to monitor the air temperature. The probe is connected to the main control panel which allows the definition of the air temperature. The main function of the control panel is highlighted in Figure 5-3b. The control panel is connected to the probe and works on an internal feedback system which controls the rate of injection. The control system features a live monitoring screen indicating the real time air temperature when in operation, highlighted in Figure 5-3c. Beneath the control panel is a dial with increments labelled from 0 (off) through 10 (maximum), highlighting operations from 0 RPM to 1995 RPM as shown in Figure 5-3d.

Figure 5-2: Schematic of baseline injection-based system.

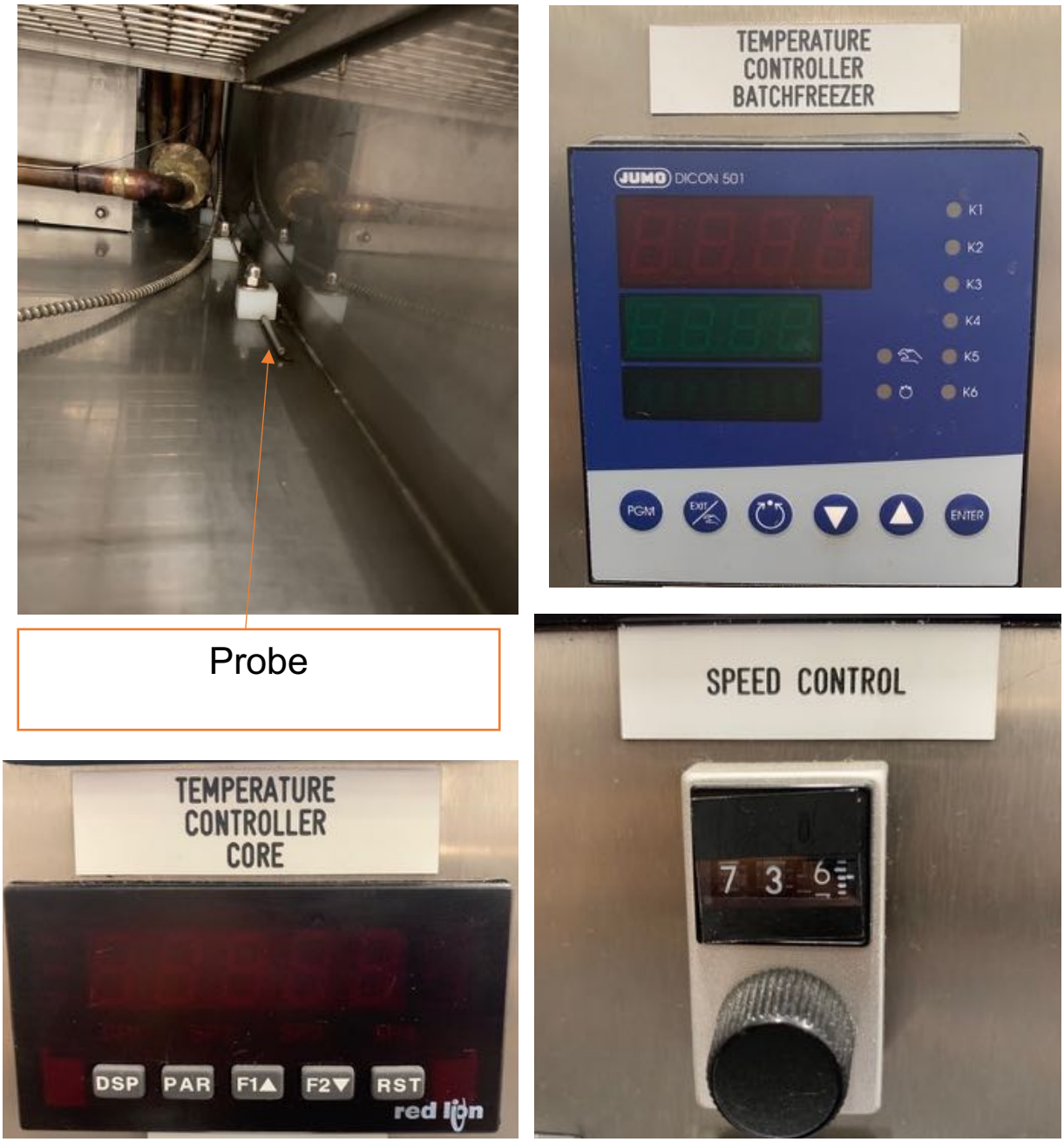

Figure 5-3 (a) Fan control (b) Internal feedback probe (c) Operational controller (d) Live monitoring

5.1.2 Prototype 1: Retrofitted Batch Freezer (POC)

The retrofitted system contains a multichannel thermosyphon as shown in Figure 5-4. The arrangement of the heat pipe consists of two sets of tube bundles with the associated bottom header. Both headers are connected by a copper tube making the system one entity. The heat pipe was charged with R134a. For the operation of the heat pipe, the use of injectors has been eliminated, with the main gas composition within the chamber being air. The operation of the chamber remains identical to section 5.1.1, including the control system shown in Figure 5-3.

Figure 5-4: Developed heat pipe model

Figure 5-5: Experimental set up of Prototype 1 (POC Model)

5.2 Liquid Nitrogen Monitoring

The consumption of liquid nitrogen is a significant factor for the commercial viability of the development of prototypes. The consumption of liquid nitrogen and the final exhaust temperature play a crucial role in the viability of cryogenic based freezers. The operation of cryogenic freezers is based on a liquid fluid entering the system, and the subsequent temperature of the exhaust highlights the effectiveness of a system from a heat transfer aspect. For example, the use of injection freezers requires direct injection but, as a result, the exhaust temperature needs to be significantly cooler than the required air temperature. As a result, the consumption of cryogenic fluids is high with minimal maximisation of the thermal capacity of the fluid/vapor. The monitoring of liquid nitrogen is a key parameter for prototype development. The study involved monitoring via two methods: the monitoring of weight and the volume of the tank. The consumption of the liquid nitrogen is determined by the weight loss of the tank between the start and the end of each experimental session. The scale in use is a Salter DS1000 Barrel scale with capacity of 500kg and readability of 0.2 kg as shown in Figure 5-7. The tank is connected to the experiment via an insulated hose (3m) to transfer the liquid as shown in Figure 5-6

Figure 5-6: (a) Liquid nitrogen supply tank (b)Vacuum insulated hose (c) Interior of vacuum insulated hose

Figure 5-7: Liquid nitrogen consumption scale

5.3 Baseline Model: Liquid Nitrogen Injection

5.3.1 Temperature monitoring

A number of thermocouples were placed throughout the system to monitor the chamber temperature, and the inlet and exhaust stream. The location of the thermocouple highlighted in Figure 5-8 shows a central probe used to monitor the air and exhaust temperatures connected to a data logger defined in section 5.3.4. The previously discussed sections 5.1.1 and 5.1.2 present the set up with an integrated monitor which only allows for live monitoring.

Product details	Thermocouple
Description	Stainless Steel Sheath insulated thermocouple with PVC insulated lead
Dimensions	(1.5mm x 2m)
Temperature Range	-200°C to +400°C
Sourced	TC Direct

Figure 5-8: Thermocouple probe details

Thermocouples are placed throughout the system for validation purposes, and to monitor the operation of the solidification of the plasma simulant and the operating conditions of the function. Specialised T-type thermocouples were installed where the thermocouples could be secured in the plasma bag. The selection of thermocouple is shown in Figure 5-9.

Product Type	Thermocouple
Description	Stainless Steel Sheath insulated thermocouple with sharp end with PVC insulated lead
Dimensions	3.3mm x 5m
Temperature Range	-200°C to +400°C
Sourced	Comark Instruments

Figure 5-9: Specialised blood plasma thermocouple probe

5.3.2 Velocity mapping

The velocity profile within the freezer operates on a grid schematic where each quadrant on each shelf refers to a recording position shown in Figure 5-11. The anemometer shown in the

table in Figure 5-10 was positioned and secured through the exhaust line. The anemometer was placed in-line with the airflow as shown in Figure 5-11. The anemometer was placed in each segment shown in Figure 5-11, to determine the velocity passing through each section. The magnified anemometer image shows a single wire probe, where the reading is dependent on the positioning of the probe. To ensure the probe was aligned, the probe was fastened through the exhaust line ducting. The device features an internal testo data acquisition software which can be exported in a multitude of data file formats. The calibration of the anemometer was conducted by Testo, traditionally the methodology to calibrate an anemometer is to equate the flow velocity in relation to convective heat transfer of the heating wire.

Product Type	Testo 425 Anemometer
Temperature Range	-40°C to +85°C
Velocity measuring range	0 to 20m/s
Accuracy	±0.03 m/s ±0.7 °C (below 0°C)

Figure 5-10: Testo 425 anemometer probe

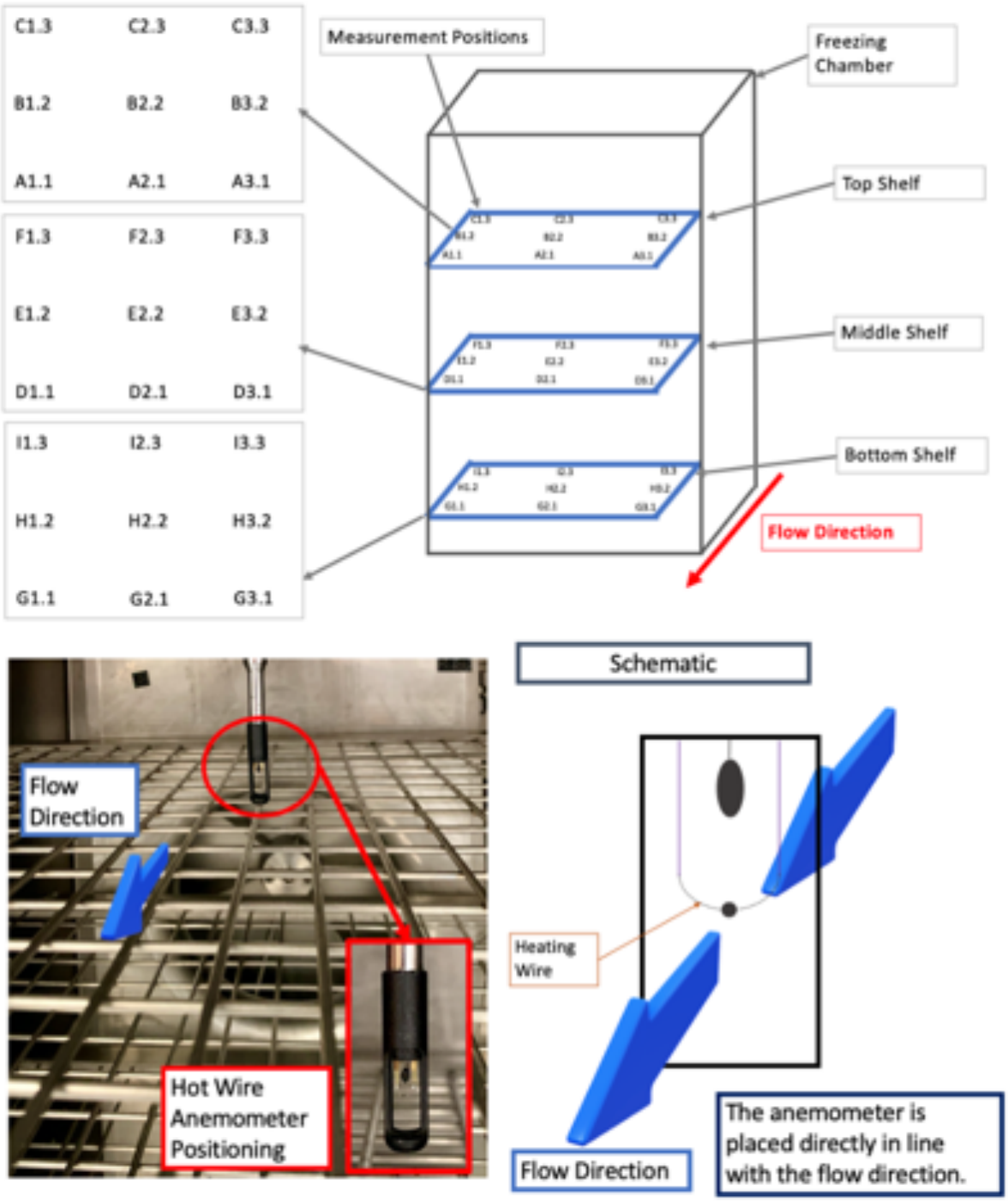

Figure 5-11: Anemometer probe positions

5.3.3 Liquid nitrogen feed

The liquid nitrogen feed is controlled by two gate valves shown in Figure 5-12. The valves are connected to a controller module shown in Figure 5-13. Both valves are placed within the inlet feed with the associated thermocouple monitor placed within the exhaust stream. The control thermocouple is connected to a variable panel where the corresponding exhaust temperature can be set, and also be used for system optimisation, highlighting the relationship between exhaust and air temperature within the chamber. The control panel involves a safety valve which can be used to isolate the system.

Product Type	ASCO Solenoid Valve
Part Number	E210C087SCA8
Maximum Working Pressure	9 Bar
Operating Temperature	-170°C to +50°C

Figure 5-12: Control and supply LIN valve

Figure 5-13: Liquid nitrogen feed controller

5.3.4 Data Logging

The operation of the data logging system was conducted using a 64-channel data acquisition (DAQ) system controlled by LabVIEW Real-Time software from National Instruments. The DAQ system has a Compact DAQ chassis equipped with four 16-channel thermocouple amplifier modules connected to the controller's terminal blocks. The output signals are transmitted to a screen monitor. A program written in LabVIEW Real-Time controls the DAQ system and records data in real time. The system allows for a maximum of 4 modules of 16 thermocouple channels. The baseline and POC models presented in sections 5.4 and 5.5 are connected to a single 16 channel module as shown in Figure 5-14.

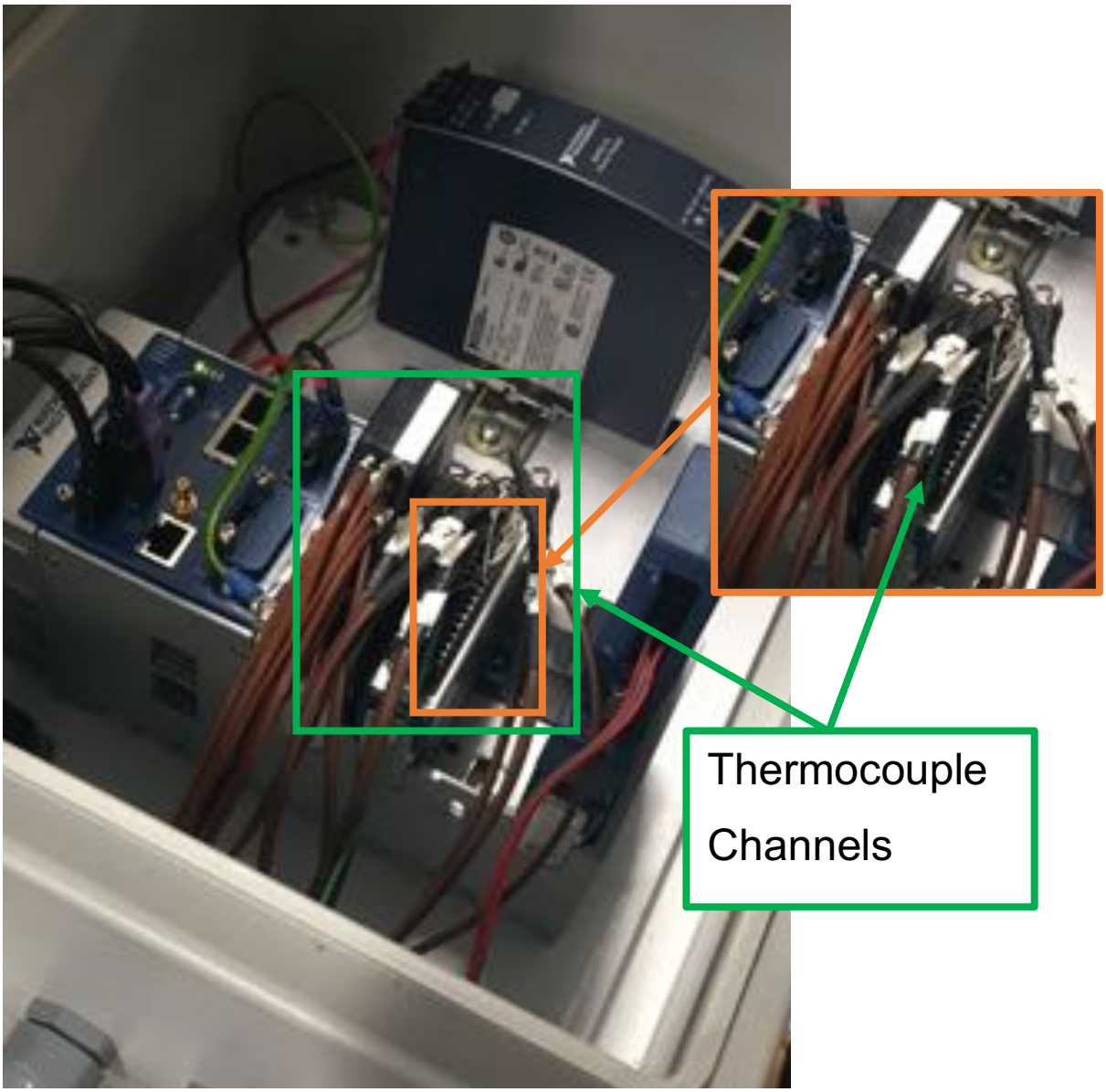

Figure 5-14: Data Acquisition system

5.4 Prototype 1: Retrofitted Batch Freezer (POC)

The operation and connections of the retrofitted system remain the same as the components listed in section 5.3. The main variable within this system is the deactivation of the liquid nitrogen injectors and the addition of the heat pipe, which contains one thermocouple on both left and right tube bundles to monitor its wall temperature as shown in Figure 5-15. The thermocouple measurements will also show if the heat pipe reaches any operating limits. Both monitoring and determination of the velocity profile within the chamber have been discussed in section 5.3.2.

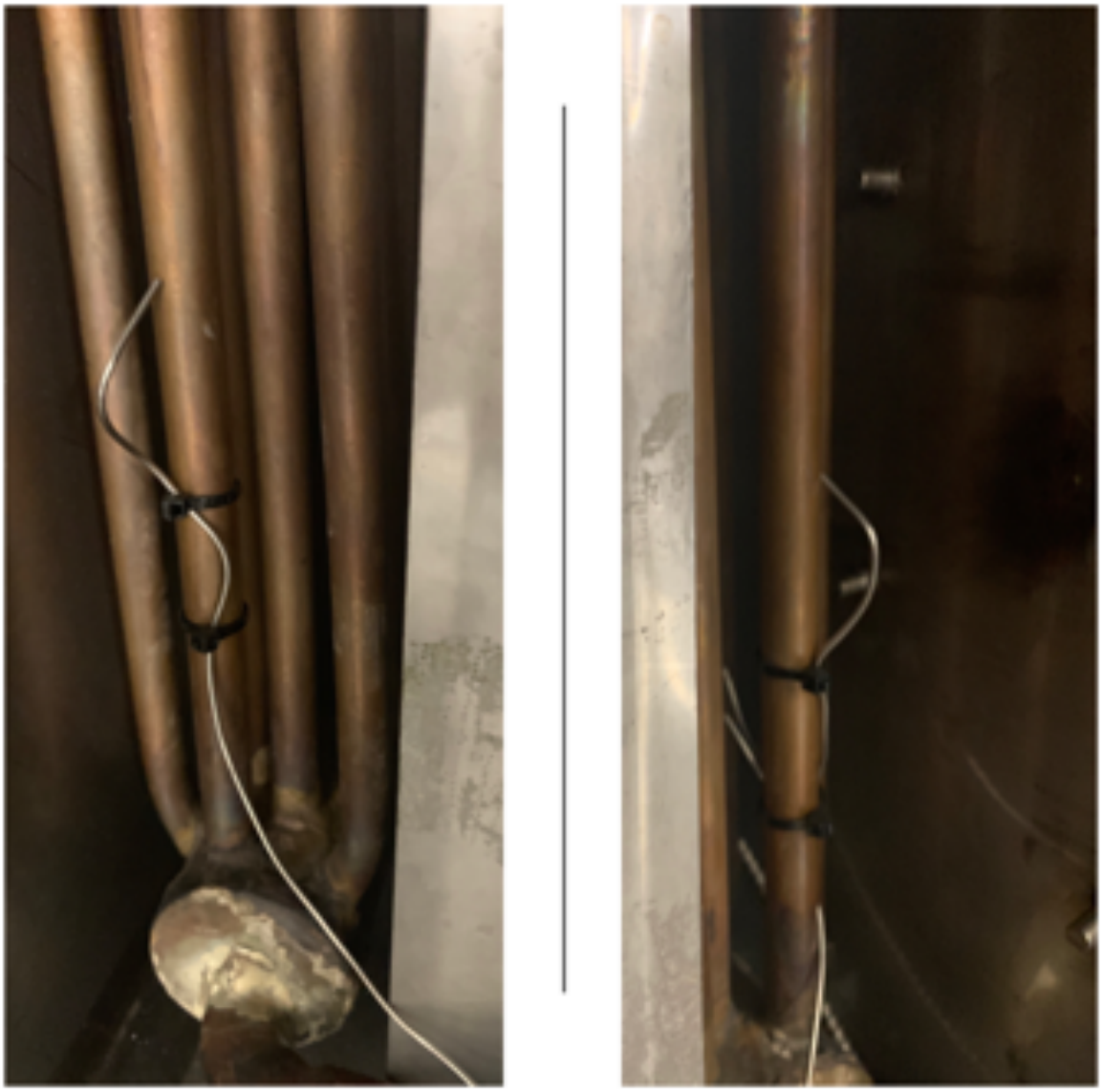

Figure 5-15: Thermocouples to monitor heat pipe temperature

5.5 Preparation of the Blood Plasma Simulant

The composition of blood plasma exists as a suspension of various soluble minerals, amino acids and proteins. The fluid acts as a suspension fluid to aid bodily functions. The variance in pH and concentricity determines the composition of the plasma. The determination of a plasma simulant can exist in two main forms: a synthetic replicant or a simulated body fluid. Both show successful applications highlighted in section 2.8. The use of simulated body fluid is developed in milligrams for the application of gene therapy, whereas synthetic replicants can be reproduced in masses. Yoshida et al [1]reported the use of synthetic replicants as a substitute for blood-based isolates. The study highlights a mixture of aqueous glycerine, with the concentricity being 10 parts water to glycerine.

The composition of the plasma bag consists of a DEHP-DHT plasticiser shell containing several inlet and feed tubes highlighted in Figure 5-16. The plasma bag contains 380ml of an aqueous glycerol liquid acting as a simulant. The plasma bags contain a single opening, also highlighted in Figure 5-17, to allow for the thermocouple discussed in section 5.3.1 to be installed. The plasma thermocouples are connected to the data acquisition system defined in section 5.3.4.

Product details	DEHP-PHT Blood Plasma Bag
Description	Composite polymer blood plasma bag
Dimensions (L x W x H)	250mm x 130mm
Sourced	NHS Blood Supply
Maximum Capacity	600ml
Filled Capacity	380ml

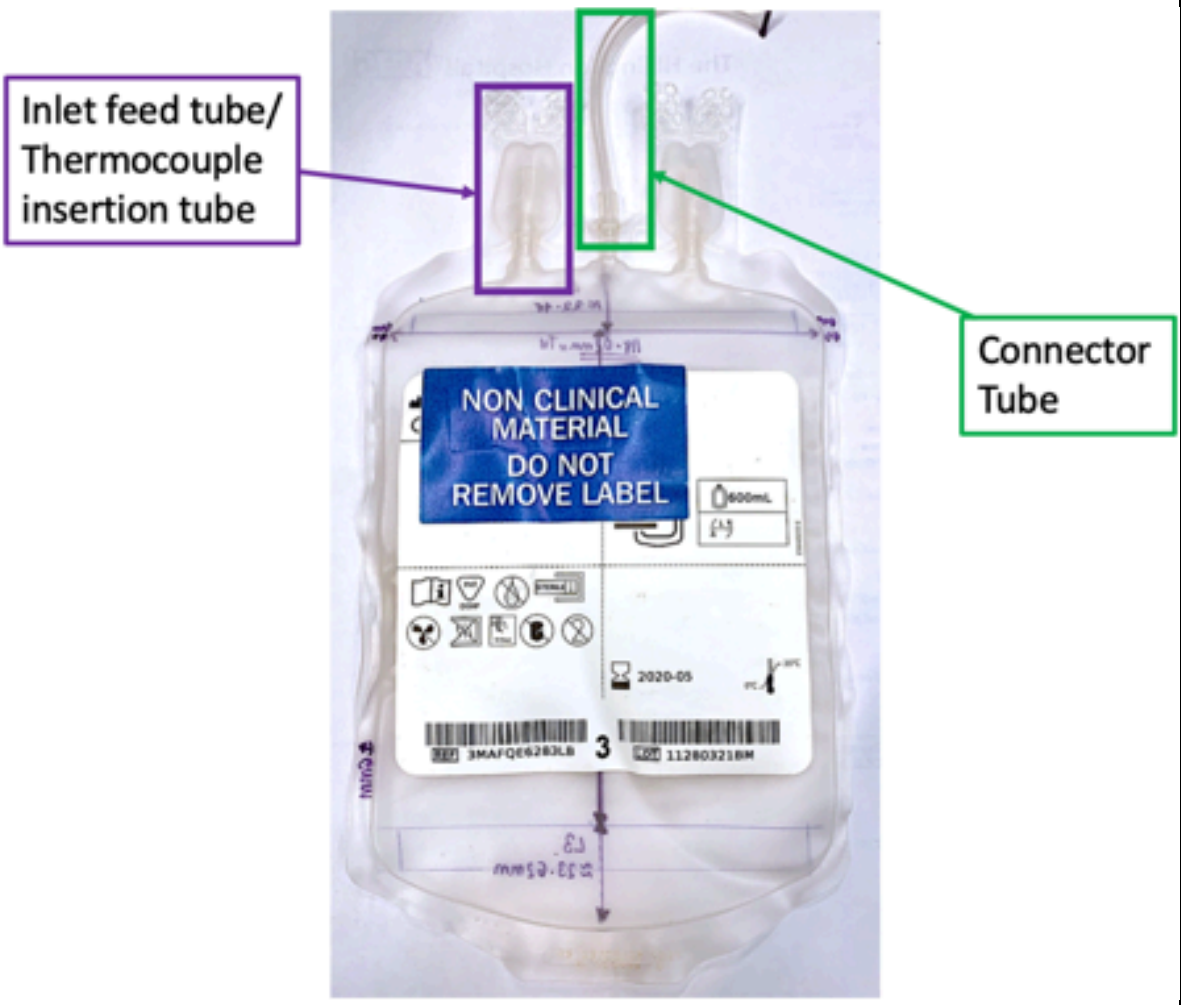

Figure 5-16: Plasma bag

Figure 5-17: Installed thermocouple in plasma bag

5.6 Heat Transfer Coefficient Set up

The heat transfer coefficient was measured with a heated copper disc and monitoring the cooling rate of the freezer system as shown in Figure 5-18. The heat transfer coefficient study acted as a baseline and was conducted with an unloaded configuration. The heat transfer coefficient can be calculated by:

$$h = \frac{m.C_p.\left(\frac{DT}{\Delta t}\right)}{A.\Delta T} \qquad 5\text{-}1$$

where:

h is the mean heat transfer coefficient W/(m^{2}K)

A is the surface area of the copper disc (m^2)

ΔT is the temperature difference between the product temperature and the chamber air (K)

m: mass (kg)

C_p: Specific heat (J/(kg.°C))

DT: Difference in disc temperature (K)

Δt: Difference in time (s)

The procedure involves the heating of copper discs, containing a thermocouple to monitor and record their cooling rate. The discs are placed within a water bath with a pre-defined temperature to heat them up to 80°C The temperature of the discs is kept constant. The placement and use of the copper discs are dependent on the set point temperature of the freezing system. The system will aim to reach the set point temperature and allowing for a period of steady state operation. The heated copper burgers are placed within the system and allowed to cool to observe the cooling rate of the system. The obtained data allows us to estimate an average heat transfer coefficient.

Figure 5-18: Heat transfer coefficient determination

The physical properties for the coper disc are defined by Table 5-1

	Weight (kg)	Diameter (mm)	Thickness (mm)	Surface Area (mm^2)	Specific Heat (kJ/kg.°C)
Copper Disc	0.9	100	12	0.019	0.38

Table 5-1: Thermophysical properties of copper disc

5.7 Error Analysis

The level of uncertainty for experimental values can be determined from the sensitivity and accuracy of the thermocouple and the data logger. The data logger has an uncertainty of 0.25% beyond -40°C, whereas the thermocouple has an uncertainty of 0.8% ±0.02. As the data acquisition operates in an environment below -40°C, a cold junction needs to be considered. The cold junction is at 100% sensitivity

Where the error E_x can be determined by:

$$E_x = A_{daq} \times \frac{S_{daq}}{S_{CJ}} \times A_{TC} \qquad 5\text{-}2$$

Where the terms denote:

A_{daq}: $Accuracy\ of\ data\ aquisition\ system$

S_{daq}: $Sensitivity\ of\ data\ aquisition\ system$

S_{CJ}: $Sensitivity\ of\ Cold\ Junction$

A_{TC}: $Accuracy\ of\ thermocouple$

Table 5-2: Error Analysis results

Temperature	Error ± (°C)
-100	0.8
-75	0.805
-50	0.81
-25	0.815
0	0.82

5.8 Data Analysis

The selection of the correct statistical analysis tool can identify any numerical deviations and quantify the relationship between the sets of data. The thesis presents two sets of data. The data obtained from the experimental studies has a corresponding CFD model used for validation. The basis of the CFD models act as predictive models based on the boundary conditions based on observations made during experimentation. Statistical models used to compare predictive data is commonly conducted by applying the “mean absolute percentage error”. The mean absolute percentage error calculates the accuracy of a predictive model, the resultant value highlights the relative deviation between two data points. The experimental results are treated as actual values denoted by A_t and the numerical model acting as a forecast denoted by F_t. The mean percentage error can be calculated as;

$$M = \frac{1}{n}\sum_{t=1}^{n}\left|\frac{A_t - F_t}{A_t}\right| \qquad 5\text{-}3$$

The values produced are absolute, therefore the positive and negative error connotations can be eliminated. The mean average percentage error can be applied to each data point. The relative deviation between the two values highlights the accuracy between each forecast point and experimental data point. The results presented in the thesis will highlight and justify the largest deviations.

5.9 Chapter Summary

The chapter defines the instrumentation used to characterise the performance of both heat pipe and injection based freezers. The chapter defined the key differences between both systems highlighting the similarities between them. As the heat pipe prototype was a retrofitted injection freezer, the only difference was the addition of a copper heat pipe and the resultant increase in data acquisition channel.

Chapter 6 : CFD Simulation of a two-phase solidification of blood plasma simulant

The modelling of the solidification of a plasma simulant requires a set of boundary conditions and definition of the phase properties of the two-phase process. Typically, the application of numerical modelling allows for the visualisation of processes and flow regimes previously unknown. The visualisation allows a better understanding of the process which can be used to validate procedures based on experimental observations. This chapter will define the two-phase solidification process experienced by the plasma bag containing a blood plasma simulant. The contents of the chapter define the conditions within a single load chamber, for solidification to occur in an injection based freezing chamber and, in a heat,-pipe freezing chamber. The change in operational conditions, performance and thermal variation within the chamber will be investigated in Chapter 7.

6.1 Introduction to Computational Fluid Dynamics (CFD)

The application of CFD modelling allows for a set of governing equations to be solved to define specific phenomena occurring within a flow field. The flow field contains many other phenomena including heat and mass transfer alongside thermophysical property changes as a result of convective and conductive processes and boundary conditions. The variation of the flow field can be determined by a range of numerical and experimental investigations.

The application of experimental investigations has previously allowed for utilisation of equipment and accurate measurement tools to determine phenomena via physical testing. The problems with experiments are generally linked to the technical difficulties which can arise during the tests, ranging from a number of complexities including calibration to failure. Typically, the operation and maintenance of experimental equipment is also costly, and some experiments can be potentially problematic to scale. Experimental investigations provide a key part in the validation of numerical models. The relation between numerical models and experimental testing is vital for the validation of each set of data where the reliability and accuracy of each needs to be determined. Typically, the utilisation of CFD employs a finite volume method where a set of governing equations are applied to a set control volume. CFD simulations allow for the visualisation of complex flow regimes suited to a range of applications with different sets of governing equations, highlighting its versatility. As the simulations involve the entire set of control volumes, the problem can be analysed as a whole, which is more difficult during experimental investigations.

6.2 Multiphase modelling

Multiphase modelling consists of two or more phases existing within a system, where the interactions between phases need to be accounted for. A number of multiphase numerical models exist depending on the phase interactions, and before this can be determined a set of conditions need to be applied, such as:

- Number of phases present - this can be a mix of liquid, solid and gas, dependent on the flow regime.
- Identification of governing equations required, to account for the conservation of mass, momentum and energy, which directly influences the numerical results. The parameters can be altered with the utilisation of User defined functions (UDF)

6.2.1 Approaches to multiphase modelling

The modelling of multiphase processes can be determined by two methods, a Langrangian-Eulerian approach or a Eulerian-Eulerian approach. Both methods have been widely used in the literature to effectively model multiphase phenomena. The application of the Euler-Lagrange technique allows the fluid phase to be solved through a time-averaged Navier-Stokes equation, and the secondary phase is tracked via particles and bubbles through the control volume. The approach is commonly referred to as a discrete phase model. Euler-Lagrange methods are commonly applied to simulations involving the tracking of particles and bubbles where the trajectories are required. The key assumptions for this model require a low volume fraction of less than 10%. On the other hand, Eulerian-Eulerian methods treat the phases as a continuum and have predefined volume fractions which are a function of space and time. The Volume of Fraction (VOF) model is a well-known solidification model which adopts a closed volume where the summation of both solid and liquid fractions must equate to 1. The different multiphase models are further explained in Figure 6-1.

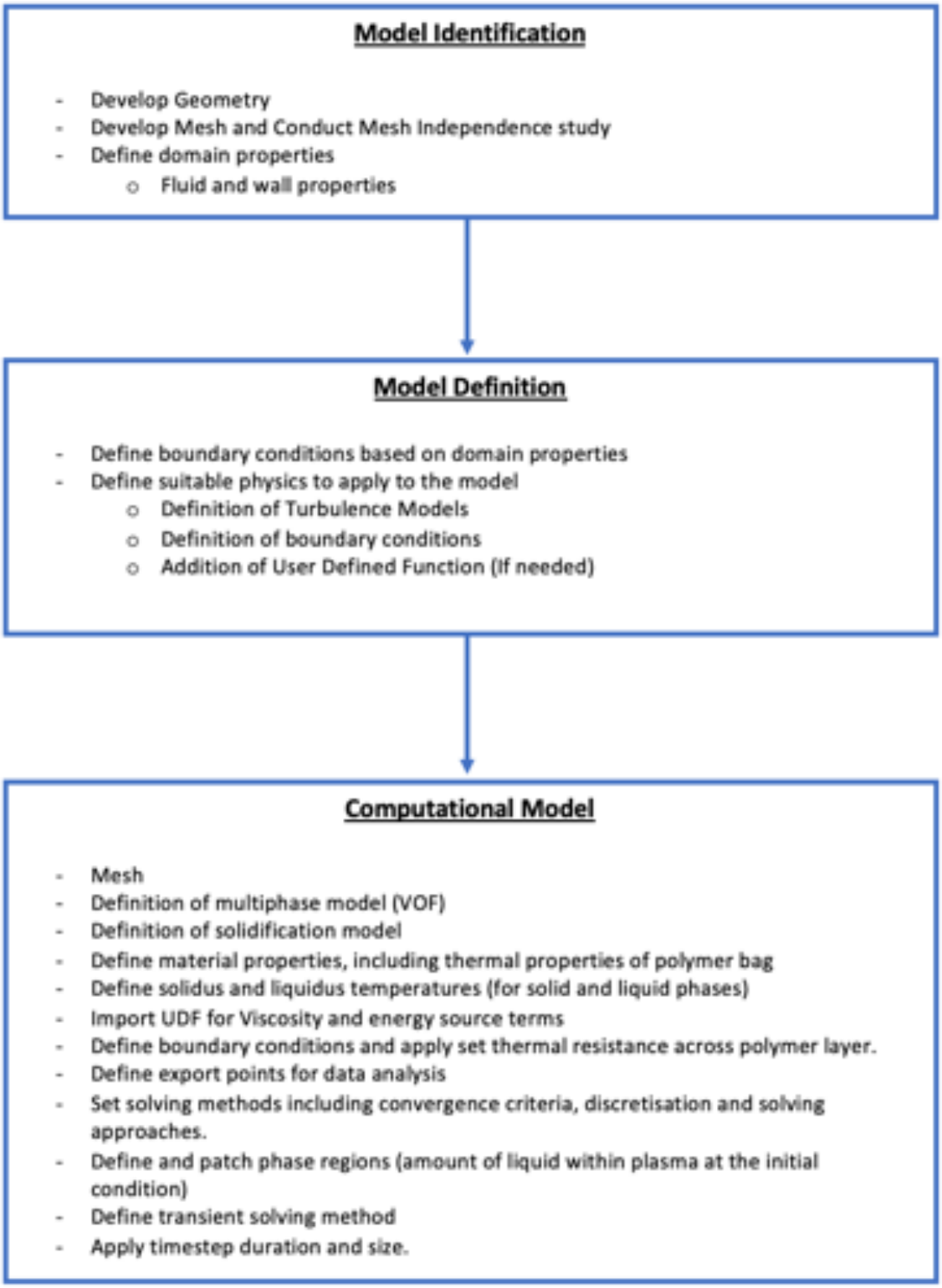

Figure 6-1: CFD Solution Process

6.2.2 VOF and Solidification Model

The modelling of the two-phase process has been discussed at length in the literature, with many applications and limitations to each multiphase model available, and explanations on why the problem cannot be modelled using the assumption of single-phase flows. One of the key parameters for multiphase modelling is the definition of phases and the movement of the liquid-solid interface. With the changing of phase, the changes of both density and viscosity need to be considered. The VOF model allows for the development of a simple multiphase model, on the basis of the definition of phases for liquid and solid. The application of the solidification model within ANSYS Fluent allows the definition of two phases including the solidus and liquidus temperatures. When external conditions are applied, the defined liquid and solid phases can be altered allowing for an accurate visualisation of the solid-liquid interface. The position of the interface can be determined by a surface tracking technique which can be applied to a fixed mesh.

The VOF model is primarily based on the volume fraction of each phase, where each cell defined in the fixed grid has a numerical allocation specific to each control volume. The cell could contain one or more phases, which can either be the volume fraction of the liquid α_l and/or the volume fraction of the solid α_s. The volume fractions can be defined as:

- $\alpha_l = 1$: assigned phase volume is fully liquid
- $\alpha_l = 0$: assigned phase volume Is fully solid
- $0 < \alpha_l < 1$: cell contains both phases

The solidification model assumes phase change when the assigned fluid reaches the solidus temperature. The solidification model further defines the liquid fraction α_l in the form:

- $\alpha_l = 1 : T < T_{solid}$
- $\alpha_l = 0: T > T_{solid}$

The above assumptions form the basis of the energy equation further defined in section 6.2.2.3.

6.2.2.1 Continuity Equation

The effect of the continuity equation is often determined by the assumptions applied to the simulation. Equation 6-1 shows a generalised continuity equation.

$$\frac{\partial P}{\partial T} = -\nabla P.(\rho \vec{u}) \qquad 6\text{-}1$$

The applied assumptions allow the alteration of the continuity equation. The first assumption is a laminar flow regime and almost stagnant, as the Reynolds number in the solidification process is low and turbulent effects are not taken into account. The simulation makes an initial assumption of constant thermophysical properties such as: thermal conductivity (k), specific heat (c_p), and thermal expansion coefficient (β). The constant assumption allows the simulation to be simplified due to the low impact over a fixed and limited range of the solidus temperature. During the solidification process, the liquid phase is travelling at a low velocity where the density can be assumed to an independent property unrelated to pressure and velocity. The relationship between temperature and velocity can be defined through the Boussinesq approximation defined in section 6.2.2.2 Given these assumptions, the continuity equation can be reduced to:

$$\nabla.\vec{u} = 0 \qquad 6\text{-}2$$

6.2.2.2 Momentum Equation

As the model is based on an enthalpy-porosity model, the method assumes the mushy zone/ liquid-solid interface to be modelled as a porous region. The porosity of the interface is based on the temperature conditions set in section 6.2.2. The definition of porosity for each cell is determined by the liquid fraction for each grid cell. During the solidification process, the porosity of solid zones is set to zero, eliminating any velocity terms. Equation 6-3 highlights the general equation for the conservation of momentum. shows the general equation for the conservation of momentum. The introduction of the solidification model alters its form to account for additional source terms, which must account for the Boussinesq approximation and Darcy's Law.

$$h = h_{ref} + \int_{T_{ref}}^{T} c_p \, dT \qquad 6\text{-}3$$

Boussinesq Approximation

The Boussinesq approximation is made in the density terms of the fluid, which accounts for the buoyancy terms caused by temperature variations. Typically, the rate of density change within the fluid in relation to the gravitational effects must be considered. The approximation

must only be taken into account when the change in density is greater than the effects of gravity, which can then be omitted from the inertial terms. The Boussinesq approximation can be determined by a function of temperature described in 6-4.

$$\rho(T) = \rho_0 + \frac{\partial P}{\partial T}\Delta T \qquad 6\text{-}4$$

which can be reduced into a function of the thermal expansion coefficient as shown 6-5:

$$\rho = \rho_0 \left(1 - \left(\beta(T - T_m)\right)\right) \qquad 6\text{-}5$$

where T defines the temperature within the fluid domain, T_m is the reference temperature at initialisation and β is the thermal expansion coefficient, which can be defined as:

$$\beta = -\frac{1}{\rho}\frac{\partial \rho}{\partial T} \qquad 6\text{-}6$$

The corresponding source term can be defined to introduce the gravitational terms as follows:

$$\vec{s}_b = -\vec{g}\beta(T - T_m) \qquad 6\text{-}7$$

Darcy's Law

The Darcy law terms characterise the influence of the solid and the solid-liquid interface in the velocity field for the control volume. Typically, the velocity functions for the mushy zone can be defined as:

$$\vec{u} = -\left(\frac{K}{\mu}\right).\nabla P \qquad 6\text{-}8$$

As the interface is treated as a porous zone, K denotes the permeability of the interface which can be derived from the solid fraction. By taking the porosity parameters into account the source terms can be defined as follows:

$$S_u = -A\vec{u} \qquad 6\text{-}9$$

where A is a parameter that defines the porosity of the solid-liquid interface. It is important to note that the convective terms are omitted from modelling closed volumes, due to the complexity of the natural convection between the liquid phase towards the solid-liquid interfaces. Such source terms can be applied to areas such as continuous casting, which requires a velocity pulling the solid phase outside the fluid domain.

6.2.2.3 Energy Equation

The solidification model is based on an enthalpy-porosity model where the location of the interface is not explicitly tracked, but rather the association and volume of phases within a fixed grid. The calculation of the liquid phase is based on an enthalpy balance which is recomputed at each iteration. Zones where the liquid fraction lies between 0 and 1 are denoted as mushy zones and interpreted as the interface of the model.

The enthalpy of the fluid zone is computed as a sum of latent and sensible heats as shown in equation 6-10.

$$H = h + \Delta H \qquad 6\text{-}10$$

where:

H denotes the total enthalpy (kJ/kg)

h defines the sensible enthalpy where $h = cT$

ΔH defines the latent heat

The sensible enthalpy can also be defined as:

$$h = h_{ref} + \int_{T_{ref}}^{T} c_p \, dT \qquad 6\text{-}11$$

where:

h_{ref} defines the reference enthalpy

T_{ref} defines the refence temperature (K)

c_p defines the specific heat with the assumption of constant pressure. (J/kg.K)

The latent heat ΔH is constrained by the limits:

$$0 \leq \Delta H \leq L \qquad 6\text{-}12$$

where L represents the latent heat of fusion of the fluid. Each phase fraction can be defined as:

$$Liquid\ Fraction\ (\beta): \frac{\Delta H}{L} \qquad 6\text{-}13$$

$$Solid\ Fraction: 1 - \frac{\Delta H}{L} \qquad 6\text{-}14$$

The latent heat content can be rewritten in terms of the latent heat of the fluid:

$$\Delta H = \beta L \qquad 6\text{-}15$$

where the latent heat content can be varied from 0 (solid) and L (Liquid) as defined in equation 6-12

The implementation of the solidification transforms the energy equation in the form of equation 6-16.

$$\frac{\partial}{\partial t}(\rho H) + \nabla.(\rho \vec{v} H) = \nabla.(k \nabla T) + S \qquad 6\text{-}16$$

which highlights the conservation of energy, where:
H represents the enthalpy (equation 3-1)
ρ represents the density (kg/m^3)
$\vec{v}$ represents the fluid velocity (m/s)
S represents the source term to account for the latent heat defined by equation 6-17.

$$S = -\nabla.(\rho \vec{v} \Delta H) \qquad 6\text{-}17$$

6.3 User Defined Functions (UDF)

6.3.1 User Defined Functions

User Defined Functions (UDFs) are external functions written in C language for multiple programming software. UDFs can be applied throughout ANSYS Fluent allowing for the definition of multiple parameters. UDFs can be developed and imported as a header file into ANSYS Fluent and can be used as source terms to define phase properties. UDFs can also be applied for the alteration of existing source terms for energy and momentum equations, or can be implemented to improve existing governing equations, which may not consider important factors such as source terms to account for the latent heat during the phase change process. Figure 6-2 highlights the process and integration of a User Defined Function.

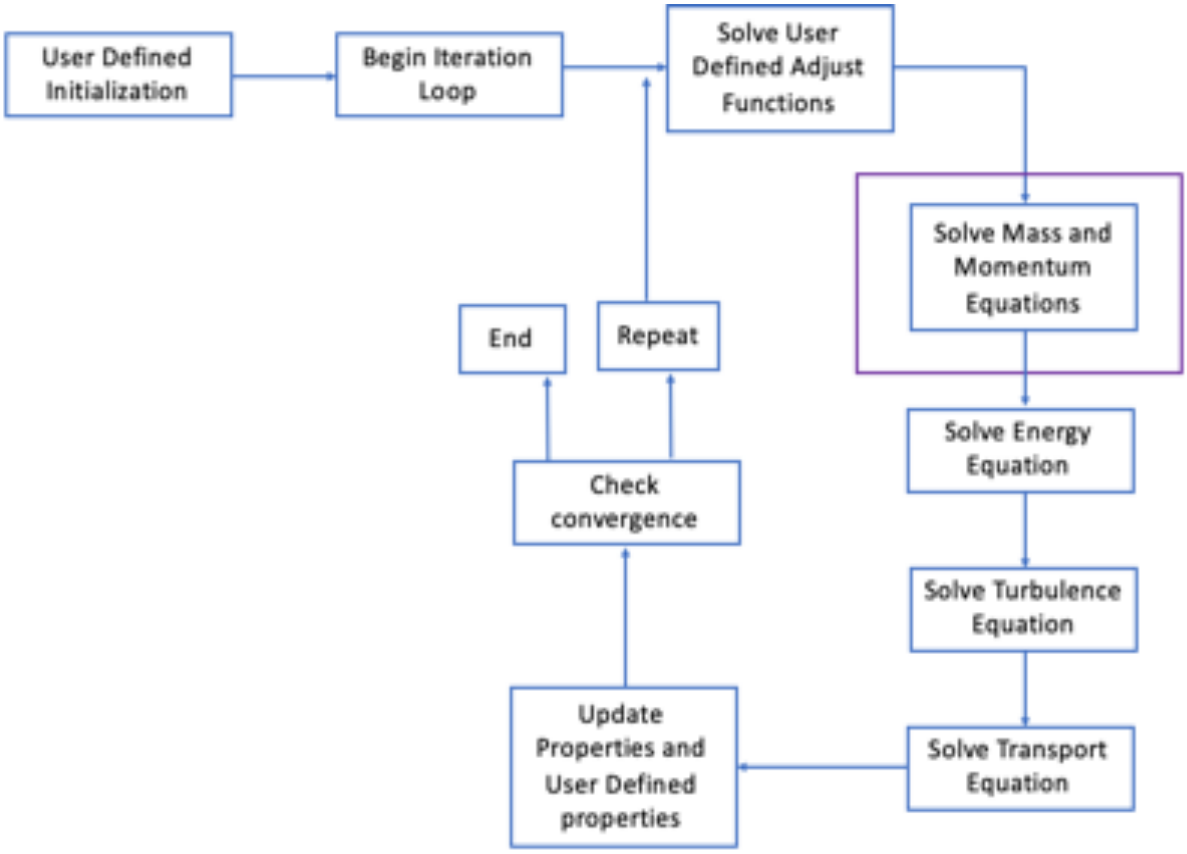

Figure 6-2: User Defined Function Integration

6.3.2 Source Equations

Source terms can be integrated within the CFD models in the form of UDFs, where the source terms can denote additional physical phenomena to ensure satisfaction of the governing equations. The simulations in this research contain multiple source codes from both a thermophysical aspect and real time derivations. Section 6.2.2 discusses the governing equations, where a problem was identified with the definition of the density term within the simulations. The applied source terms to account for the change in plasma fluid density during the solidification process were shown in equations 6-6 and 6-7

As the simulations are based on the classical solidification method, the derivation of the source term implemented within the system must account for the latent heat. The conservation of energy equation further needs to be developed to account for the phase change process. The development of the source term for the energy equation begins at equation 3-1, where a distinction is made between the latent heat component from the enthalpy and sensible heats. Equation 3-1 leads to the development of the energy equation shown in 6-16. The derived energy equation shows the derivative of a volume fraction as a function of time, which can be prone to variation across time and the control volume. The mitigation of the effects of

convection in relation to the volume fraction is often omitted. The studies conducted by Voller and Swaminathan [83] discussed the conversion of the energy equation into an iterative form, where the liquid fraction differential requires discretisation. The discretisation scheme applied allows for discrete constants to be adopted, allowing the singular definition of a source term, as shown in equation 6-18

$$S_h = d_p\left[H_p^m - H_p^{m+1}\right] \quad 6\text{-}18$$

Equation 6-18 can also be rewritten as a function of the liquid fraction as follows:

$$S_h = d_p\left[f_p^m - f_p^{m+1}\right] \quad 6\text{-}19$$

6.4 Model Geometry

6.4.1 Geometry

A three-dimensional model was developed to simulate the solidification of the blood plasma simulant and the associated two-phase process. The plasma bag is defined as a closed system constructed from a PHT- DEHP polymer, with a thickness of 35mm and a length and width of 177.3mm and 130mm, respectively. Figure 6-4 shows the annotated plasma bag denoting the volume of the blood plasma simulant. The monitoring of the plasma bag was conducted via a specialised T-type thermocouple defined in Chapter 5. According to the defined experimental set up, the thermocouple fits into the inlet channels, which records the plasma temperature, as shown in Figure 6-6. The developed geometry is shown in Figure 6-5

6.4.2 Mesh

The three-dimensional model was constructed and meshed through ANSYS ICEM, which is a grid generation software. The mesh generated consists of a structured hexahedral mesh. The polymer wall surrounding the plasma volume contains 27,301 hexahedral cells. The geometry features a near wall mesh surrounding the polymer barrier, to accurately model the heat transfer between the solid wall and the surrounding plasma simulant. The initial cell size is 0.2mm, with a growth rate of 1.2mm. To ensure the optimum mesh has been produced, a mesh independence study was carried out. Different mesh sizes were investigated, with the average solid and liquid temperatures taken at an arbitrary position.

Table 6-1 shows the results obtained from the mesh independence study. The results reflect a difference between 7,203 (coarse) level cells and 27,301 (fine) level cells and highlight the sensitivity of the simulation to relate both liquid and solid phases. The results of the medium and fine meshes show a small difference, addition of a finer mesh can improve the aspect

ratio thus improving the stability of the simulation. A mesh density of 27,301 was then applied. The final mesh produced is depicted in Figure 6-7.

Cell Type	Cell Density	Aspect ratio
Hexahedral- Coarse	7,203	0.729
Hexahedral- Medium	17,238	0.777
Hexahedral- Fine	27, 301	0.872

Table 6-1: Mesh independence study results

A grid independence study was created on the volume of cells in relation to solve the computational simulation. As the plasma simulant parameters are fixed, the change in cell density will give askew results due to the lack of cell refinements. The large cell size will not correctly identify the phasic fraction between each cell due to the large gap between each cell. The mesh convergence study highlighted in Figure 6-3 shows the internal plasma temperature at the defined measurement at 1500s. The initial points shown in the figure are stagnant due to divergent results, with the mesh density being too coarse to solve. The increase in element count showed an improved solidification operation, allowing for an interface to fully develop. Towards 25,000 cells, the data point temperature becomes stagnant highlighting the mesh has reached maximum accuracy.

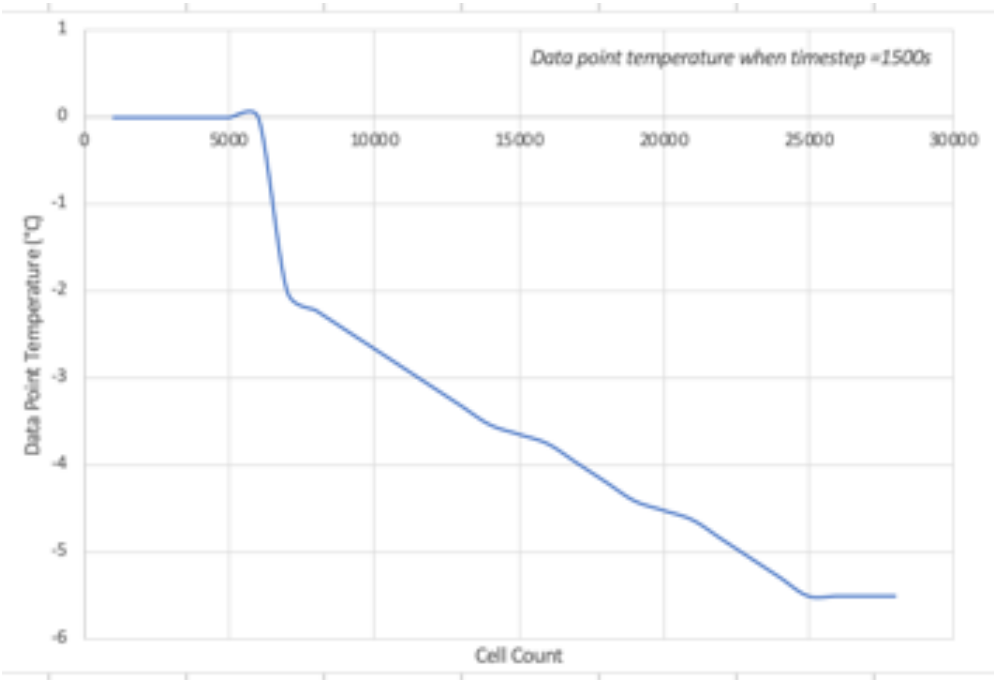

Figure 6-3: Mesh convergence study results

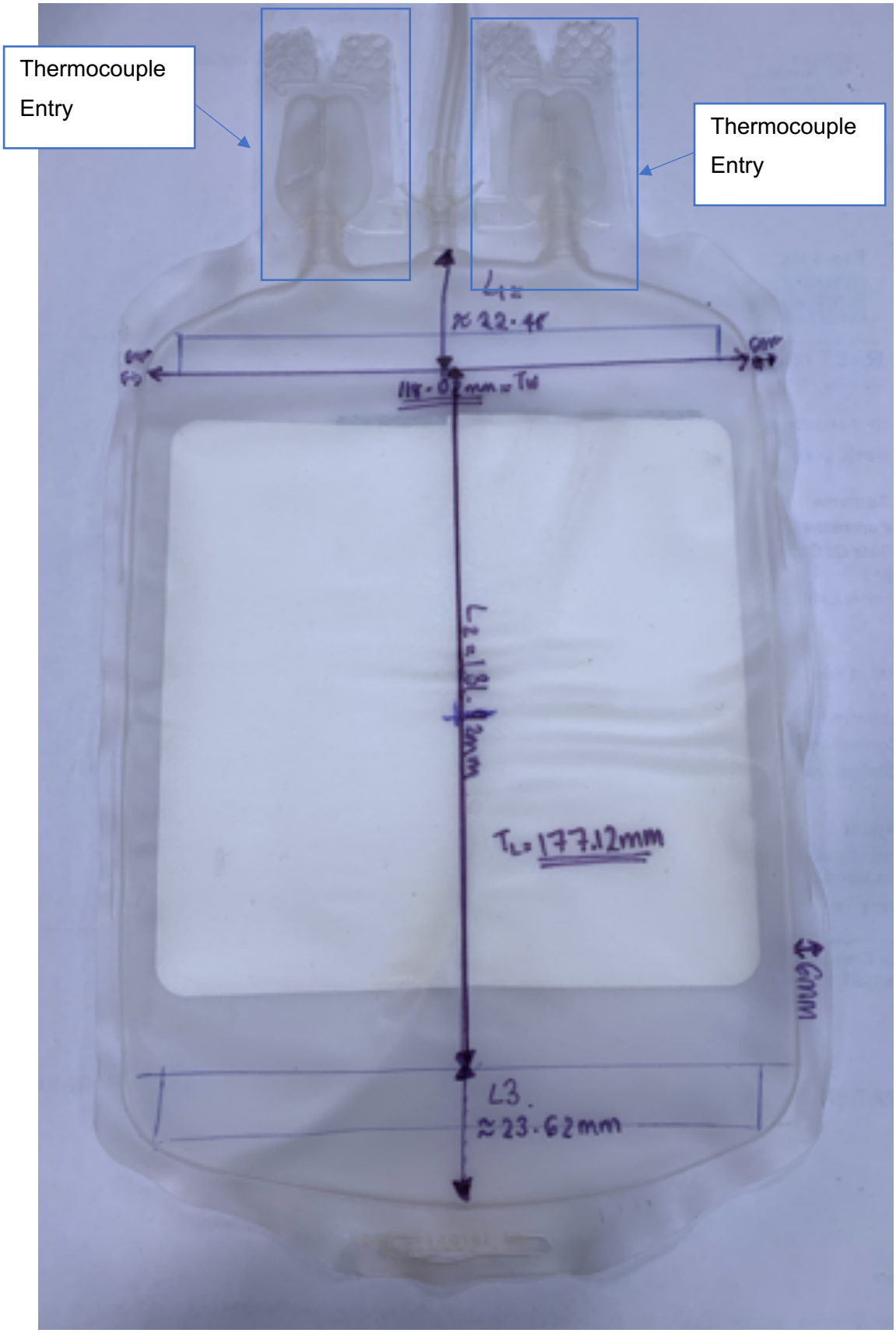

Figure 6-4: Plasma Bag

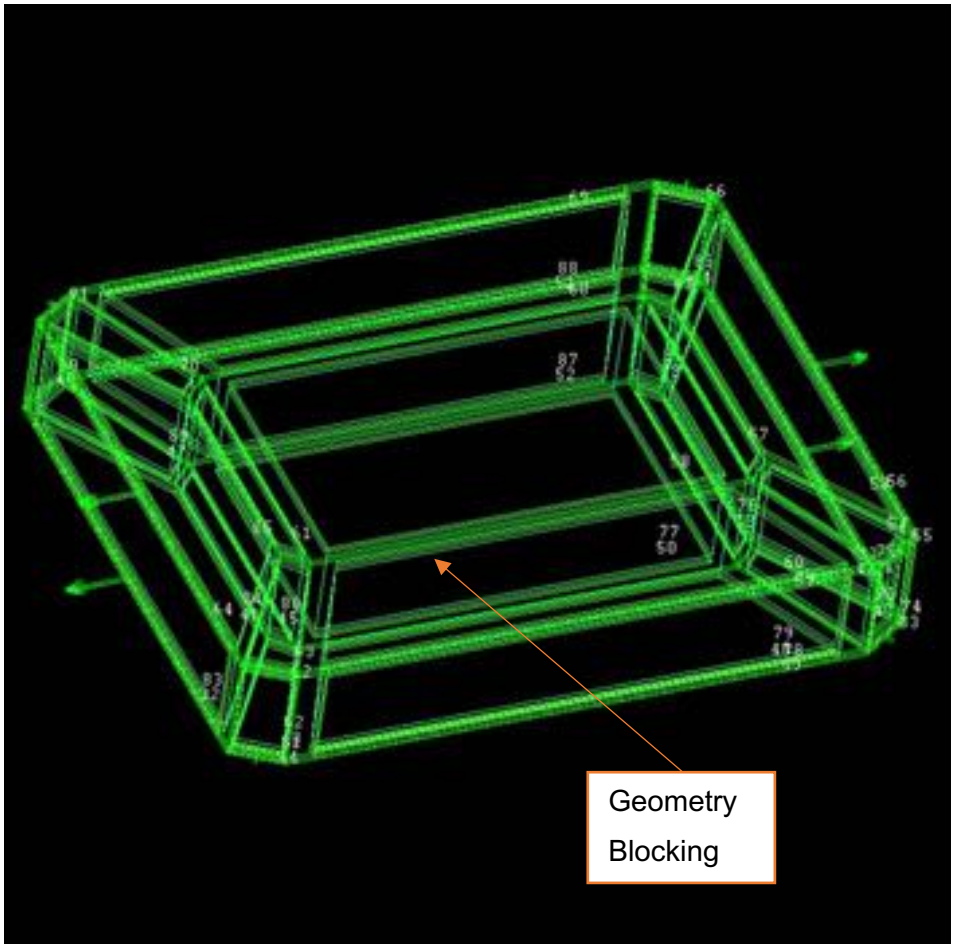

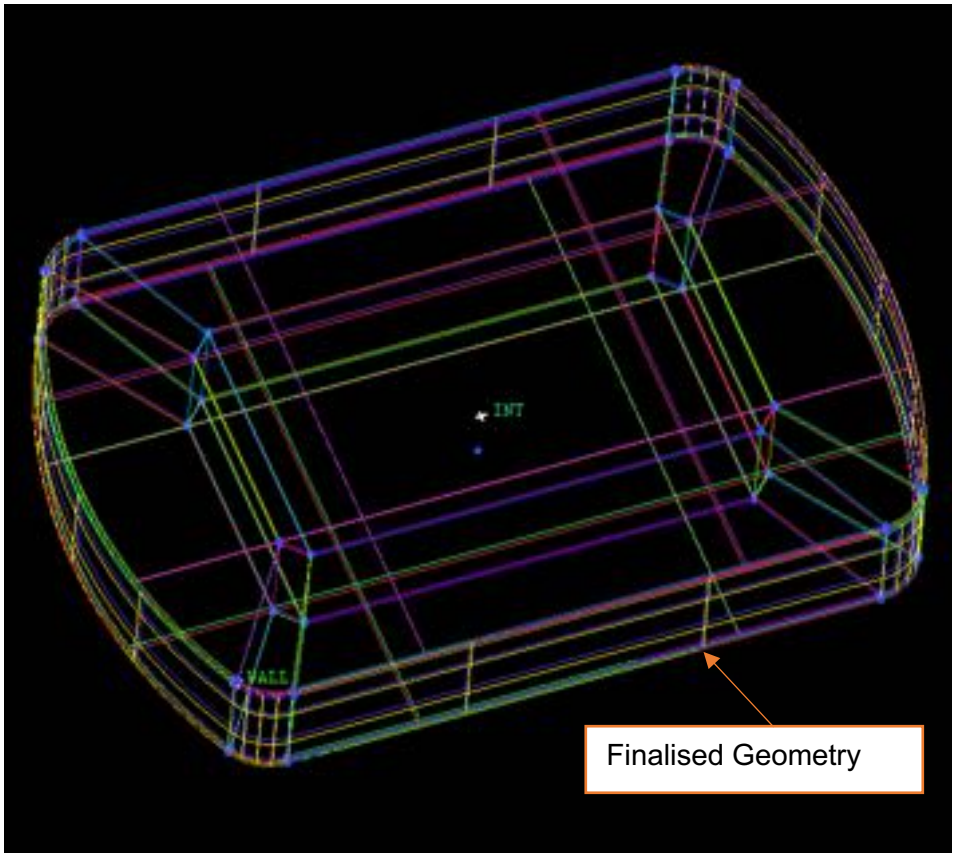

Figure 6-5: ICEM developed geometry

Figure 6-6: Thermocouple Positioning

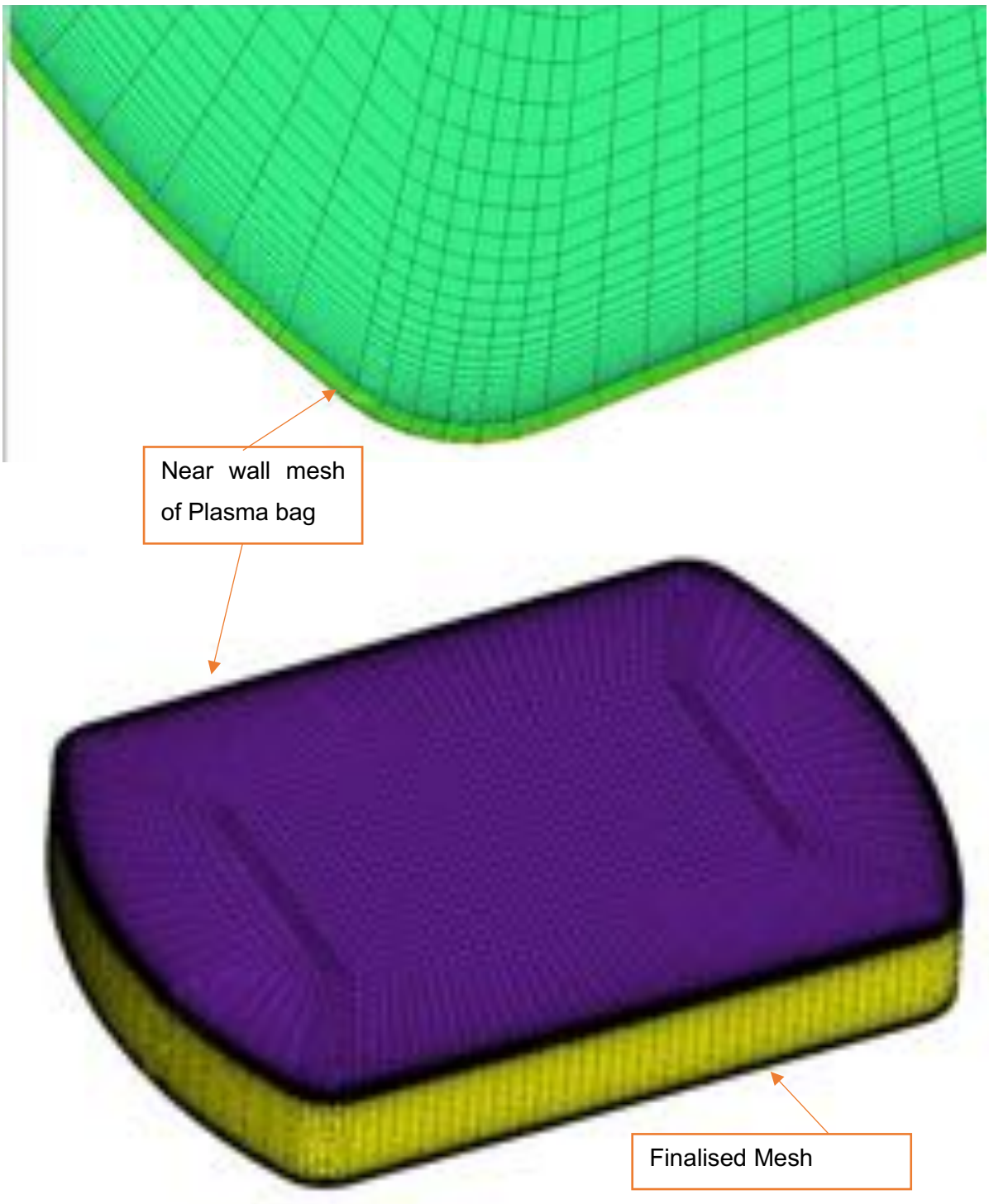

Figure 6-7: Produced plasma bag mesh

6.5 Boundary Conditions

6.5.1 Contact Resistance

The resistance diagram discussed in chapter 3 showed the resistances experienced during the solidification process, where the contact resistance from the plasma bag wall to the fluid is defined. The contact resistance can be defined as an electrical analogy as shown in Figure 6-8.

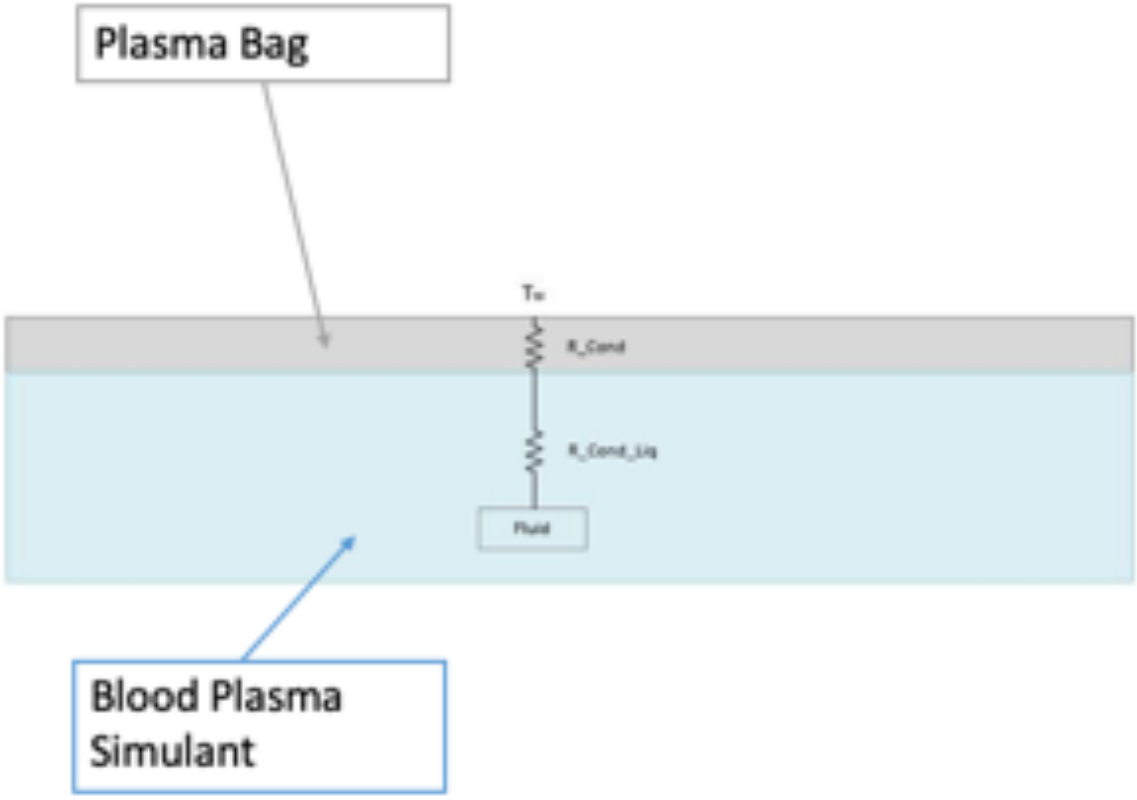

Figure 6-8: Resistance Diagram highlighting contact resistance

The applied resistances are highlighted in Table 6-2:

Contact Resistance	Units	Value
Front Position	K/W	0.125
Side Position 1	K/W	0.283
Side Position 2	K/W	0.283

Table 6-2: Contact Resistances

6.5.2 Determination of free stream temperature

The determination of the boundary conditions requires the definition of a free stream temperature highlighting the temperature around the plasma bag during operation. The setting of the free stream temperature was determined using the thermocouples described in chapter 3 to determine the air temperature. The positioning of the thermocouples is shown in Figure 6-9. The velocity profile was obtained at a set point temperature at -40°C, at 997RPM. The obtained free stream temperatures are defined in Table 6-3.

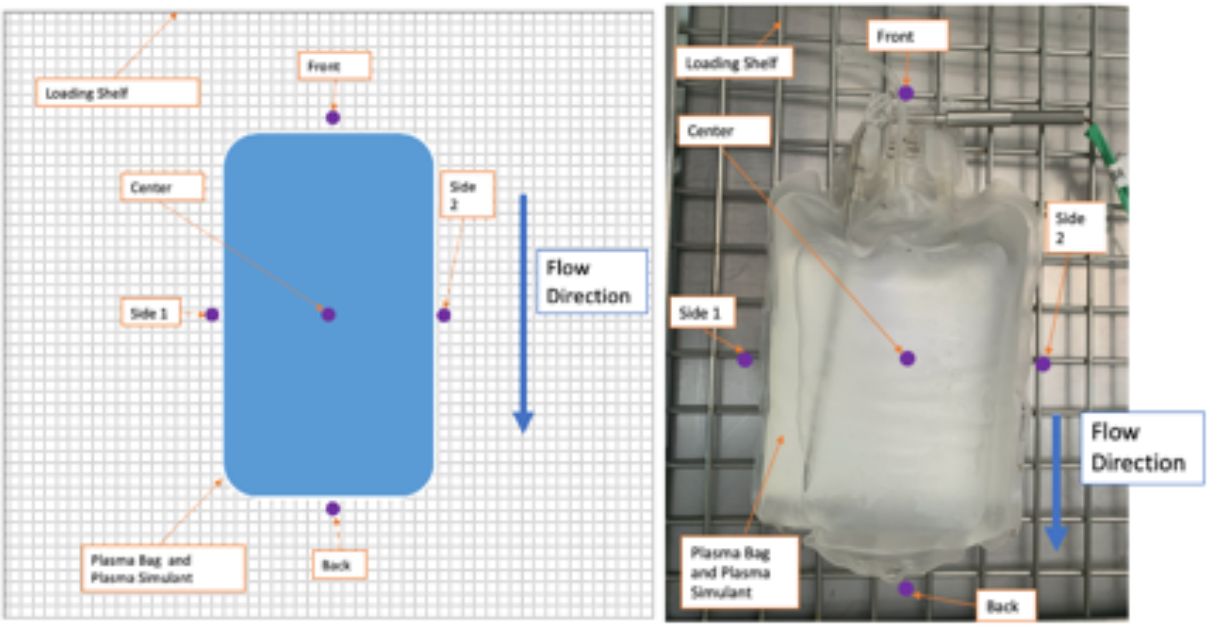

Figure 6-9: Freestream temperature measurement points

Free Stream Position	Unit	Value
Front Position	°C	-21°C
Side Position 1	°C	-23°C
Side Position 2	°C	-23.12°C
Middle Position	°C	-30°C
Back Position	°C	-26.7°C

Table 6-3: Free stream temperature values

6.5.3 Boundary Conditions

The boundary conditions are defined by using an appropriate list in ANSYS Fluent. The boundary conditions applied at the inner wall of the plasma bag are assumed to be a non-slip condition. One of the key assumptions made for the simulations is the omitted convective effects, meaning the thermal boundary conditions are purely conductive. A surface conductivity was applied for the bottom base of the plasma bag where the plasma bag is in contact with a mesh shelf. As only a fraction of the plasma bag is in contact with the shelf, a

porous wall function has been applied. The associated top wall of the plasma bag is coupled with the free stream temperature, shell conduction and resistances derived from chapter 3. The combination of boundary conditions takes into the heat transfer across the wall, from the free stream temperature across the plasma bag via a resistance. The side walls follow a similar schematic where a coupled thermal boundary condition was applied where the external flow stream temperature was acting, with a shell conductance with a thermal resistance defined in chapter 3. The interface between solid wall and fluid is defined as a coupled wall to ensure heat transfer between the plasma bag and the simulant fluid. Figure 6-10 highlights the applied boundary conditions.

The CFD model considers the plasma bag to be filled with a blood plasma simulant, as discussed in Chapter 5. The plasma bag geometry is assumed to be fixed, which does not consider any geometrical changes occurring as a result of solidification. The fluid volume was defined using the patch function to account for the plasma bag being filled. The density conditions remain constant throughout the simulation, where the fluid properties are defined in Table 6-4. As both liquid and solid phases have different thermophysical properties. The simulation begins as a fluid the initial liquid viscosity will need to be defined at freezing point. As the fluid cools, the fluid increases in viscosity, therefore an initial value is needed.

Property	Unit	Value
Density	Kg/m^3	1236.9
Specific Heat	j/kg-k	3930
Thermal Conductivity	W/m-k	0.55
Viscosity	kg/m-s	0.20813

Table 6-4: Blood plasma simulant physical properties

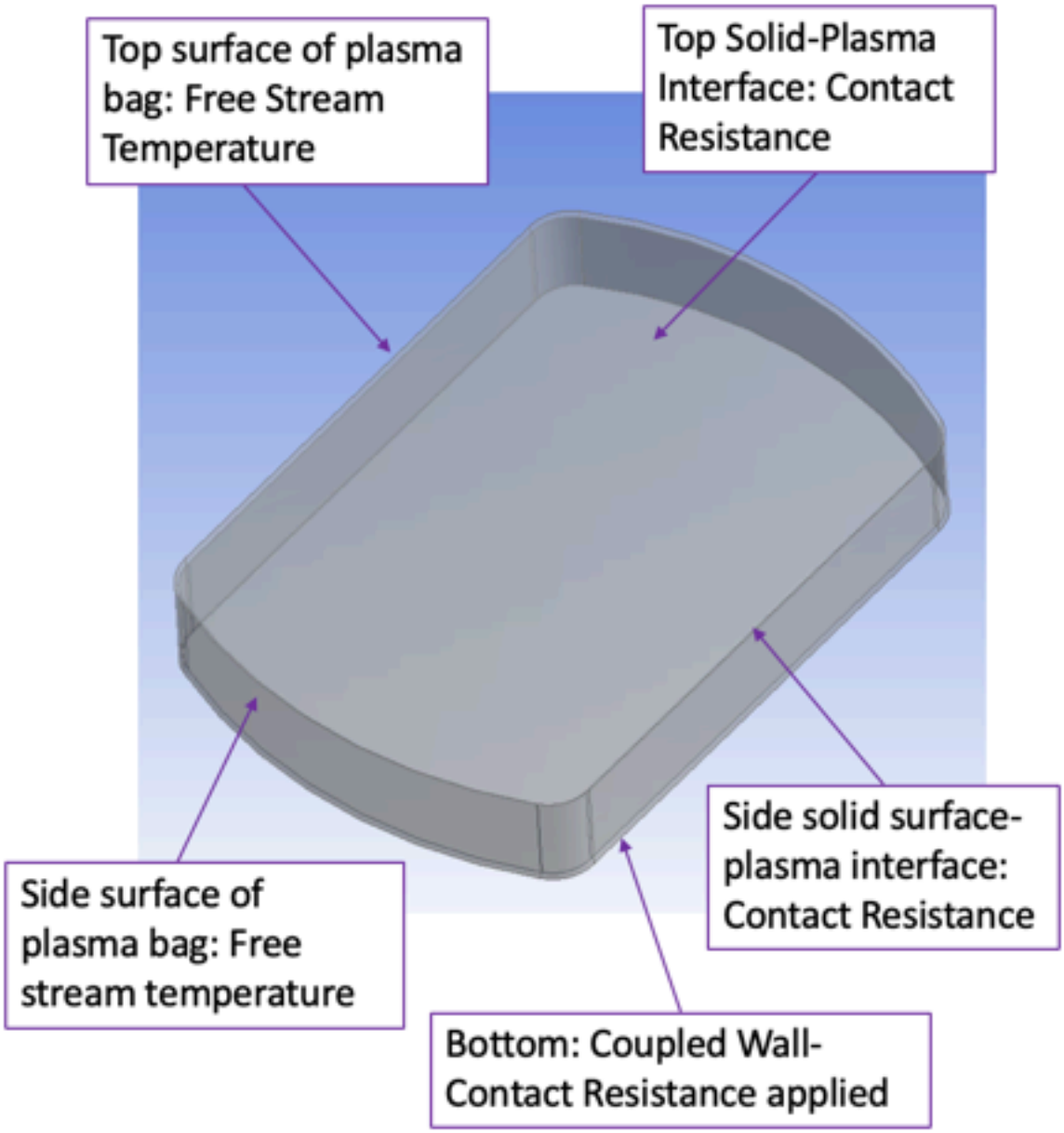

Figure 6-10: Applied Boundary Conditions

6.5.4 Solution strategy and convergence criterion

The simulations were carried out through a transient schematic (time averaged) with a timestep of approximately 60s for the solidification of a blood plasma simulant. The size of the timestep is based on the Courant number which is an indication as to how the fluid moves through each cell. As the main body forces are assumed to be gravity and buoyancy as a result of a Boussinesq approximation, with constant external boundary conditions. The phase change of the solidification is assumed to be in a steady rate, the problem can be defined as linear, and a function of time. As a result of this, a large time step has been applied.

The selection of the solver plays a key role in both the stability and accuracy of the simulation. The initial point of the simulation was defined as a pressure/density solver to ensure maximum stability whilst optimising computational power. The simulation is based on a SIMPLE algorithm for a pressure-velocity coupling and a first order upwind scheme. The calculation of gradients within the simulation was done by using a least squares method. The premise of the method is based on calculating a gradient where the change in cells is defined by a linear relationship. Both energy and momentum equations are solved as a second order upwind method. PRESTO has been applied for the pressure; thus, removing any assumptions of gradients applied within the system. The volume fraction was applied via geo-reconstruct which allows the definition of cells being filled with one or more phases. The reconstruction scheme allows the representation of the interface between two fluids using a piecewise linear approach, which assumes that the interface between two phases is represented as a linear slope. The method creates a linear interface between both phases relative to the centre of a partially filled cell, based on the applied volume fraction. The approach calculates the fluid in each cell, depending on the properties of each cell, including the recalculation of the volume fraction in each cell. The alternative is a donor-acceptor scheme, which defines a completely filled phase with one or more phases. The scheme is based on a donor scheme where the cells are treated as donors or acceptors. The cell containing the fluid donates the fluid to a neighbouring cell for the same amount of fluid. Figure 6-11 highlights the difference between both interpolation methods at the phase interface[97]. The methodology of the simulation is defined in Figure 6-12. The definition of the volume fraction needs to be initially patched to set the initial condition, alongside the initialisation temperature at the freezing point.

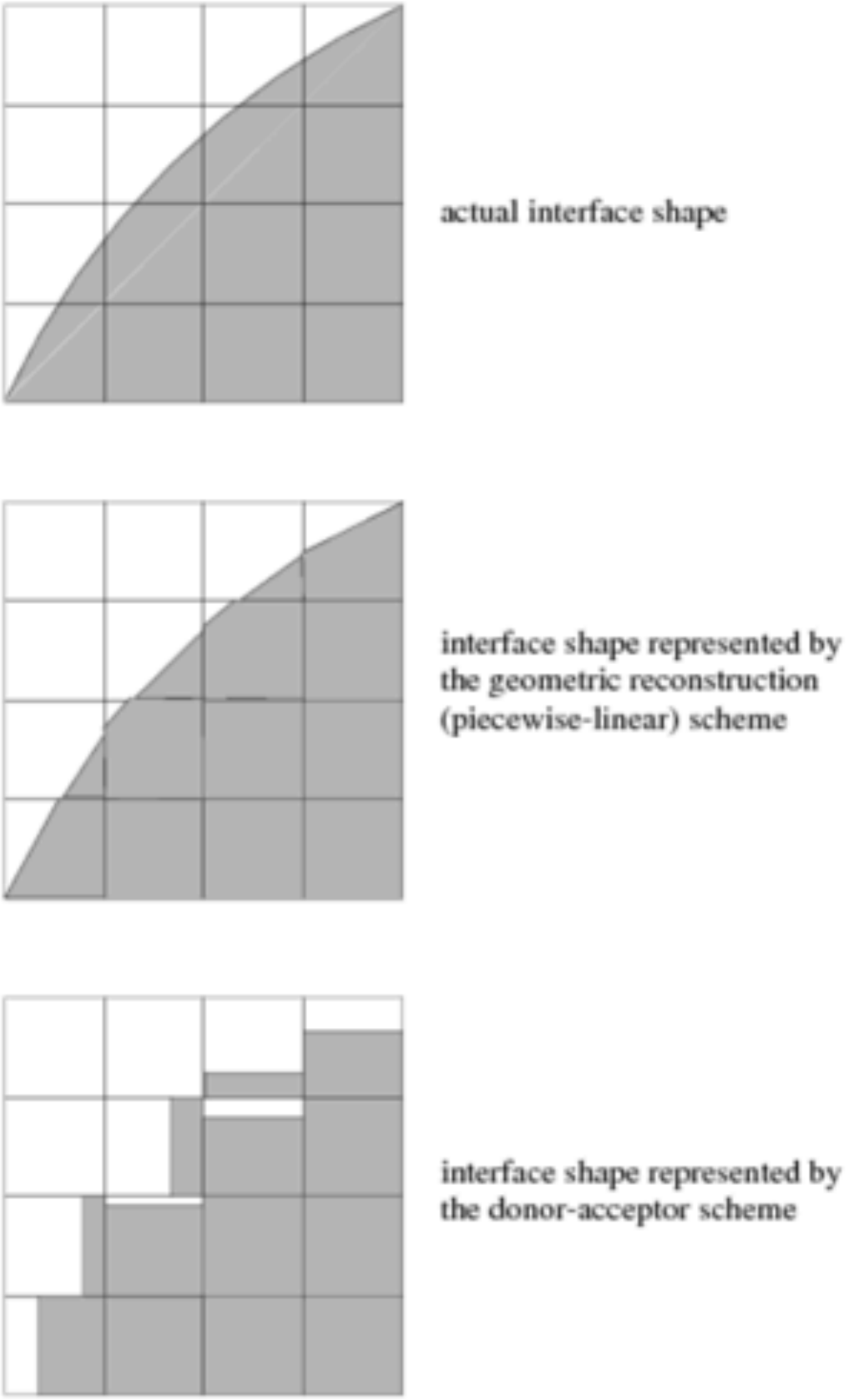

Figure 6-11: Volume fraction at the interface

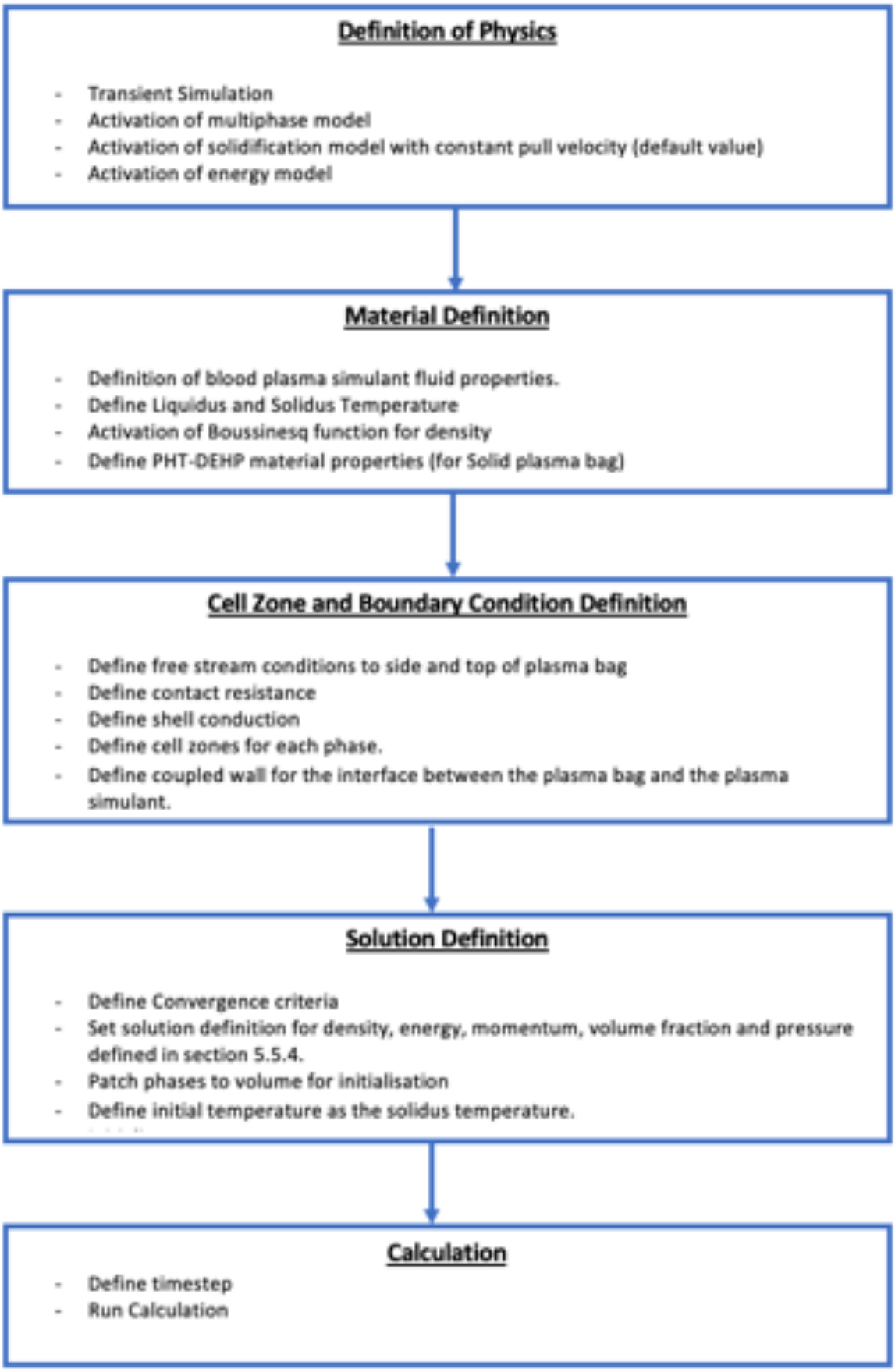

Figure 6-12: Solving Methodology

6.6 CFD Simulation Results

The utilisation of CFD provides the capabilities to visualise a comprehensive solidification regime from liquid to solid phase during a solidification process. The process of solidification allows for a visualisation at -40°C at 997RPM, where the loading position has been mapped as defined in section 7.2.2. As the obstruction of additional plasma bags is removed and the external flow profile remains undisrupted, a more uniform temperature distribution is obtained as discussed further in Chapter 7. An assumed surface temperature and contact resistance has been applied which acts as an estimation point as discussed in section 6.5.

6.6.1 Heat Transfer Process

Figure 6-13 shows the initial conditions where the plasma bag is at the initial phase change and the fluid is slightly above the liquidus temperature. The associated air temperature highlights the free stream temperature applied within the boundary condition functions. The progression of the thermal profile can be seen in Figure 6-14 to Figure 6-27, where the phase change shows the temperature decline past the solidus temperature. The temperature contours highlight the progression of the solidification of the plasma simulant. One of the key trends shown in the results reflect the difference in solidification at the plasma bag boundaries. Although the resistances and free stream temperatures define the boundaries, the variation between the side and upper boundaries is further discussed in Figure 6-28. The reflected contour plot highlights a slower solidification rate at the upper level due to the increased resistance in comparison to the side profiles. The associated thermal contours show the progression to the set point temperature where the resistance caused by the interface allows for an array of temperature variations through the plasma bag. The thermal contour plots highlight a decline dominated by the top and bottom walls, considering the improved air flow over the plasma bag and subsequently the high thermal conductivity of the stainless-steel wire mesh.

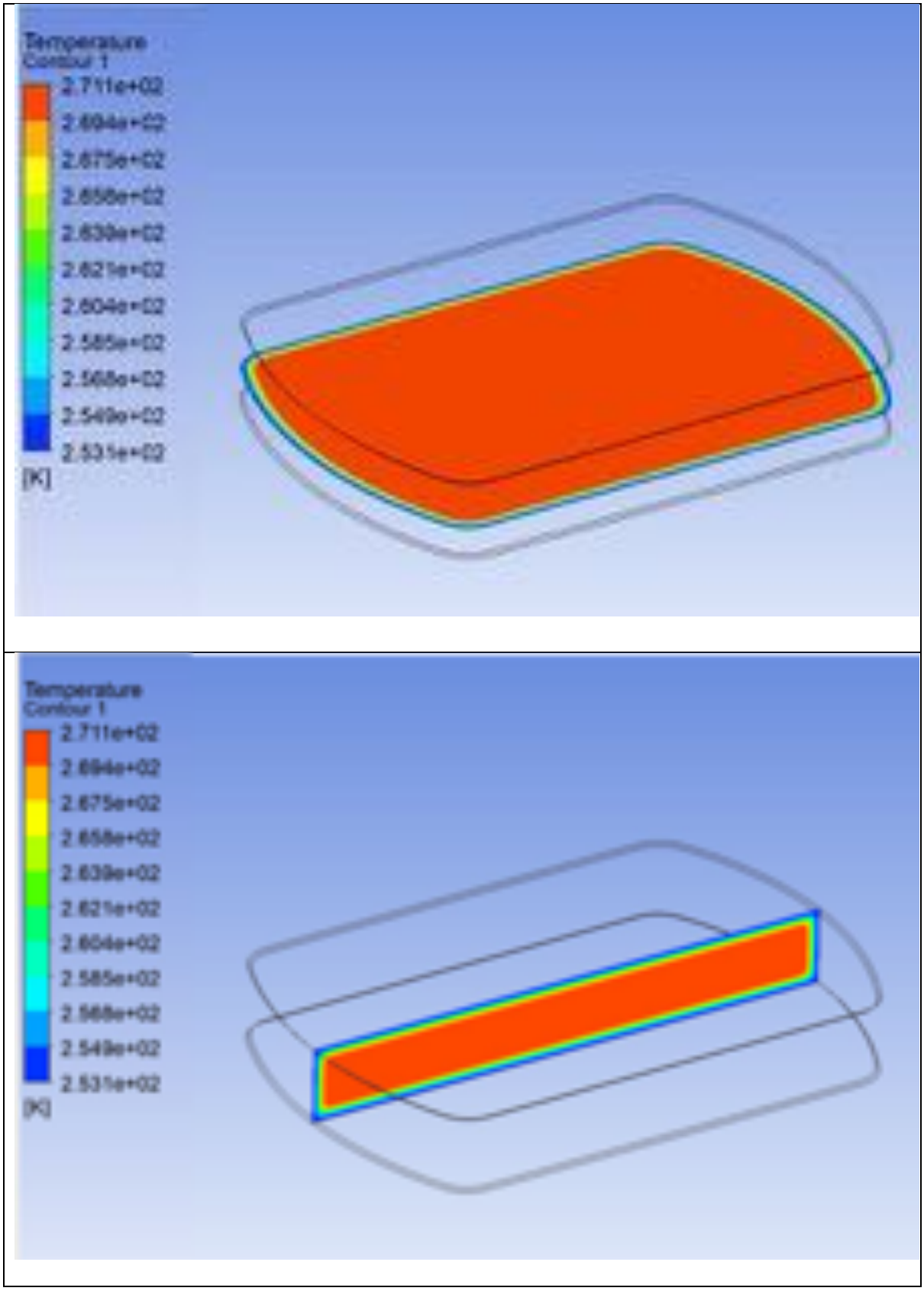

Figure 6-13: Thermal Contour Plot at 1 minute and 15 seconds

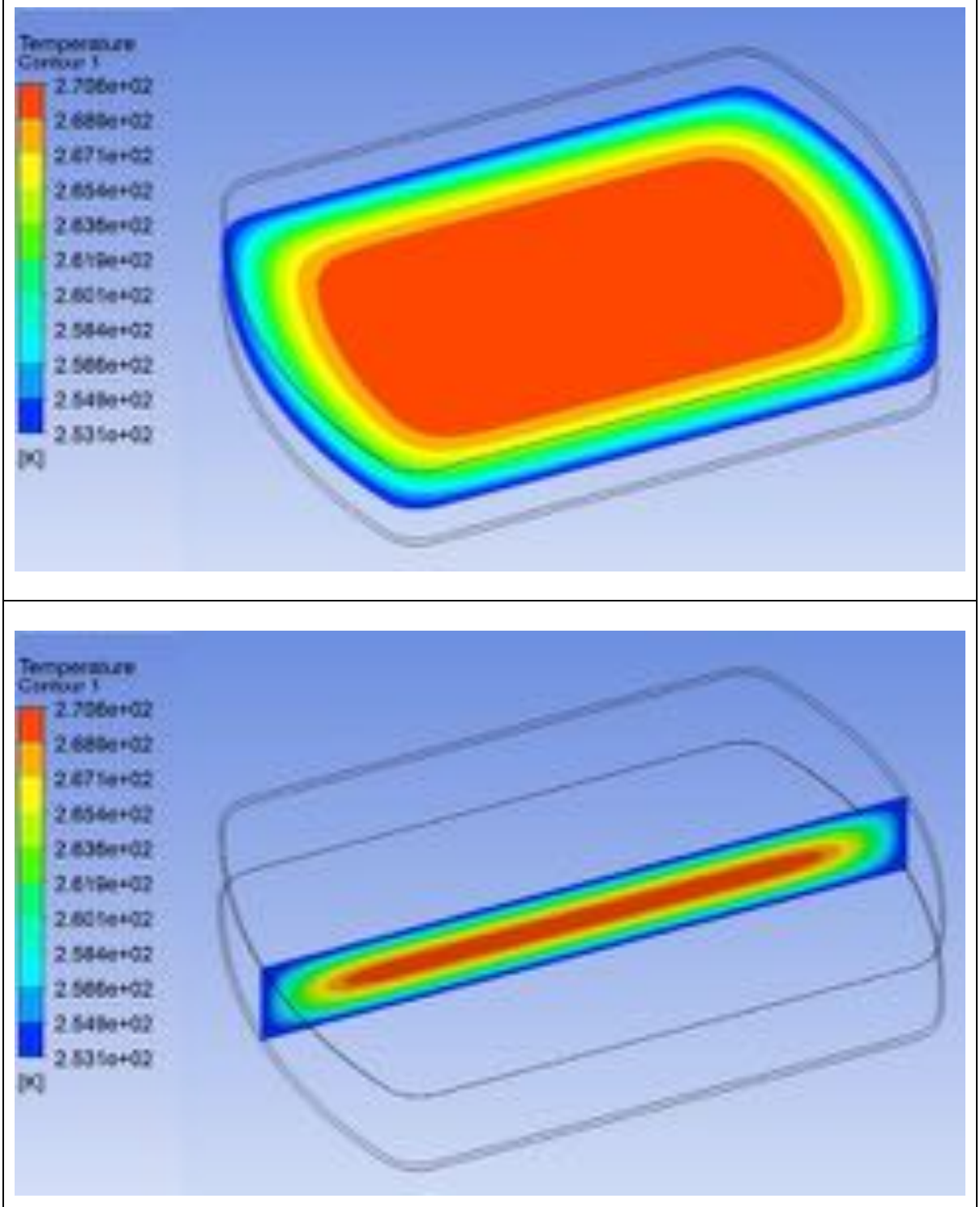

Figure 6-14: Thermal Contour Plot at 2 Minutes and 45 seconds

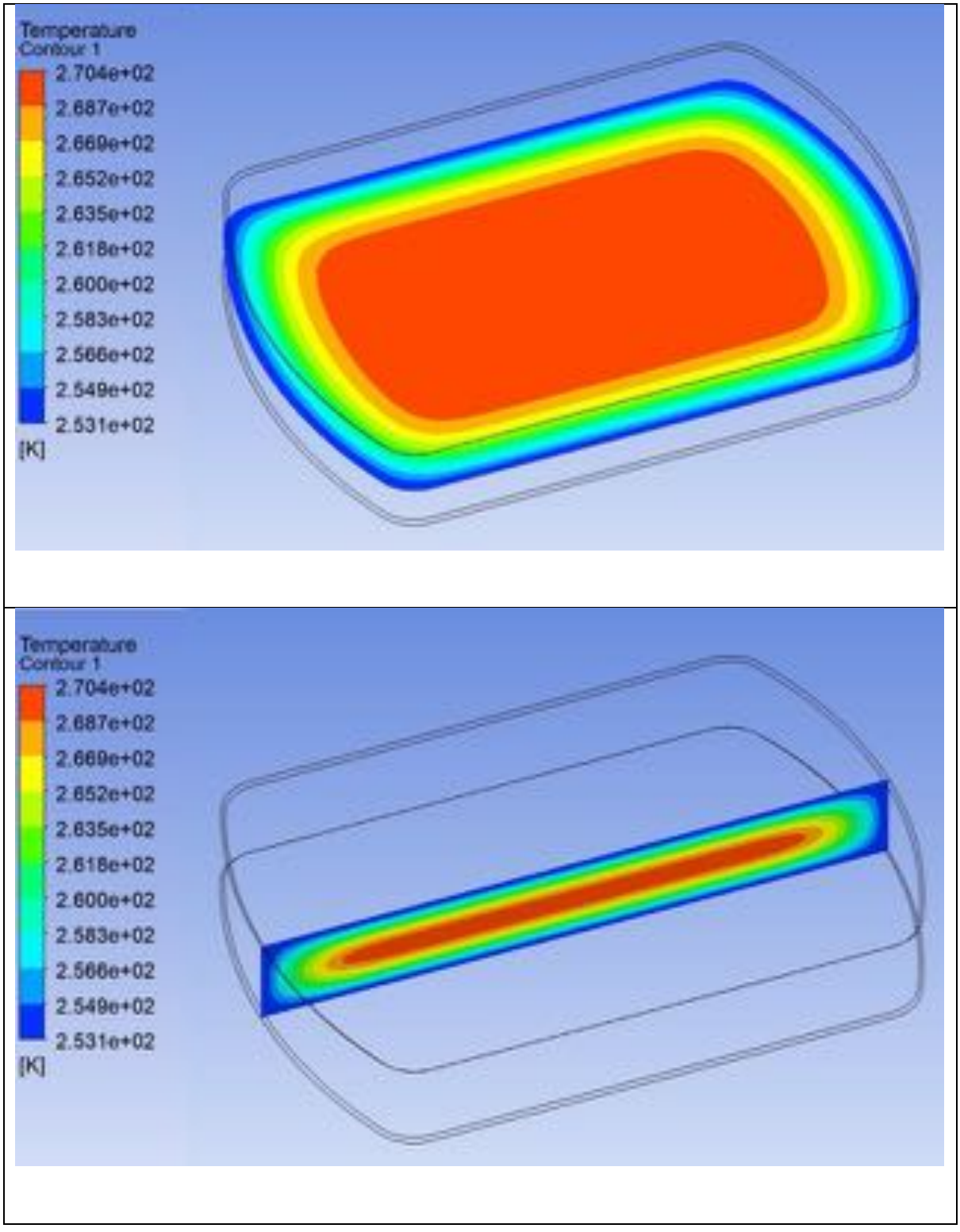

Figure 6-15: Thermal Contour Plot at 4 minutes and 15 seconds

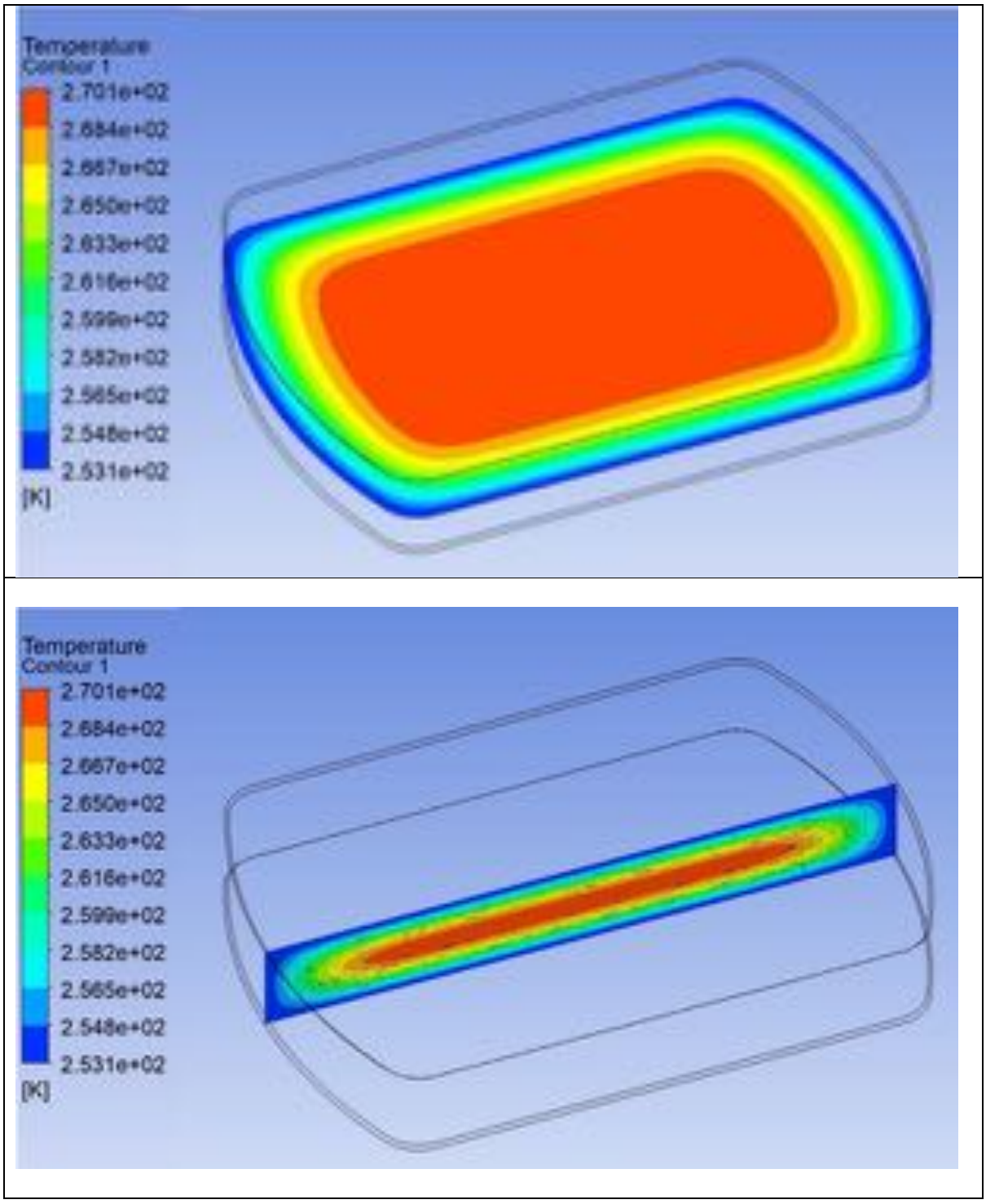

Figure 6-16: Thermal Contour Plot at 5 minutes 45 seconds

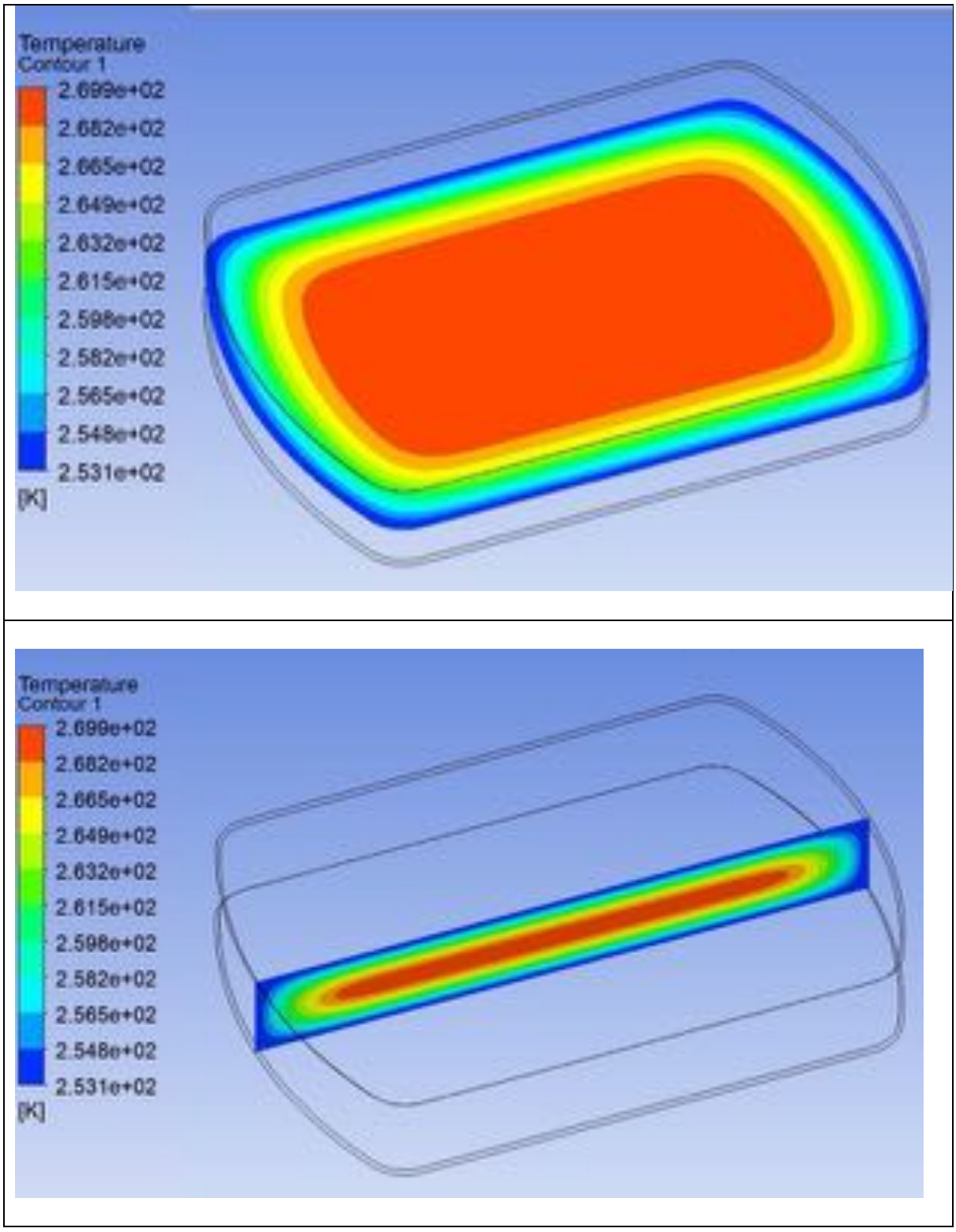

Figure 6-17: Thermal Contour Plot at 7 minutes and 15 seconds

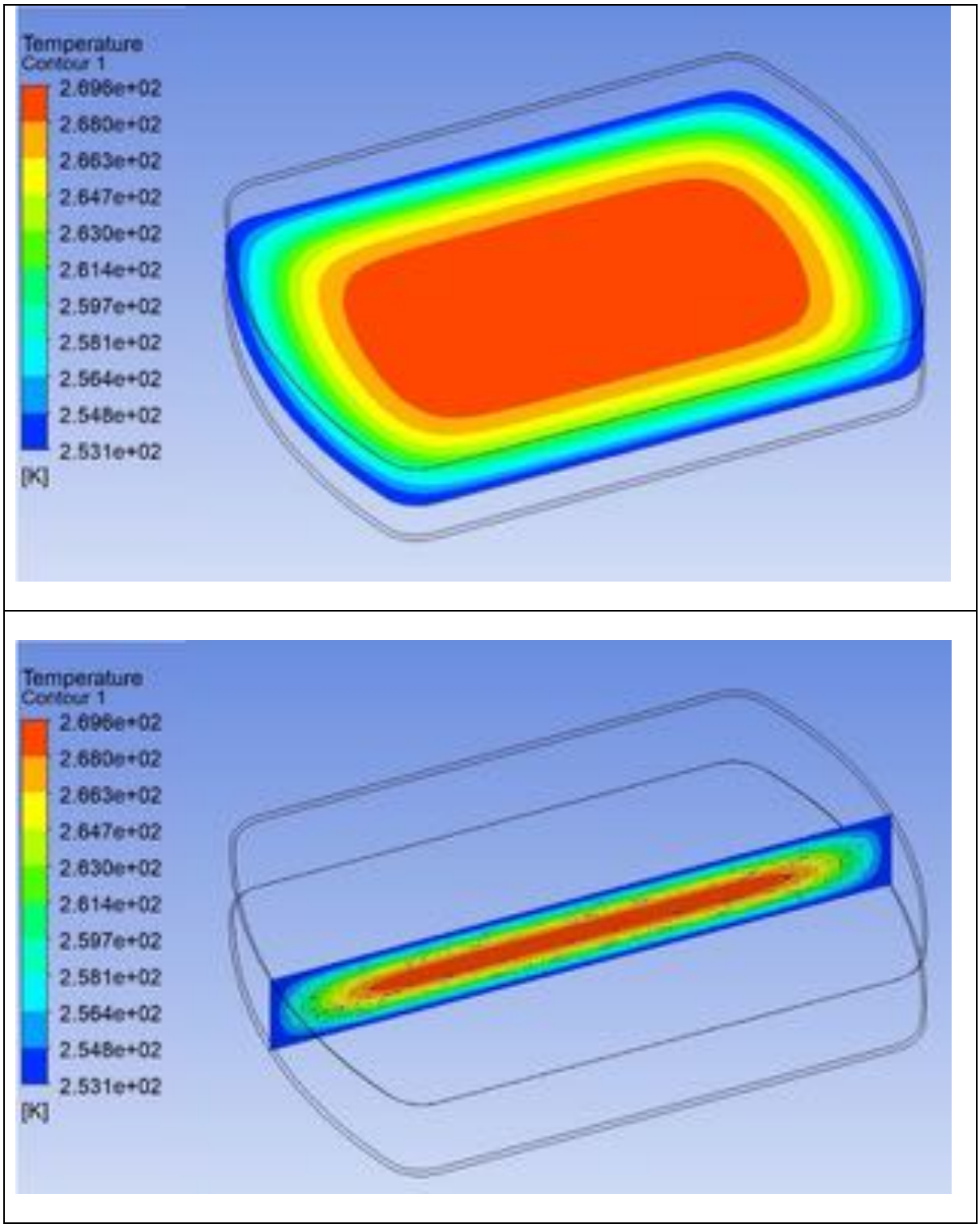

Figure 6-18: Thermal Contour Plot at 8 minutes and 45 seconds

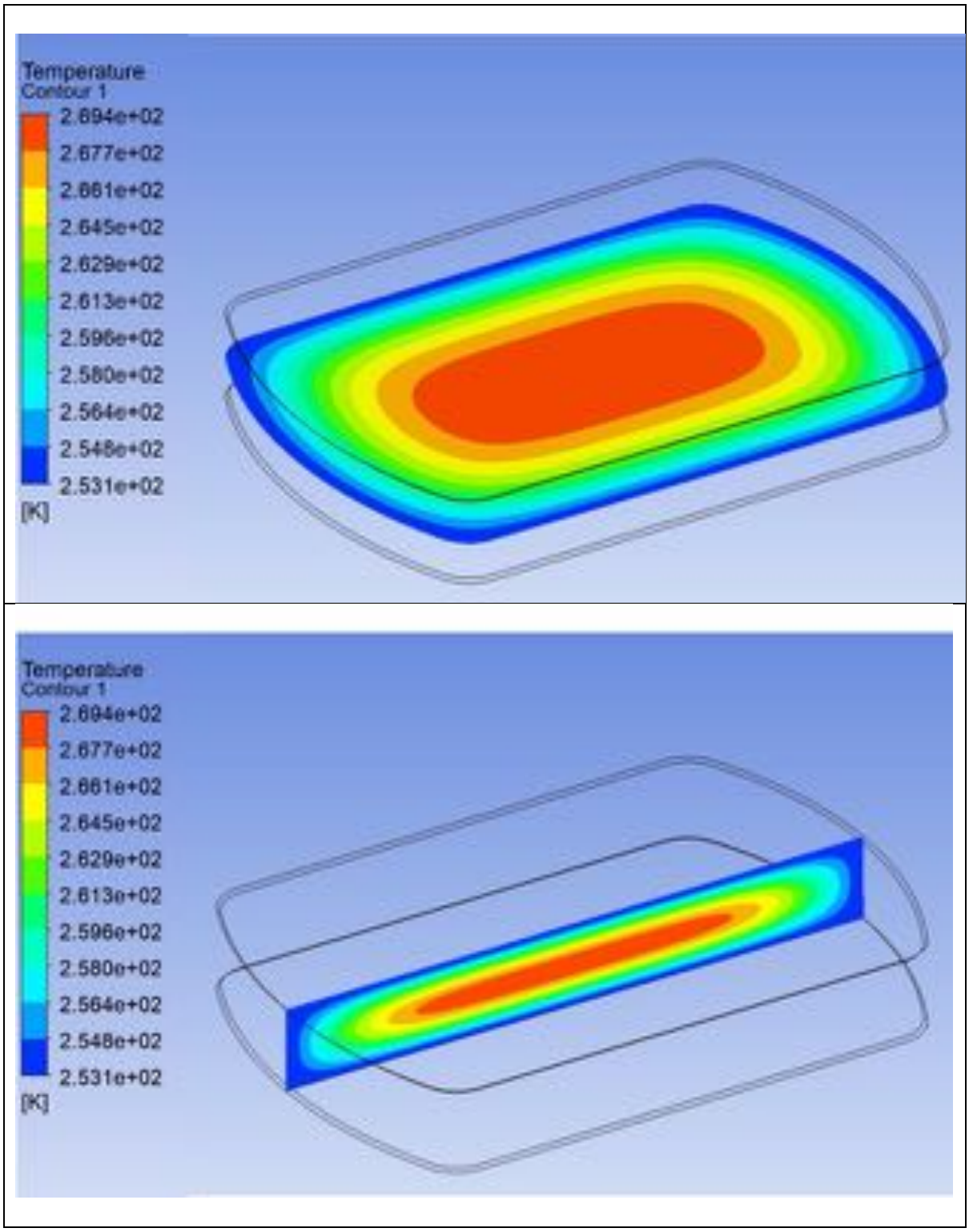

Figure 6-19: Thermal Contour Plot at 10 minutes and 15 seconds

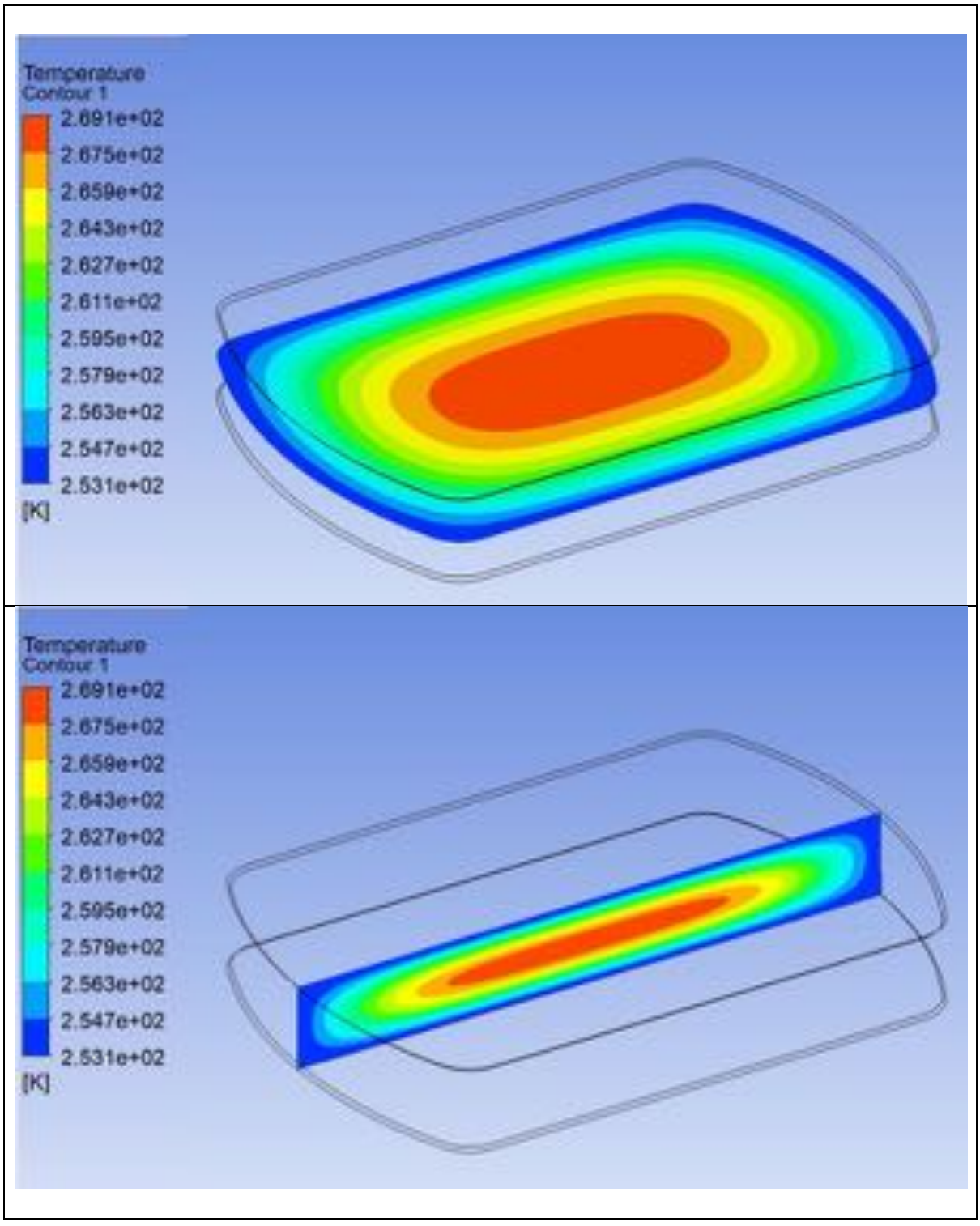

Figure 6-20: Thermal Contour Plot at 11 minutes and 45 seconds

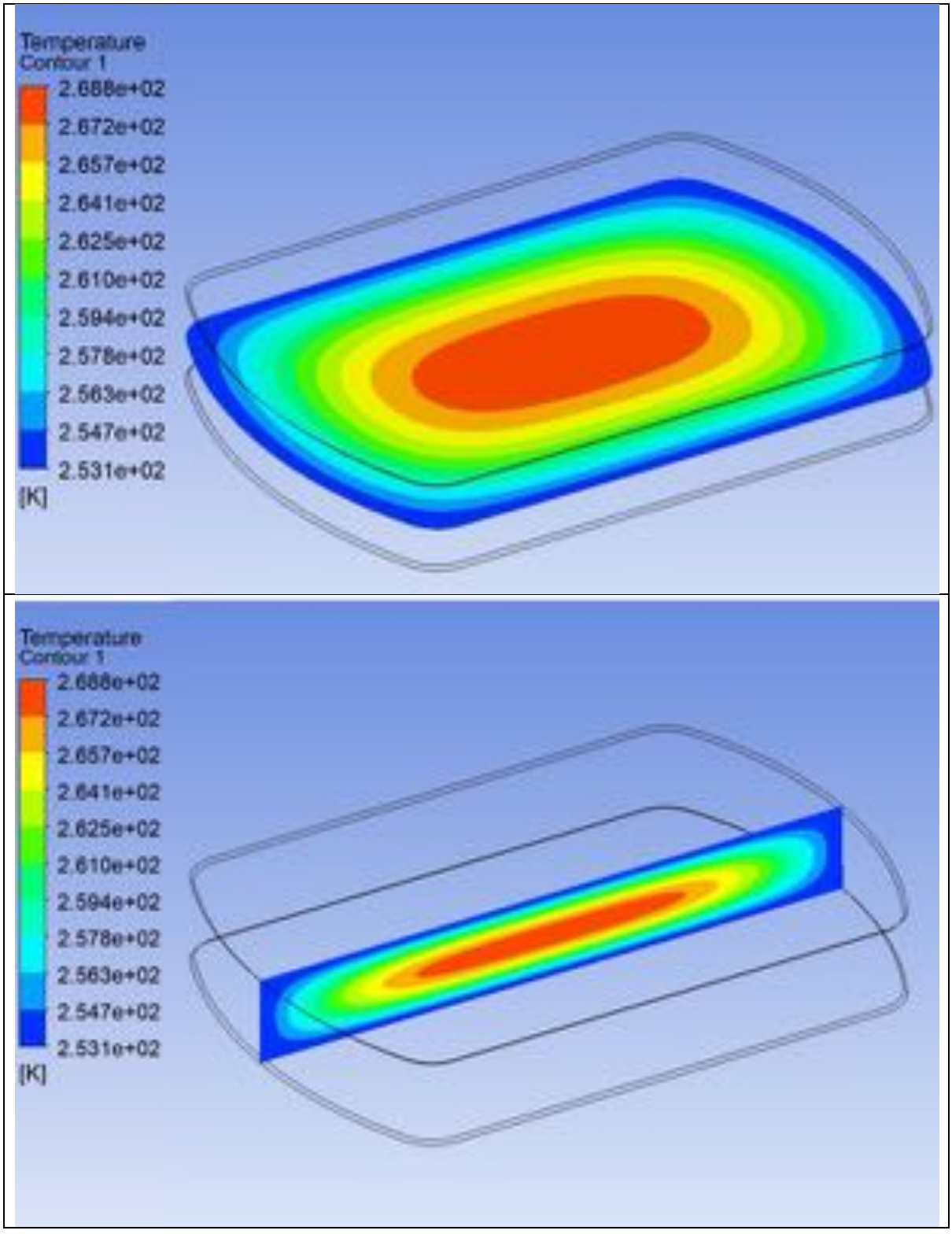

Figure 6-21: Thermal Contour Plot at 13 minutes and 15 seconds

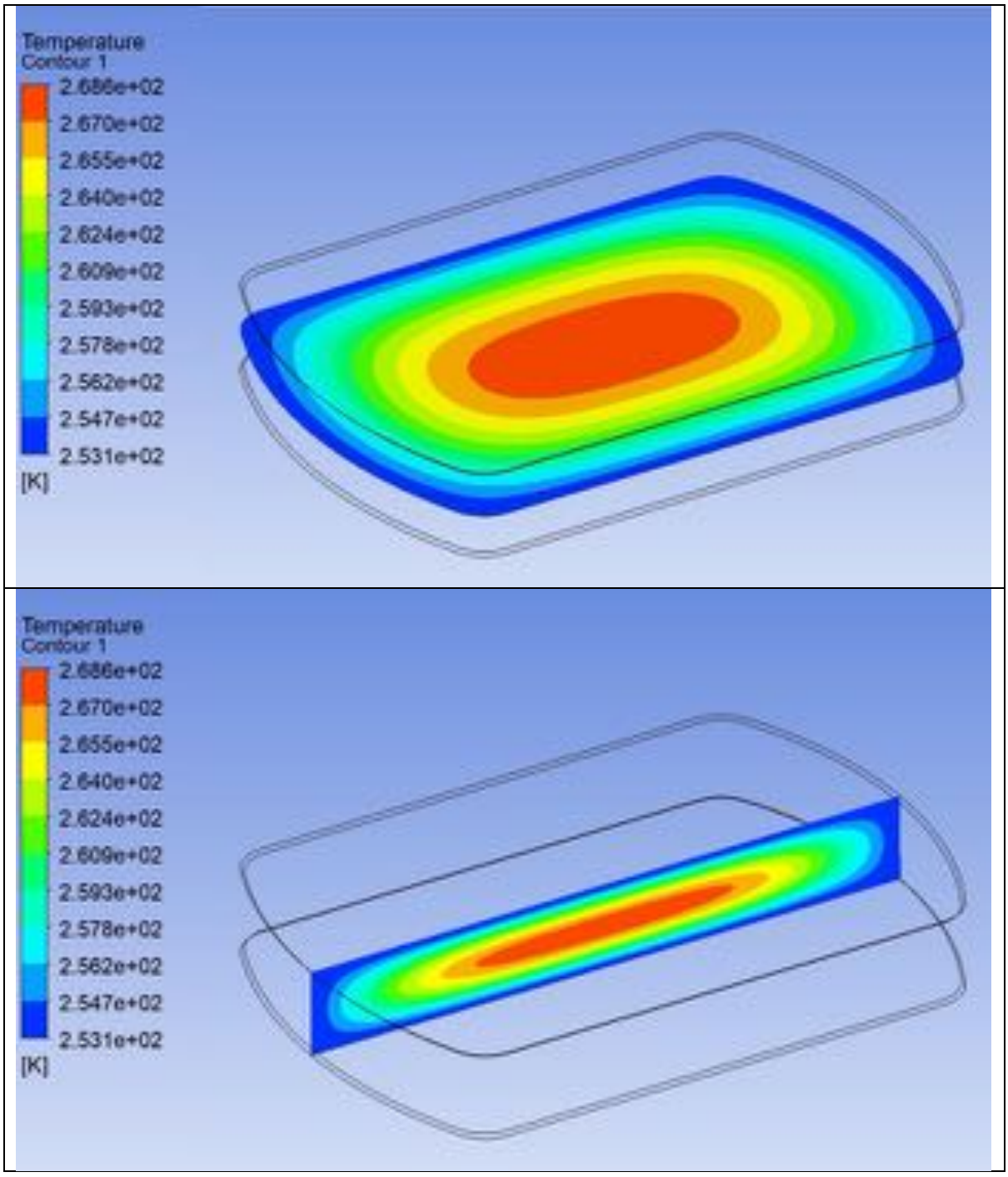

Figure 6-22: Thermal Contour Plot at 14 minutes and 45 seconds

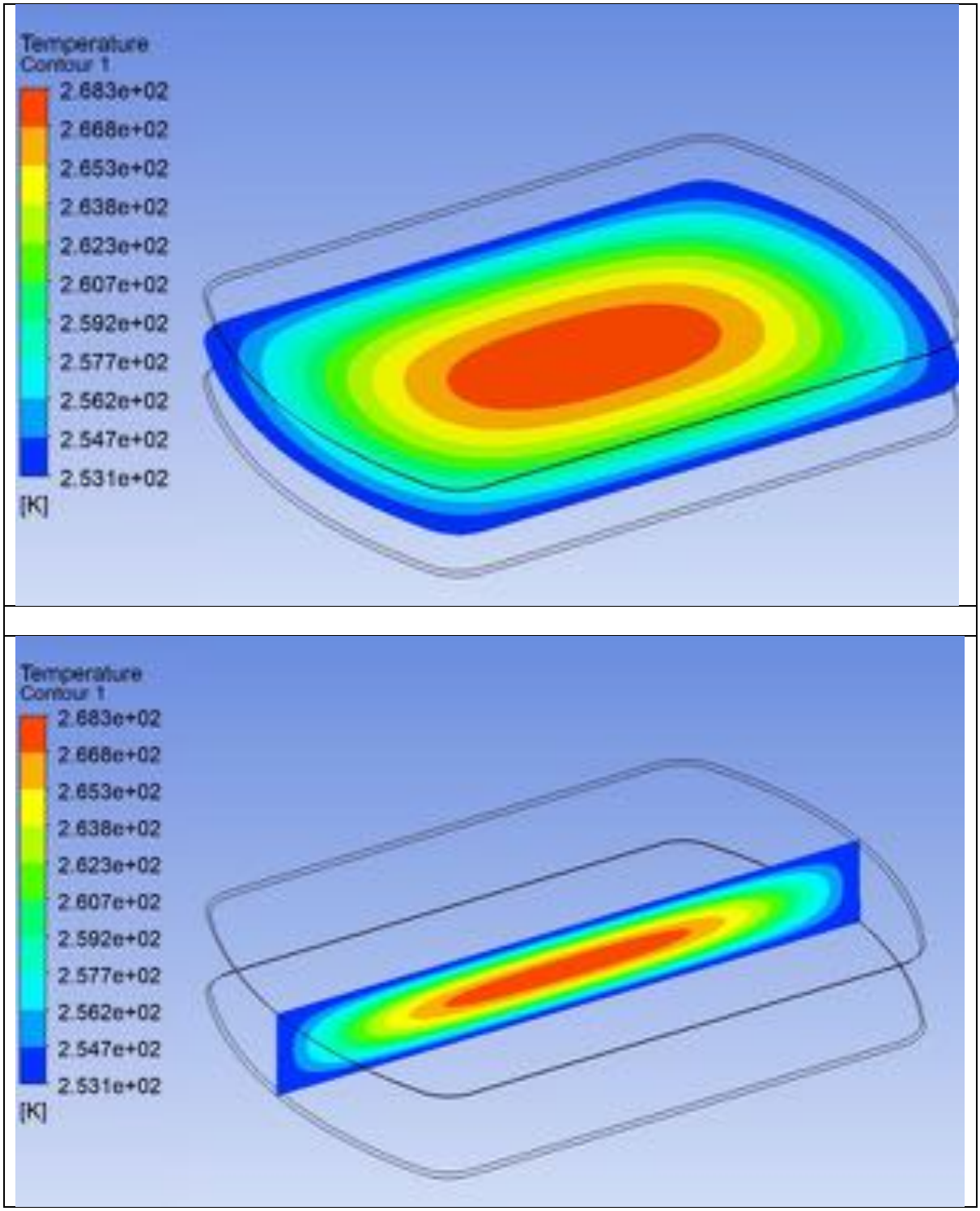

Figure 6-23: Thermal Contour Plot at 16 minutes and 15 seconds

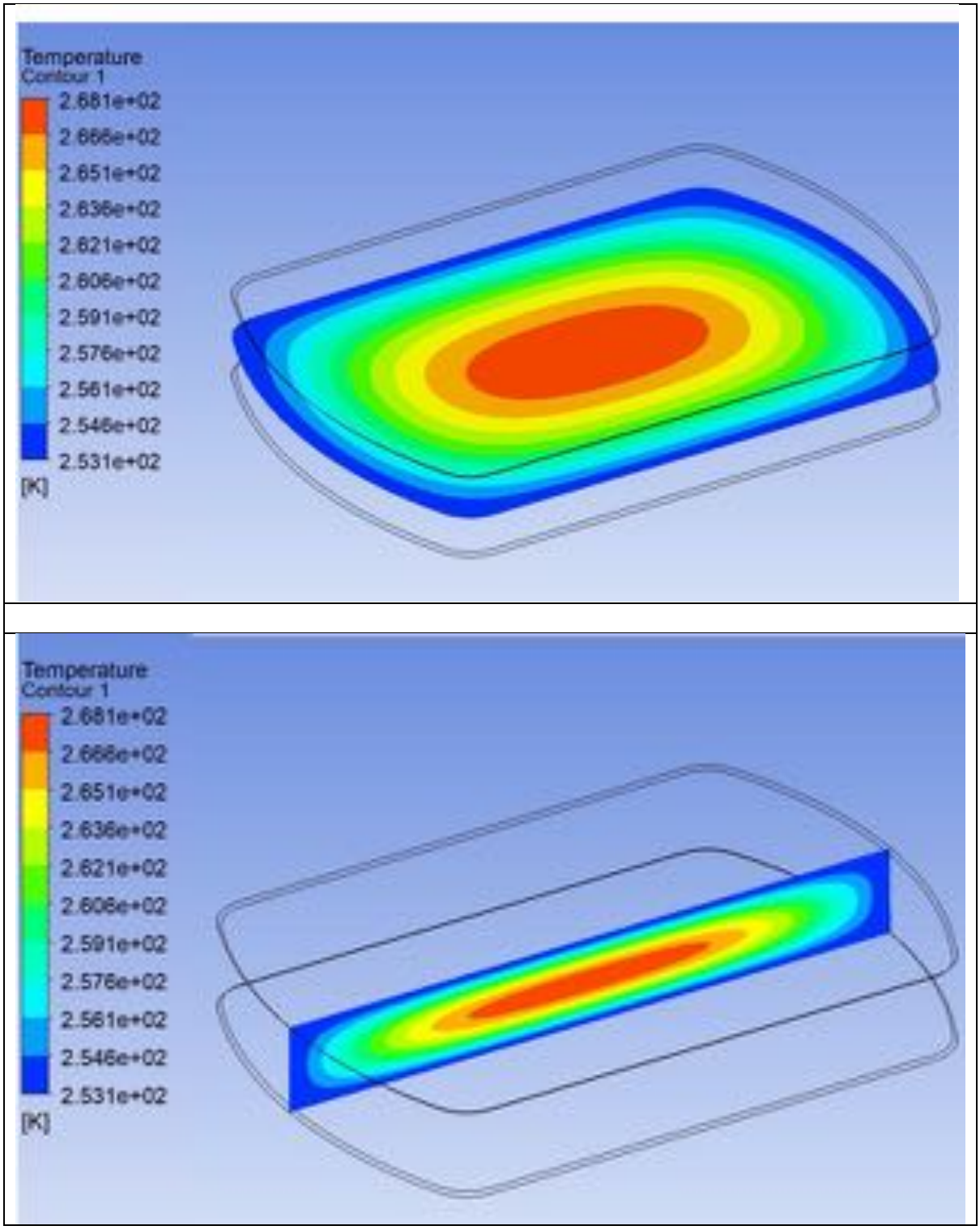

Figure 6-24: Thermal Contour Plot at 17 minutes 45 seconds

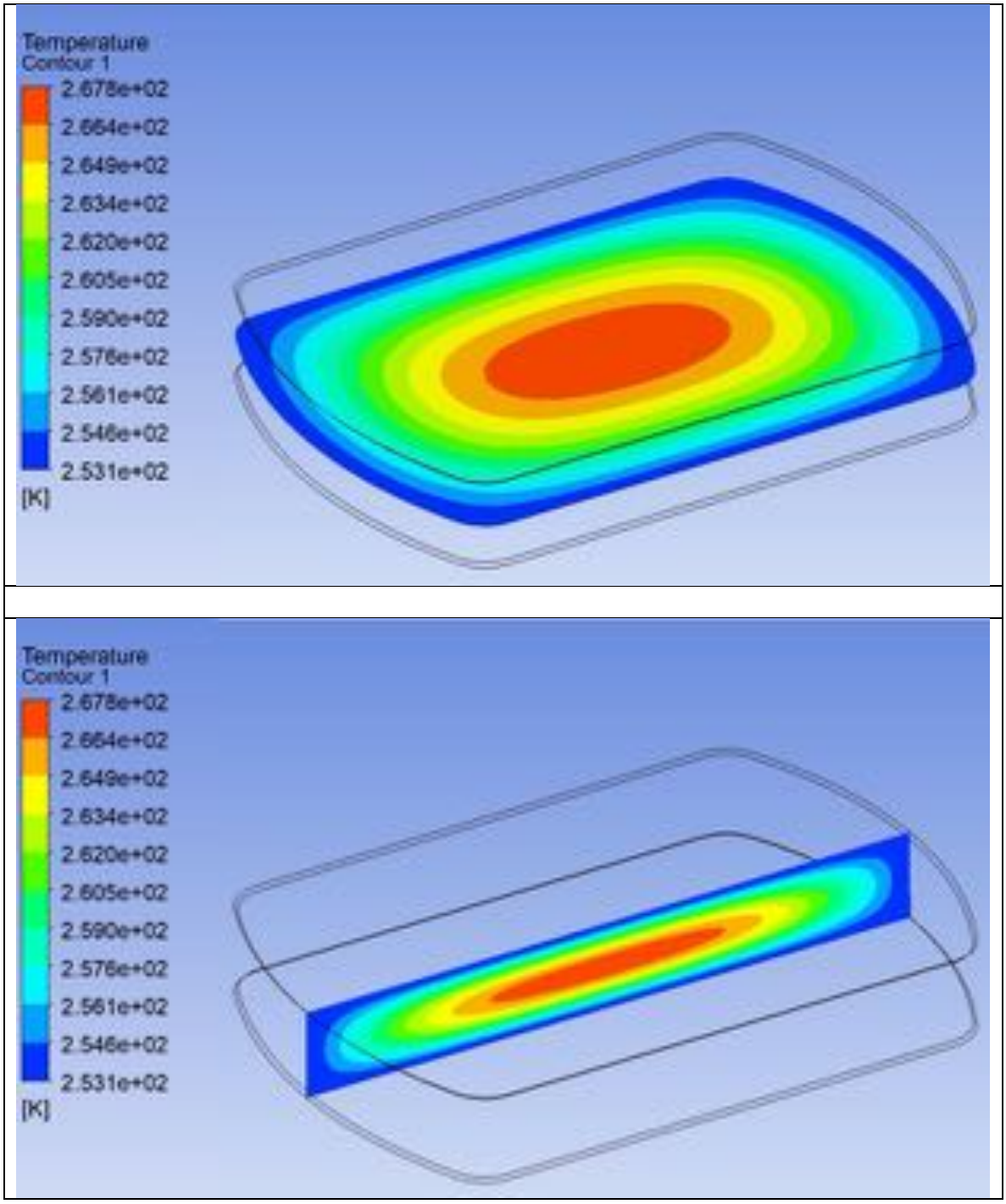

Figure 6-25: Thermal Contour Plot at 19 minutes 15 seconds

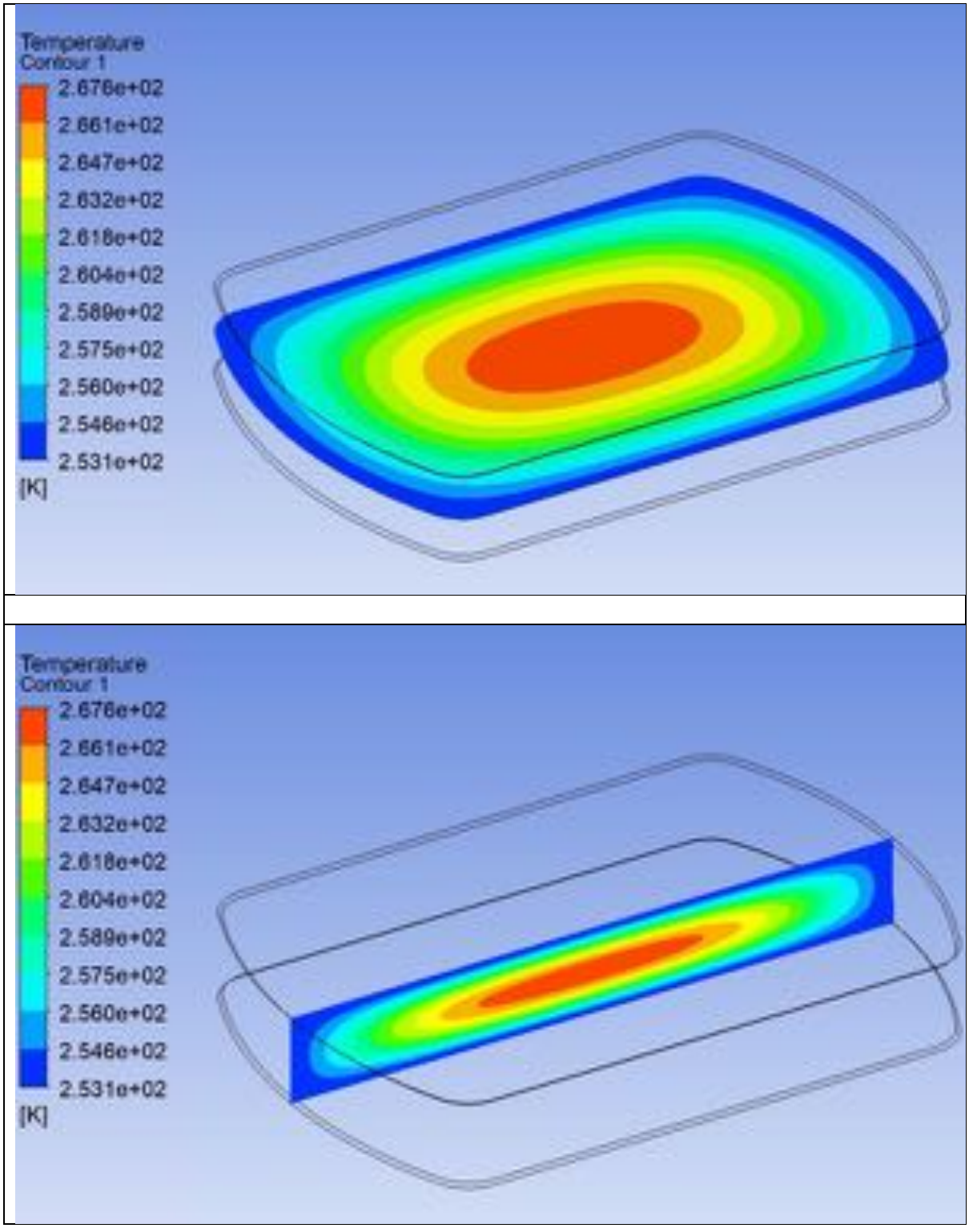

Figure 6-26: Thermal Contour Plot at 20 minutes and 45 seconds

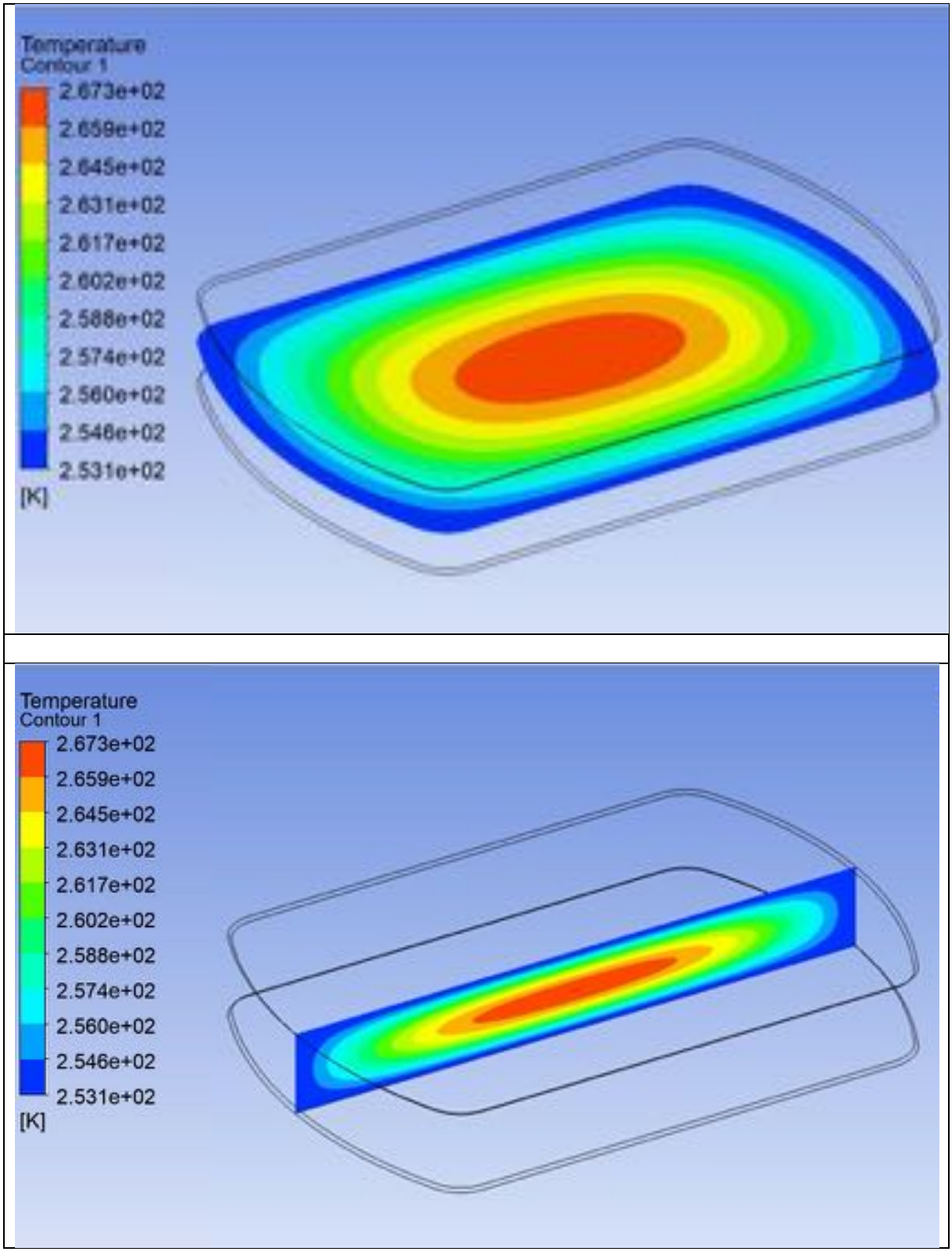

Figure 6-27: Thermal Contour Plot at 22 minutes and 15 seconds

6.6.2 Volume Fraction

The difference between the phase fractions highlights the progression and separation of each phase, whether the phase is denoted by a solid or a liquid. Unlike the thermal contour plots shown in section 6.6.1, the volume fraction denotes the position of the interface between solid and liquid phases. The contour plots in Figure 6-29 to Figure 6-37 show the associated volume fraction. The location and progression of the volume fraction highlights the trend of a conduction rate through the top and bottom faces of the plasma bag leading to uneven solidification rates throughout the plasma. The interaction of the bottom wall of the plasma with the conductivity of the stainless-steel wire mesh is evident. As the plasma bag is located in an unloaded system, the lack of obstructions highlights a symmetrical flow profile and a resultant similar heat transfer rate.

The change in interface position has been tracked from each wall boundary as a function of time. The location of the interface determines the position of the mushy zone. The data shown in Figure 6-28 shows a minute difference of approximately 1mm between the front interface and the back. The change in the interface location is determined from the applied free stream temperatures defined in Table 6-3. The intake of the airflow at the back is significantly cooler due to the fan profile shape. The immediate interaction between the cold air and the back of the plasma bag results in a large temperature differential in comparison to the front of the plasma bag. The difference in heat transfer rates contributes to the different interface progression rates.

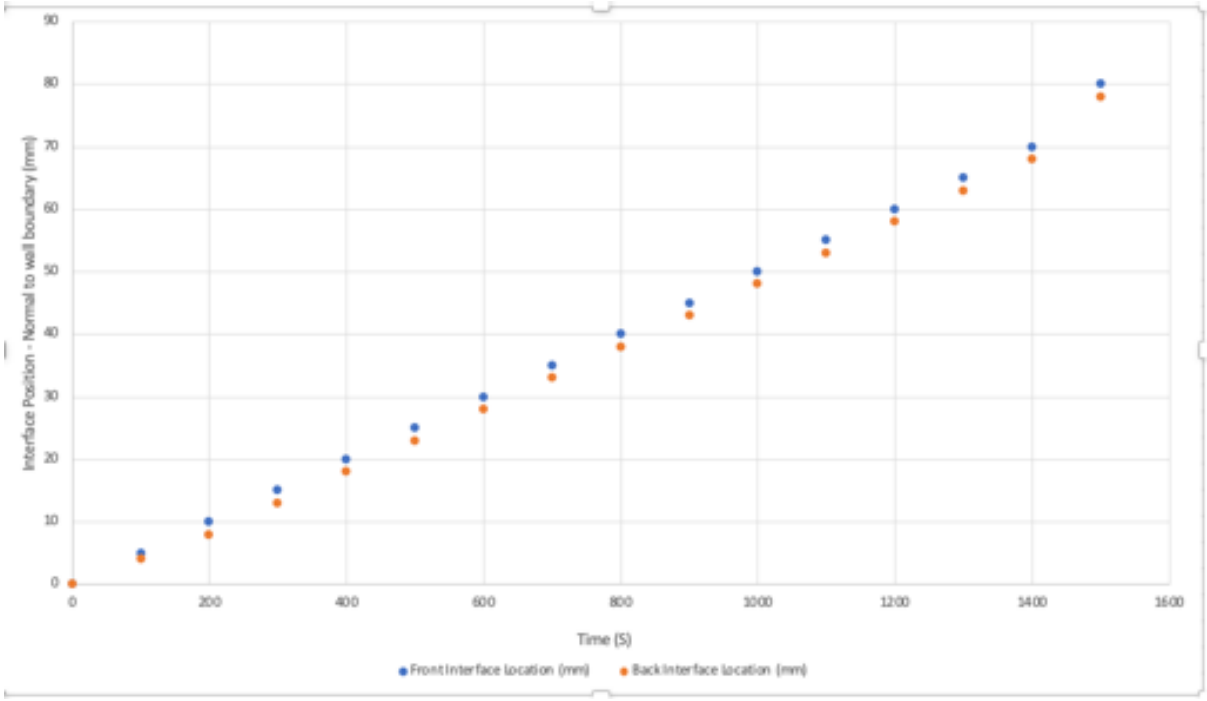

Figure 6-28: Interface position change in response to time.

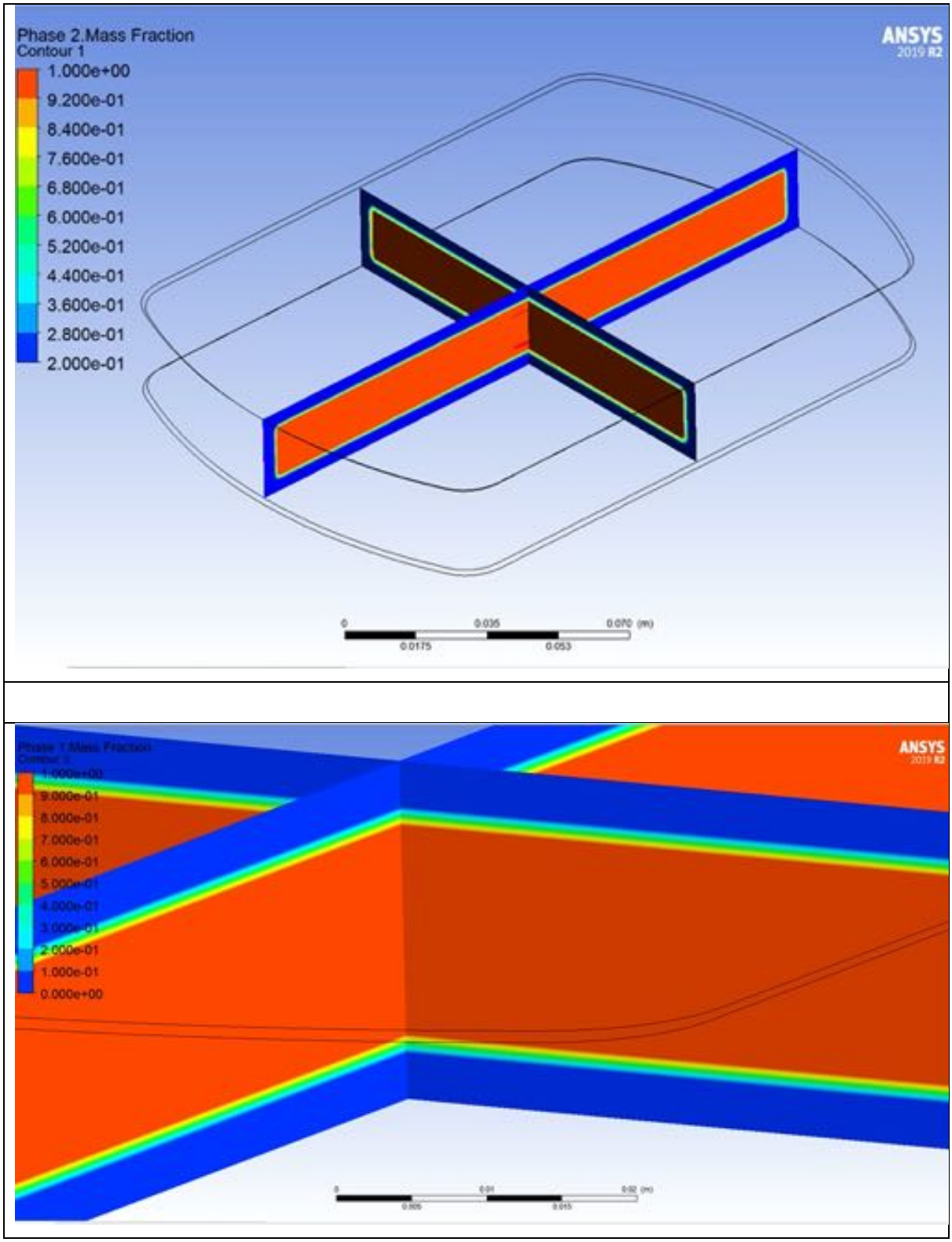

Figure 6-29: Volume Fraction-2minutes 45 seconds

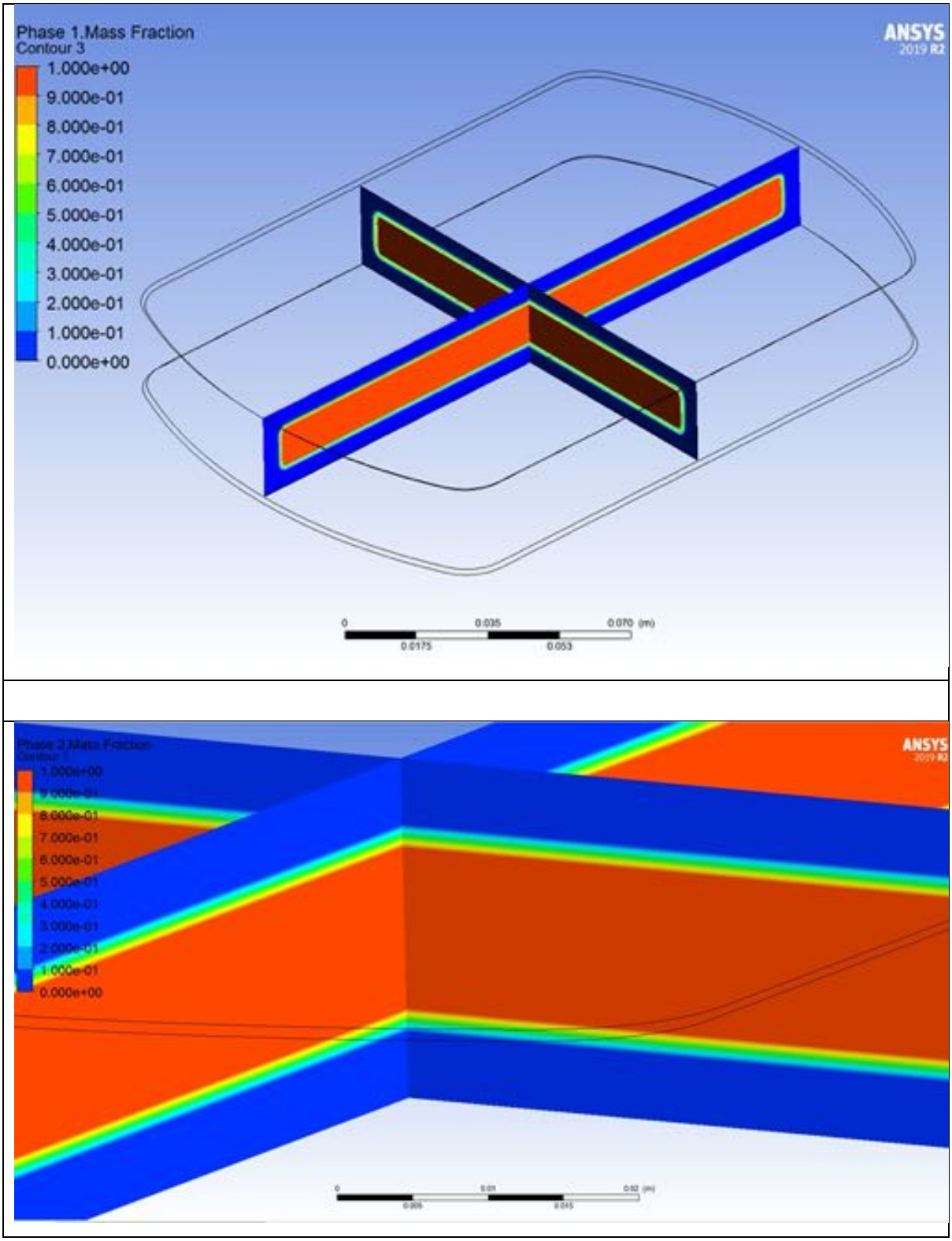

Figure 6-30: Volume Fraction at 5 Minutes

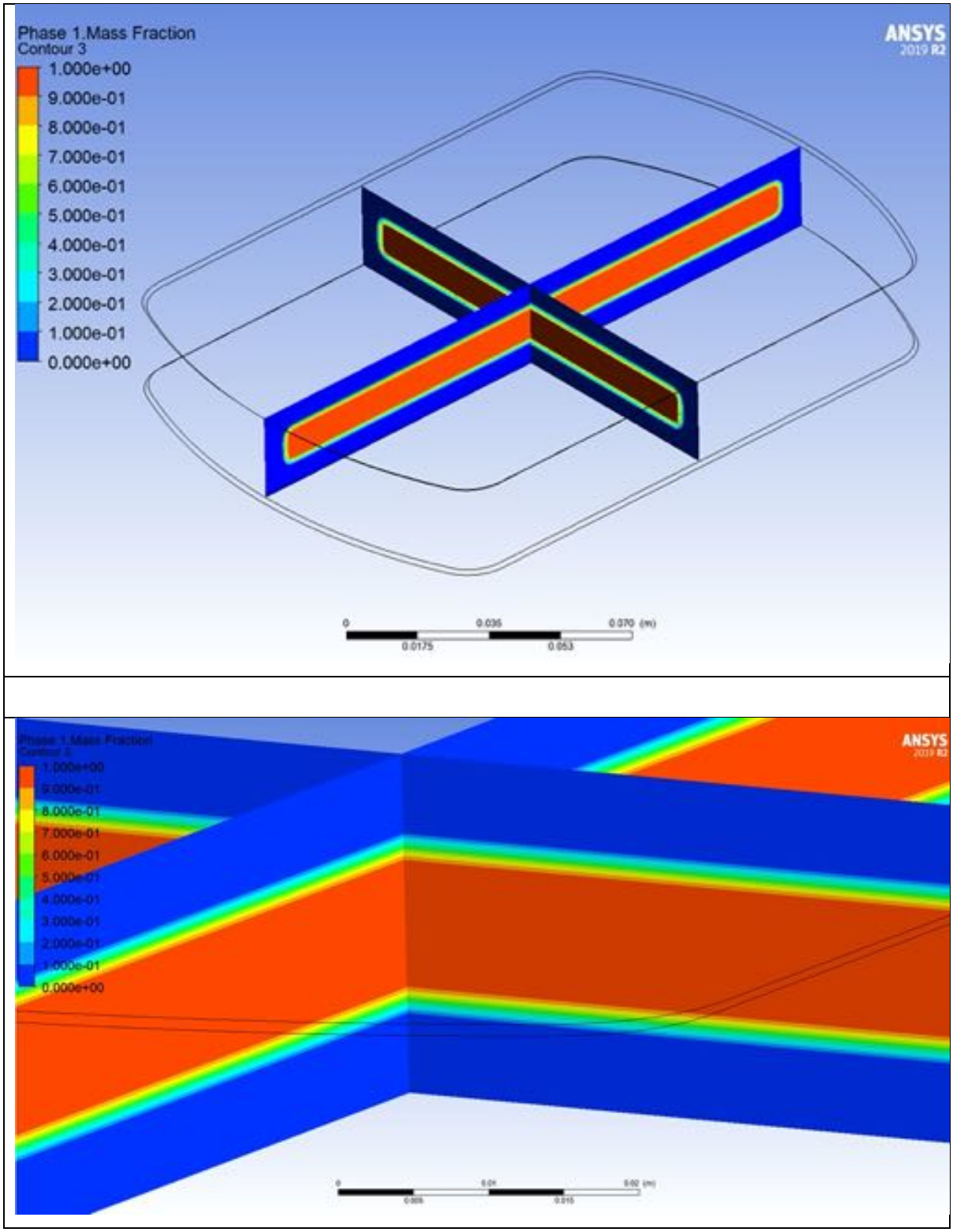

Figure 6-31: Volume Fraction at 7.5 Minutes

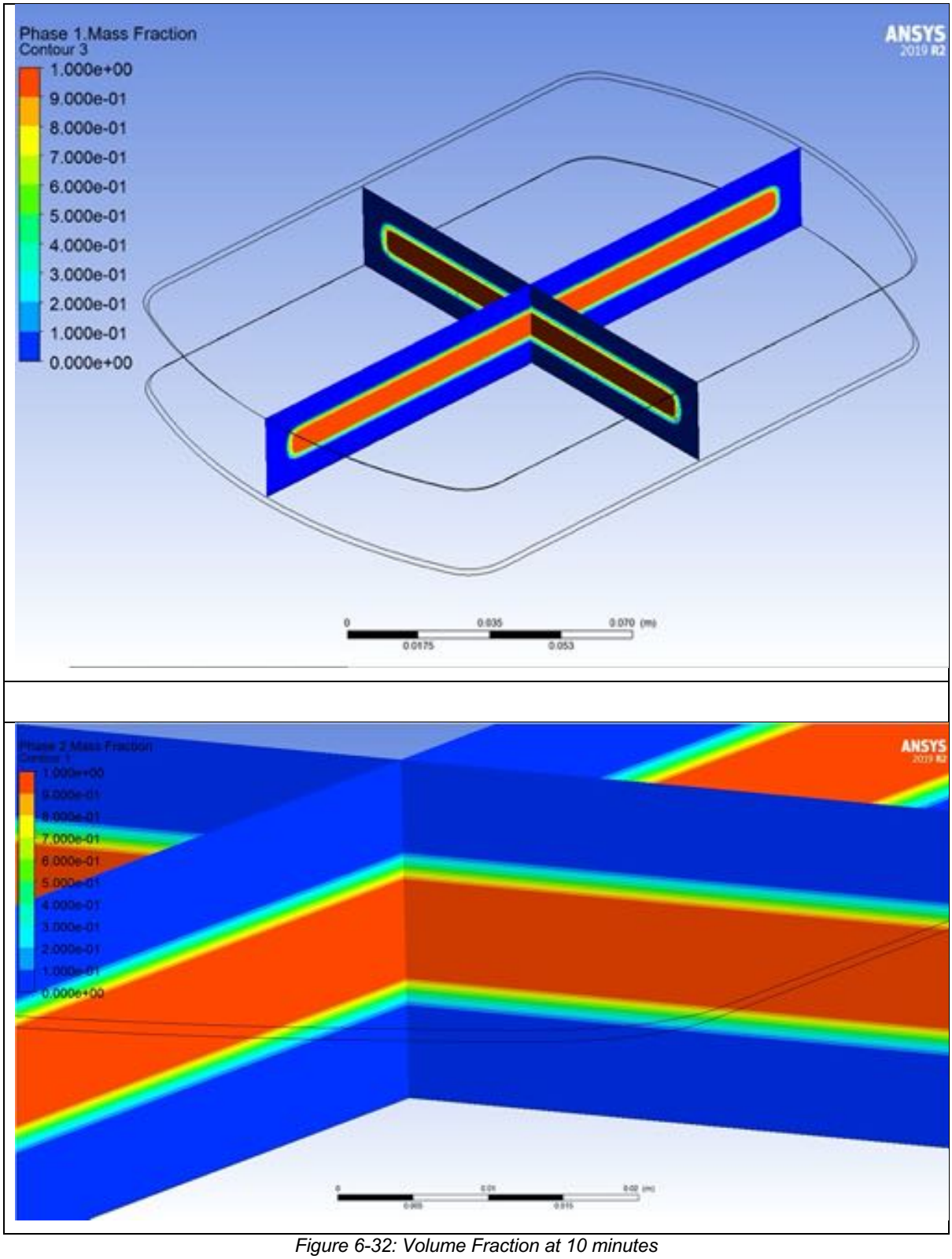

Figure 6-32: Volume Fraction at 10 minutes

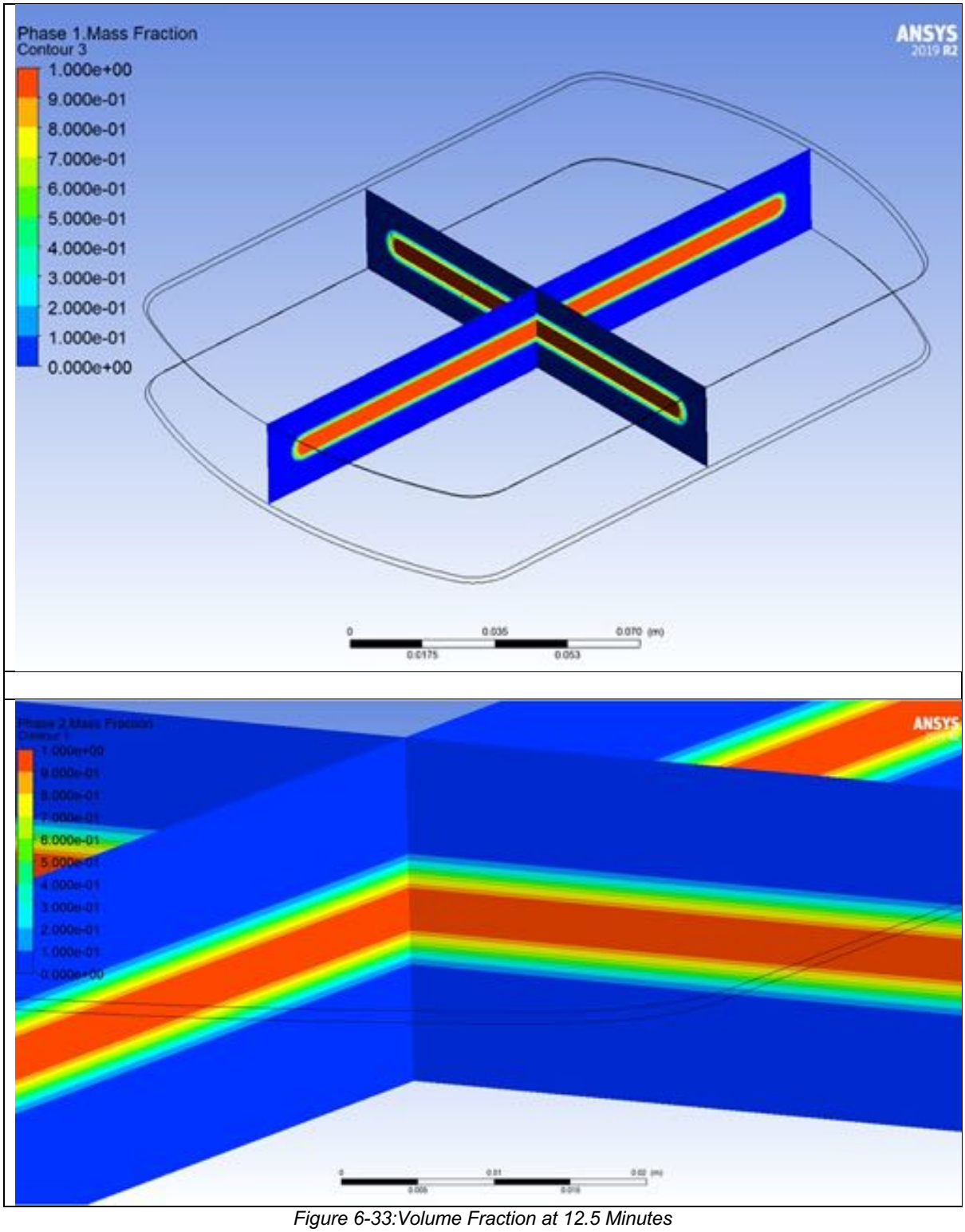

Figure 6-33:Volume Fraction at 12.5 Minutes

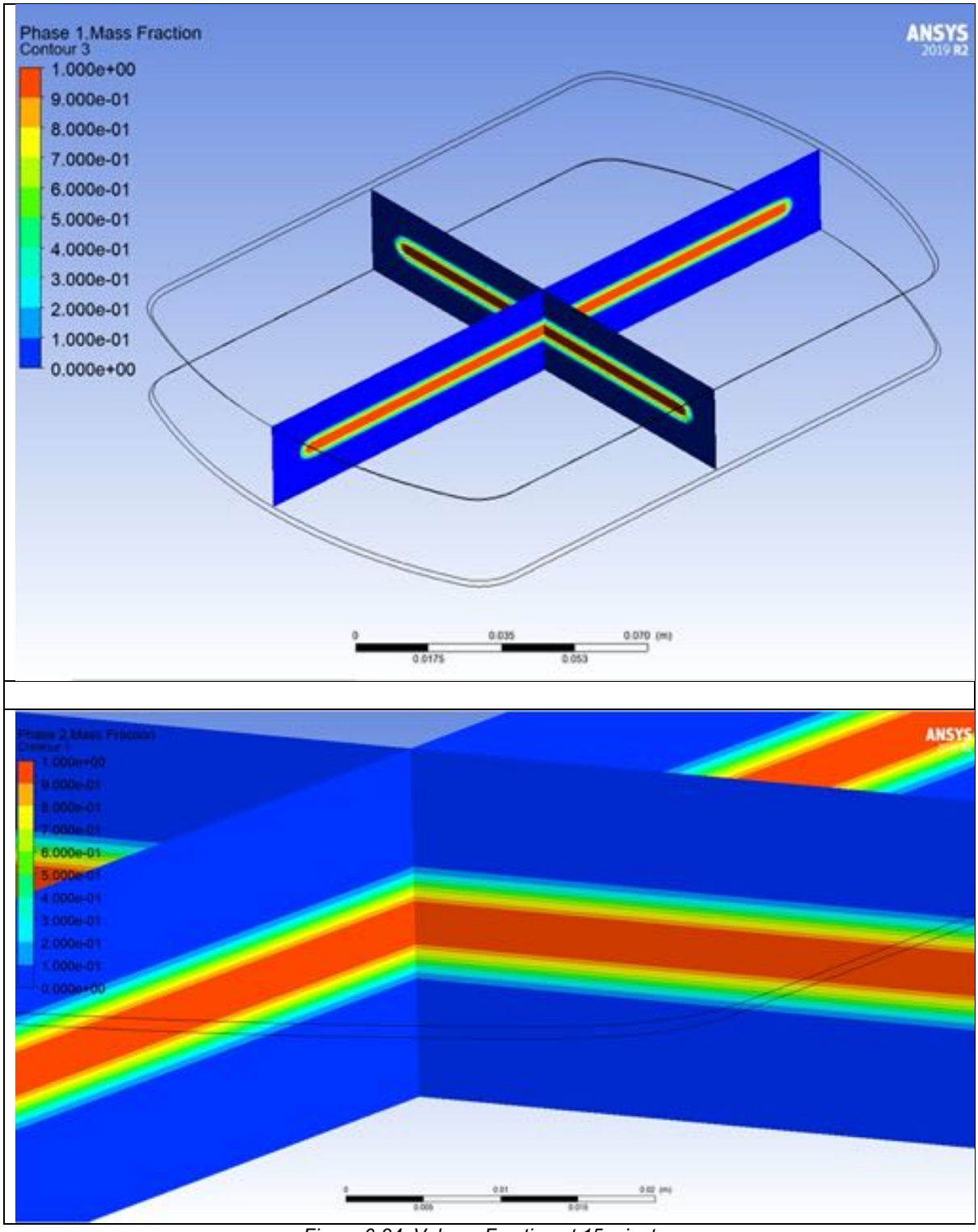

Figure 6-34: Volume Fraction at 15 minutes

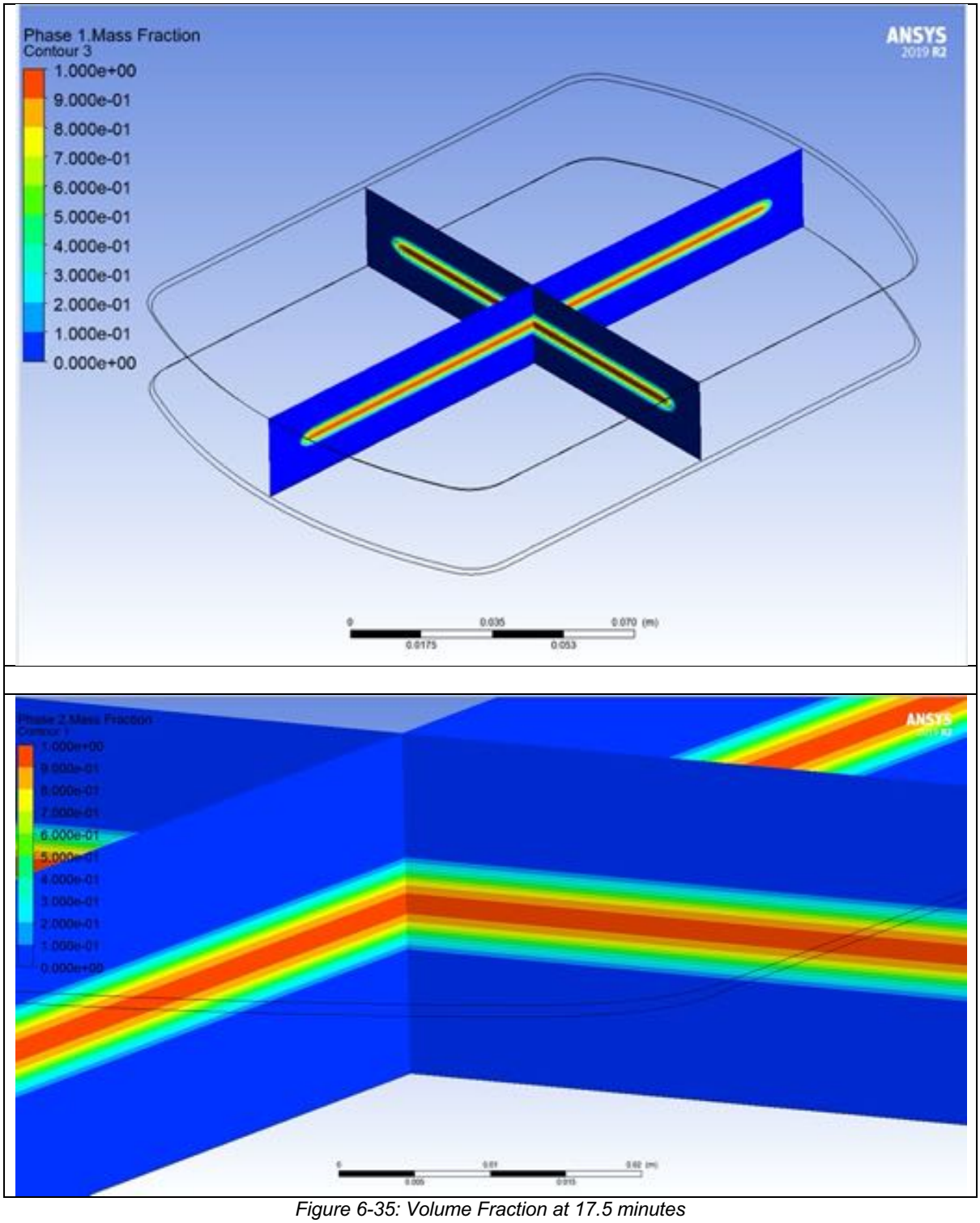

Figure 6-35: Volume Fraction at 17.5 minutes

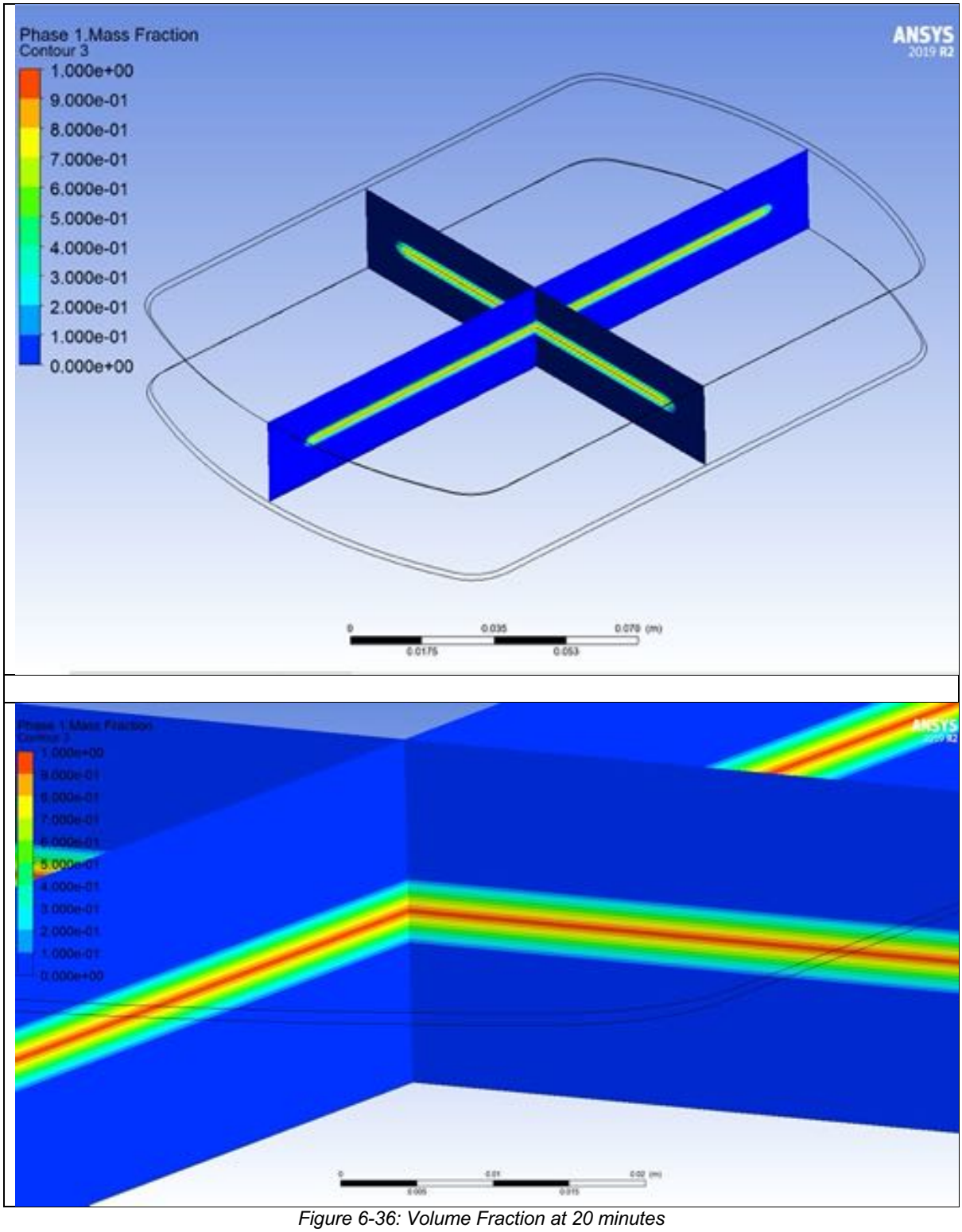

Figure 6-36: Volume Fraction at 20 minutes

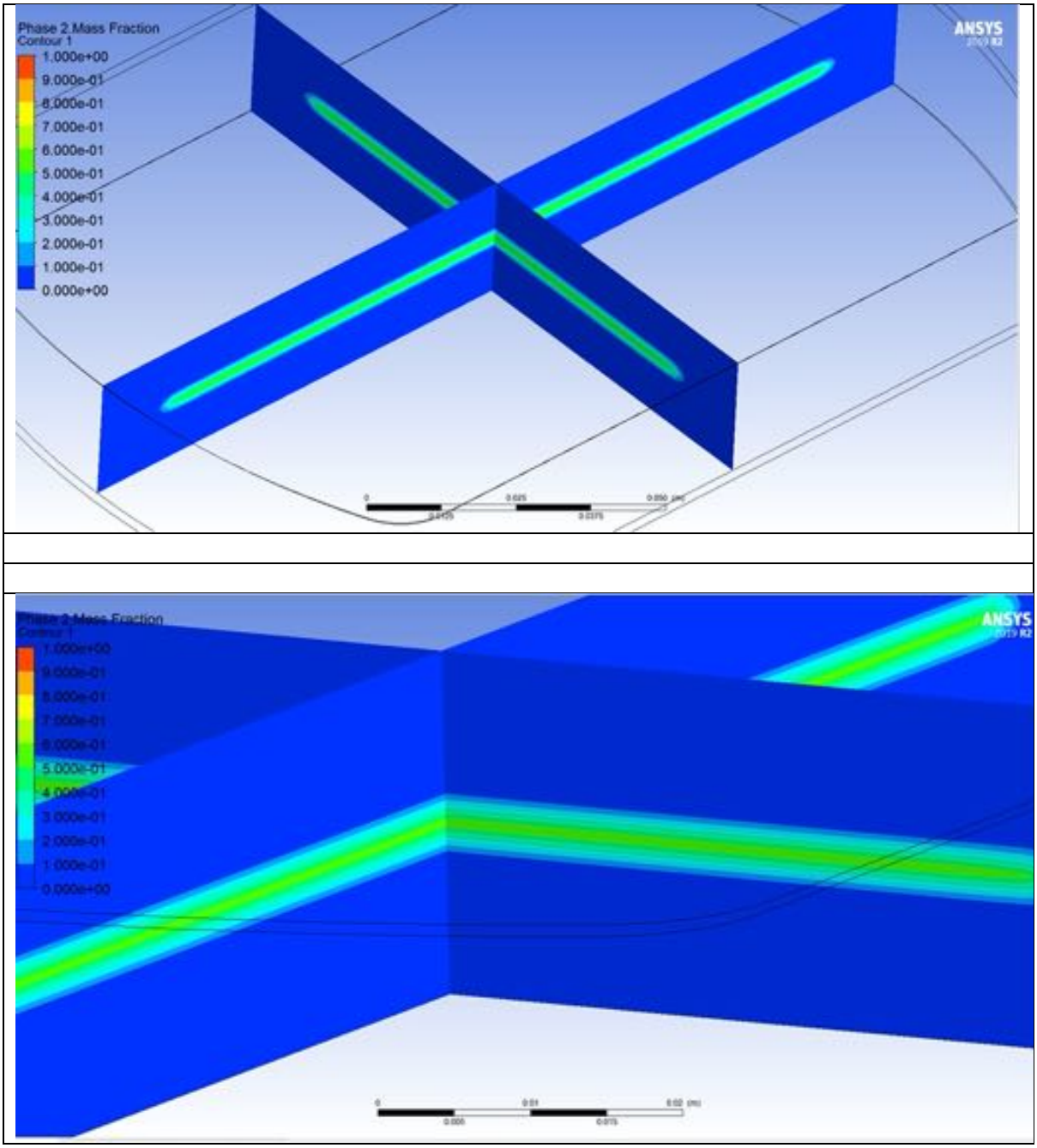

Figure 6-37: Volume Fraction at 22.5 minutes

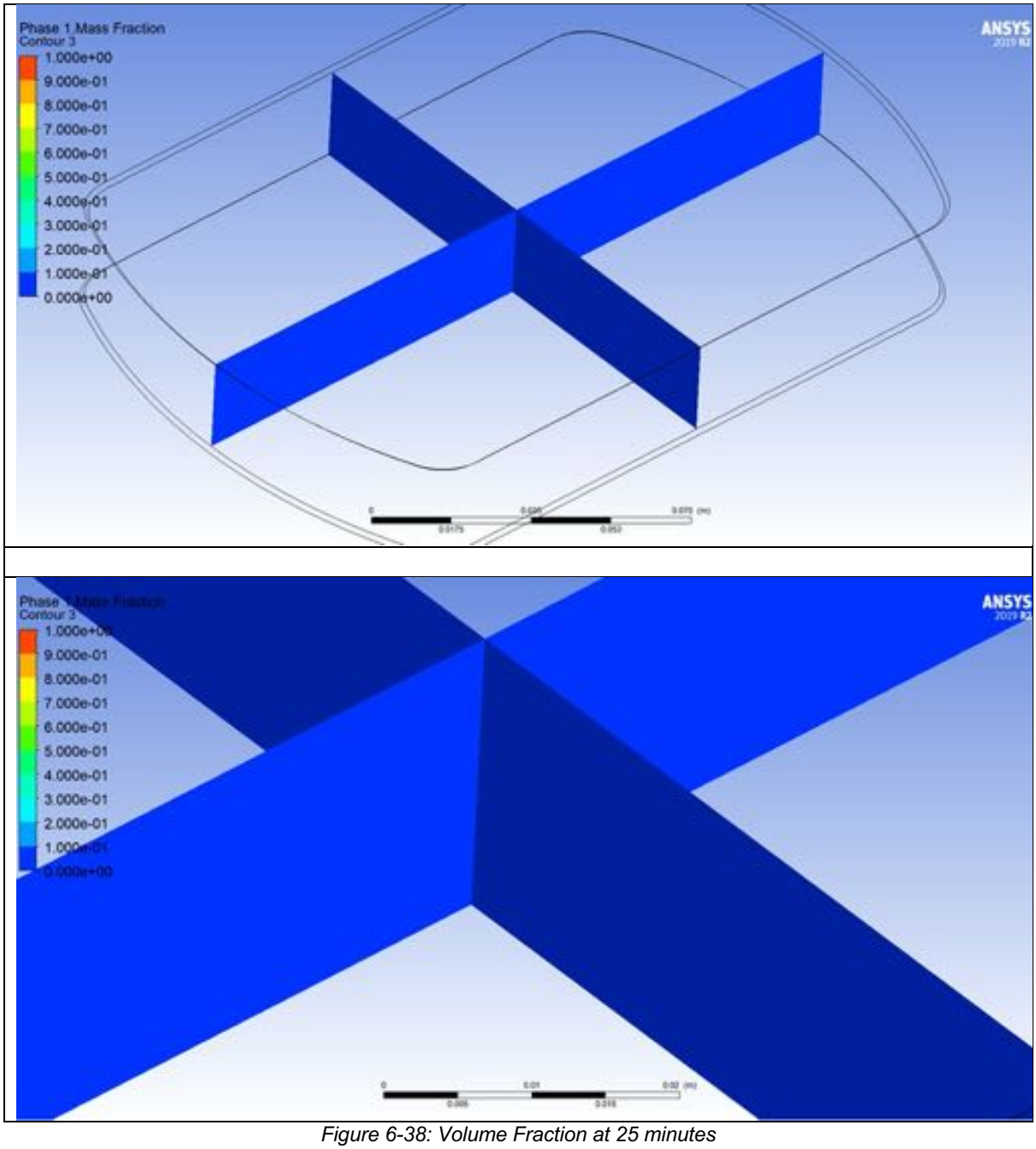

Figure 6-38: Volume Fraction at 25 minutes

6.6.3 Experimental Validation

The results shown in Figure 6-39 compare the experimental and CFD results obtained in section 6.6.2. The results reflect an identical decline throughout the phase change operation with minimal variation. Throughout the solidification of the plasma simulant, the CFD values present a minor over-prediction in the rate of solidification. With the liquidus and solidus temperatures being fixed values, the root cause of the differences can be determined from multiple factors including the density approximation applied throughout the control volume. The Boussinesq approximation acts as a supplementary function to improve the accuracy of the simulation, but other fluid factors may cause a deviation from this.

The analysis of the results was compared via mean average percentage error to compare the accuracy of the simulation in relation to the experimental results defined in Chapter 4. The experimental values were assumed to be the actual values, and the CFD model being a predictive forecast model. The data was obtained via a specialised plasma bag thermocouple shown in Figure 6-9. The thermocouple position was further included in the CFD model to record identical data points at an identical location. As the phase change occurs at approximately -2°C. The simulations' initial condition was defined before the phase change point. Similarly, to ensure an adequate solidification profile and a full solidification, the solidification rate continued until the desired volume fraction was achieved. The difference between CFD and experimental results showed a maximum numerical accuracy deviation 3%, which is quite acceptable in this case.

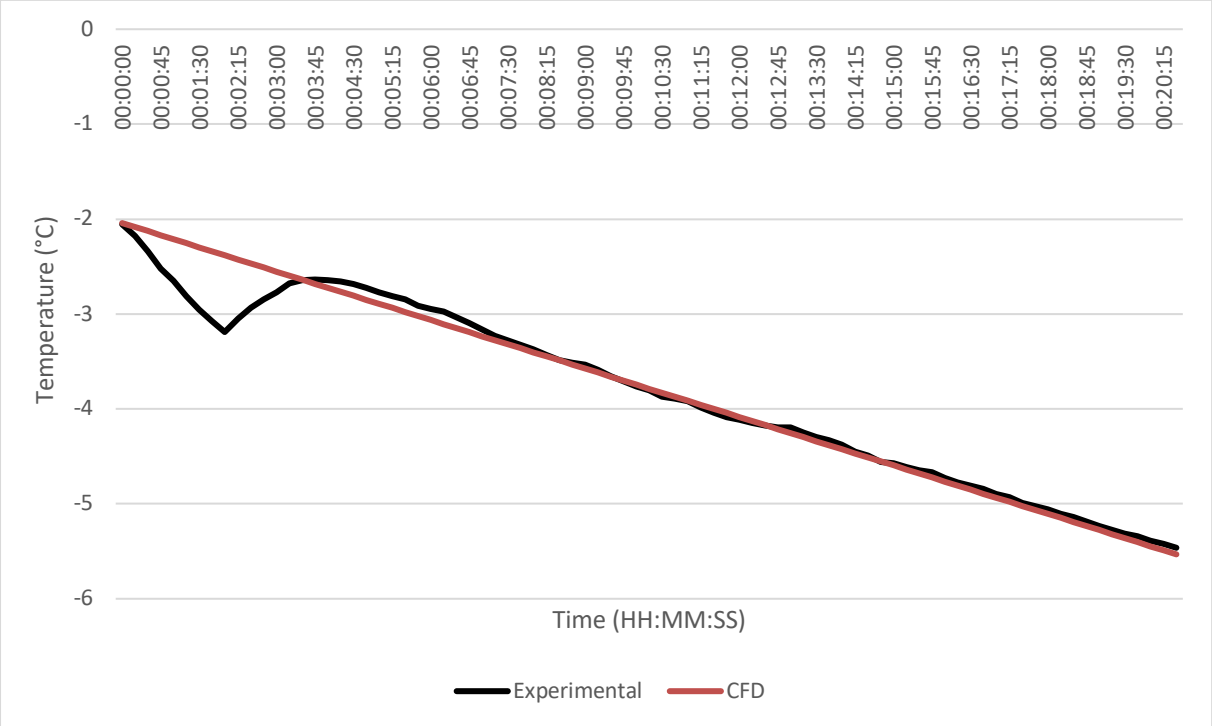

Figure 6-39: Experimental and CFD results for the phase change process

6.7 Chapter Conclusion

The outcome of the chapter highlights the successful modelling of a blood plasma simulant with the prescribed boundary conditions from the heat pipe cryogenic freezer. The solidification CFD model shows the potential to be applied within other applications with a relatively acceptable accuracy. The location of the thermocouple and the data point reflected in the CFD model show a good agreement as per the data of Chapter 6.5.

Chapter 7 : Application

The investigation presented in chapter 6 discusses the simulation process of the solidification experienced during the initial loading within the retrofitted heat pipe-based freezer. The visualisation of the chamber space remains a key parameter in the applicability of remote cooling via heat pipe technology. The development will cover the testing and simulation of an initial baseline injection system and a retrofitted heat pipe system discussed in section 5.1.4. The outcome from the development of the heat pipe system will allow the visualisation of a novel preservation system which has not been reported in the existing literature. The content of this chapter will be primarily focussed on the validity and thermal characterisation of a heat-pipe based cryopreservation system.

The validation of the experimental results was conducted via CFD simulations and is based on several different operating conditions such as fan speed and set point conditions.

7.1 Baseline Injection Model

7.1.1. Model Geometry and Mesh

A three-dimensional geometry based on the experimental set up described in section 5.1 was constructed within ANSYS DesignModeler as shown in Figure 7-1. The development of the system includes the shelving storage, a fan, and a separation plate contained within a freezer chamber. Table 7-1 highlights the material details used within the simulations.

Cell Zone	Simulation Property
Plasma Bag	PHT with DEHP plasticiser
Freezing chamber walls	Stainless Steel
Loading Shelves	Stainless Steel
Fan	Stainless Steel
Separation Plate	Stainless Steel

Table 7-1: Geometry Material Definition

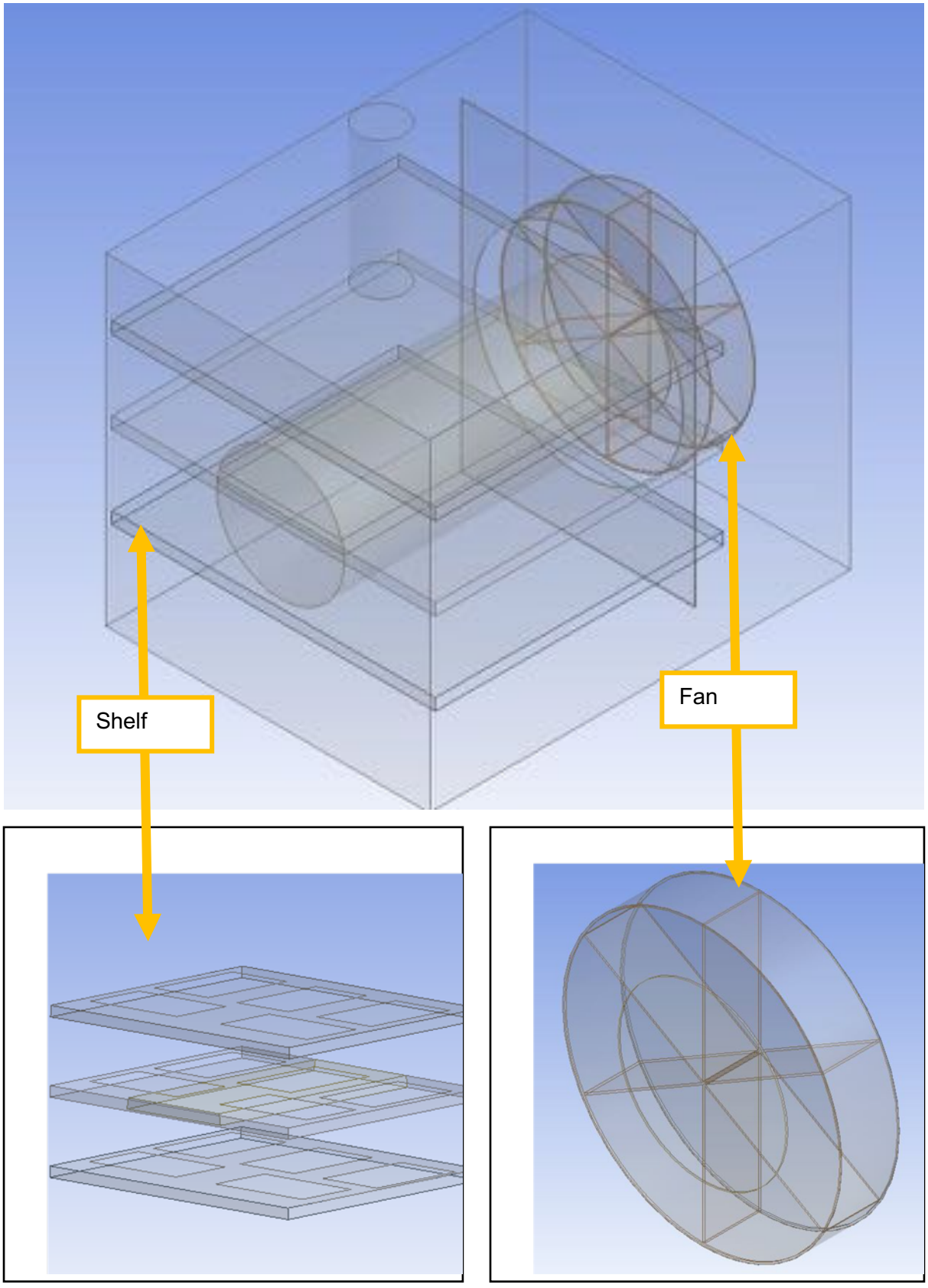

Figure 7-1: Baseline Geometry

The mesh development was conducted in ANSYS Meshing due to the combination of parts to form an assembly of the geometry, including the operation of an axial fan. A mesh independence study was conducted to maximise the accuracy of the simulation whilst minimising computational effort. The study was conducted using parametric conditions which investigated a multitude of mesh densities ranging from fine to coarse, and different cell types. Table 7-2 shows the results from the mesh independence study. The results highlight the increased accuracy of the simulation with an increase in cell density. The comparison between tetrahedral (tet) and hexahedral (hex) meshes is significant, as the tet mesh shows capabilities to match the accuracy of a hex mesh but at a significantly higher node count. The significant increase in node count is unadvisable due to increased computational time. The comparison between coarse and fine mesh densities highlights the significant increase in accuracy and cell quality, with a noticeable difference between medium and fine densities. Therefore, the assembly mesh produced consisted of a fine hex mesh.

Level	Number of Cells	Cell Type	Skewness	Time per Iteration
Coarse	506,402	Hexahedral	0.656	5-10s
Coarse	566,030	Tetrahedral	0.701	5-10s
Medium	1,402,790	Hexahedral	0.732	10-12s
Medium	1,497,204	Tetrahedral	0.759	10-14s
Fine	2,059,241	Hexahedral	0.895	15s+
Fine	2,504,259	Tetrahedral	0.851	15s+

Table 7-2: Mesh Independence Study

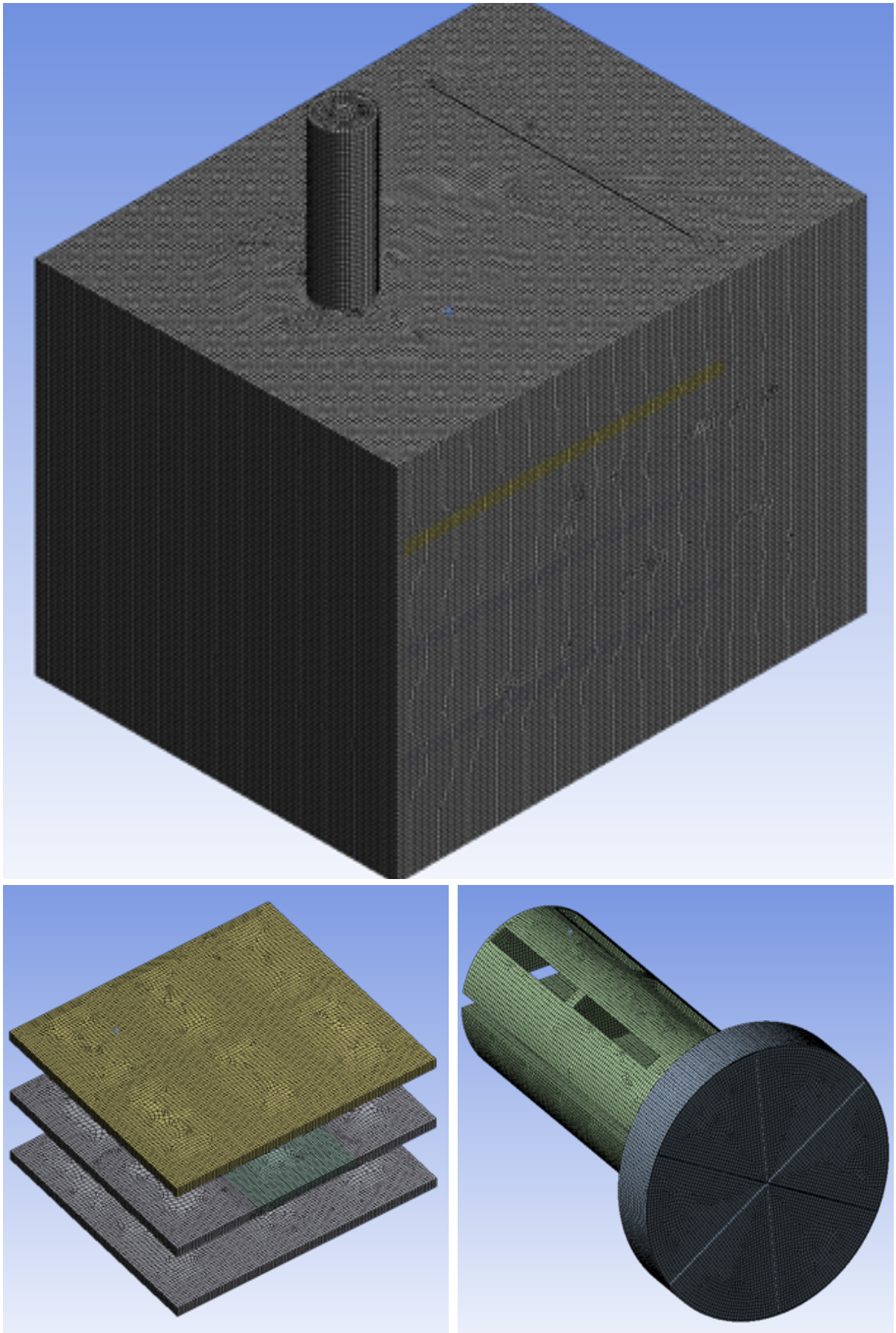

Figure 7-2: Developed Assembly Mesh

7.1.2 Boundary Conditions

The definition of boundary conditions accounts for the convective effects and dynamic behaviour of the axial fan and highlights the initial solving conditions of a simulation. The selection of boundary conditions must be compatible with the selected turbulence model to allow for a steady convergence and accurate results. One of the key conditions of the system is the definition of the thermal profile within the chamber without utilising the vaporisation of liquid nitrogen droplets. Figure 7-3 shows the implemented User Defined Function (UDF) for the initial gas condition. The premise of the UDF is based on a generic function of time to freeze the plasma simulant, plus a mitigation to ensure the chamber temperature reaches the desired set point. The function of the boundary conditions is to define the operation of the initial set point conditions. The boundary conditions for the surrounding zones such as the chamber walls have been set to adiabatic, to minimise heat transfer to the surroundings. To ensure that a correct amount of air passes through the shelves, a set porosity has been applied to account for the wire mesh structure.

```
#include "udf.h"

DEFINE_PROFILE(inlet, thread, position)
{
    face_t f;
    real t = CURRENT_TIME;
    begin_f_loop(f, thread)
    {
        F_PROFILE(f, thread, position) = 253.15 + 1 * t;
        if (t > 1140)
            F_PROFILE(f, thread, position) = 193.15;
        else (t < 1140);
        F_PROFILE(f, thread, position) = t*-0.001 + 283.15;
    }
    end_f_loop(f, thread)
}
```

Figure 7-3: Air Temperature User Defined Function (UDF)

Property	Condition
Exhaust	Outflow
Body Wall	Wall
Separation Plate	Wall
Plasma Bag	Wall

Table 7-3: Assigned Boundary Conditions

The definition of the cell zones is applicable to the fluid zones within the simulation, the model is mainly split into 4 zones as reflected in Table 7-4. The zones allow the definition of the chamber properties alongside the activation in MRF (moving reference frame) methods to mimic the rotation of the fan. The definition of the fan is determined by the setting of an angular velocity alongside the direction of rotation.

Cell Zone	Condition
Fan	MRF
Fan Fluid	Interior
Chamber	Interior
Shelf	Porous Wall

Table 7-4: Assigned Cell Zone Properties

The basis of the simulation operates in a transient schematic where the decline in temperature is a function of time, which allows for a fixed time step to be defined. To define the turbulent behaviour effectively, with robustness due to a swirling flow, the realizable k-epsilon turbulence model was utilised. A scalable wall function was activated to add a level of stability to near wall flows. The simulation was based on a SIMPLE algorithm, which allows coupling the relationship between the velocity and pressure corrections to satisfy the conservation of mass. A second order discretisation scheme was applied for momentum, energy and a standardised pressure function. The surrounding walls have no-slip boundary conditions alongside the assumption of adiabatic walls. The volume of the plasma bag was assumed to be set at an ambient temperature of approximately 20°C, as observed experimentally. The initial temperature condition represents the average temperature of blood plasma before being frozen

7.1.3 Flow Visualisation of CFD Results

The velocity mapping of the injection-based system was simulated in both a loaded and an unloaded chamber to investigate the change in flow fields. Figure 7-4 and Figure 7-5 show the flow field of the system at 285 RPM (10Hz) and 1995RPM (70Hz), reflecting both minimum and maximum operations of the fan. The initial unloaded simulations highlight an overall uniformly distributed flow, with minimal disruption. The difference shown in Figure 7-4 highlights the effect of single and double layers of plasma bags. The difference between both layers highlights the increase in resistance as the flow starts to pass each load. Similarly, the

differences in results between both loads confirms the development of wake areas, which is an indication of poor heat transfer allowing for an uneven freezing regime.

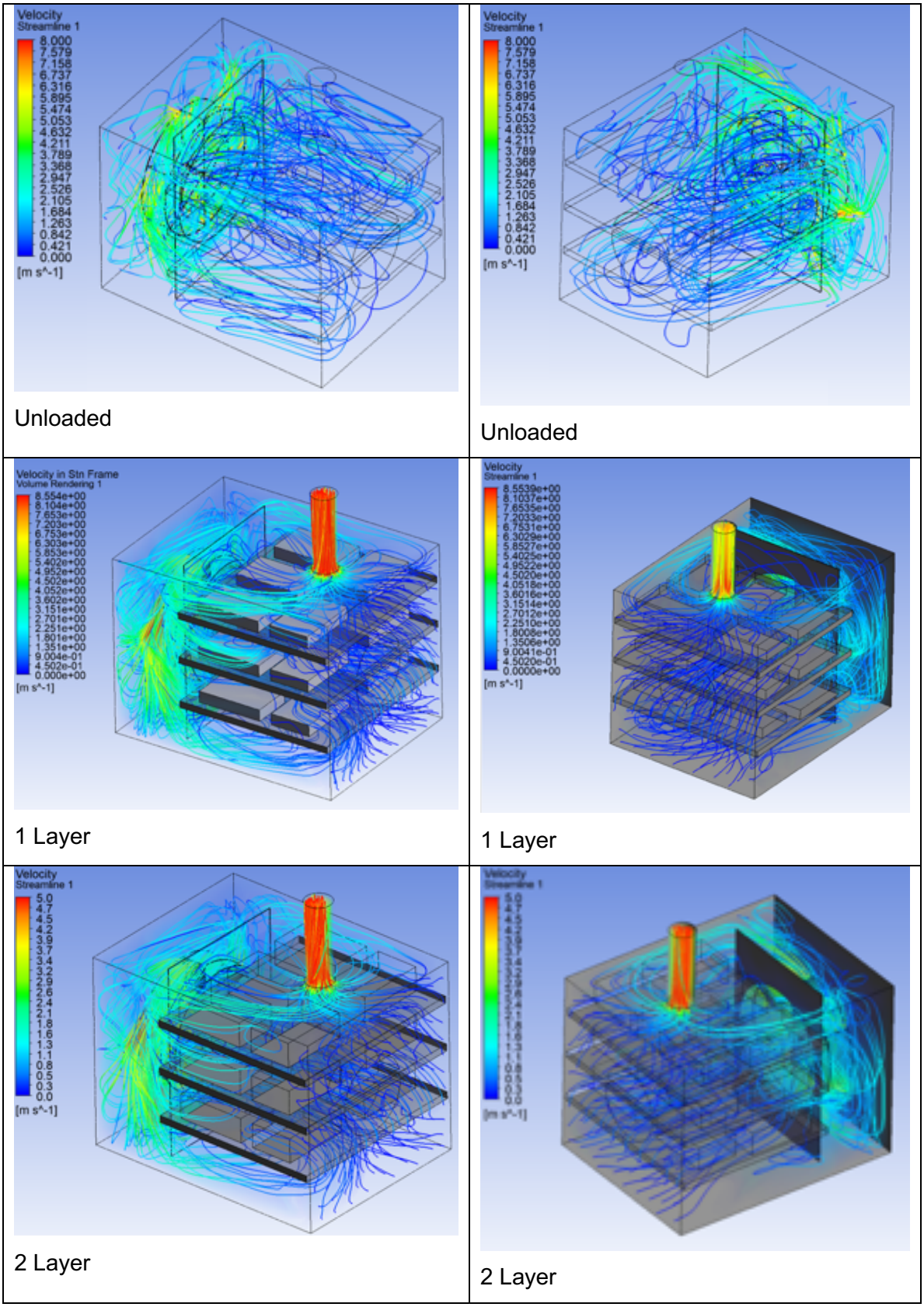

Figure 7-4: Velocity Profile at 285RPM

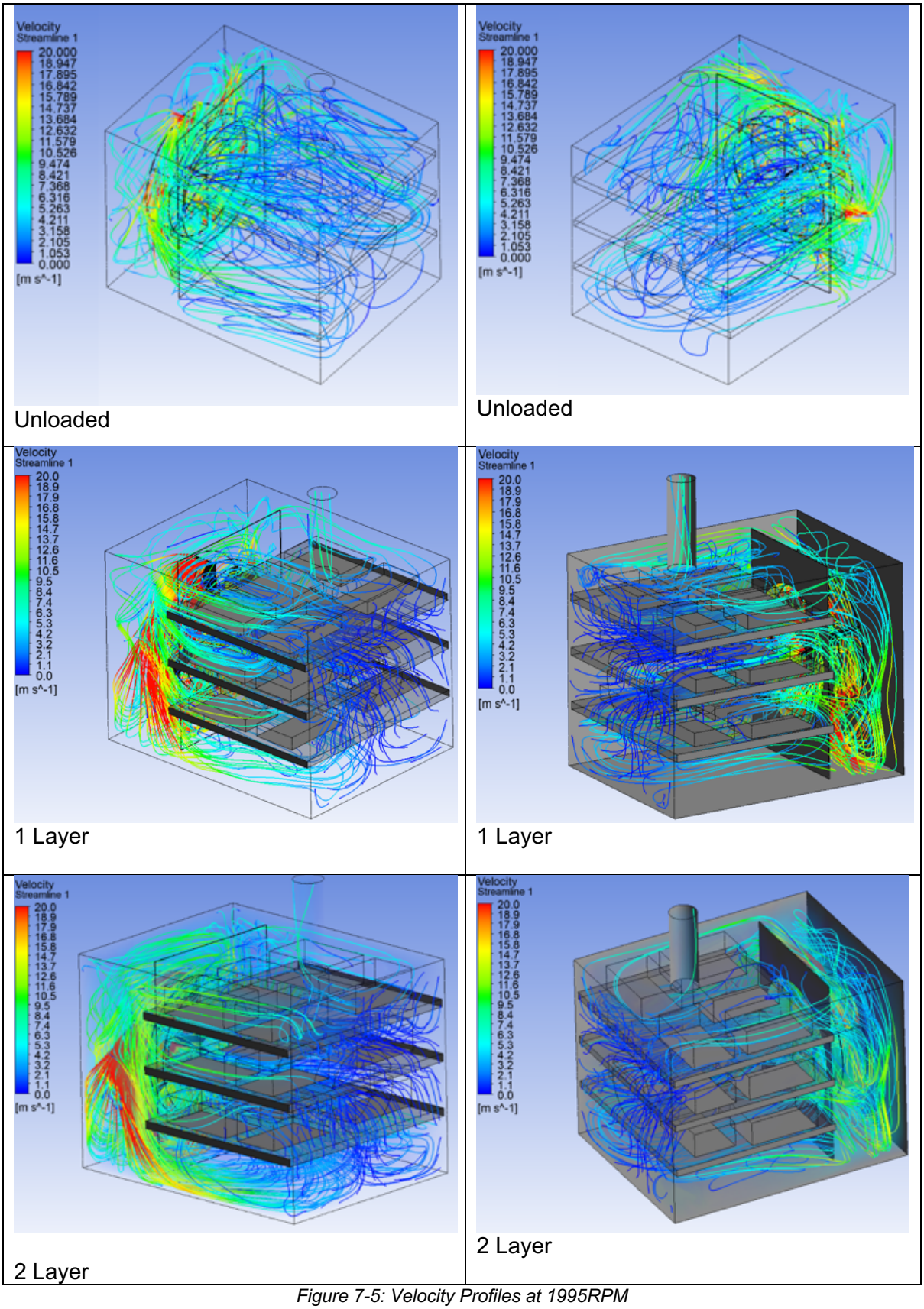

Figure 7-5: Velocity Profiles at 1995RPM

7.1.4 Thermal Variation of Plasma bag

The thermal profile of the air chamber is based on a function of time to cool down the chamber to a set point temperature. The subsequent heat transfer between the cooling medium and plasma bags will be purely dependent on the convective effects of the fan. The plasma bags were investigated in double and single layers, in an inline configuration at both 285 RPM and 1995 RPM. Figure 7-6 and Figure 7-7 show the thermal variations between systems with a double and a single layer for 285RPM at a set point temperature of -70°C. Both results reflect an extremely high heat flux towards the corners of the plasma bags, which is more evident in loads located towards the fan. The increased heat flux located in those specific regions represent the function of the liquid nitrogen injectors. In reality, the liquid nitrogen typically evaporates turning into a gaseous form, with the presumption being an entirely gas form. What happens in reality is that a finite concentrated amount of liquid nitrogen droplets interact with the corners of the plasma bag. The subsequent influence of the liquid nitrogen injection is immense, as the heat transfer coefficient of the liquid nitrogen droplets is 10,000 Wm^2/K.

Figure 7-6 presents the results obtained from -40°C to -70°C at 285RPM for a single loading configuration. The results highlight the phenomenon previously described to show high localised heat flux. The progression of the heat transfer throughout the system shown in Figure 7-6 highlights a level of thermal discrepancies throughout the system. The variation throughout the system is defined by the lack of circulation where the convective effects are significantly lower. The difference is evident where the variation is present on loads placed in series. The plasma bags in Figure 7-6 highlights the variation between two plasma bags placed in line. The reflected contour demonstrates that both plasma bags cool down to the desired set point but due to the inline configuration, the plasma bag in series is left in the wake of the more prominent plasma bag. The resulting effect is reduced convective flow, which is an evident trend for each plasma bag shelf location. The numerical and experimental results which are shown in section 7.1.3 highlight the discrepancy regarding the airflow circulation through each shelf level. The results show that, as the middle shelf is located in the annulus of the fan, it produces an improved convective heat transfer. A comparison between the top and bottom shelves shows an evident difference. The top and bottom shelves experience a lower heat transfer coefficient, and their thermal distribution is comparatively less than that of the middle shelf. The convective effects are considered to be lower given the observations in section 7.1.3, where the prominent plasma bags experience significantly lower heat transfer effects.

Figure 7-7 shows the results for a higher thermal load, where the plasma bags are stacked. The results from the double stacked layer highlights similar trends to a single layer. The positioning of the plasma bag shows similar trends where the plasma bag located towards the injectors contains areas of high heat transfer coefficient due to the interaction of the liquid nitrogen droplets on the surface of the plasma bag. The circulation around the freezing chamber shows a high level of variation, where both top and bottom layers are similar. The thermal distribution for the neighbouring plasma bag is increasingly varied. The neighbouring plasma bag bank immediately behind the prominent plasma bag highlights a further level of discrepancy, where the plasma bag temperature is significantly higher. In comparison to both single and double layers, the thermal variation and the increase in thermal load is evident. The increase in load further increased the resistance in flow path, reducing and increasing the available surface area. The change in heat transfer is evident in the comparison of single and double-layer configurations. The difference shows the significant decreased heat transfer coefficient value due to the decline in convective effects, reducing the overall circulation, and causing the subsequent decline in heat transfer.

Figure 7-8 presents a single layer inline operation similar to Figure 7-6, but with a higher fan operation at 1995RPM. The contour plots reflect similar thermal trends to Figure 7-7 where plasma bags placed in series have a level of variation. This trend is evident throughout the system, where the plasma bags located further away from the fan have a noticeably lower heat flux. The thermal variation between plasma bags located in the bottom shelf is significant compared to the heat flux of the middle shelf, which is located in the annulus of the fan. It is evident that the bottom shelf experiences reduced convective effects, contributing to the thermal variation across the chamber. Due to the increased fan speed, the convective effects are subsequently increased. The relationship between the plasma bag and the liquid nitrogen injector is evident. The plasma bags placed at the boundaries of the system experience significantly high heat flux due to the heat transfer coefficient of the liquid nitrogen droplets.

Figure 7-9 shows a layered schematic at 1995 RPM. The contours highlight the heat flux from -40°C to -70°C. The results show similar trends of thermal variation, where the plasma bags located in series experience lower convective effects due to the in-line positioning. As previously discussed, the layered plasma bag arrangement experiences similar thermal contours as in Figure 7-7. The main difference between Figure 7-9 and Figure 7-7 is the change in heat flux due to the increased convective effects.

-40°C	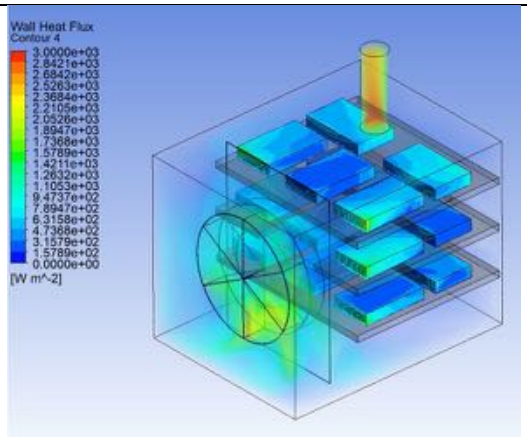	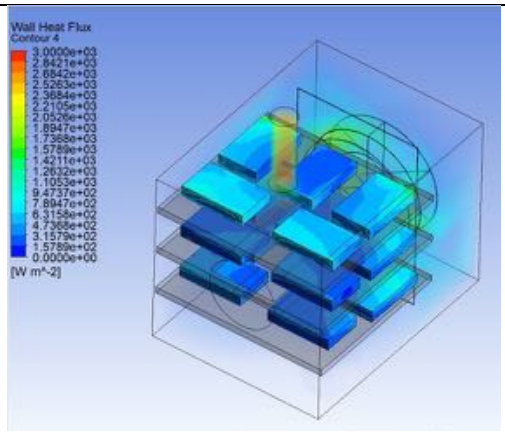
-50°C	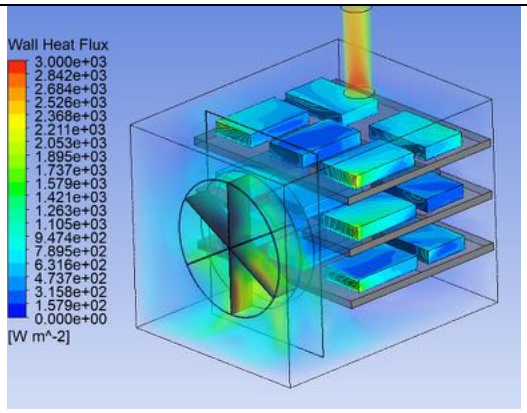	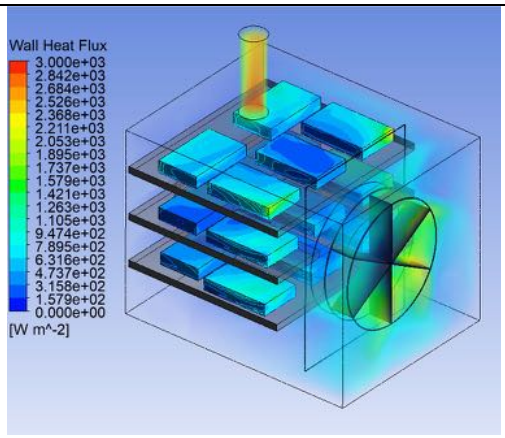
-60°C	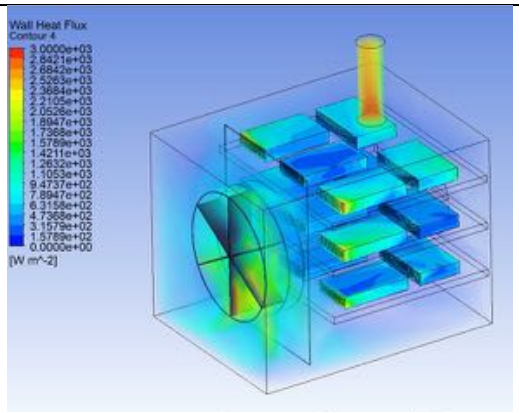	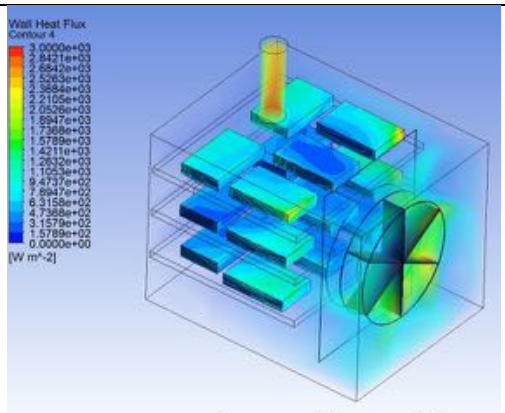
-70°C	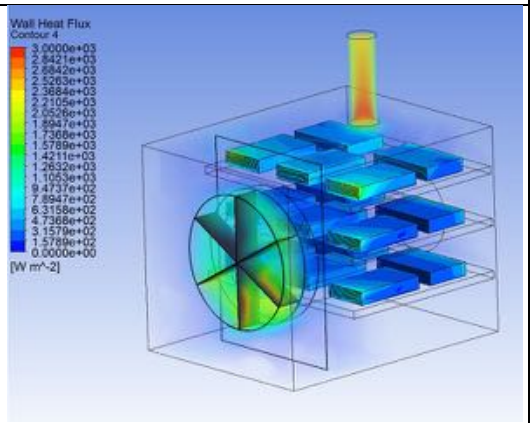	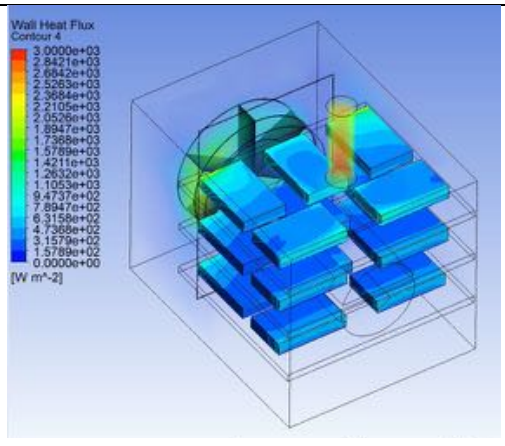

Figure 7-6: Thermal contour plot at 285RPM with single plasma bag layer

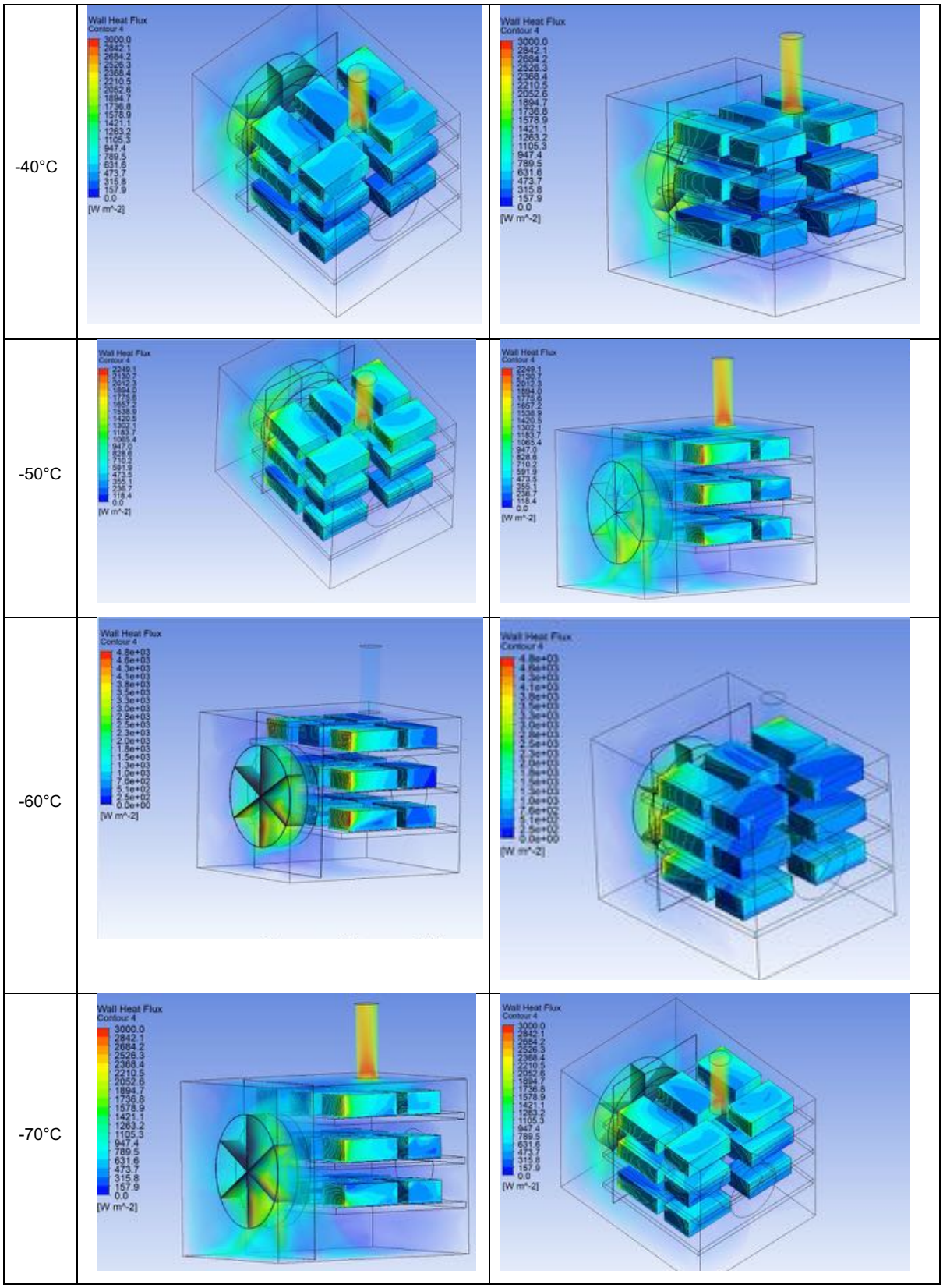

Figure 7-7: Thermal contour plot at 285RPM with double plasma bag layer

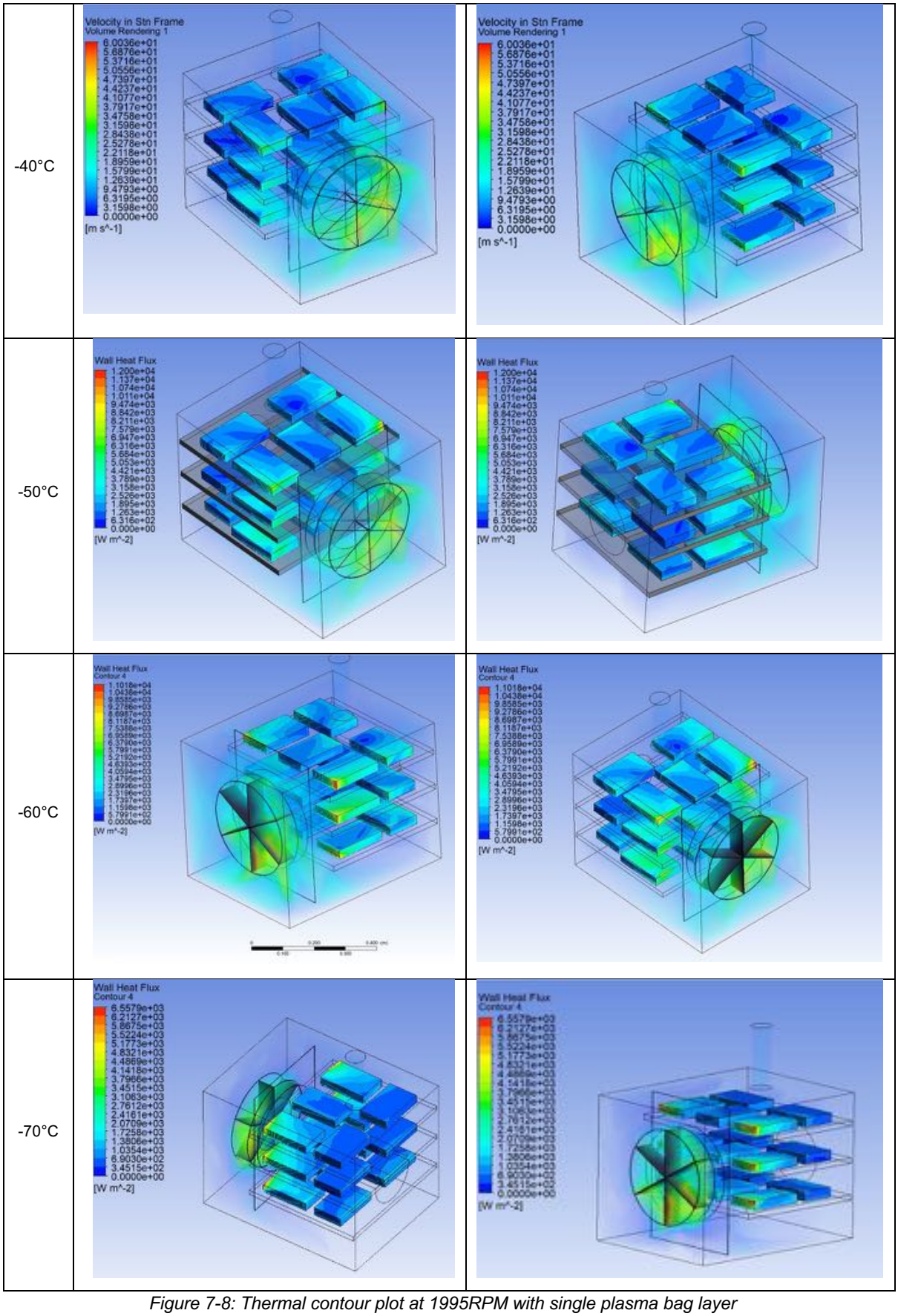

Figure 7-8: Thermal contour plot at 1995RPM with single plasma bag layer

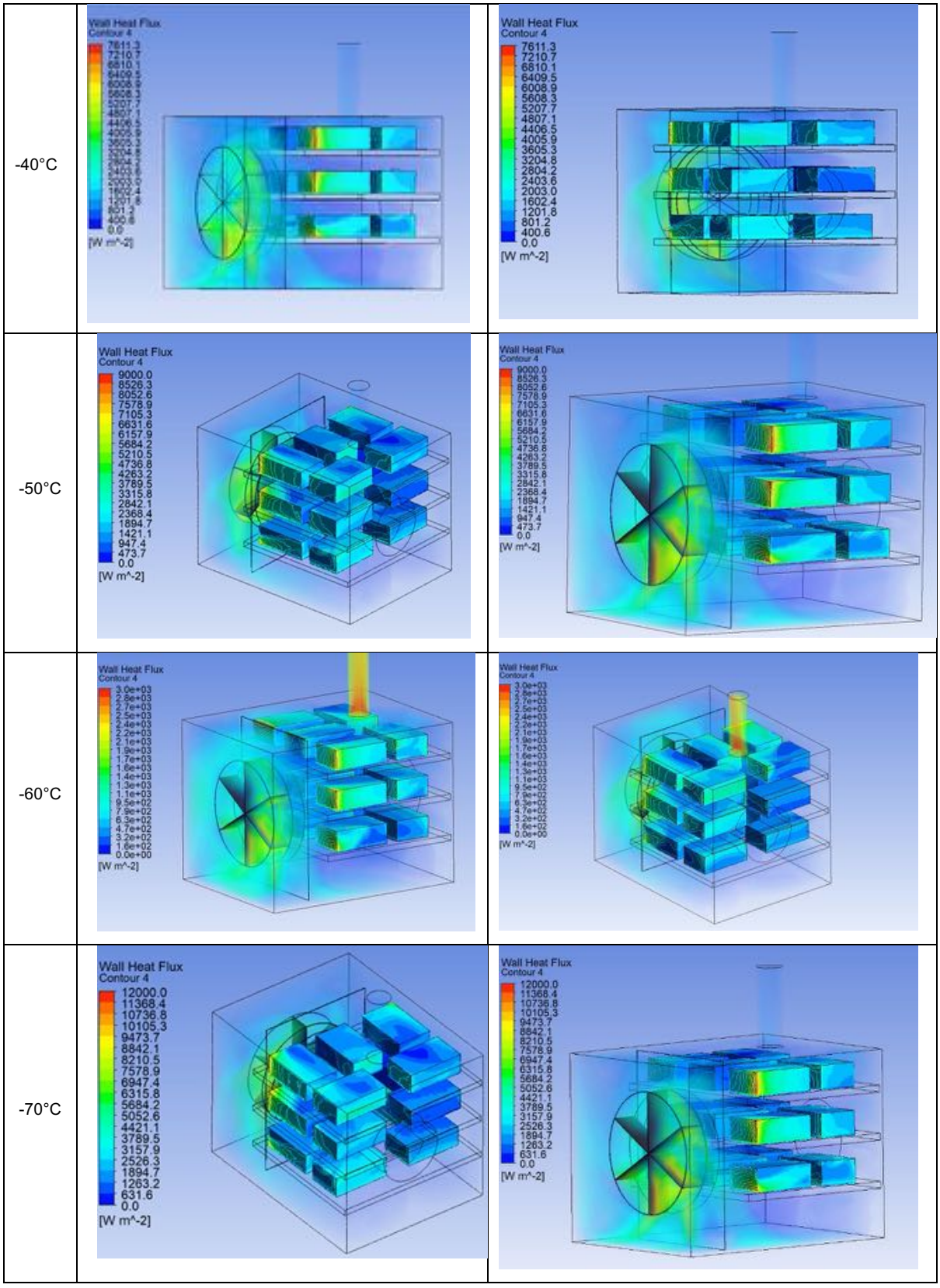

Figure 7-9: Thermal contour plot at 1995RPM with double plasma bag layer

7.1.5. Experimental Results

7.1.5.1. Determination of Velocity

The mapping of the velocity profile inside the chamber was conducted in a quadrant schematic, by using a grid system to characterise each section as shown in Figure 7-10 and defined in Chapter 5.

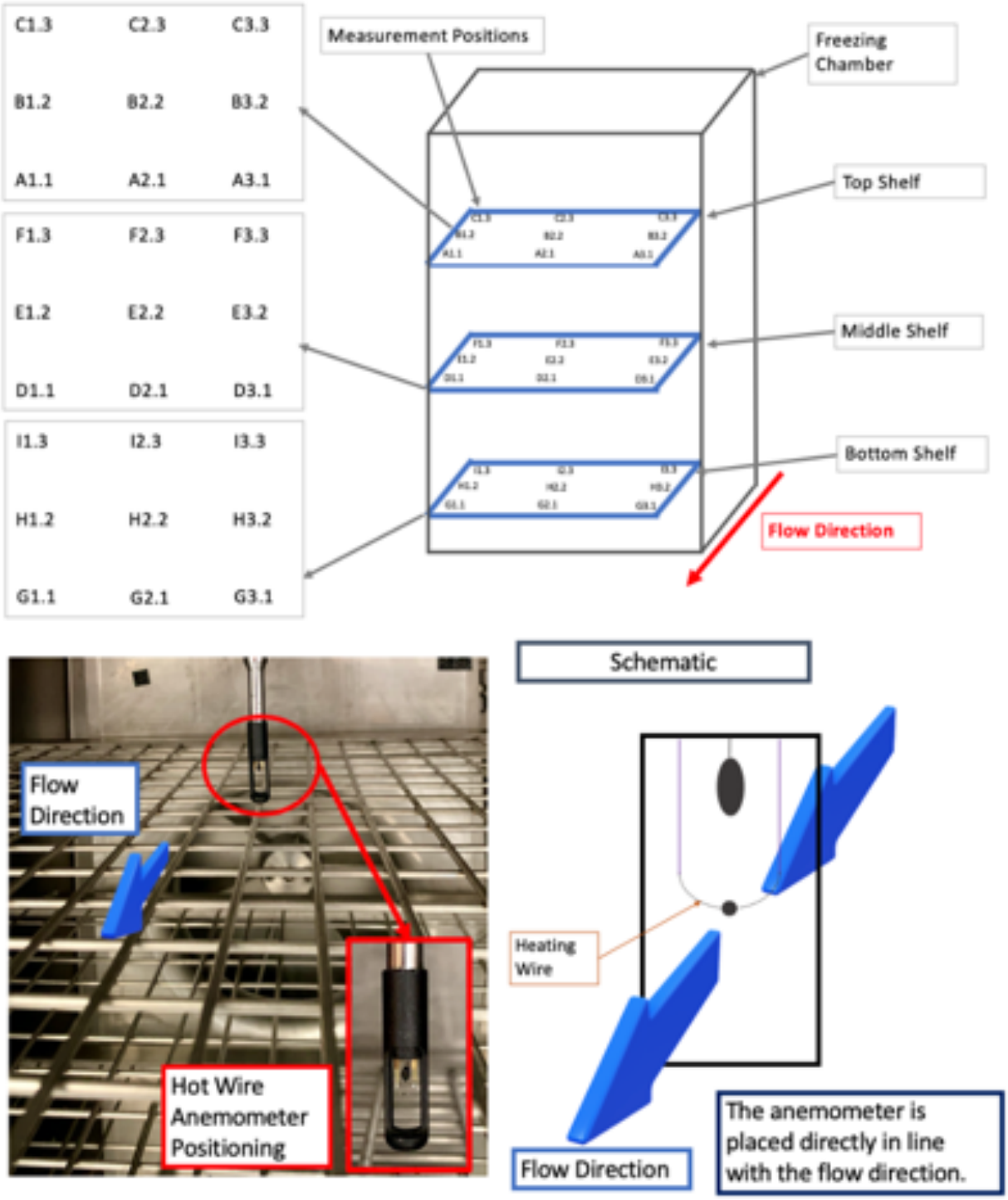

Figure 7-10: Grid Schematic for Velocity Positions

A Testo 425 hot wire anemometer was used to characterise the airflow around the chamber, positioned and secured in the locations highlighted in Figure 7-10. The characterisation of the chamber was conducted in both an empty and a full schematic at an ambient temperature. Table 7-5 presents the results from an empty chamber. The variation between the reading points is large, with the general trend being that the central flow field is comparatively higher than the edges of the shelves and chamber space (high velocities highlighted in red, and low velocities highlighted in blue). Locations such as C2.3 are between the injectors and away from the direct path of the fan, showing a significant decrease in recirculation. In comparison, location F2.3 indicates one of the highest recorded velocities as it is located directly along the flow field. Both locations within the grid system are identical, with the only variable being the change in elevation. The variation itself is evident between identical shelving positions and its relation to the elevation within the chamber. The trend appears for both the 285RPM and the 1995RPM cases.

	Empty Freezer			
	285 RPM (10hz)		**1995 RPM (70Hz)**	
	Loading Location	Velocity Reading	Loading Location	Velocity Reading
Top Shelf	C1.3	1.06 m/s	C1.3	7.24 m/s
	C2.3	0.68 m/s	C2.3	2.12 m/s
	C3.3	0.69 m/s	C3.3	2.10 m/s
	A1.1	0.62 m/	A1.1	3.03 m/s
	A2.1	0.72 m/s	A2.1	3.82 m/s
	A3.1	0.54 m/s	A3.1	3.79 m/s
Middle Shelf	F1.3	1.16 m/s	F1.3	4.12 m/s
	F2.3	1.31 m/s	F2.3	8.75 m/s
	F3.3	0.67 m/s	F3.3	3.86 m/s
	D1.1	0.50 m/s	D1.1	3.3 m/s
	D2.1	0.70 m/s	D2.1	3.92 m/s
	D3.1	0.39 m/s	D3.1	2.73 m/s
Bottom Shelf	I1.3	0.59 m/s	I1.3	4.54 m/s
	I2.3	1.41 m/s	I2.3	8.43 m/s
	I3.3	0.47 m/s	I3.3	5.46 m/s
	G1.1	0.42 m/s	G1.1	2.59 m/s
	G2.1	0.91 m/s	G2.1	4.88 m/s
	G3.3	0.49 m/s	G3.3	2.59 m/s

Table 7-5: Unloaded Velocity Results

In comparison, the fully loaded results show a similar flow pattern. The operation of the loaded section shows that the central locations of the system have the highest velocities. The planar sections of the system show an overall variable flow field with the front section of each shelf elevation. The variation itself highlights the deviation caused by obstacles. The comparison between unloaded data points demonstrates a larger difference in zone conditions. For example, the location C1.3 for an unloaded configuration at 1995RPM presents a recorded value of 7.24m/s, while the corresponding loaded value is 3.52 m/s. A similar relationship is highlighted with the large change in flow velocities in relation to elevation, as observed in the unloaded function.

	Full Freezer			
	285 RPM (10hz)		**1995 RPM (70Hz)**	
	Location	Velocity Reading	Location	Velocity Reading
Top Shelf	C1.3	1.77 m/s	C1.3	3.52 m/s
	C2.3	0.54 m/s	C2.3	3.66 m/s
	C3.3	0.71 m/s	C3.3	2.51 m/s
	A1.1	0.68 m/s	A1.1	3.64 m/s
	A2.1 (No Load)	0.44 m/s	A2.1 (No Load)	1.99 m/s
	A3.1	0.94 m/s	A3.1	2.75 m/s
Middle Shelf	F1.3	0.88 m/s	F1.3	5.72 m/s
	F2.3	1.53 m/s	F2.3	10.3 m/s
	F3.3	1.02 m/s	F3.3	4.84 m/s
	D1.1	0.51 m/s	D1.1	3.16 m/s
	D2.1 (No Load)	0.52 m/s	D2.1 (No Load)	2.61 m/s
	D3.1	0.73 m/s	D3.1	2.07 m/s
Bottom Shelf	I1.3	0.76 m/s	I1.3	4.41 m/s
	I2.3	1.64 m/s	I2.3	9.58 m/s
	I3.3	0.78 m/s	I3.3	3.74 m/s
	G1.1	0.44 m/s	G1.1	1.61 m/s
	G2.1 (No Load)	0.76 m/s	G2.1 (No Load)	4.24 m/s
	G3.3	0.56 m/s	G3.3	2.39 m/s

Table 7-6: Loaded Velocity Results

Figure 7-11 demonstrates the validation of the results for both CFD and experimental values. The validation of the velocity profile was based on a grid system shown in Figure 7-10, where the grid numbers reflect the positioning of an anemometer. The same points were exported into the CFD model, as a point of reference for data collection. The results highlight the

associated values for low RPM and high RPM values for a loaded chamber operation. The results reflect an over-prediction of the CFD values, but this can be due to a multitude of factors related to the turbulence model used, the associated boundary conditions, etc. Similarly, the discrepancies can be related to instrumentation errors. The results demonstrate an overall variation of 16% for a high RPM function, and an overall variation of 9% for a low RPM operation.

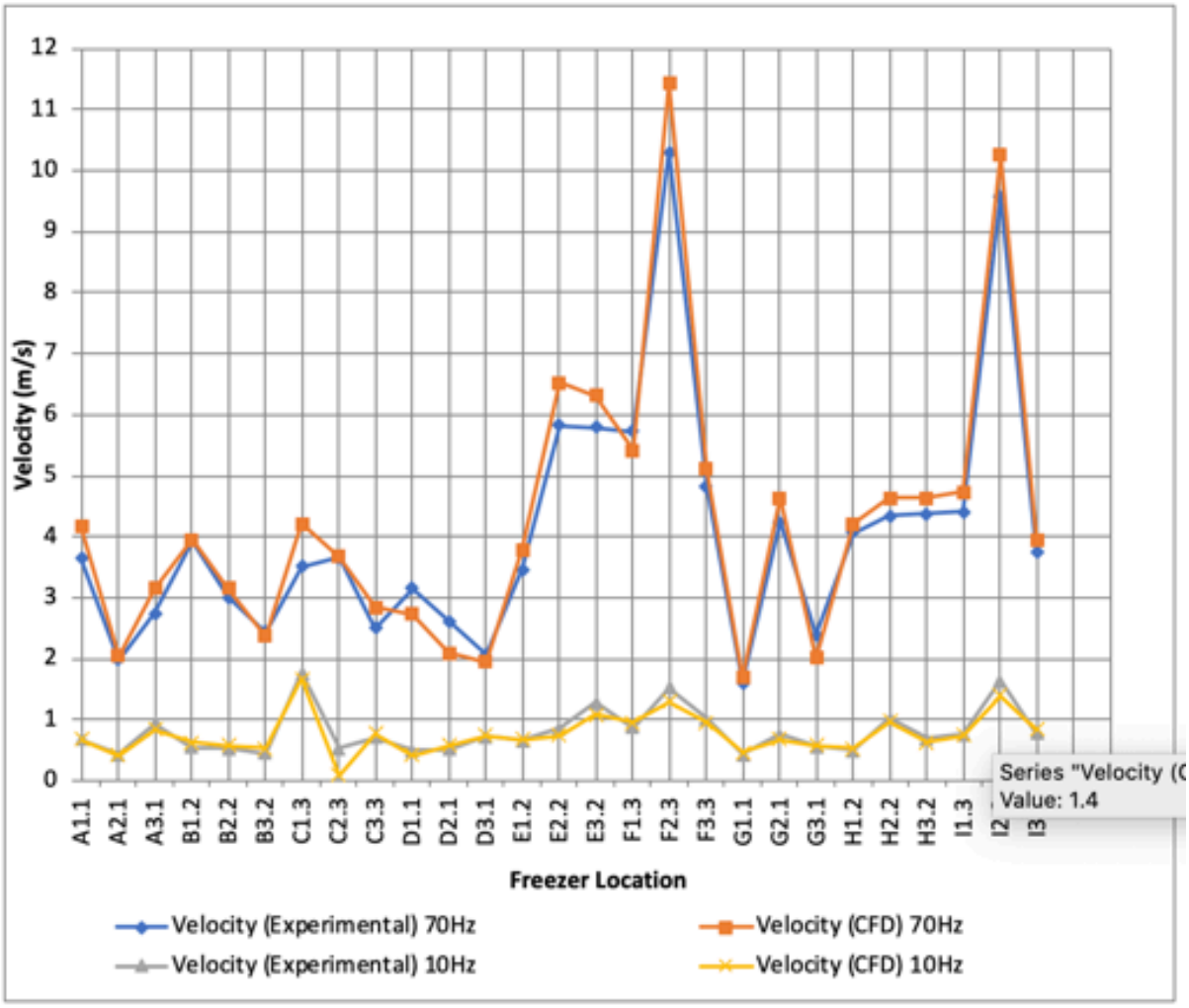

Figure 7-11: Velocity Validation

7.1.5.2. Plasma Temperature

The function of the injection-based batch freezer is based on an internal feedback system where the freezing rate is a fixed operation to achieve the set point nitrogen temperature. The freezing curve of the plasma bag is defined in Figure 7-12. The initial conditions of the plasma bag were at ambient conditions before being loaded into the freezing chamber. The overall trend of the operation shows a steady decline to the set point temperature. The data reflect an area of stagnation at the point where phase change occurs. The stagnation in the data reflects the transfer of latent heat, where the initial conditions were primarily sensible heat.

The data highlight the extent of thermal variation where C1.3 has the fastest decline of the set point with the minimal phase change time. The location of the plasma bag itself is close to the injector indicative of the rapid temperature decline. The variation is evident with location I1.3 being the most prolonged freezing time, the positioning of this plasma bag is indicative of this result. The position of i1.3 is located on a bottom shelf furthest away from the injector and, as a result, this places the plasma bag in a detrimental thermal position and, consequently, a reduced convective effect.

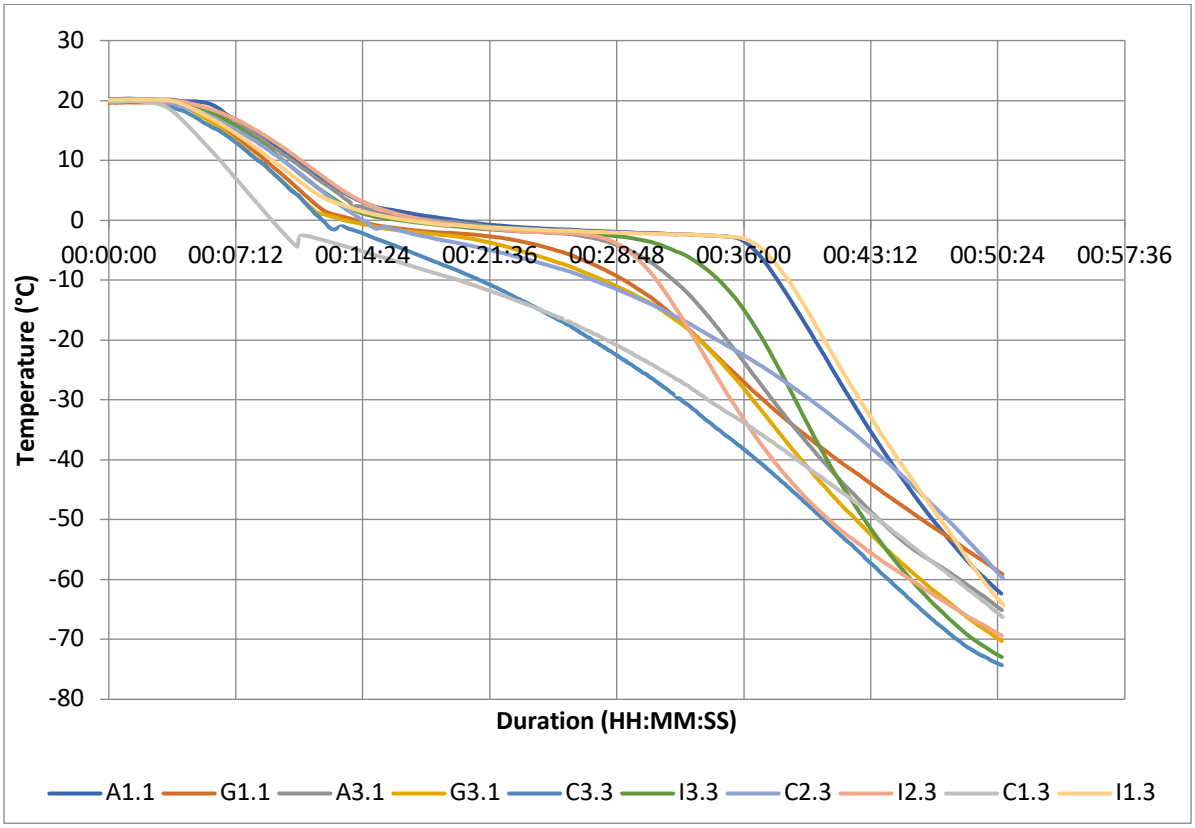

Figure 7-12: Plasma bag freezing curve overview to a set point of approximately -60°C.

Zone A.

The definition of zone A is determined by Figure 7-10, where the location is on the top level behind plasma loading zone C. Because of its location, it is evident that the zone will experience a lower heat transfer rate due to being located in the wake of an adjacent plasma bag. The location of the plasma bag load can be determined by the positioning of the plasma bag near the extremities of the system and towards the exhaust. Both CFD and experimental values show very similar trends, with the CFD values showing a maximum under-prediction of 12.4% but following the overall trend of the experimental data. Both experimental and CFD results show a prolonged horizontal period when the core temperature reaches freezing point due to the transfer of latent heat to the surroundings. Zone A is also located near the exhaust and influenced by the vacuum properties created by the exhaust during operation. The thermal effects of the glycerine-filled bags at these locations are discussed in section 7.1.4 with the

aid of contour plots. The variation in temperature between zone A1.1 and zone A3.1 is due to the positioning of each bag, despite them being in the same zone. The temperature variation between both bags highlights the effect of the exhaust suction, with zone A1.1 being most affected by the exhaust causing a delayed freezing to reach the desired set point. Both sets of experimental and CFD data show a steady and smooth decline in temperature.

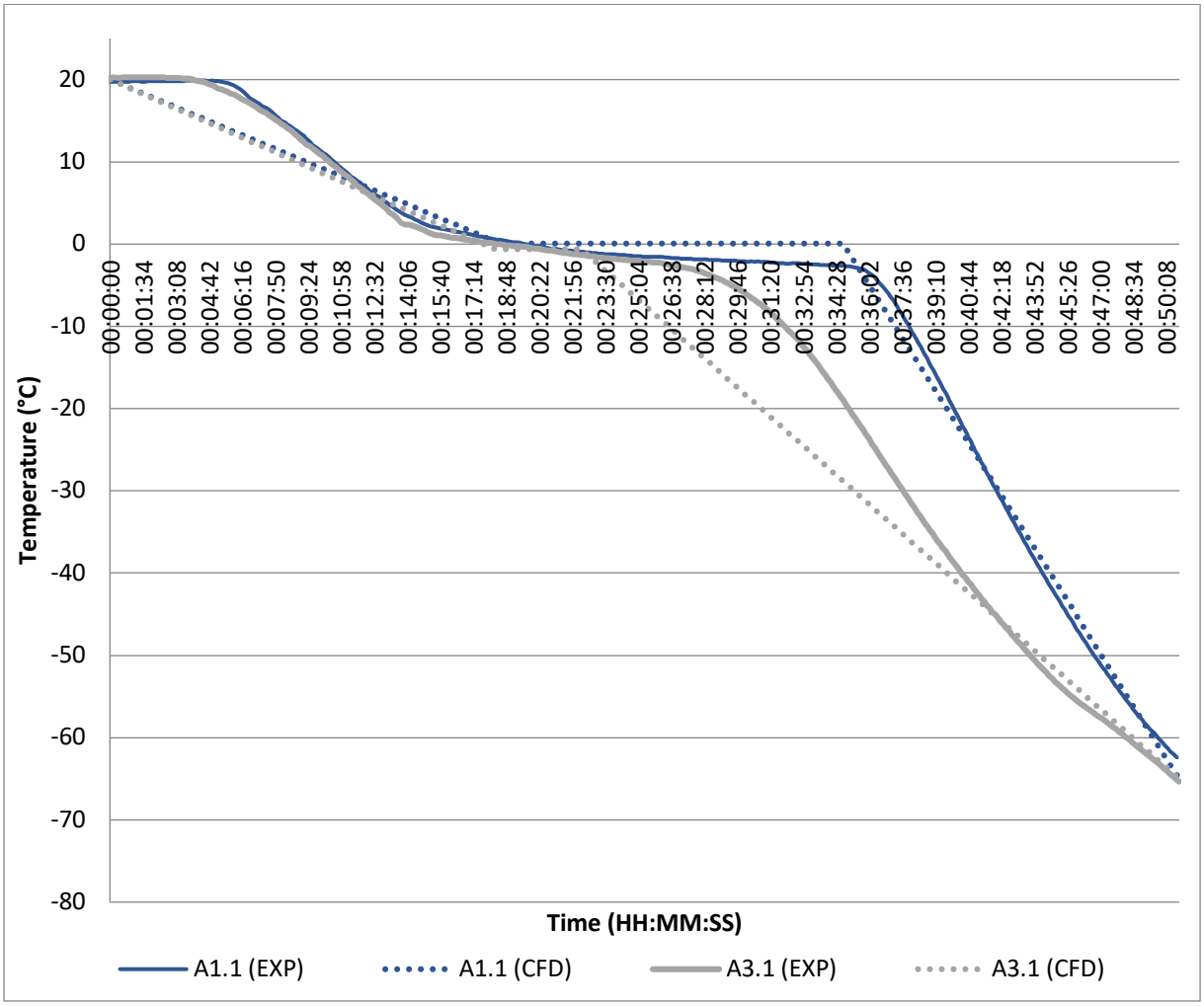

Figure 7-13: Experimental and CFD freezing curve for Zone A

Zone C.

The positioning of loads in zone C is shown in Figure 7-10. Zone C is located closest to the injectors on the top shelf. The experimental data show a singular sharp spike in temperature due to the increase in injection resulting in droplets interacting with the surface of the bag, as shown in Figure 7-14. The CFD data for zones C1.3, C2.3 and C3.3 do not reflect this spike in temperature due to the UDF applied to the load in zone C. The UDF implies a phase change point which is significantly higher than the experimental data. As the UDF is based on an arbitrary freezing curve, a level of variation exists during the phase change stage. The

experimental results reflect a sudden but small spike in temperature due to the proximity to the injectors. The results highlight a steady decrease. Similar to previous results, the UDF does not highlight the horizontal period experienced experimentally at the start of the test. The lack of horizontal period reflected in the experimental data implies a quicker transfer of latent heat in the specific area. The temperature difference between experimental and CFD data highlights a smooth decline to the set point temperature. The CFD UDF utilised over-predicts the freezing pattern for zones C2.3 and C3.3. The average variation between the loading conditions to reach the set point temperature has a maximum difference of 52.5% and 45.5% for zones C2.3 and C3.3, respectively, in comparison to 27.2% in zone C1.3. The over-prediction is more pronounced in the results for the phase change point to the set point.

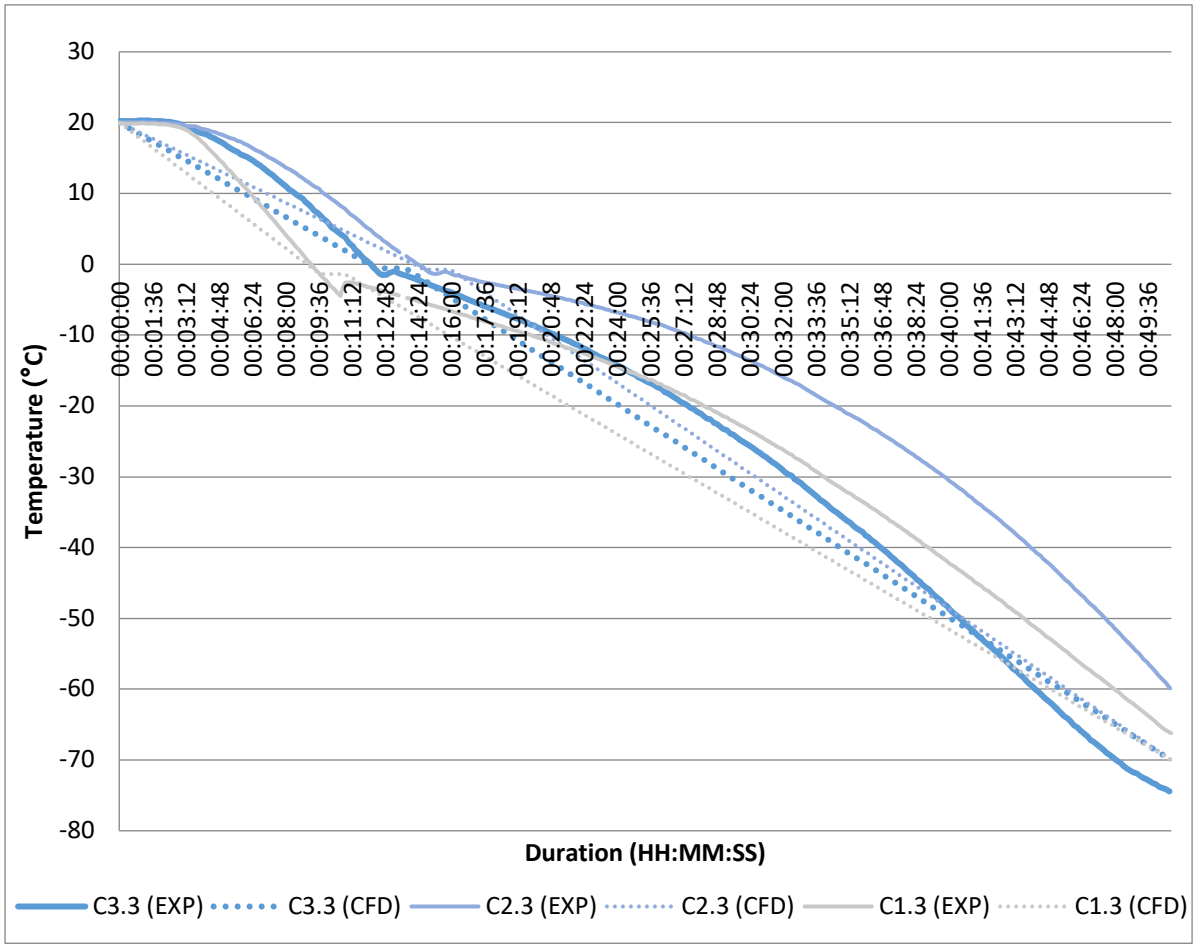

Figure 7-14: Experimental and CFD freezing curve for Zone C

Zone G.

The location of zone G is shown in Figure 7-10, indicating the position of the glycerine-filled blood bags. The relative location of Zone G is on the bottom shelf, located close to the freezer door, which will experience a level of leakage of ambient temperature air. The freezing curve of the bags is shown in Figure 7-15 for both experimental and CFD data. The loading position

in comparison to zone A follows a similar trend due to the proximity between both zones. The data reflect the progressive decrease to the set point temperature without sudden temperature spikes. The UDF applied to zone G highlights a prominent over-prediction in zones G1.1 and G3.1. The maximum over-prediction between the experimental and CFD results for zone G1.1 is 55%, in comparison to G3.3 with an over-prediction of 69%. Both zones reflect a steady decline to the set point temperature. The location of zone G itself is towards the back of the system and indirectly placed from the exhaust system. The steady decline is reflected in the location as the thermal variations experienced with suction are significantly reduced for both sets of data. The lack of suction also allows recirculation to occur in the area and in the bottom shelf. This is evident due to the relatively shorter horizontal period reflecting an increased transfer in latent heat between the gas and glycerine filled bags. As experienced with all numerical simulations, a level of difference will always exist between numerical prediction and the obtained experimental results.

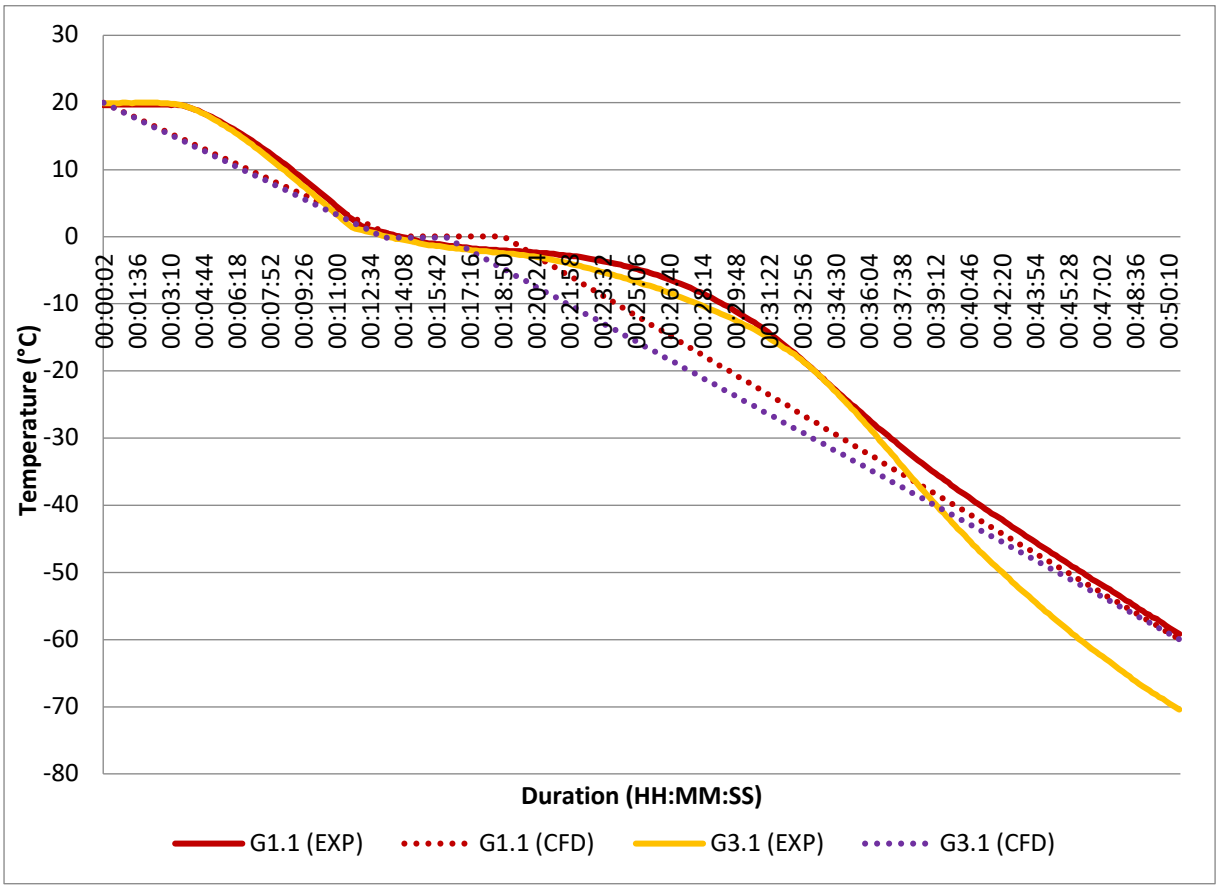

Figure 7-15: Experimental and CFD freezing curve for Zone G

Zone I.

Similarly, to zone G, zone I is located directly beneath zone C and follows an identical loading pattern as shown in Figure 7-10. Figure 7-16 depicts both CFD and experimental sets of data.

Zone I is located just under the injector. Both CFD predictions for zones I2.3 and I3.3 highlight a reasonably significant over-prediction with a maximum difference of 46.5% and 96.1% between CFD and experimental results. Unlike previous data sets, a small amount of under-prediction exists in Zone I2.3 between -22°C and -70°C, which may be due to the assumption of a steady decline to the set point temperature. Unlike zone C, the freezing curve of zone I shows a horizontal trend in which transfer of latent heat is occurring. As the glycerine-filled bags are located furthest away from the exhaust, the relatively prolonged freezing time may be due to the poor recirculation within the region. This trend is discussed in section 7.1.5.1, showing an increased temperature along the upper surface of the bags highlighting a region of poor recirculation. The region of poor recirculation is evident because of the temperature variation between each zone shown in section 7.1.5.1. The recirculation primarily affects the transfer of latent heat but, after the freezing point has been reached, the zone experiences a rapid decrease in temperature to the set point.

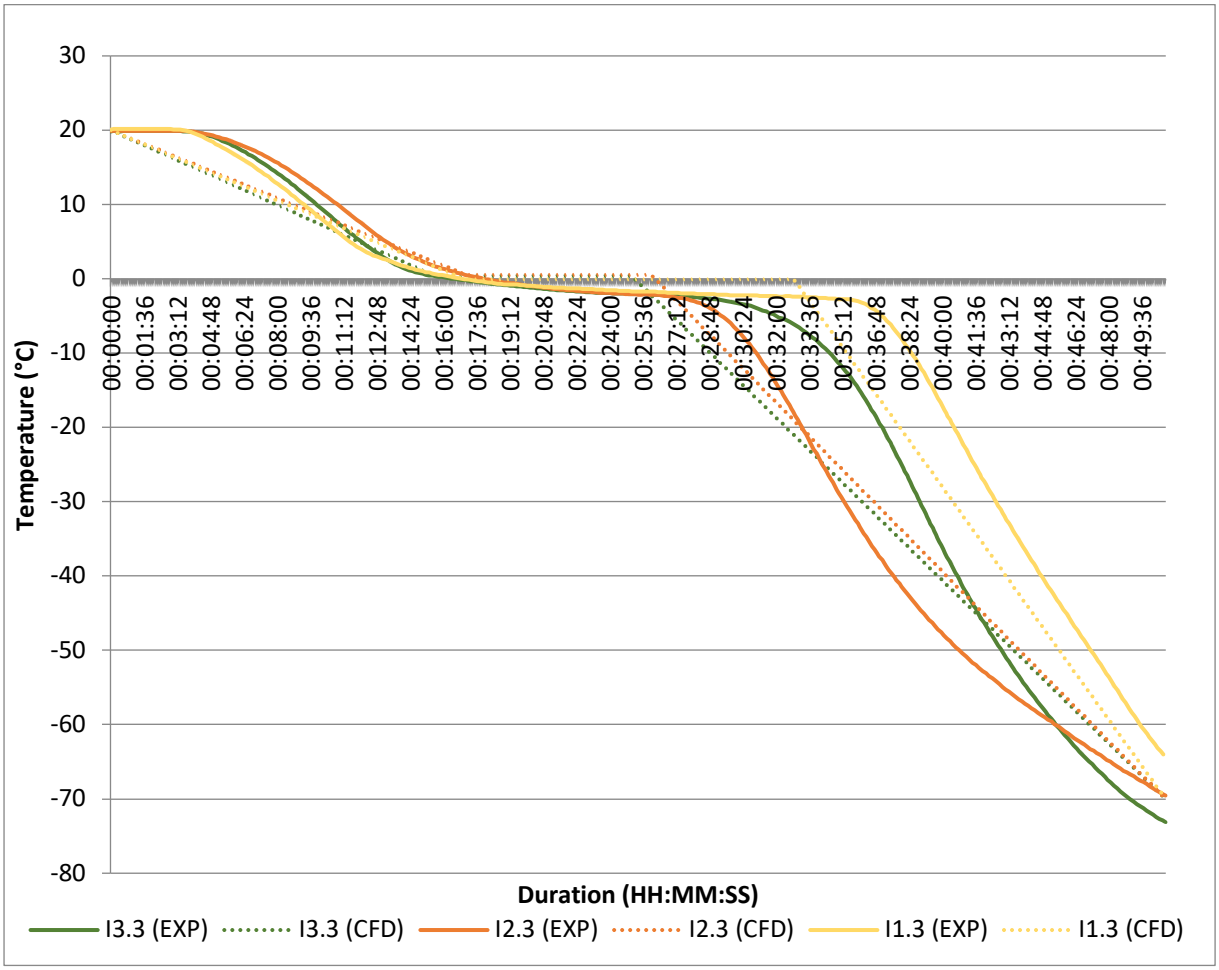

Figure 7-16: Experimental and CFD freezing curves for Zone I

7.2 Heat Pipe Model

7.2.1. Model Geometry and Mesh

The developed geometry is based on the design explained in section 3.4.9 and shown in Figure 7-18. The heat pipe contains only the heat pipe section, where the cooling coil has been omitted due to the two-phase process not being modelled. A three-dimensional model was developed based on the previous chamber geometry, with the latest addition being the copper heat pipe, shown in Figure 7-18. Table 7-7 shows the material properties used within the simulation.

Cell Zone	Simulation Property
Plasma Bag	PHT with DEHP plasticiser
Freezing chamber walls	Stainless Steel
Loading Shelves	Stainless Steel
Fan	Stainless Steel
Separation Plate	Stainless Steel
Heat Pipe	Copper

Table 7-7: Geometry Material Definition

The development of the mesh was conducted in ANSYS Meshing, to form an assembly mesh following a similar procedure to that discussed in section 7.1.1. The mesh accounts for an effective representation to simulate the convective effects of the model. A parametric study was conducted where an array of mesh densities was investigated alongside the change in cell style. Table 7-8 shows the results for the mesh independence study. The results highlight the justification for a tetrahedral mesh. The results show similar skewness values for each respective cell type. The main difference between the cells is the level of flexibility required to model the complex geometry of the heat pipe, where a tetrahedral mesh has the advantage. As both cells are similar, the difference between a fine tetrahedral and a hexahedral mesh is minimal. The final produced mesh is shown in Figure 7-19.

Level	Number of Cells	Cell Type	Skewness	Time per Iteration
Coarse	762,272	Hexahedral	0.6	5-7s
Coarse	898,281	Tetrahedral	0.52	5-7s
Medium	1,586,454	Hexahedral	0.55	9-11s
Medium	1,787,468	Tetrahedral	0.62	9-11s
Fine	2,578,448	Hexahedral	0.47	10-15s
Fine	2,687,672	Tetrahedral	0.44	10-15s

Table 7-8: Mesh Independence Study Results

A convergence study was conducted to evaluate the accuracy of the assembly mesh. The mesh was evaluated at different cell types and cell densities, as shown in Figure 7-17. The assembly mesh was evaluated against the outlet temperature, which acts as an independent variable, the outlet temperature will determine the level of heat transfer occurring for each mesh density. The data shows the increase in outlet temperature as the cell density increases. The tetrahedral data shows less than 1°C in comparison to hexahedral data. The added advantage of flexibility allowed the usage of a tetrahedral mesh. Both cell types show a flat profile, highlighting the maximum accuracy of a mesh has been achieved. As the simulation is heavily dependent on boundary conditions, a level of variation between the mesh density and the observed experimental values is expected.

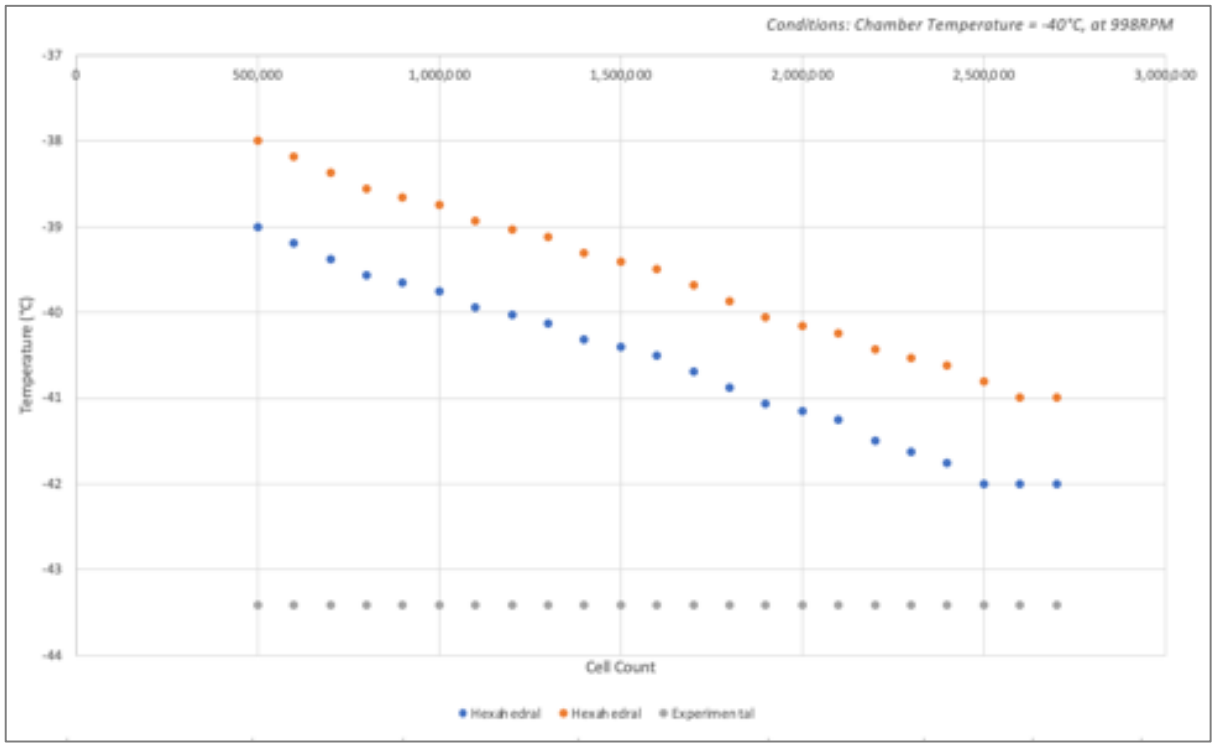

Figure 7-17: Mesh convergence study results

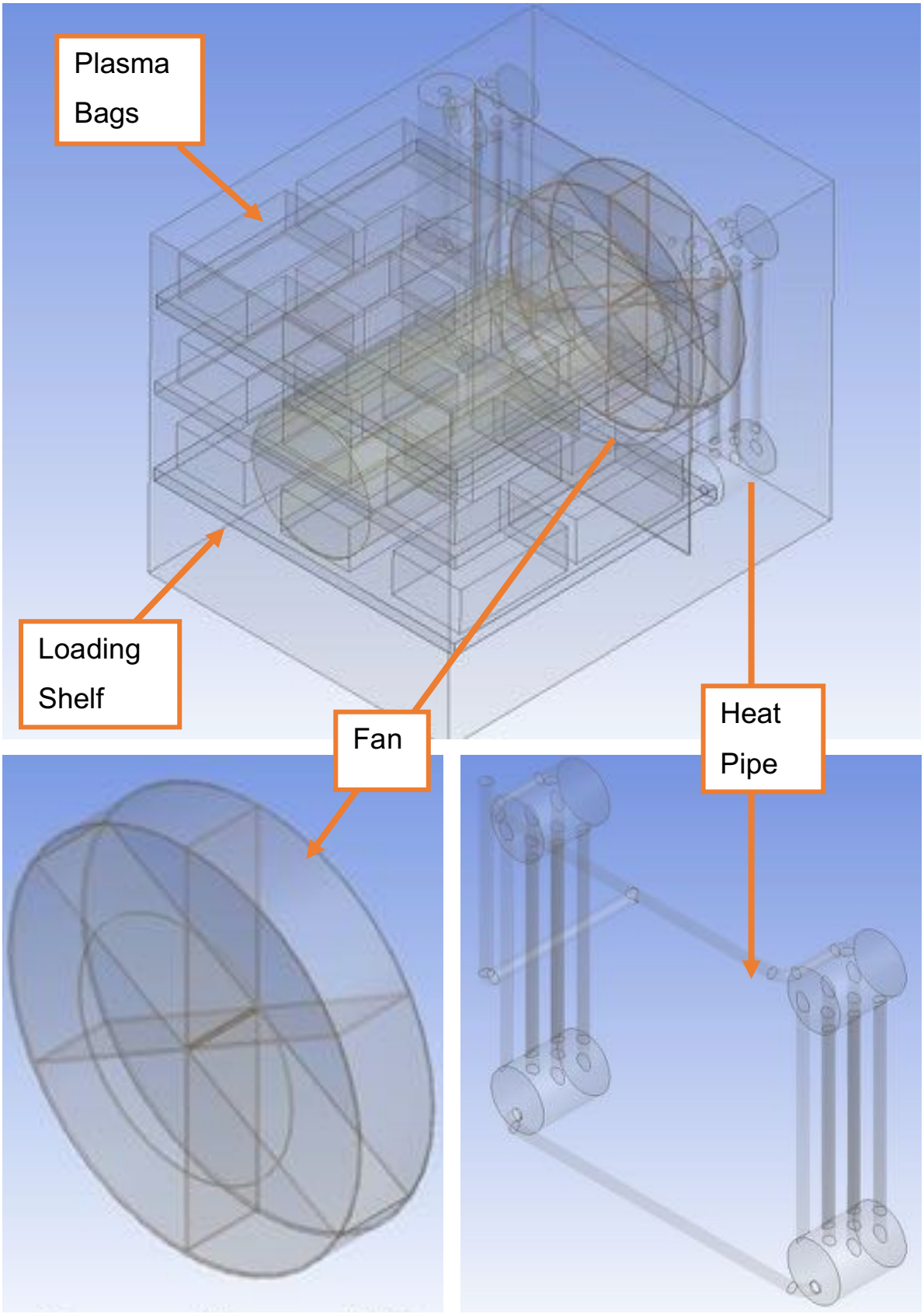

Figure 7-18: Geometry of Heat Pipe based Batch Freezer

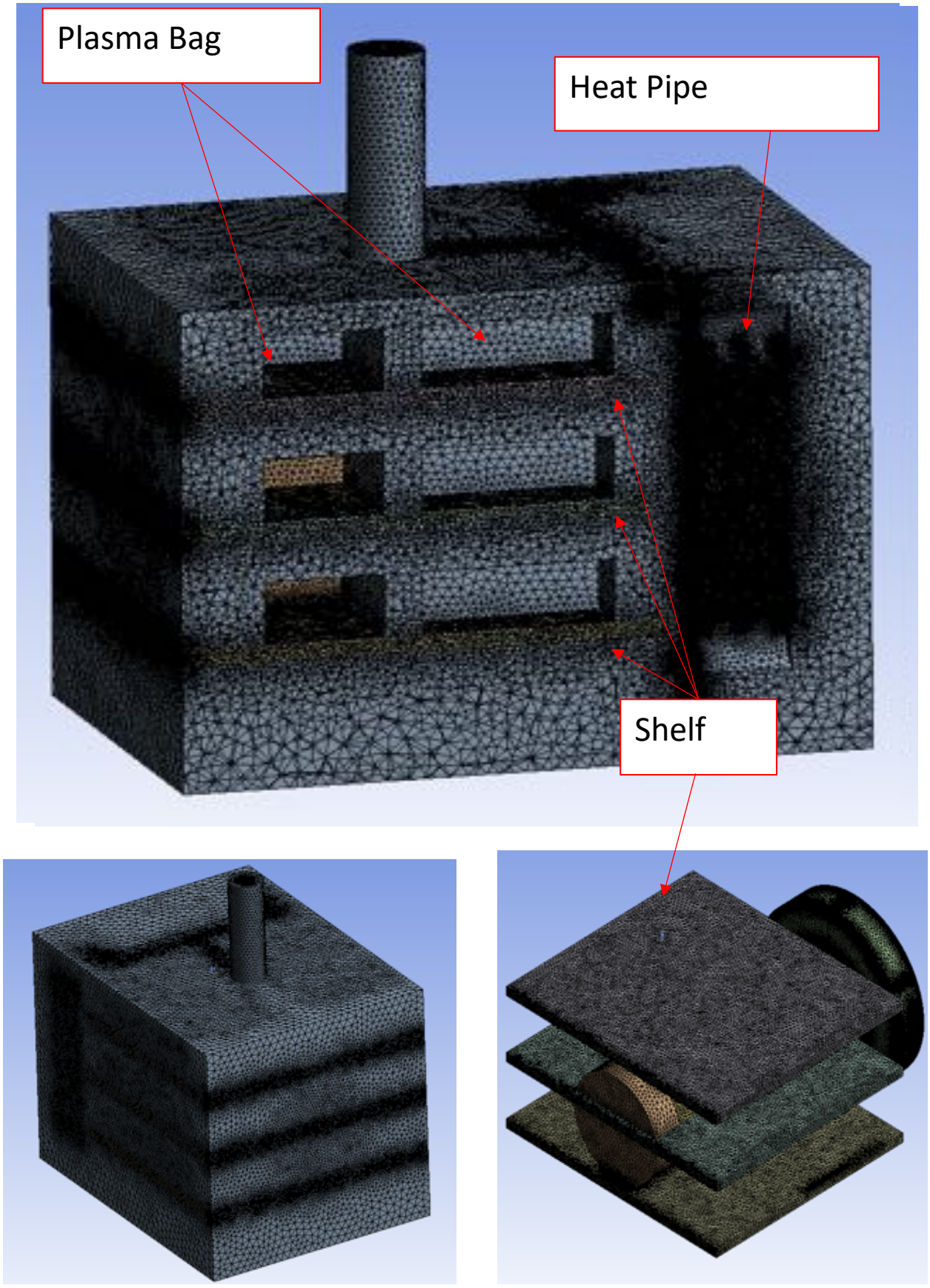

Figure 7-19: Final Developed Mesh

7.2.2 Boundary Conditions

The selection of boundary conditions is similar to that listed in section 7.1.2, where the decline in temperature is related to a function of time. The function is dependent on the average time to freeze plasma. As the proposed heat is an initial model, the UDF has been adapted to account for the prolonged freezing time. The adapted UDF is shown in Figure 7-20.

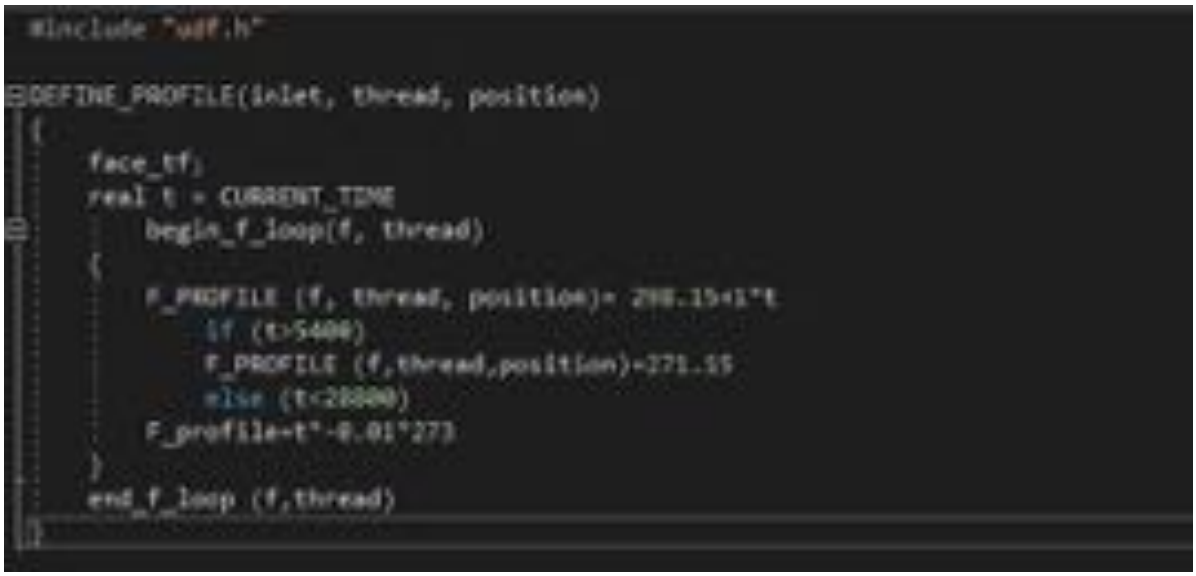

Figure 7-20: Adapted UDF

The definition of cell zones is identical to the initial injection model. The cell zone contains the addition of a defined heat pipe zone, where the material properties of the heat pipe can be defined. The integration of the heat pipe and the associated thermal model can be simulated through conjugate heat transfer. The basic premise of conjugate heat transfer involves the definition of the interaction between liquid and solid with the consideration of conduction and convection for multiple bodies. The thermal conductivity of the heat pipe has been set a value based on the resistances defined in Chapter 4. Table 7-9 and Table 7-10 define the allocated cell zones and boundary conditions.

Property	**Condition**
Exhaust	Outflow
Body Wall	Wall
Separation Plate	Wall
Plasma Bag	Wall
Heat Pipe	Wall

Table 7-9: Heat pipe CFD model boundary condition

Cell Zone	Condition
Fan	MRF
Fan Fluid	Interior
Chamber	Interior
Shelf	Porous Wall
Heat Pipe	Interior

Table 7-10: Assigned boundary conditions

Similar to the boundary conditions listed in section 7.1.2, the simulation operates on a transient schematic where the time step is fixed and dependent on the decline in temperature. The turbulence model applied remains as the realizable k-epsilon model, where a scalable wall function was applied to improve the stability for near wall flows. The simulation was solved using a SIMPLE algorithm, which couples pressure and velocity. A second order discretisation was applied for the momentum and energy equations with a standardised pressure function. The assignment of wall boundary conditions is similar to those presented in section 7.1.2. The assigned boundary conditions remain as no-slip boundary conditions, where the chamber walls are considered to be adiabatic. The start-up of the system including the definition of the heat pipe is assumed to be ambient at approximately 20°C.

7.2.3 Flow Visualisation of CFD Results

The velocity mapping of the heat pipe-based system was simulated in both a loaded and an unloaded chamber to investigate the change in flow fields, similarly to the injection-based system. Figure 7-21 and Figure 7-22 shows the flow field of the system at 498 RPM (10Hz) and 997RPM (70Hz), reflecting both minimum and maximum operation of the fan. The initial unloaded simulations show an overall uniformly distributed flow, with a level of disruption due to the flow over tube bundles, in comparison to the injection system where both fan contours have similar recirculation patterns. The difference highlighted in Figure 7-21 and Figure 7-22 reflects the change in streamlines between single and double layers. The difference between both layers is similar to those presented in section 7.1.3. The results reflect an increase in resistance as the flow passes over each load. Given the trends depicted in Figure 7-21 and Figure 7-22, it will be evident that the plasma bags located in series will face a similar poor heat transfer.

Single Layer	Double Layer
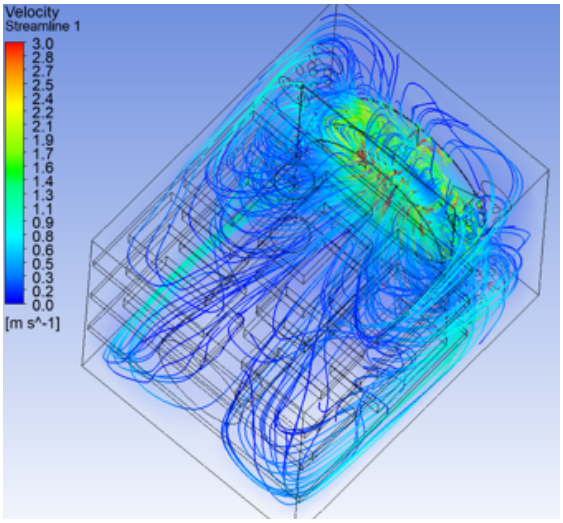	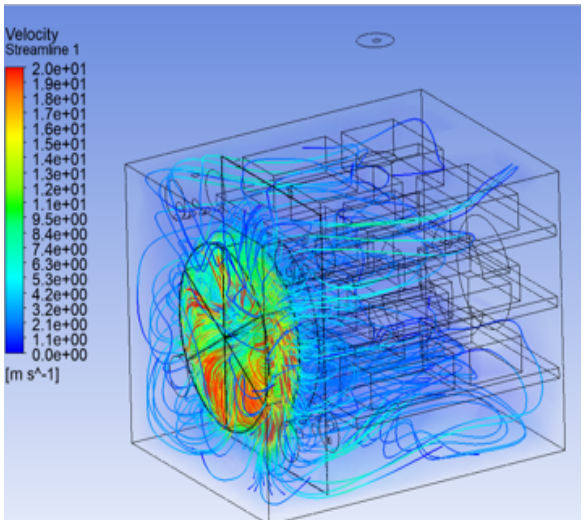
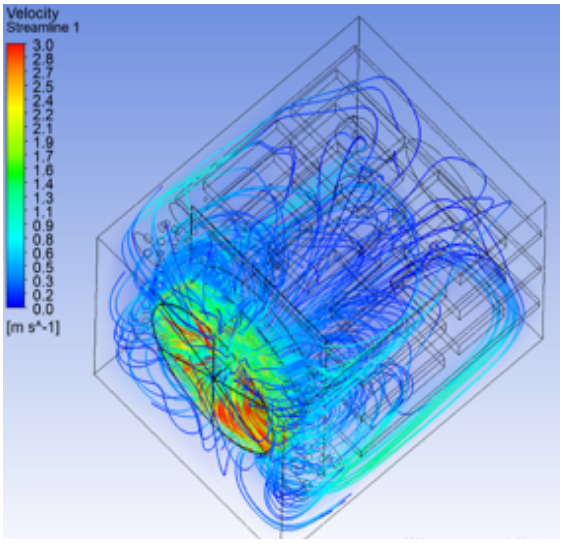	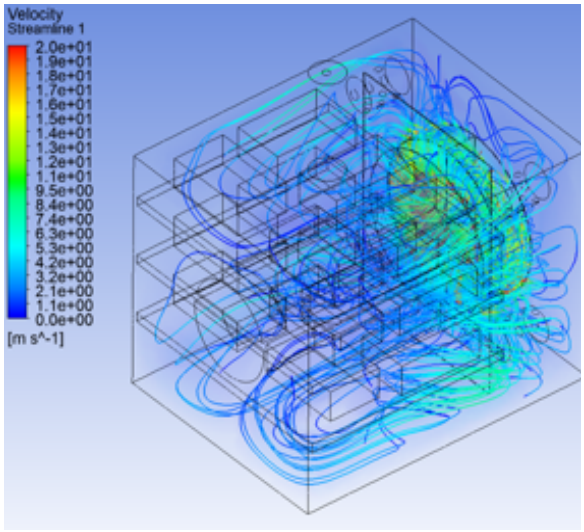

Figure 7-21: Velocity streamlines at 498RPM- heat pipe model

Single Layer	Double Layer
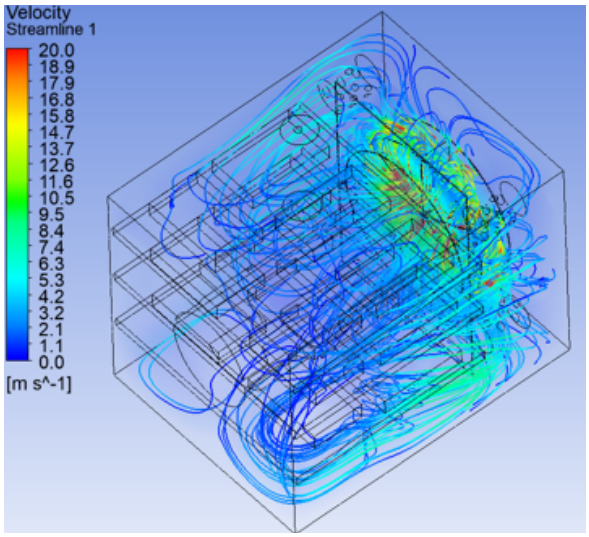	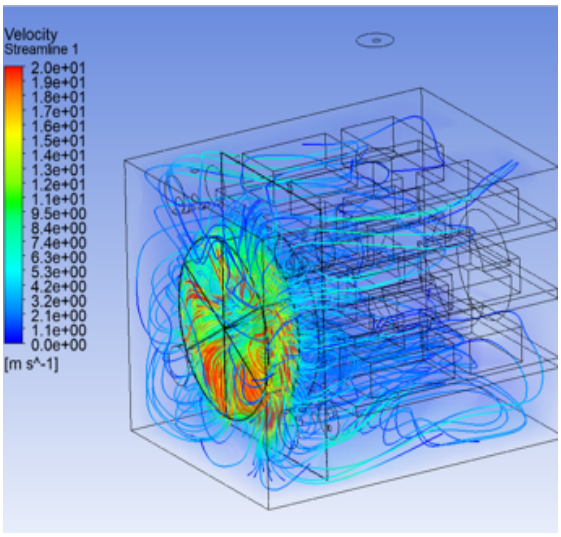
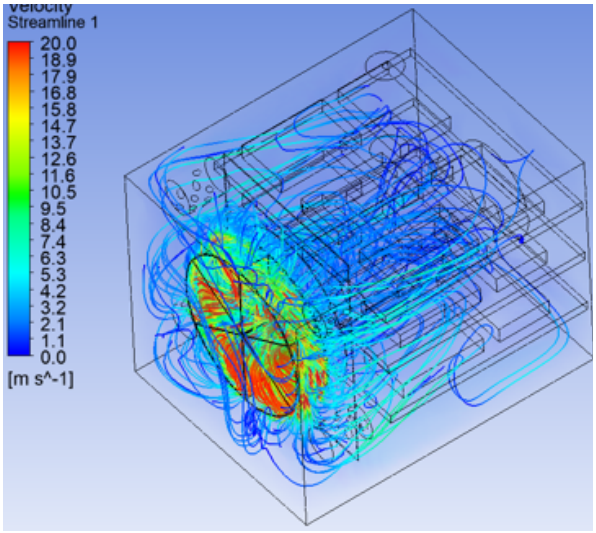	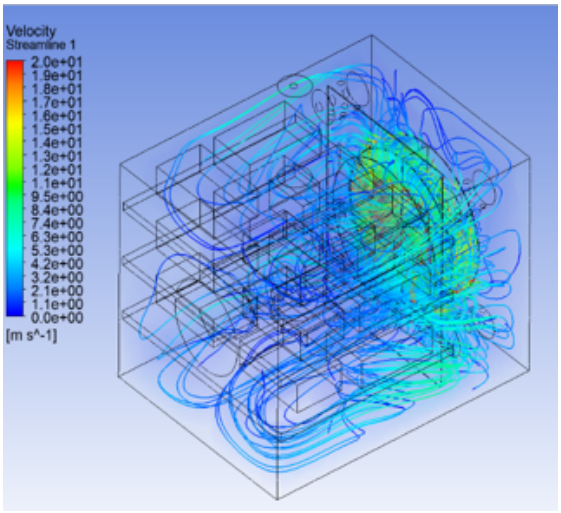

Figure 7-22: Velocity streamlines at 997RPM- heat pipe model

7.2.4 Thermal Variation of Plasma bags

The heat pipe prototype batch freezer is based on an external controller module which controls the nitrogen feed in relation to the exhaust temperature. Similar to the injection system, the heat transfer is mainly due to the convective effects which occur due to the forced convection of the fan. The loading follows a similar schematic described in section 7.1.4, where a single layer will be investigated until a set point of -70°C. The results reflect a lack of high heat flux located at the corners of the plasma bag, due to the lack of liquid nitrogen droplets. Without nitrogen injection, the air remains within the freezing chamber.

Figure 7-23 shows the results obtained from -40°C to -70°C at 498RPM at a single loading configuration. The results highlight a level of homogenous temperature distribution across the plasma bag. The high heat flux prevalent in the injection-based model has been eliminated, due to the steady operation of the heat pipe, where the temperature distribution is no longer dependent on injection frequency. The temperature variation throughout the system as a whole highlight a difference between the plasma bags located in zone A, which are unlike Zone C. The main discrepancy follows a similar trend for plasma bags placed in series. As the plasma bags in zone A are located in the wake stream of plasma bags in zone C, the velocity stream flowing around the plasma bag is significantly lower. The lower velocity stream also results in reduced convective effects. In comparison, the effect of wake zones is evident where the thermal variation exists throughout a single plasma bag. The plasma bags location in zones A, D and G highlight a discrepancy where half the plasma bag is in-line with the flow, but due to their orthogonal placing, the temperature distribution is uneven. A similar relation exists between the shelves, as the injections are no longer in concentrated trajectories, and as the heat pipe is relatively isothermal, these concentrated streams are eliminated. The thermal variation across each shelf is significantly lower. Similarly, the areas located in a higher velocity zone, shows a significantly high heat transfer due to the increase in convective effects. As the flow exiting the fan structure occurs past the separation point, the plasma bags located in this region reflect a significantly higher heat flux.

Figure 7-24 shows the results of a higher thermal load, where the plasma bags are stacked. The results reflect contour plots between -40°C and -70°C, at a minimum fan operation at 498 RPM. The plasma bags highlight a similar trend to an injection-based system, where the additional layer increases the thermal resistance within the chamber. The plasma bags show a similar trend with minimal high heat flux at their corners, due to the lack of liquid nitrogen injections. The relationship between the top and bottom plasma layers highlights a level of homogeneity, where the main discrepancy lies between the first and second rows of plasma bags. Due to the increase in thermal load and the increased flow resistance, the discrepancy

is inevitable. The relationship between shelf position and plasma row is evident, where zones C, F and I depict similar relationships due to the isothermal properties of the heat pipe and the symmetrical fan flow streamlines.

Figure 7-25 highlights a single layer plasma loading configuration at 997 RPM, at maximum fan operation. The plots reflect the heat flux between -40°C and -70°C. The contour plot highlights a similar trend to Figure 7-23, terms of thermal distribution, and reflect an increased heat transfer coefficient in comparison to Figure 7-23 due to the increase in convective effects. The contour plots shown in Figure 7-25, reflect an overall thermal variation occurring on each shelf, where the plasma bags located towards the heat pipe experienced significantly less variation in comparison to the plasma bags located behind. As previously discussed, this may be due to the positioning of the plasma bag being in the wake stream of an adjacent plasma bag. Compared to the plasma bags in series, the plasma bags located in the wakes suffer due to the lack of convective effects, which is an evident trend throughout the shelf loading positions. In comparison to a single stack operation, the higher heat flux shown in the thermal contours are a result of the significantly cooler air past the separation point. As the plasma bags with higher flux are located close to this separation point, the localised increase transfer leads to an asymmetric heat flux profile.

Figure 7-26 shows a double layered schematic at 997 RPM. The contours depict the heat flux from -40°C to -70°C. The plasma bags reflect a similar trend to Figure 7-24, where the plasma bags towards the heat pipes and the annulus of the fan experience a uniform heat flux. Zones C, F and I are located closer to the heat pipe and along the flow stream of the freezing chamber. The effect of an additional thermal load layer reflects an increase in resistance from both a thermal and flow distribution aspect. Figure 7-26 reflects the general consensus previously discussed, where locating a plasma bag in the wake stream is detrimental. The onset effect of an uneven heat transfer regime risks uneven freezing, which can be detrimental to the processing of blood plasma. The increase in fan rotation, increases the overall heat transfer due to the increase in convective effects. As a result of this, localised wall heat flux points are significantly higher in comparison to the 285RPM operation. The double layer configuration highlights a similar trend to previous configurations, as the plasma bags located closest to the separation plate, experienced a significantly higher heat flux.

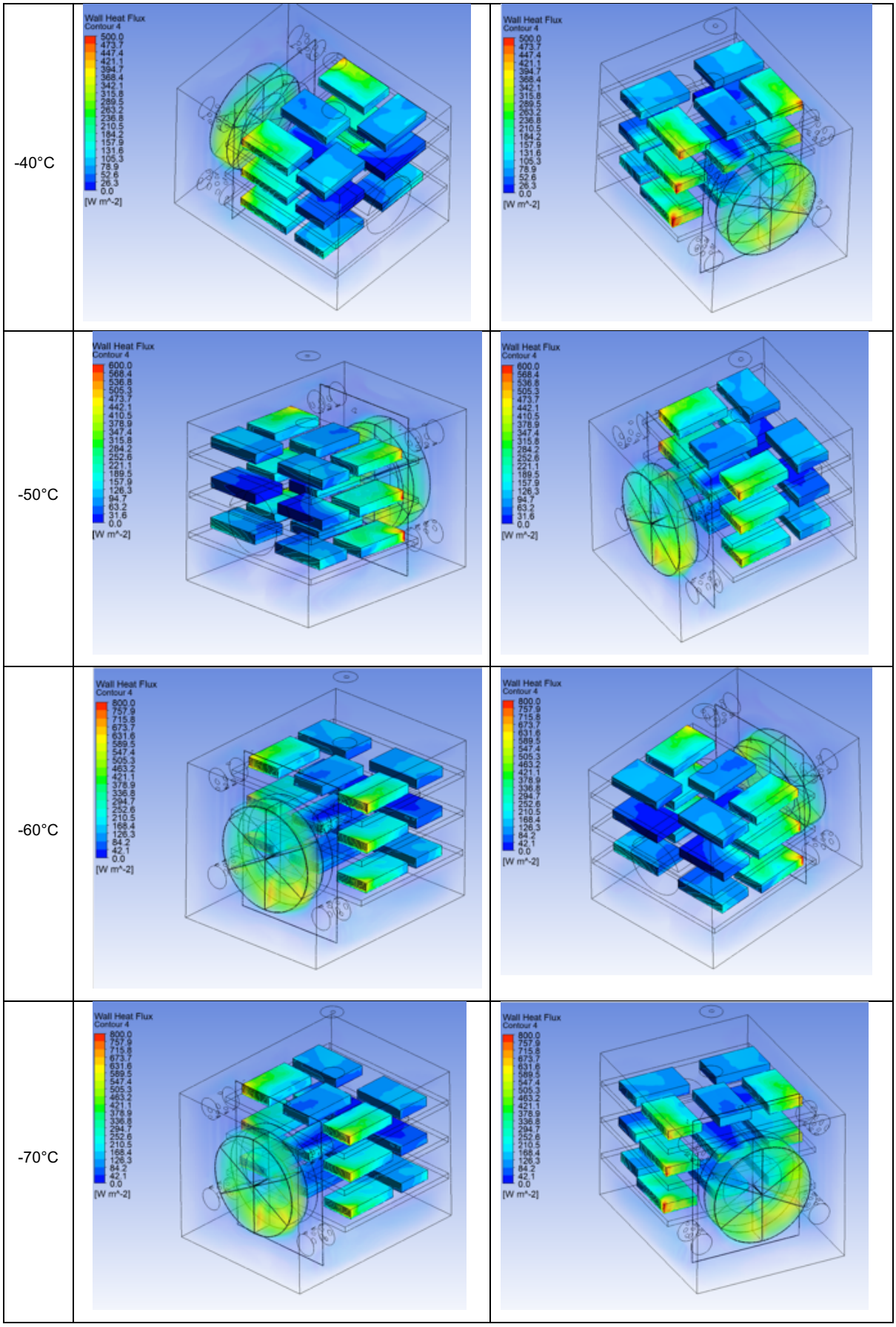

Figure 7-23: Thermal contour plot from -40°C to -70°C at 498RPM for a single plasma layer

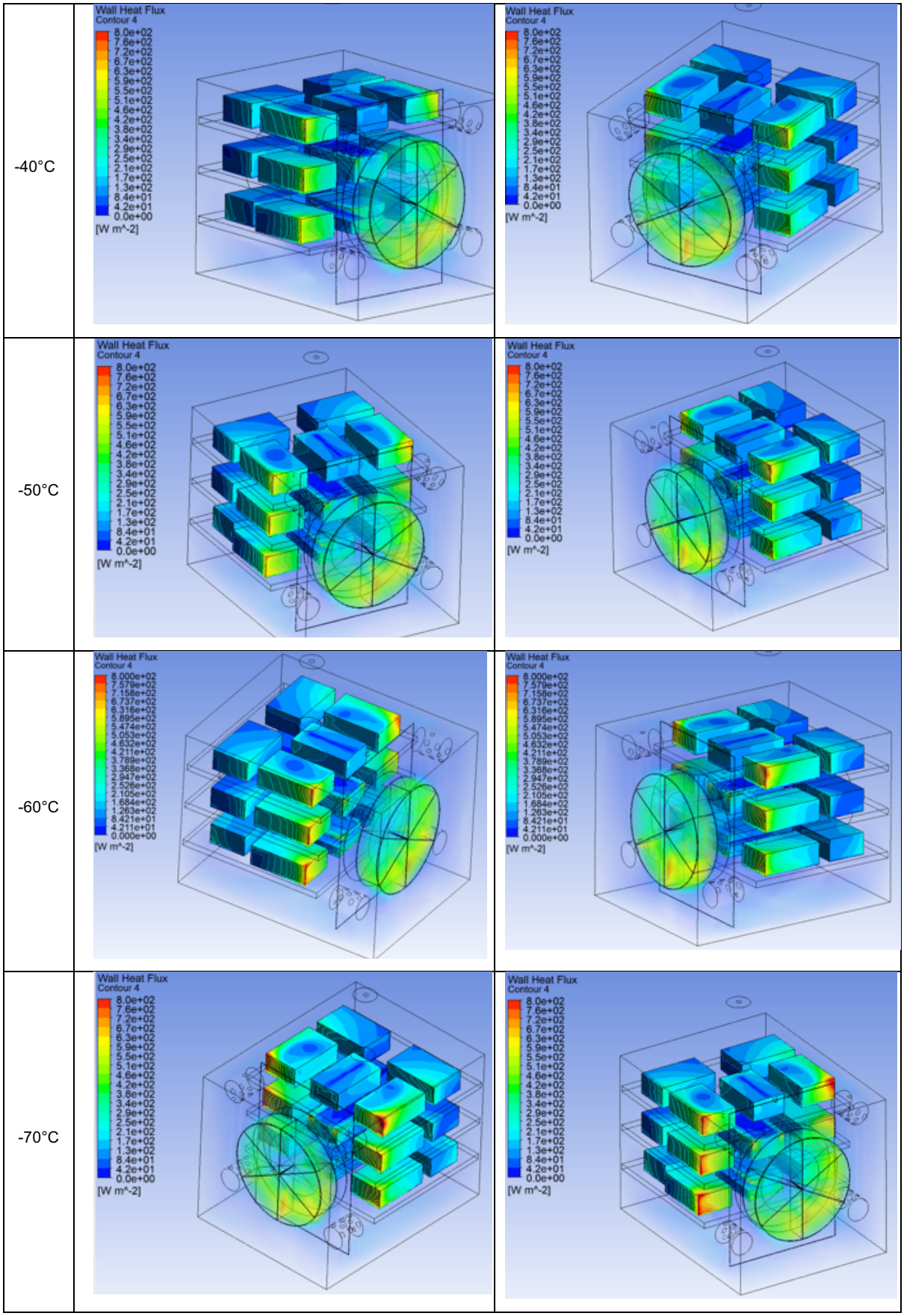

Figure 7-24: Thermal contour plot from -40°C to -70°C at 498RPM for a double plasma layer

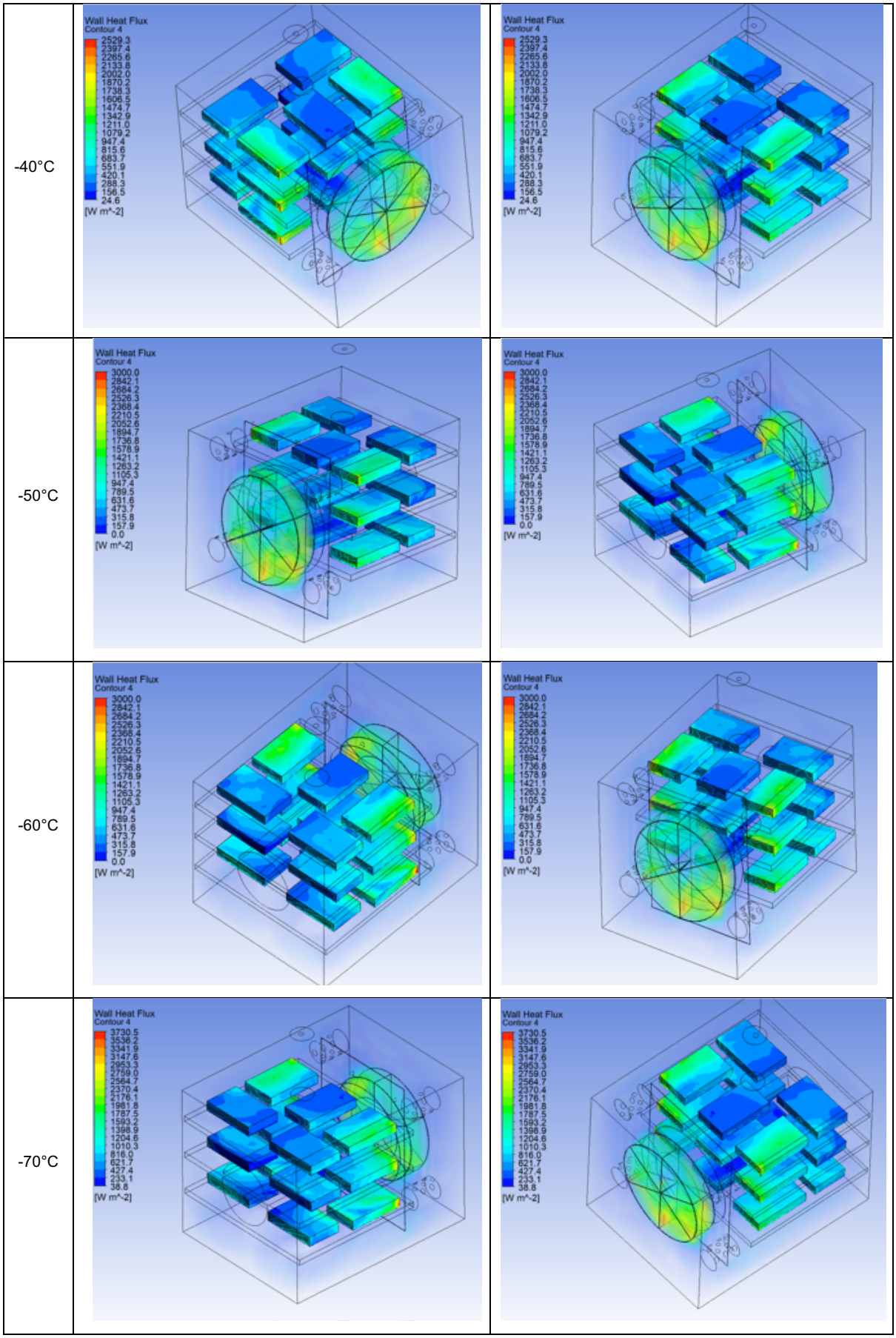

Figure 7-25: Thermal contour plot from -40°C to -70°C at 997RPM for a single plasma layer

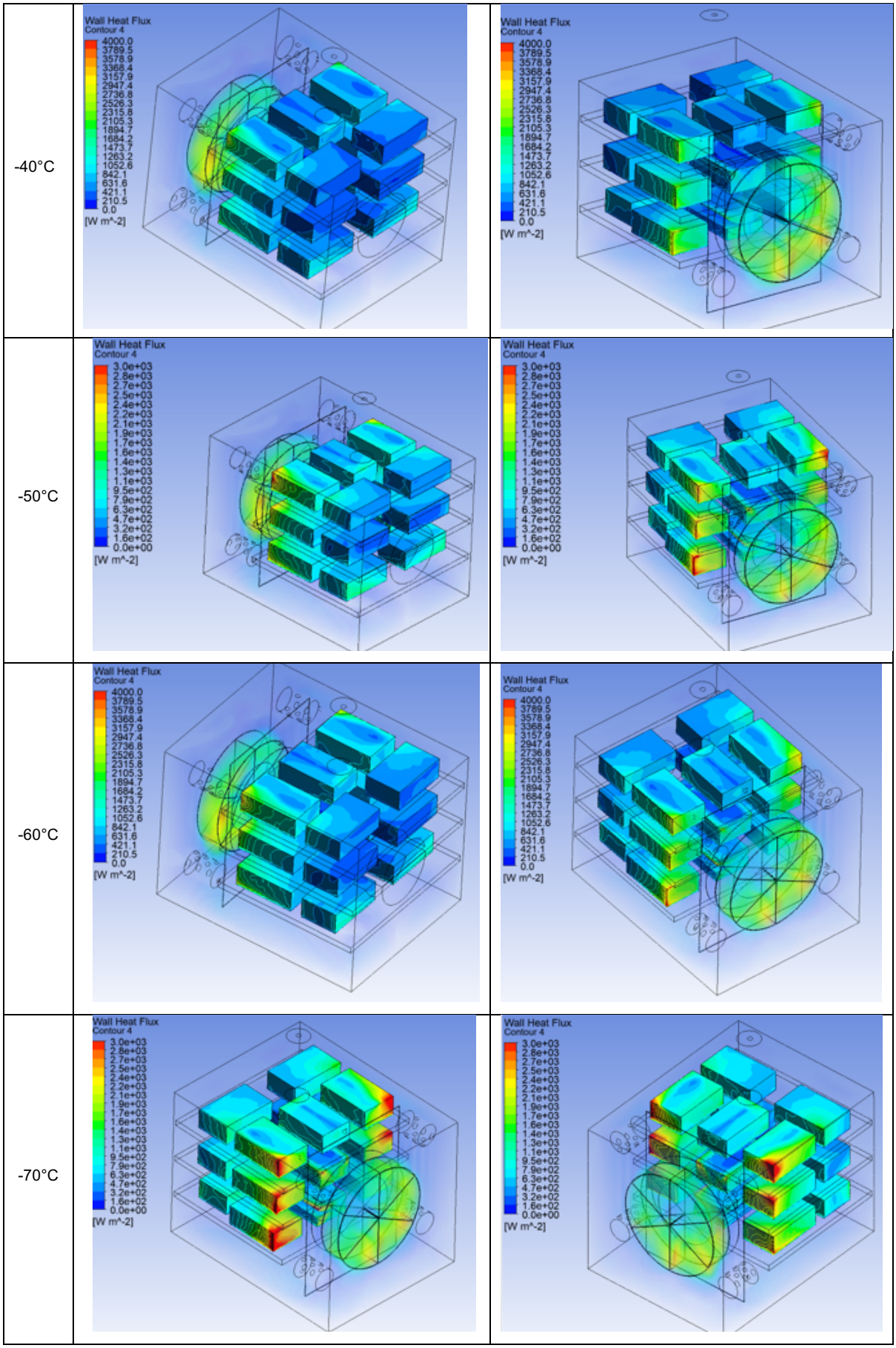

Figure 7-26: Thermal contour plot from -40°C to -70°C at 997RPM for a double plasma layer

7.2.5. Experimental Results

7.2.5.1. Plasma Temperature

7.2.5.1.1 -40°C at 997 RPM

The operation at approximately -40°C is defined in Figure 7-27, where the general trend shows a steady decline to the set point temperature. The overview indicates the variation in liquid nitrogen feed due to the feedback monitor of the liquid nitrogen flow. As the feedback monitor is related to the exhaust temperature, the predefined value controls the valve operation. The feed itself is based on an on-off operation, to allow for a limited amount of liquid nitrogen which can cause a variation in steady state operation.

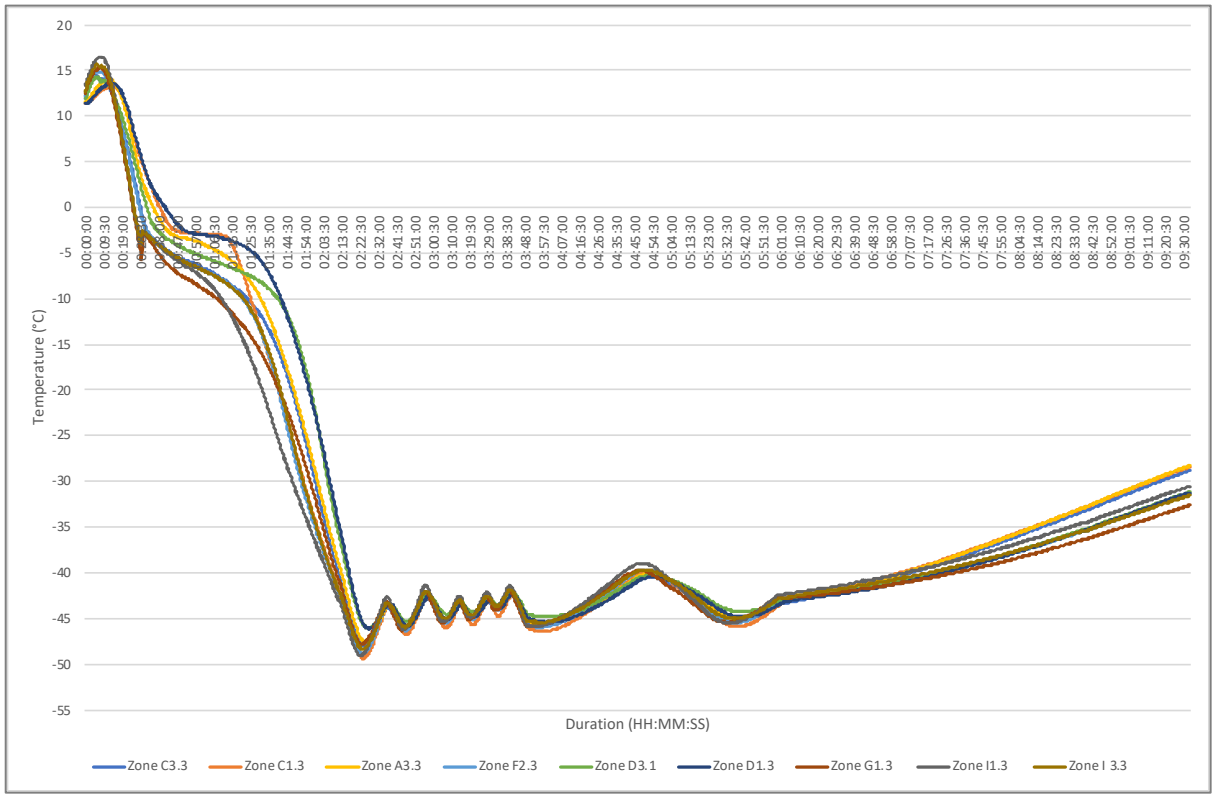

Figure 7-27: Overview of Plasma Temperature at -40°C at 997RPM

Zone C

The location of Zone C denotes the plasma bags on the top shelf, closest to the heat pipe reflected in Figure 7-10. The results are shown in Figure 7-28. Following the analysis of the velocity plots defined in section 7.2.3, the flow stream envelops the top plasma bag allowing for an unsymmetrical heat transfer highlighted in the experimental results for zone C. Zone C1.3 does not follow a traditional cooling curve where the area of stagnation denoting the phase change process is non-existent. The results in zone C3.3 reflect a steady decline indicative that the phase change process is prolonged with a slower decline to the set point temperature. This can indicate that the convective effects are lower in this region. The associated CFD validation is based on the UDF defined in section 7.2.2, where the data represents a generalised temperature decline as a function of time. The comparison between the experimental and CFD results shows a similar trend where the CFD results reach the set point temperature. The UDF defines a linear relationship to the decline to the set point temperature. Zone C1.3 shows a high level of accuracy where the level of variation is over-predicted by 256%. Zone C3.3 follows a similar trend for C1.3 but the CFD model slightly over-predicted the temperature decline, the result being a variation of 36%. The level of variation can be due to the data not following a typical plasma freezing curve.

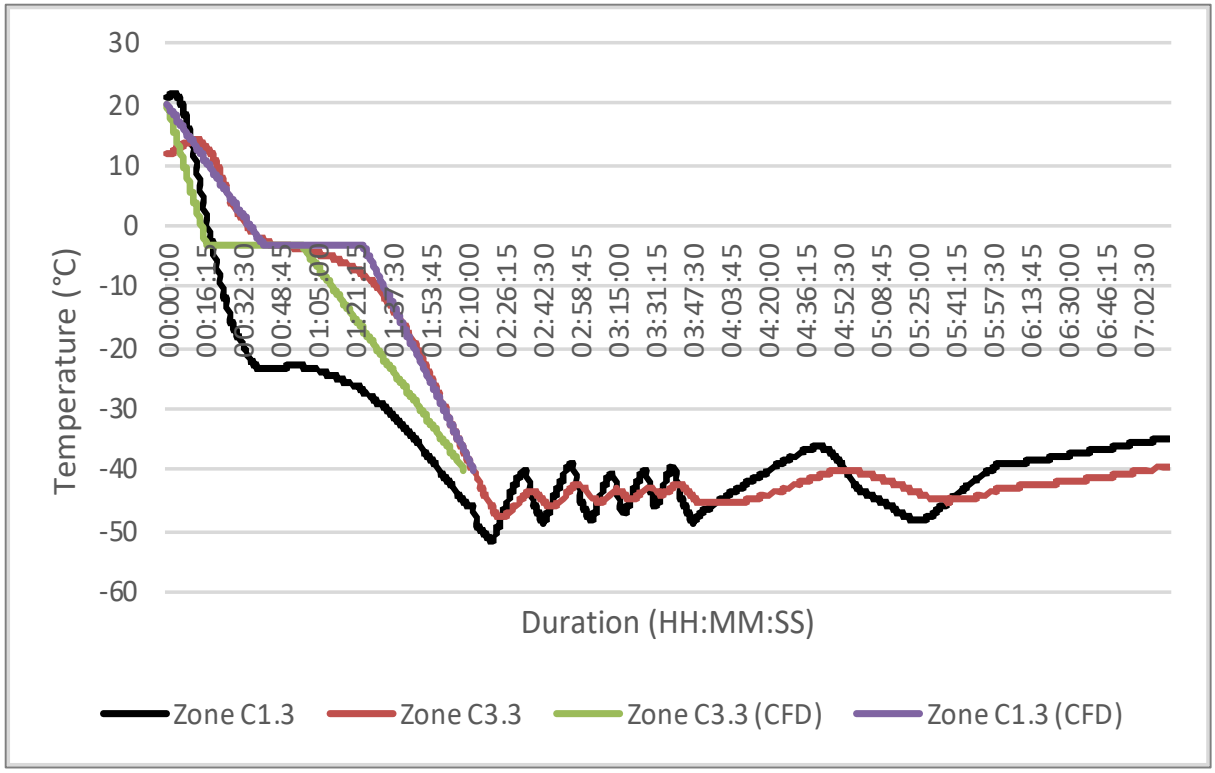

Figure 7-28: Zone C Plasma freezing curve at -40°C at 997RPM

Zone A

Zone A2.3 is located behind Zone C and furthest away from the heat pipe. The freezing curve for zone A is shown in Figure 7-29, reflecting a prolonged freezing time. The experimental data highlights the point of phase change in Zone A to begin at 48 minutes, whereas in Zone C it begins at approximately 35 minutes. The lack of convective effects is evident due to the prolonged freezing time, in comparison to the data in an adjacent zone. The experimental results follow the traditional phase change trend, where the stagnation time reflects the point of phase change. The numerical results for Zone A1.3 show a linear profile, highlighting a level of variation between both CFD and experimental results. The CFD results show a relatively similar initial decline but an over-prediction for both phase change and set point temperature of 24.5% and 32%, respectively.

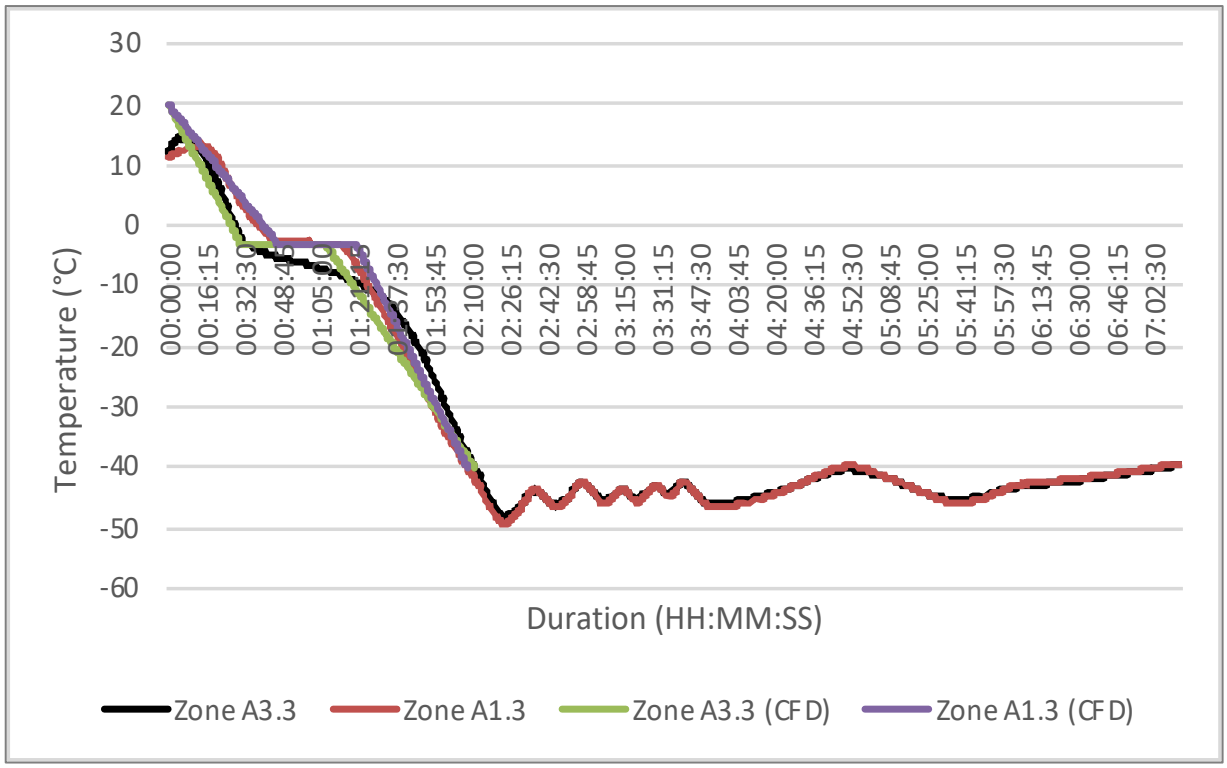

Figure 7-29: Zone A Plasma freezing curve at -40°C at 997RPM

Zone F

Zone F is located on the middle shelf, where the plasma bag load is closest to the heat pipe. The location of zone F is also in the immediate outflow of the fan, in a position where the Reynolds number is the highest. The initial characterisation defined in the velocity profile shows high velocities in comparison to other loading zones. Similarly, the CFD results under-predicted the temperature decline in the area where phase change occurs. As the time of phase change is dependent on location, and the phase change point within the UDF is based on a generalisation from a phase change profile, an under-prediction may not be applicable to all loading positions. The CFD result past the point of phase change reflects an increased convergence between both results with the difference decreasing from 34% to 10% from -3°C to approximately -40°C.

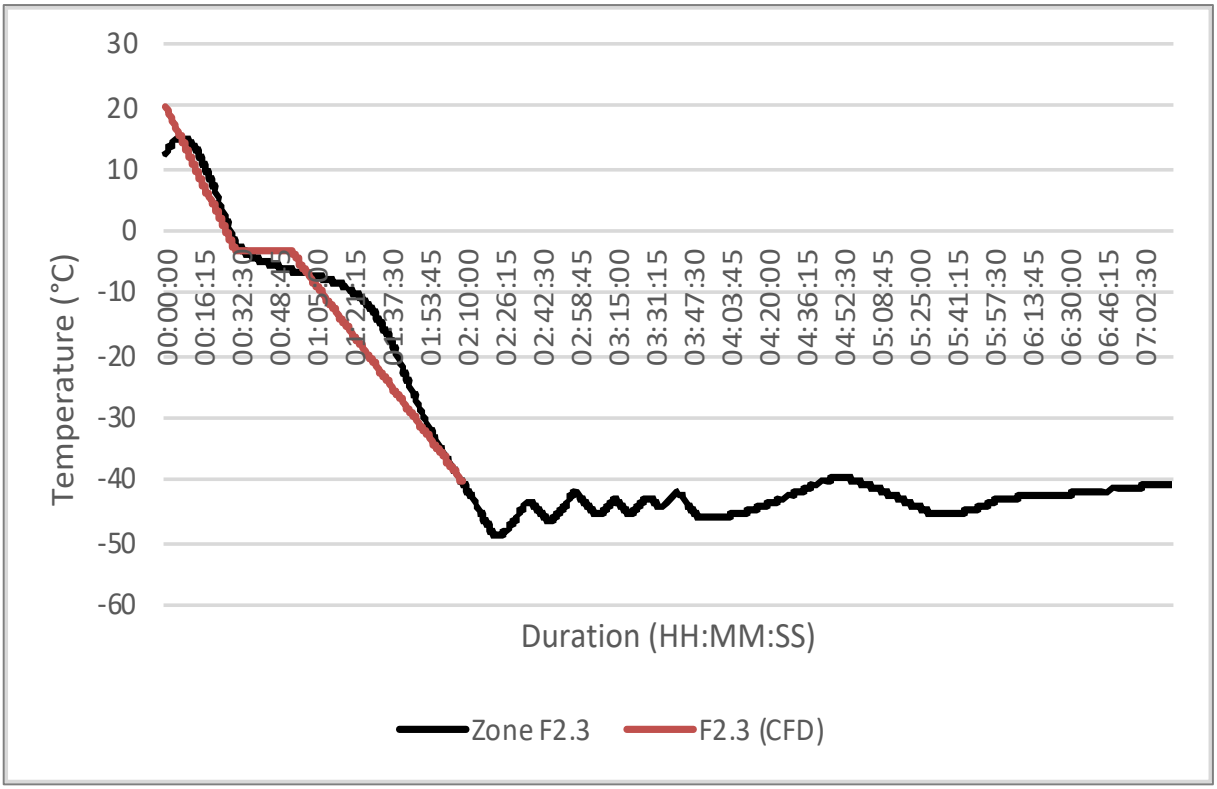

Figure 7-30: Zone F Plasma freezing curve at -40°C at 997RPM

Zone D

Zone D is located behind zone F, where the load itself is located in the wake section from the adjacent zone. The flow field defined in zone D is significantly lower as the flow velocity in zone D3.1 does not exceed 2m/s at maximum capacity and maximum operation. The results shown in Figure 7-31 reflect the relatively prolonged decline to the set point temperature. The comparison between both zone F and zone D reflects the effect of the wake zone and the decline in convective effects, the result being a prolonged freezing time where the plasma bags follow a traditional phase change trend. Both zones D3.1 and D3.3 reflect a similar profile in terms of the cool down period, where the decline to the set point temperature is symmetric. The associated CFD results reflect an over-prediction, where the divergence begins at the phase change point. Zone D3.1 has a variation of 12% during the phase change process whereas Zone D3.3 has a variation of 8% from the point of phase change. As the UDF is averaged for each shelf location, the decline to the set point temperature begins to reflect similar data points.

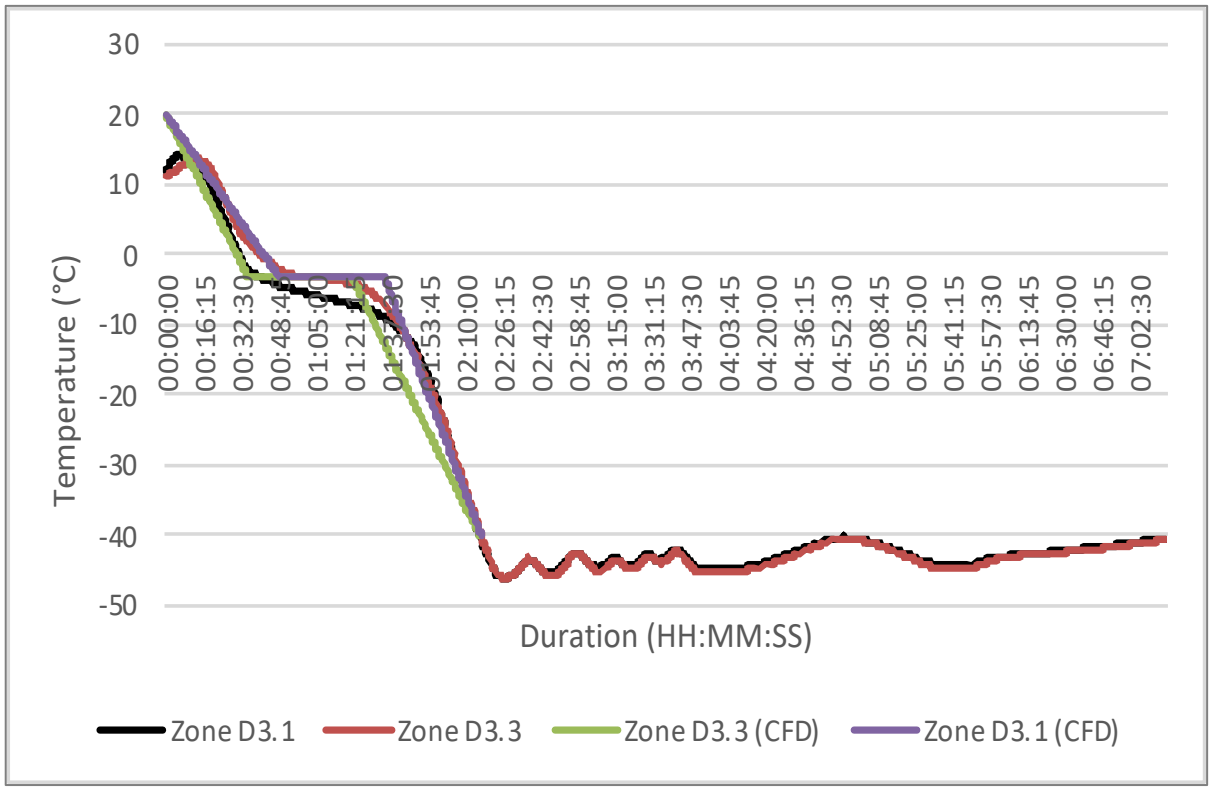

Figure 7-31: Zone D Plasma freezing curve at -40°C at 997RPM

Zone G

The final recorded shelf locations are in zone G and zone I, where zone G is located closest to the heat pipe and the fan plate. The initial analysis for a fully loaded freezer at maximum operation reflects one of the highest measured velocities. The result of this zone shows a significantly sharp decline to the set point temperature where the phase change time is substantially over-predicted by 37%. The data trends itself does not reflect a traditional profile where the duration of the phase change is at a minimum. The reflected CFD study highlights the decline to the set point temperature to -40°C. The over-prediction remains a trend throughout the data with an increased convergence in data towards the set point temperature.

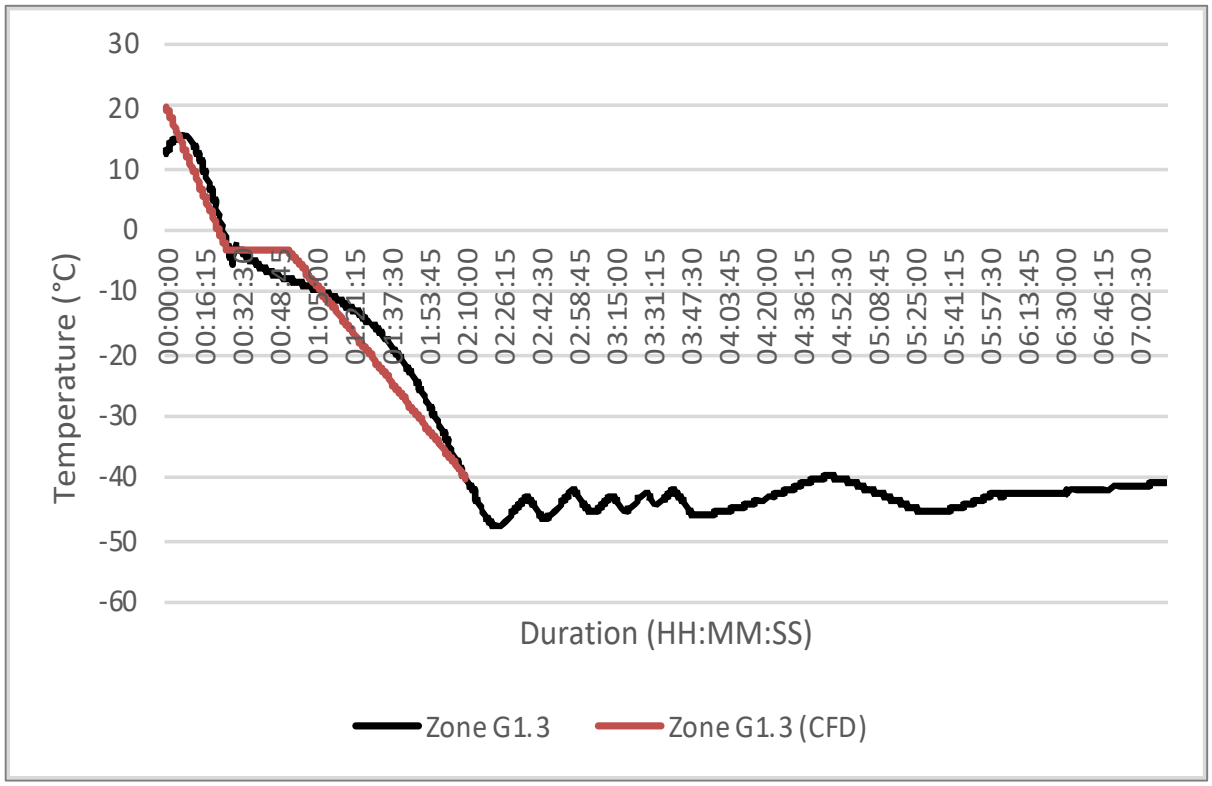

Figure 7-32: Zone G Plasma freezing curve at -40°C at 997RPM

Zone I

The location of zone I is behind zone G in the wake section of the adjacent zone. The load configuration reflects a prolonged freezing time in comparison to zone G. A comparison between the results in zone I and zone G shows a reduced convective effect as a result of plasma bag placement. The experimental results depict a traditional freezing curve, with the decline to the set point temperature following a point of stagnation due to the phase change process. In relation to the CFD results, the UDF highlights a maximum numerical accuracy discrepancy of 21% for zone I3.3, and 28% for zone I1.3. A similar trend highlighted in previous sets of data shows a prolonged stagnation point representing the phase change during the preservation of the plasma simulant. The comparison between the CFD and the experimental results highlight similar profiles during the decline to the set point temperature

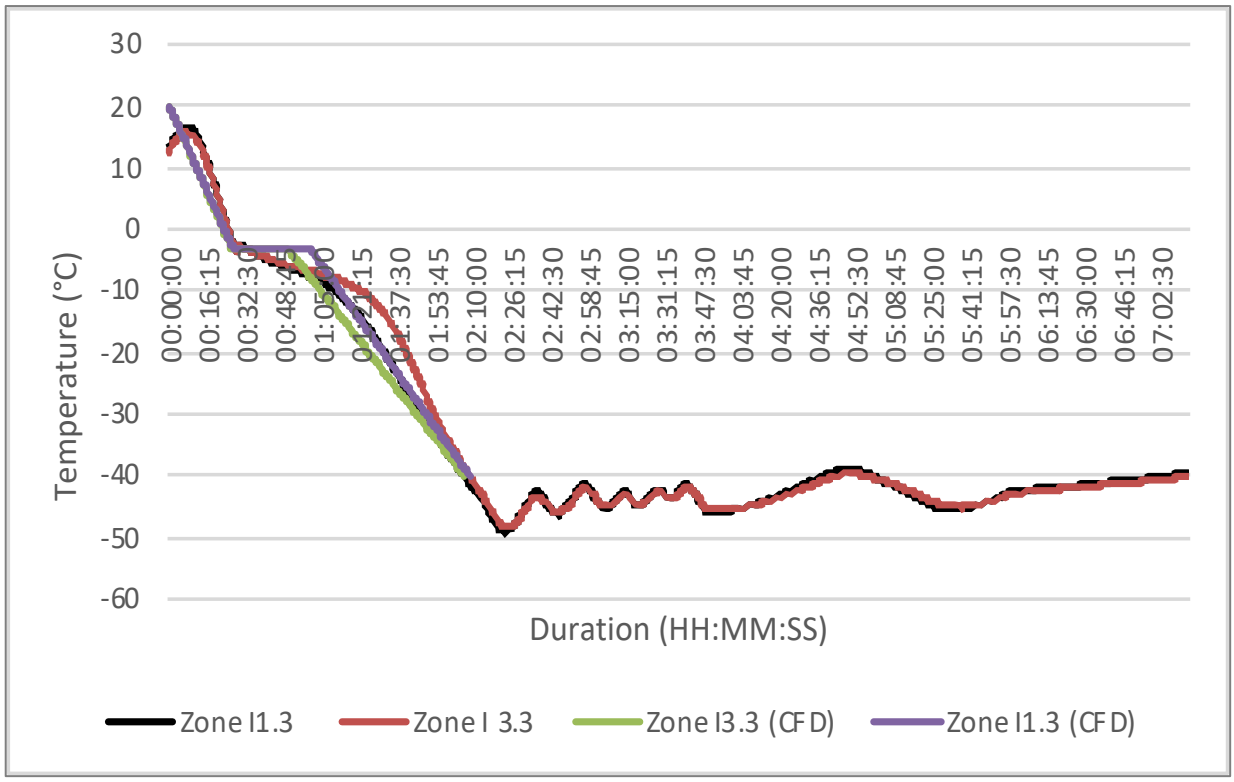

Figure 7-33: Zone I Plasma freezing curve at -40°C at 997RPM

7.2.5.2.2 -60°C at 997 RPM

The second set of data relates to the freezer operation at a set point temperature at -60°C, at a fan speed of 997RPM (50%). Figure 7-34 shows the overall freezing curve of the plasma bags from an ambient temperature to the set point, and the subsequent steady state and warm up operation. The data in Figure 7-34 shows a decline to the set point temperature, following a traditional cool down curve which features a stagnant phase change zone. The operation of the heat pipe highlights the ease of operation to a lower set point temperature without irregularities and with a consistent freezing curve. The freezing curve throughout the steady state operation shows a level of variation due to the fixed volume of nitrogen entering the cooling coil.

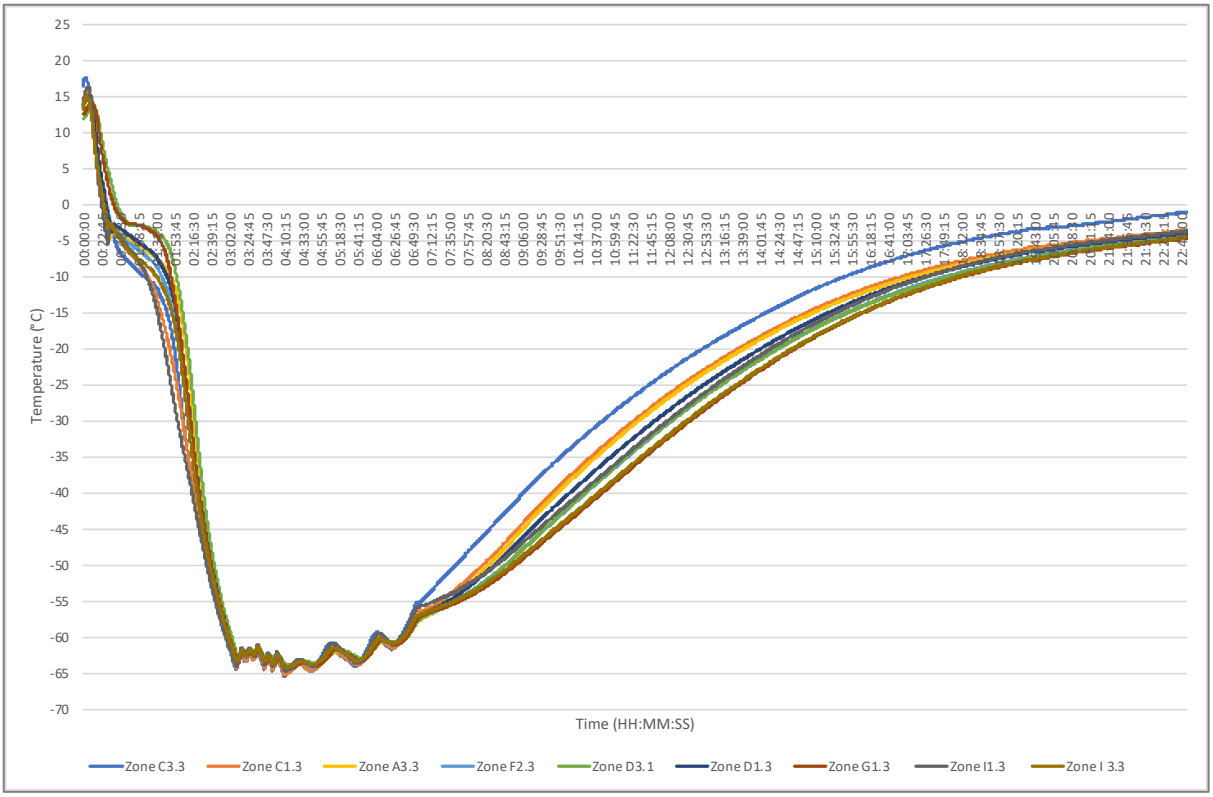

Figure 7-34: Overall Plasma freezing curves at -60°C at 997RPM

Zone C

The location of zone C is shown in Figure 7-10, where the load is located closest towards the heat pipe, on the top shelf of the system. The freezing curve for zone C is shown in Figure 7-35. The freezing curve reflects a level of asymmetric heat transfer from the initial loading point. Zone C1.3 highlights a swift decline to the set point temperature with an almost minimal phase change point. The associated plasma bag in the opposite location shows a prolonged freezing time, the difference between both sets of data reflects the inequality between flow regimes, with a significantly improved heat transfer at C1.3, with a minimal phase change duration. Similarly, the CFD results related to zone C1.3 show an over-prediction of 87% in comparison to the experimental results, with an increased similarity during the decline to the set point. Zone C3.3 is increasingly similar to the phase change diagram, where the phase change point is significant. The comparison between the experimental and CFD results highlight less variation between both sets of data. The CFD results show an over-prediction of approximately 7% for the phase change duration. The results highlight an increased similarity towards the set point temperature.

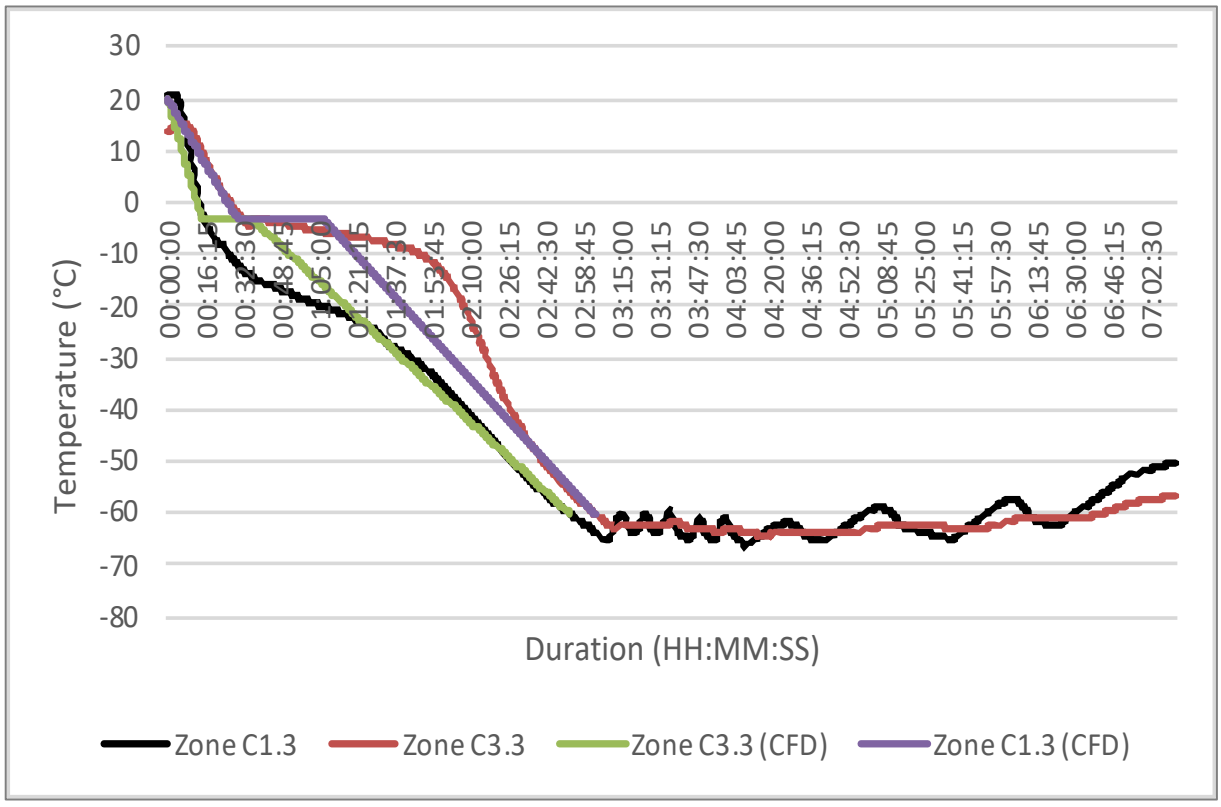

Figure 7-35: Zone C Plasma freezing curve at -60°C at 997RPM

Zone A

The position of Zone A reflects the load configuration adjacent to Zone C shown in Figure 7-10. The load itself is located in the wake zone of Zone C, where the lack of convective effects is evident and previously discussed in section 7.2.5.1.1. The results shown in Figure 7-36 are related to the freezing curve for the plasma bags located in zone A. The data reflect a symmetrical heat transfer regime, where both plasma bags have minimal amounts of variation across zone A. Both plasma bags A1.3 and A3.3 contain minor variations throughout the point of phase change where zone C3.3 shows a slightly increased phase change time in comparison to C1.3. The minor change can be indicative of the lack of convective effects from C3.3, which has been identified as a lower velocity zone. The wake stream following this results in zone A1.3 experiencing a lower convective effect. The respective CFD results shows a maximum numerical accuracy discrepancy of 67%, where the duration of phase change is comparatively lower. The CFD simulation provides an acceptable prediction for the decline to the set point temperature. The CFD results for zone C1.3 reflect a relatively accurate prediction, where a level of variation exists at the phase change point due to the small decline in temperature. The UDF provides an accurate prediction past the phase change point to the set point temperature.

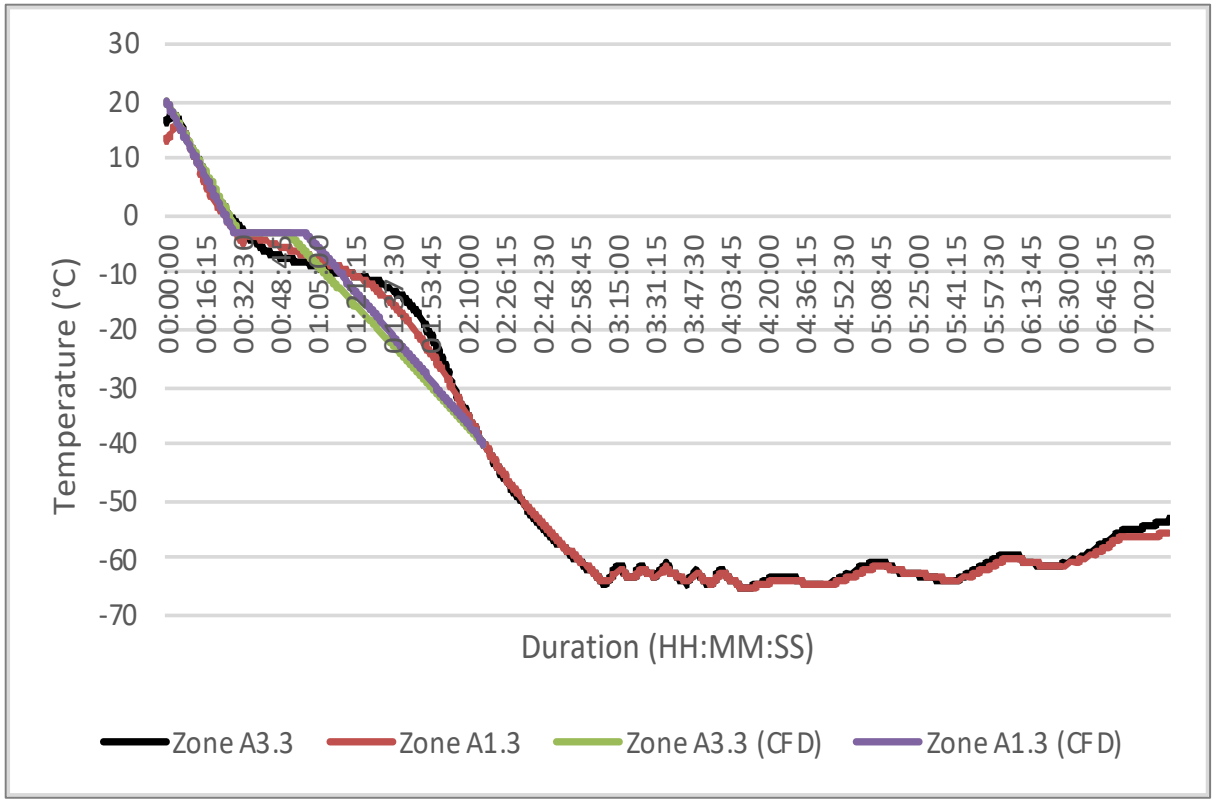

Figure 7-36: Zone A Plasma freezing curve at -60°C at 997RPM

Zone F

The position of zone F is located in the middle of the freezing chamber in the centre of the fan flow as shown in Figure 7-10.The plasma bag is located near the fan but as the fan in drawing in air, the expelled air may be slightly reduced in the specific zone. Figure 7-37 shows the freezing curve for plasma load zone F1.3, from ambient to the set point temperature. The data reflects a traditional cooling curve, as previously defined in chapter 6. The associated CFD data shows a maximum variation between the CFD and experimental data of approximately 33%. The zone higlights an increase convergence between the experimental and CFD data, towards the set point temperature. The CFD data show a small difference during the phase change process due to the defined linear relationship, which is not dictated by heat and mass transfer models.

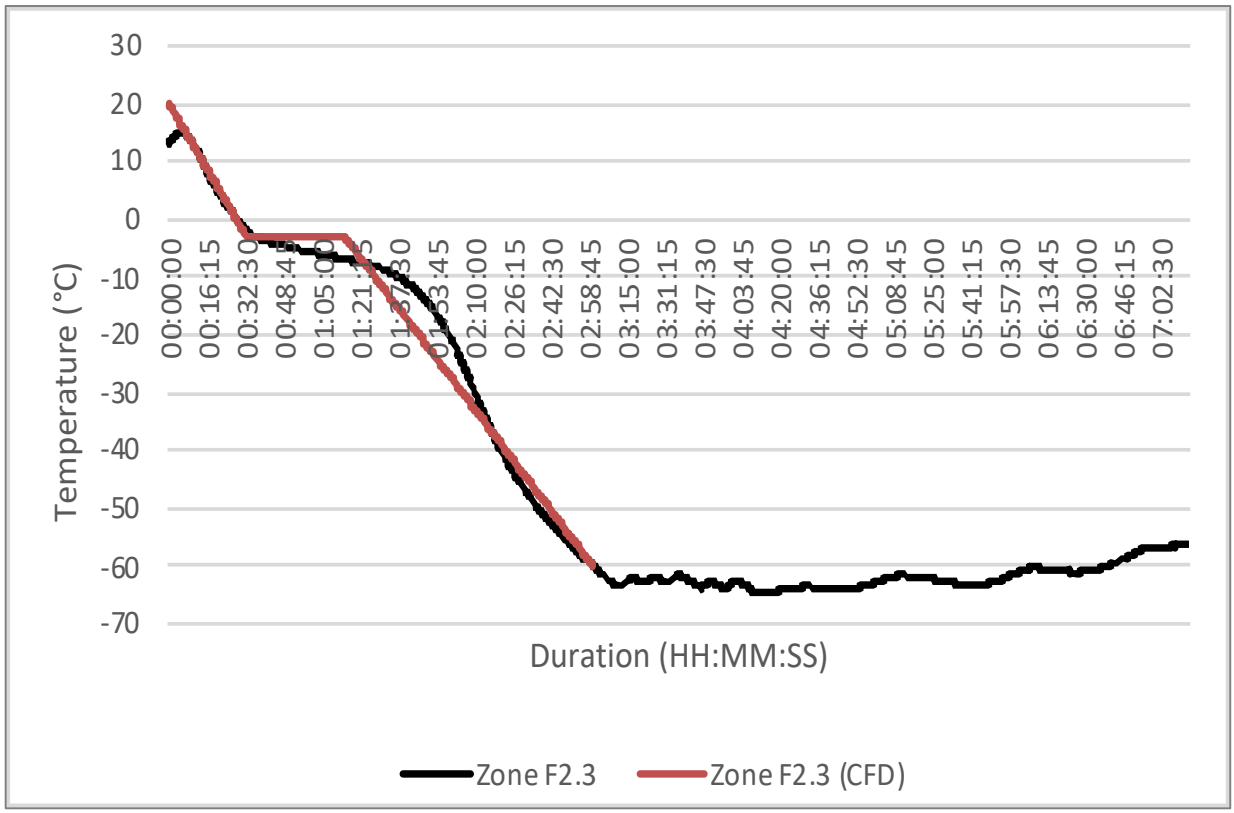

Figure 7-37: Zone F Plasma freezing curve at -60°C at 997RPM

Zone D

The loading position of Zone D reflects the plasma bag located behind zone F as shown in Figure 7-10. The experimental data depict a traditional cooling curve defined in chapter 6. The experimental results show a slower decline to the set point temperature compared to Zone F. The plasma bag highlights the end of the phase change zone at 1:37:30 for zone D1.3 and approximately 1:53:45 for plasma bag D3.3. In comparison, for zone F, the phase change time is 1:21:15. The difference between the plasma bags is evident, where the reduced convective effects are highlighted between D1.3 and F1.3. The comparative CFD results reflect a discrepancy in of both experimental plasma values, where the main discrepancy lies within the prediction of the phase change time, with a maximum numerical accuracy of 13% and 6%, respectively. Due to the over-prediction, the variation is increased from the decline to the set point temperature.

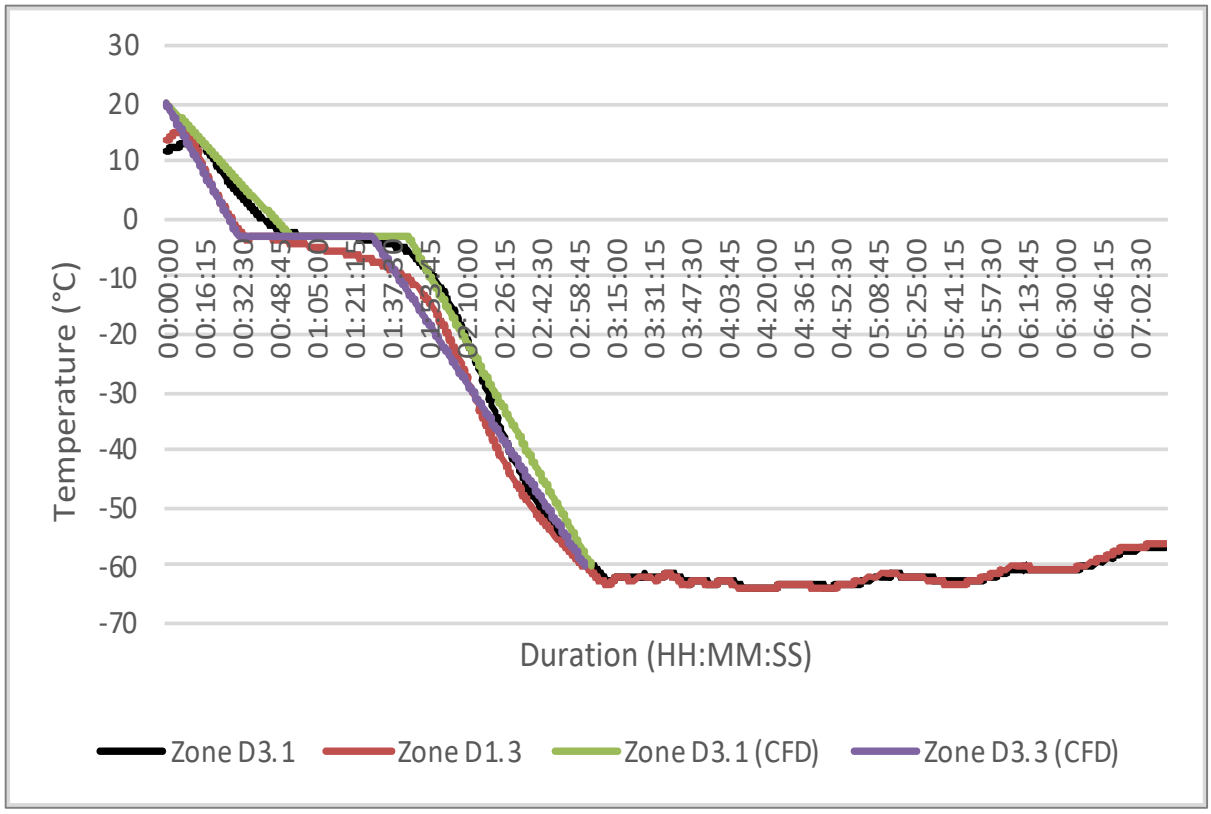

Figure 7-38: Zone D Plasma freezing curve at -60°C at 997RPM

Zone G

The final set of plasma loads is located on the bottom shelf of the freezing chamber where the plasma bags follow the configuration shown in Figure 7-10. The plasma bags follow a traditional cooling curve where the phase change zone is progressively stagnant. The position of zone G is behind zone I, furthest away from the heat pipe, the result being a prolonged freezing curve in comparison to neighbouring plasma bags. The zone highlights the end of the phase change zone at 1:45:00, whereas zone I reflect the end of phase change at: 1:21:15 and 1:37:30. The relationship between the loading conditions highlights the lack of convective effects leading to an asymmetric heat transfer across the shelf condition. The associated CFD results show a deviation in accuracy for the phase change zone which remains evident, but with a reduced variation towards the set point temperature.

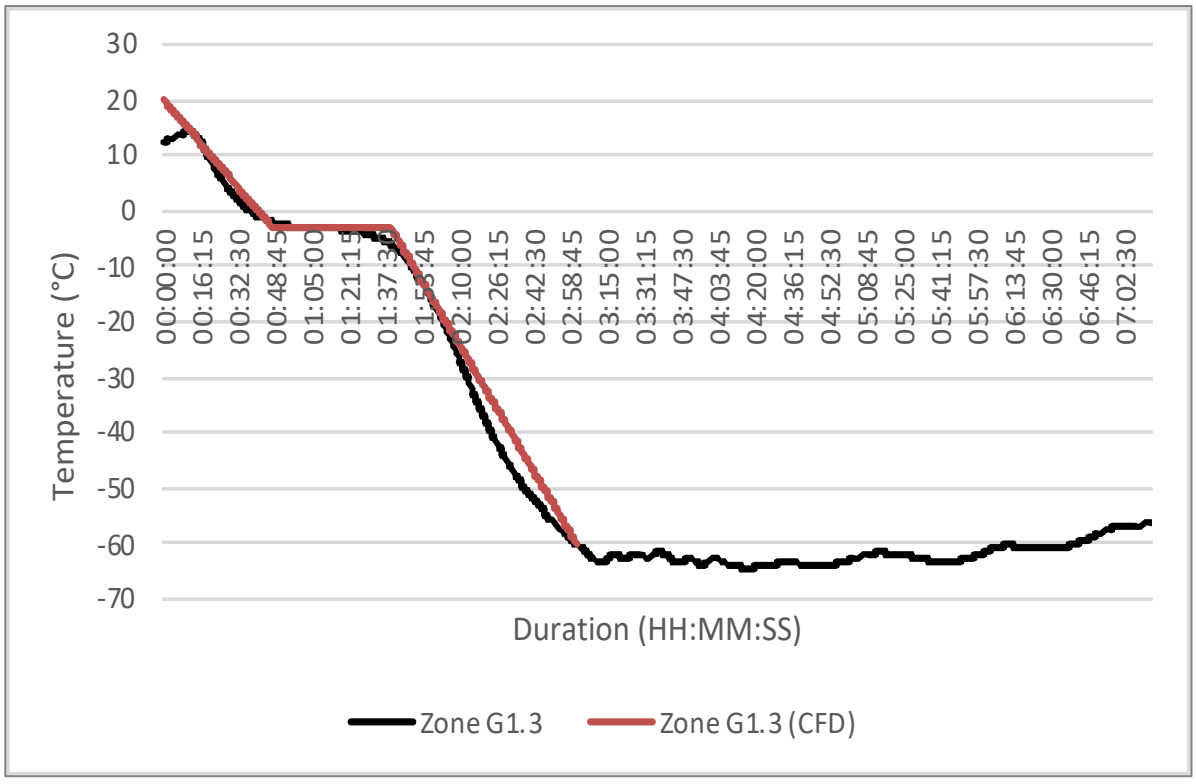

Figure 7-39: Zone G Plasma freezing curve at -60°C at 997RPM

Zone I

The final loading position, zone I, is located close to the heat pipe on the bottom shelf as shown in Figure 7-10. The loading configuration shows a discrepancy between both load conditions, the difference between both is evidenced by an asymmetric flow distribution past the heat pipe module. The flow distribution in section 7.2.4 depicts a discrepancy where the flow field creates an uneven thermal distribution across the shelf load. This trend has been evident throughout the presented data, due to the increased resistance leading to a lack of convective effects. The data in Figure 7-40 reflect a relatively accurate CFD prediction, where Zone I1.3 only shows a maximum numerical accuracy of 5%. The data reflect a relatively identical profile for the decline to the set point temperature. The adjacent plasma bag in zone I3.3 shows a similar but maximum numerical accuracy by approximately 11%. The level of over-prediction continues towards the set point temperature.

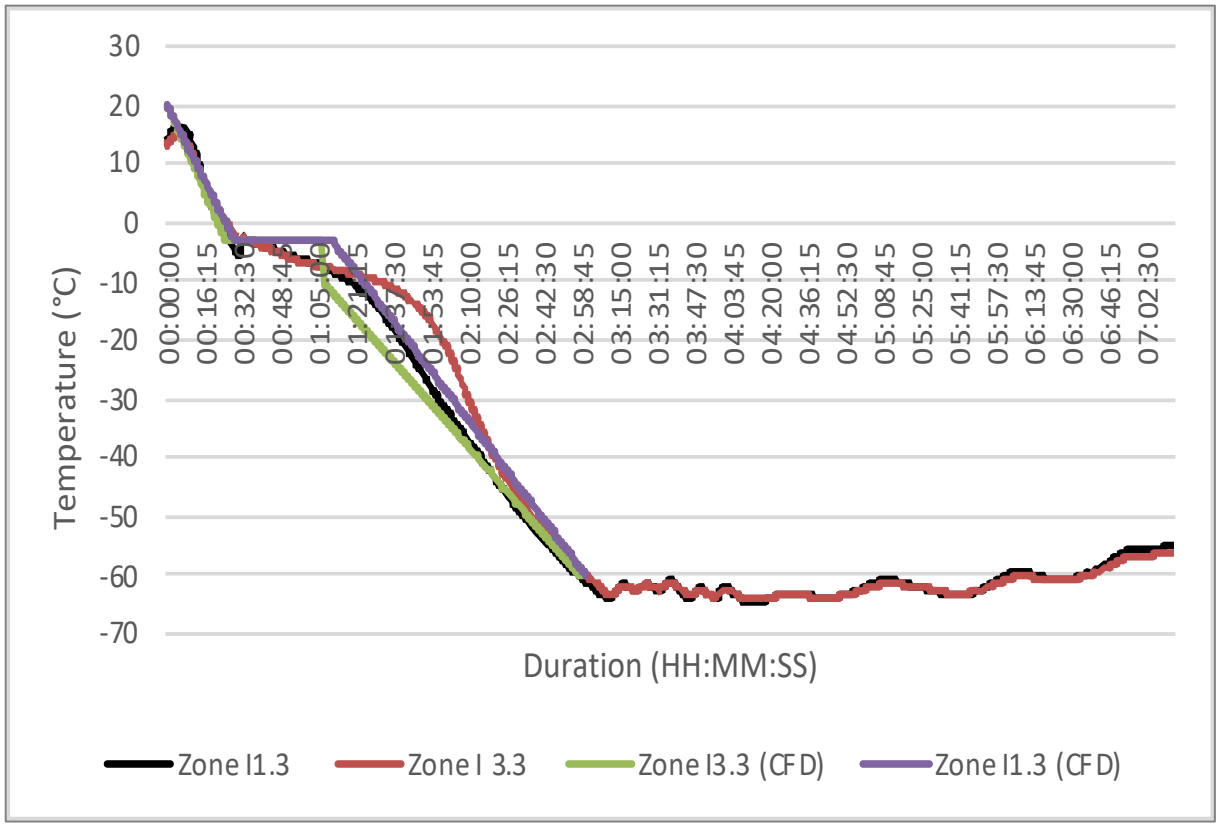

Figure 7-40: Zone I Plasma freezing curve at -60°C at 997RPM

7.2.5.2.3 -40°C at 498 RPM

Figure 7-41 shows an overall freezing curve of the blood plasma simulant from -40°C at a lower RPM than the previous sections. The data reflects an operation at 498RPM, and show a decline to the set point temperature at approximately -40°C, including a steady state operation. The decline in temperature represents an overall traditional cooling curve where the profile shows a level of stagnation due to the phase change point. The difference between 998RPM defined in section 7.2.5.2.2 and Figure 7-41 highlights a further prolonged profile, due to the lower RPM and thus lower convective effects.

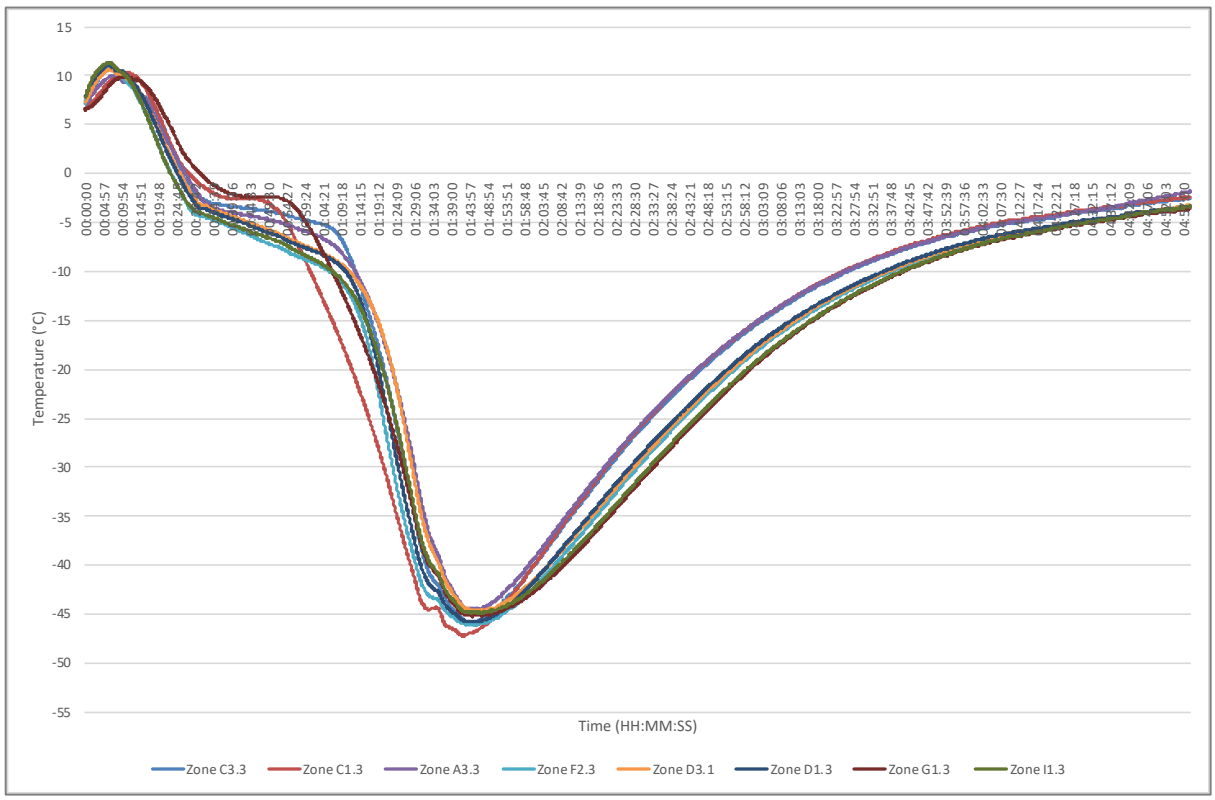

Figure 7-41: Overall Plasma freezing curve at -40°C at 498RPM

Zone C

Zone C is situated at the position of the plasma loading on the top shelf closest to both heat pipe and fan, as shown in Figure 7-10. The data shows a sharp decrease in plasma bag C1.3, where the flow streams indicated in Figure 7-21, show an envelope style flow where the outcoming stream circulates around the top section. This level of circulation is asymmetric showing a difference of 154% between C1.3 and C3.3, which is quite high. Where the plasma bag is located at C3.3 the result shows a significantly skewed form, as an effect of a poor flow distribution. The associated CFD results show an over-prediction for zone C1.3, where the unaccounted high velocity zone causes a large difference between the CFD result and the experimental result. In comparison, zone C3.3 shows a relatively accurate prediction of the experimental data. The forecast data highlights a discrepancy in the accuracy of the phase change point. The comparison between the CFD and experimental demonstrates convergence past the phase change point.

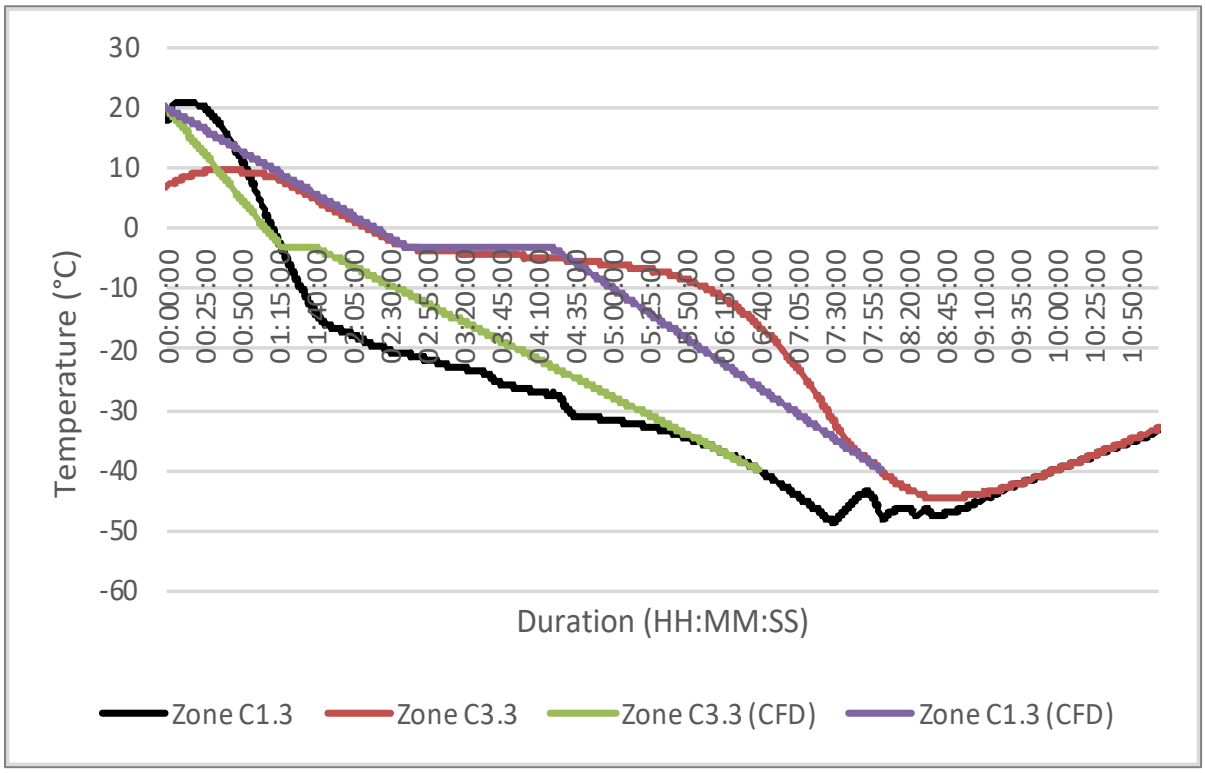

Figure 7-42:Zone C Plasma freezing curve at -40°C at 498RPM

Zone A

Zone A reflects the load condition adjacent to zone C, located in the wake stream of zone C as shown in Figure 7-10. The relationship between the loading zones has been defined in the subsequent sub-sections in 6.2.5.1. The relationship between the loading zones has been defined in sub-section 6.2.5.1 and subsequent sub-sections. The relationship is evident where the wake zone has a lower velocity in zone A, and a reduced heat transfer via convection. The respective results indicate this, with a prolonged phase change time of approximately 70 minutes. The results show a similar freezing characteristic to a traditional cooling curve as expected, where both graphical profile sets are similar. The CFD results highlight both an over-prediction and an under-prediction for zones A1.3 and A3.3, respectively. The CFD results for A1.3 shows a maximum accuracy of 9%. As the flow stream is slightly biased on the side 1.3 across the shelf due to the increased flow field through location 1.3, this resulted in an increase in convective effects. Zone A3.3 shows an under-prediction where the lack of convective effects has allowed an overshoot in the CFD estimation.

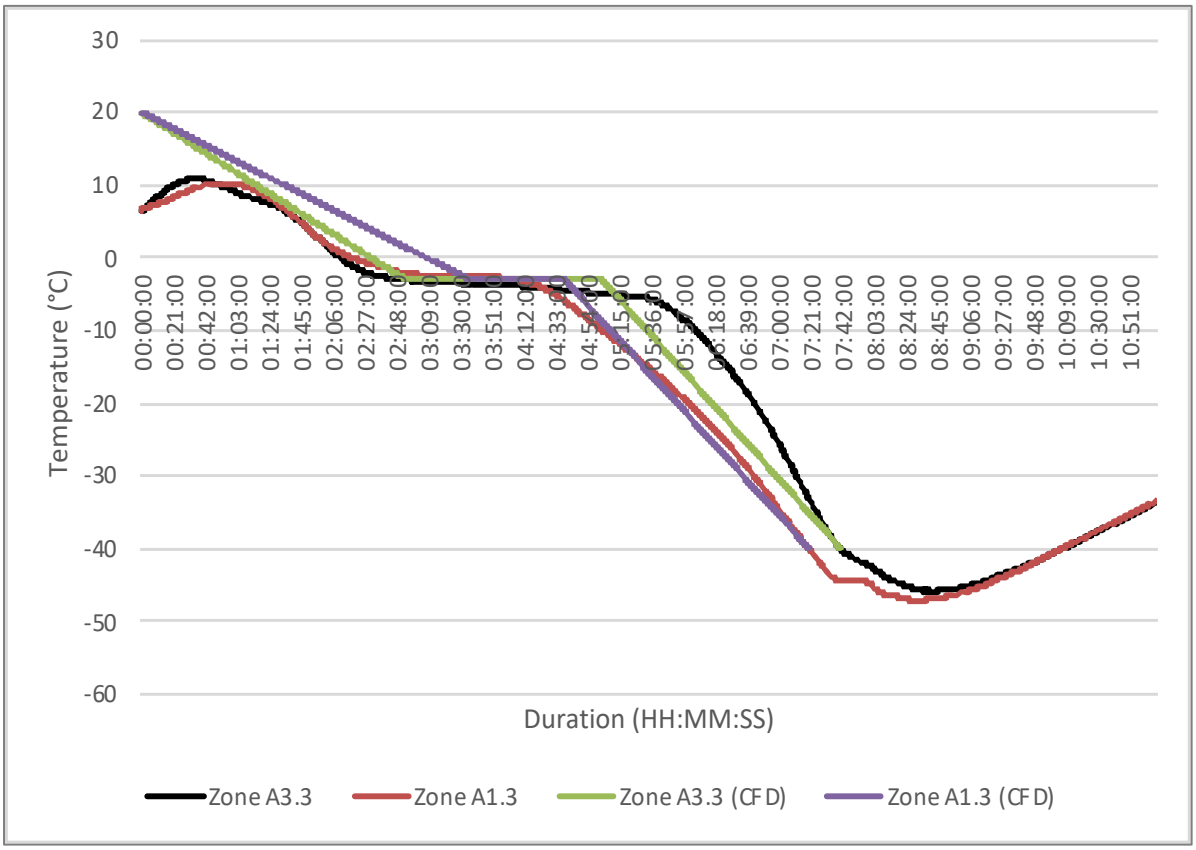

Figure 7-43: Zone A Plasma freezing curve at -40°C at 498RPM

Zone F

The position of Zone F is located the centre of the fan flow, closest to the heat pipe, on the middle shelf as reflected in Figure 7-10. The experimental results show good agreement with the CFD results, with the difference due to the assumed linear operation at the phase change point due to mass transfer being omitted. The overall accuracy of the CFD simulation being a maximum of 32%.

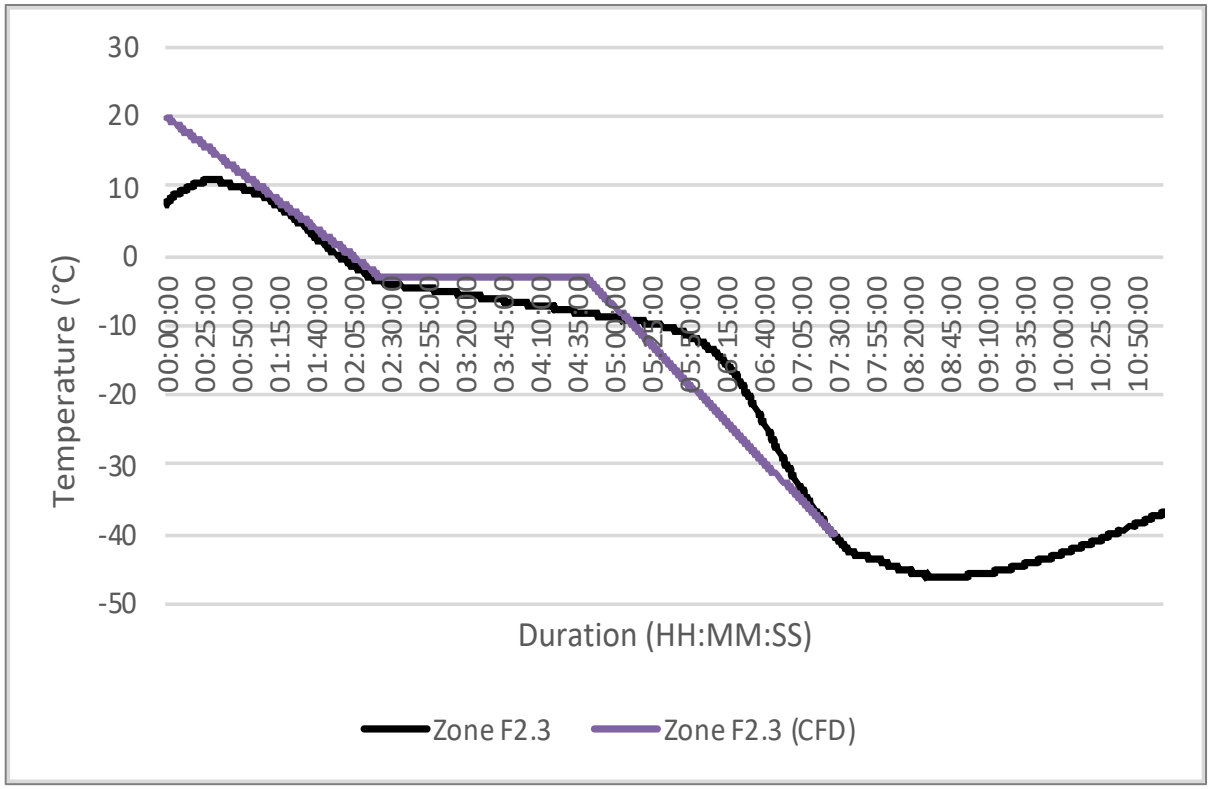

Figure 7-44: Zone F Plasma freezing curve at -40°C at 498RPM

Zone D

The location of zone D is in the wake stream of zone F, as shown in Figure 7-10. The result for the plasma bag in relation to its location shows a prolonged freezing time in comparison to zone F. The difference is of almost 30 minutes for zone D to fully solidify the plasma simulant. The delayed freezing characteristics can be determined by the location and positioning of the plasma bag, where the relationship between wake stream loads and subsequent heat transfer has been defined in previous sections. The validation of the experimental results shows a deviation in the forecast model from the point from the phase change and the set point temperature. The deviation of the forecast CFD model can be due to the approximation applied through the UDF. The results show a maximum difference of 32%, with an increased accuracy to the set point temperature.

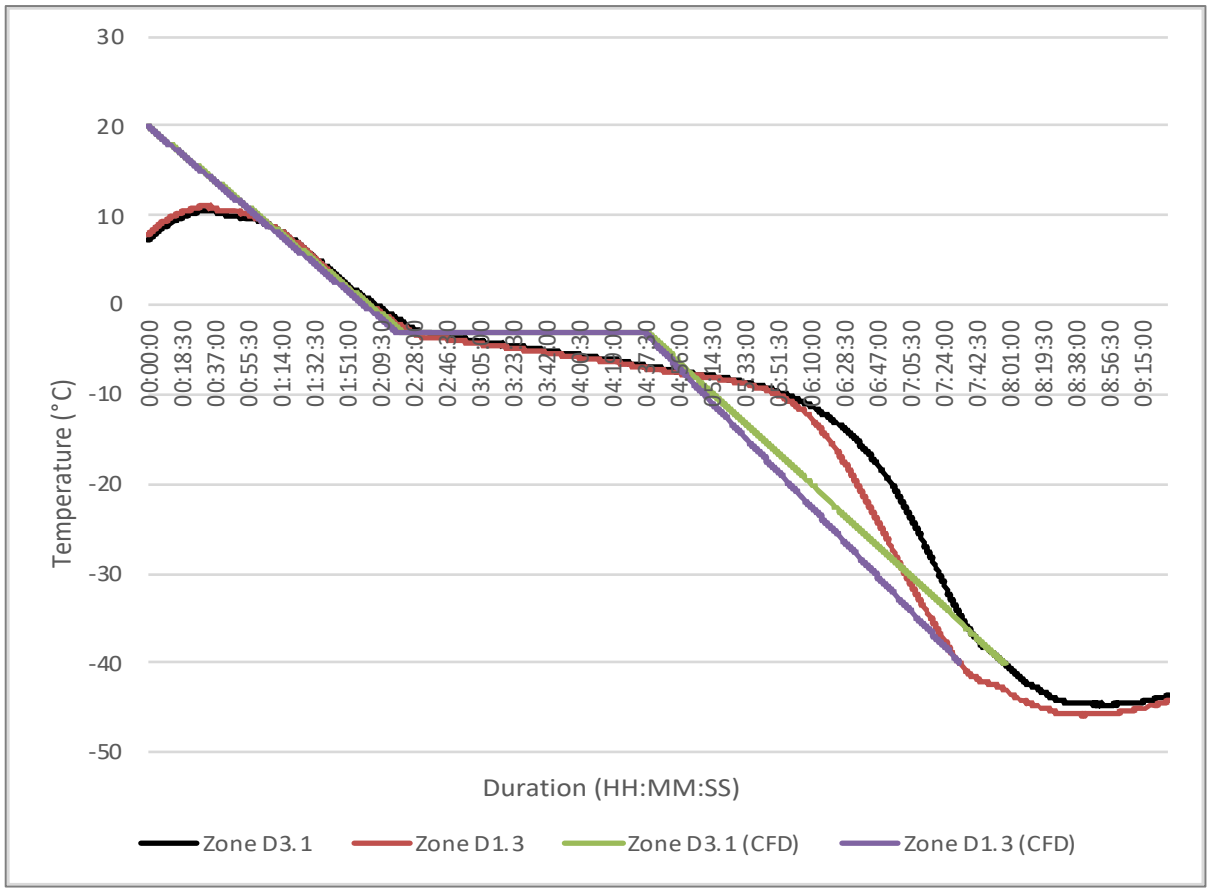

Figure 7-45: Zone D Plasma freezing curve at -40°C at 498RPM

Zone G

Zone G has a loading position on the last shelf of the freezing chamber, in the wake stream of zone I as shown in Figure 7-10. The results from zone G highlight the effects of being located in the wake stream of zone I. Due to the lower velocity in zones I and G, the results reflect a reduction in convection resulting in differences between the zones, a trend previously discussed in section 6.2.5. The CFD results highlight a slight over-prediction of 6% due to the approximations applied for the definition of the plasma bag. The UDF applied accounts for a sharp decline towards the set point temperature, where it begins to converge towards -40°C.

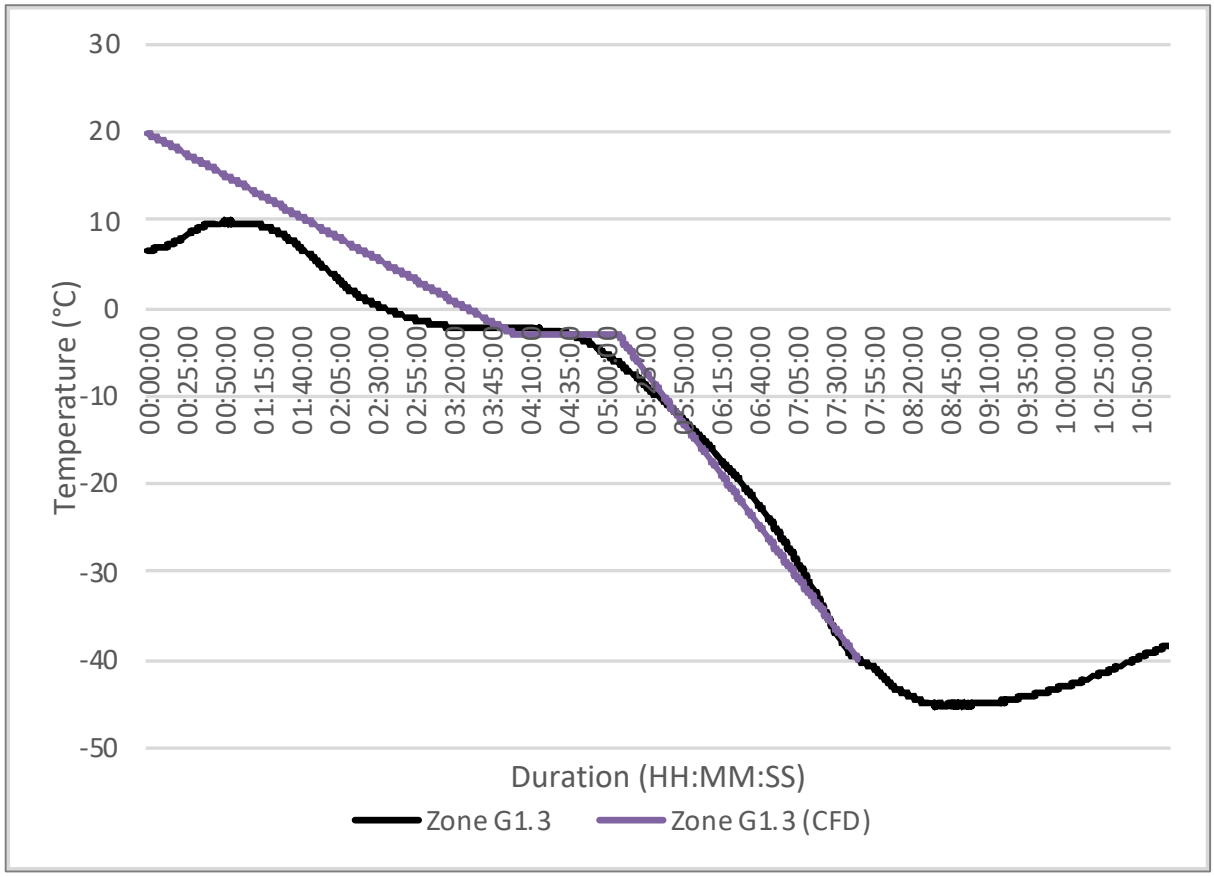

Figure 7-46: Zone G Plasma freezing curve at -40°C at 498RPM

7.2.5.2.4 -60°C at 498 RPM

Figure 7-47 shows the freezing curve for the freezing chamber at a -60°C set point at 498RPM. The figure highlights a typical freezing data profiles with an area of stagnation, the data shows a singular rapid freezing regime located in zone C1.3, which previously has been defined as having a close proximity high velocity zone. The data reflect a decline to a temperature set point of -60°C, with the data showing a small steady state operation. In comparison to section 7.2.5.4.3, the data shows a prolonged duration, but the data presented highlights a lower fan operation reducing the convective effects.

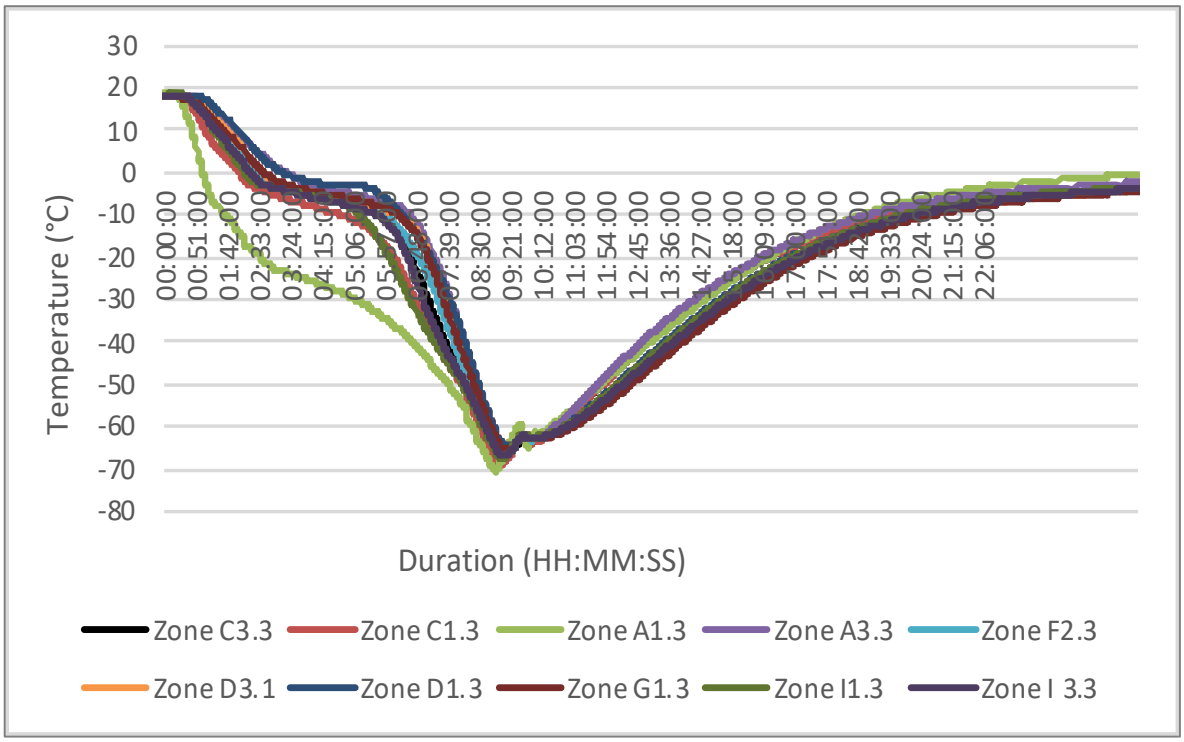

Figure 7-47: Overall Plasma freezing curve at -60°C at 498RPM

Zone C

The results in highlighted in Figure 7-48 reflect a sharp decline to the set point temperature of approximately -60°C. The data shows similar trends previously defined in section 7.2.5.4. The data highlights an extreme and rapid decline to the set point temperature with minimal stagnation time, which has been a key trend throughout the characterisation of the freezing chamber. The trend between the zone reflects an asymmetric graphical profile where zone 1.3 shows a rapid freezing regime, and similarly zone C3.3 shows a prolonged phase change time due to the lack of convective effects and differences across zone C. The corresponding CFD results show an over-prediction due to the unaccounted extreme convective effects. In comparison, zone C3.3 reflects a maximum forecast deviation of 58% between the CFD data and the experimental data.

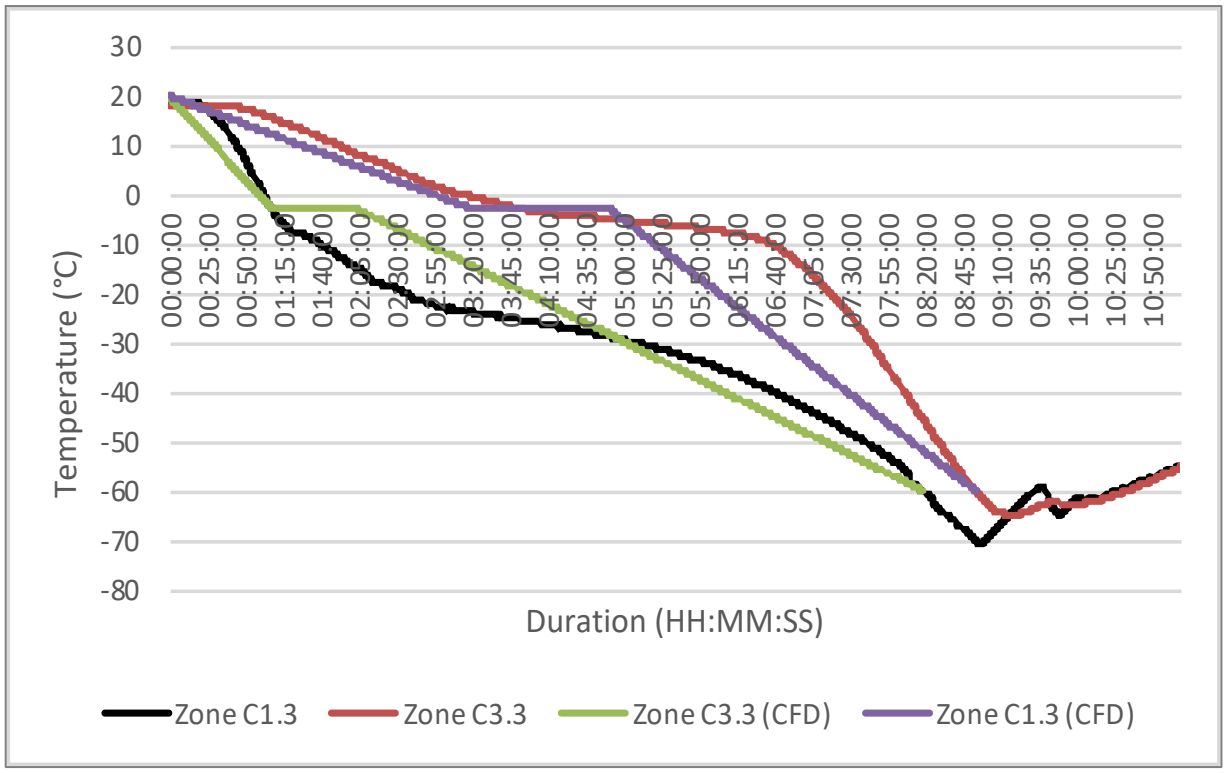

Figure 7-48: Zone C Plasma freezing curve at -60°C at 498RPM

Zone A

Figure 7-49 shows the freezing curve for Zone A, which is positioned in the wake stream of zone C as in Figure 7-10. The load is located behind zone C1.3, where the velocity is comparatively lower compared to the labelled zone number. The data reflects the trend previously defined in section 6.2.5.4, where the lack of convective effects leads to a decrease in heat transfer. The data reflected in zone A shows a similar trend with a further prolonged freezing time of 60 minutes. The differences across zone A as a whole are less evident, showing almost identical data profiles, indicating a similar level of circulation around the zone. The CFD results indicate fairly accurate predictions, with the maximum forecast deviation being 33% for A1.3.

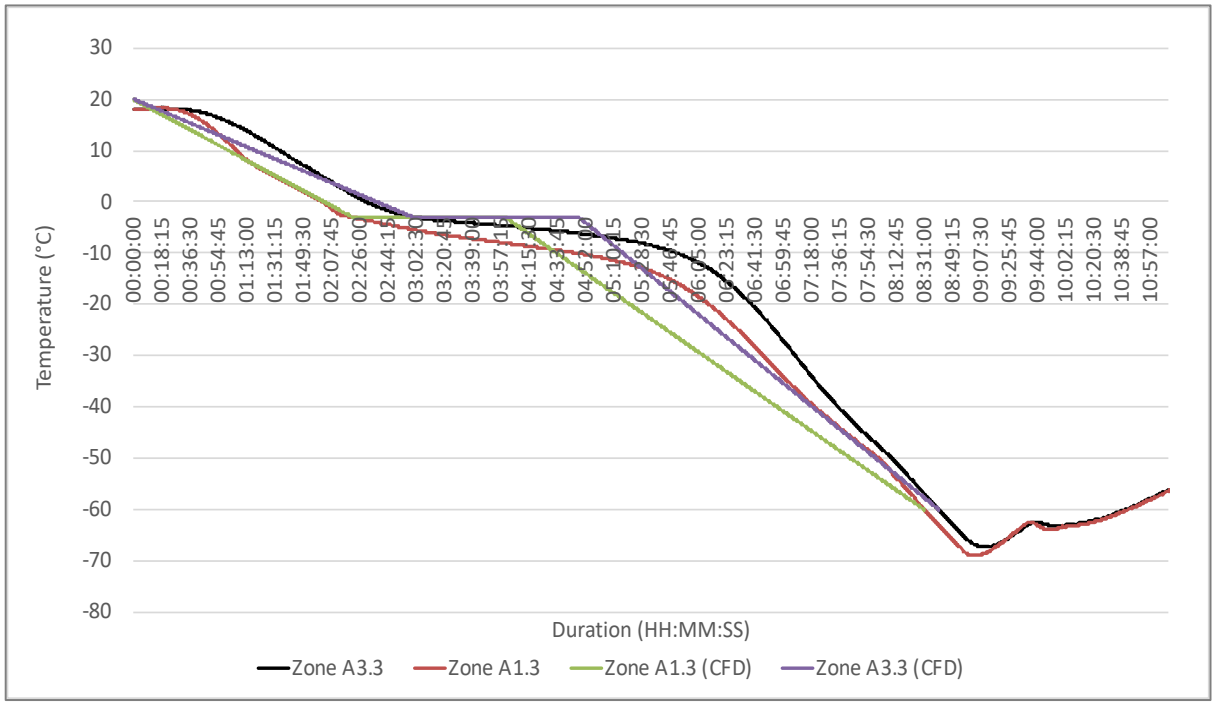

Figure 7-49: Zone A Plasma freezing curve at -60°C at 498RPM

Zone F

The results in Figure 7-50 reflect the decline in temperature in zone F, located close to the heat pipe but within the direct stream of the fan intake, as shown in Figure 7-10. The graphical results highlights a typical freezing curve where the decline is slightly prolonged due to the intake operation rather than a blower behaviour. As the fan intakes warmer air, the temperature differential between the plasma bag and air is comparatively low, resulting in a lower heat transfer rate. The associated CFD results show a maximum forecast deviation of 42% due to the assumed freezing curve allowed for the phase change period.

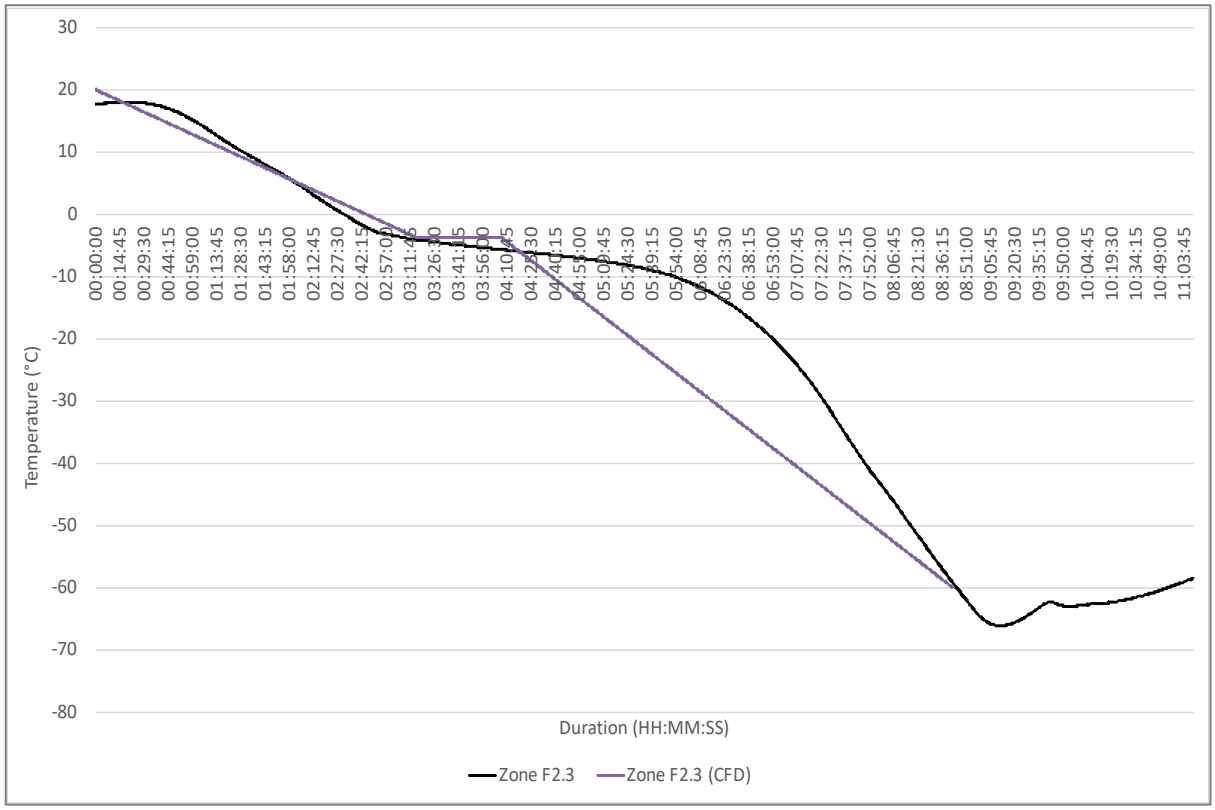

Figure 7-50: Zone F Plasma freezing curve at -60°C at 498RPM

Zone D

The results in Figure 7-51 show the freezing curve obtained for Zone D, where the loading zone reflects the positioning in the wake section as shown in Figure 7-10. The results highlight a typical freezing curve similar to the phase change diagram presented in chapter 5. The results demonstrate that both experimental sets of data have identical freezing curves past the phase change point. The associated CFD results show a fairly identical graphical profiles, with a maximum forecast accuracy of 7% for zone D3.3. The neighbouring plasma bag in zone D3.1 shows a comparatively larger maximum over-prediction of 66%.

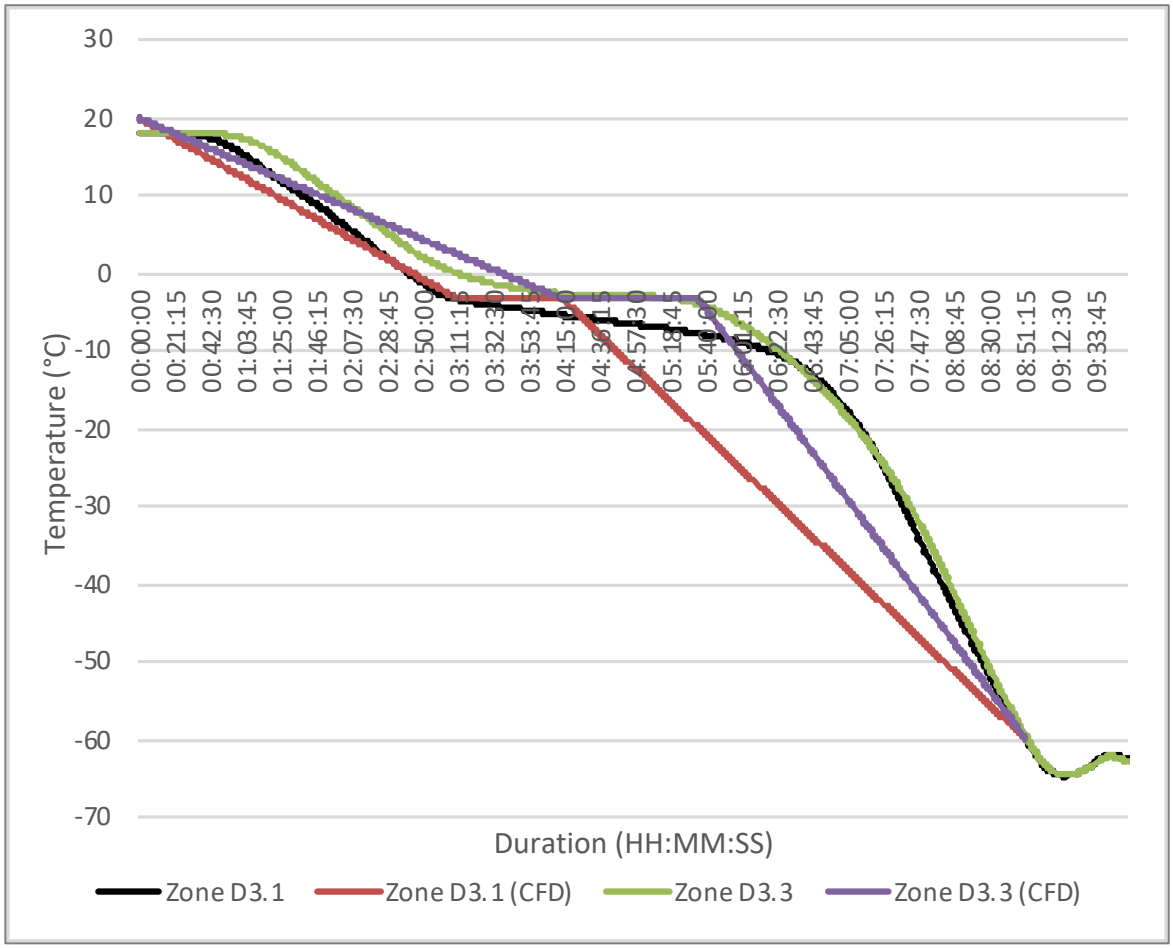

Figure 7-51: Zone D Plasma freezing curve at -60°C at 498RPM

Zone G

The results in Figure 7-52 show the freezing curve of Zone G, located towards the bottom of the freezing chamber in the wake section of zone I as shown in Figure 7-10. The data reflect the decline in temperature where the graphical data conforms to a typical freezing curve identified in chapter 5. The data reflects the decline in temperature to the set point temperature and, as the zone is located in a wake section, the decline is relatively prolonged. The zone produces a phase change time of approximately 60 minutes, whereas zone I had a phase change time of approximately 80 minutes. The effects of loading positions and wake streams have been an evident trend throughout the chapter. The associated forecast CFD results shows a deviation predicted forecast in comparison to the experimental data due to the entire effect and severity of the wake section being unaccounted due to the unpredictability.

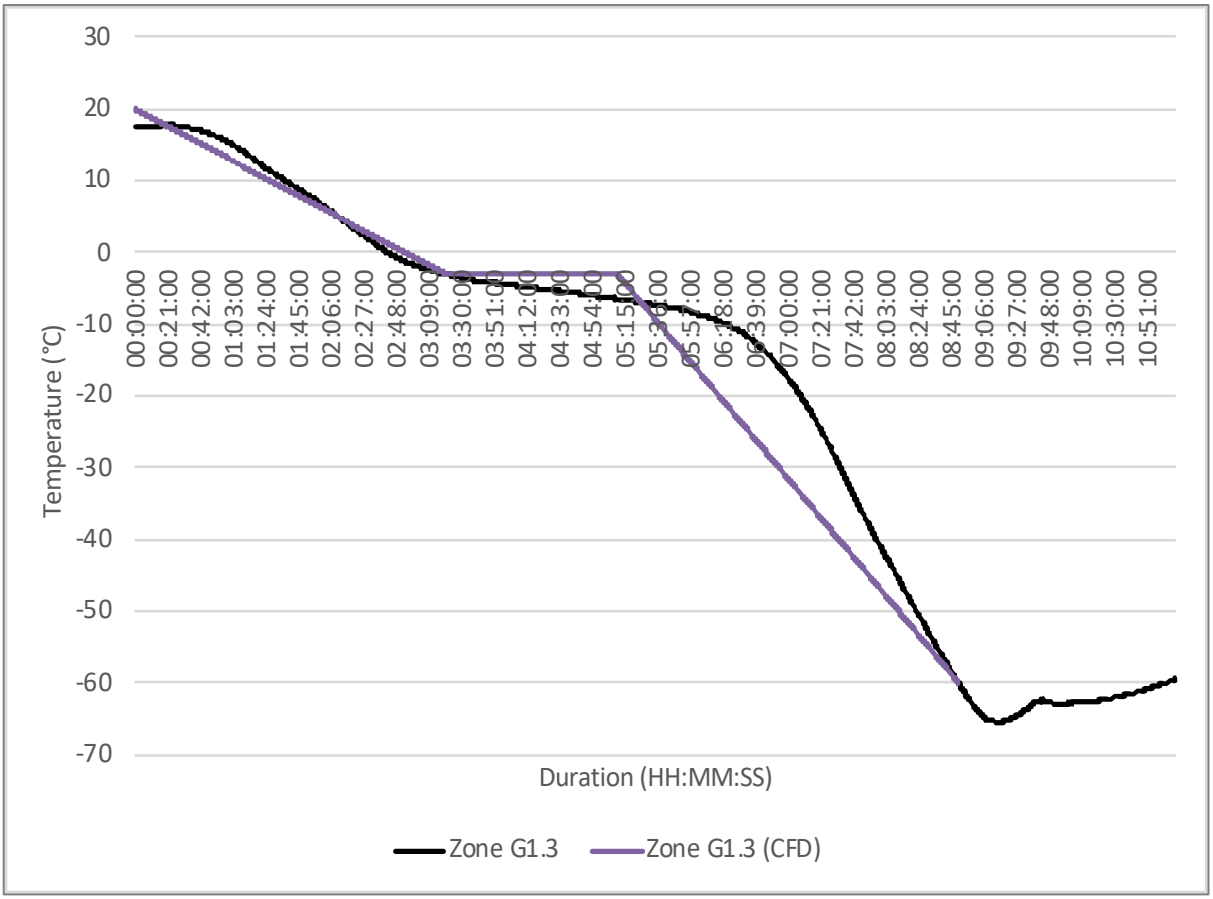

Figure 7-52: Zone G Plasma freezing curve at -60°C at 498RPM

Zone I

Zone I reflect the initial load on the bottom shelf within the chamber freezer as shown in Figure 7-10. The location of the zone is the closest to the heat pipe and fan flow stream in relation to the shelf. The data reflect the temperature decline to the set point temperature, where both plasma temperatures for zone I have similar and almost identical data trends. The loads are located close to the flow streams allowing for a decreased amount of phase change time. The CFD results indicate an accurate prediction for the phase change time, with zone I3.3 being slightly less accurate by a maximum of 24%.

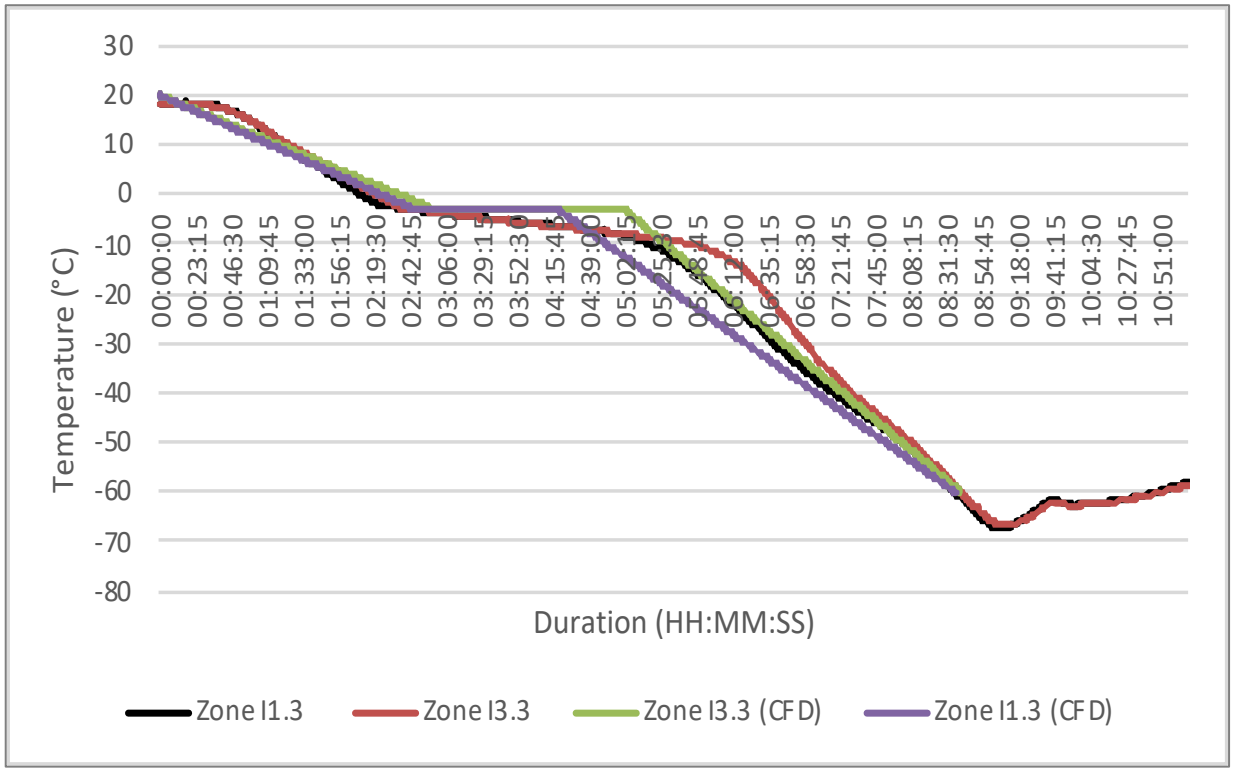

Figure 7-53: Zone I Plasma freezing curve at -60°C at 498RPM

7.3 Determination of Heat Transfer Coefficient

7.3.1 Injection based freezer Results

7.3.1.1 -40°C

The operation at -40°C reflects the obtained and average heat transfer coefficient of the system as shown in Figure 7-54. The data shown highlights the average convective heat transfer coefficient at each percentage of fan operation where 10% equates to 195 RPM and 100% equates to 1995RPM. The heat transfer coefficient obtained shows a positive trend with an increase in its value with the increase in forced convection due to the increased fan rotations. The data reflects minor fluctuations due to the change in positioning for each heat transfer coefficient calculation. The comparison between the left and right side highlight a level

of variation between the obtained heat transfer coefficient values. This may indicate a small discrepancy in the air distribution around the chamber space.

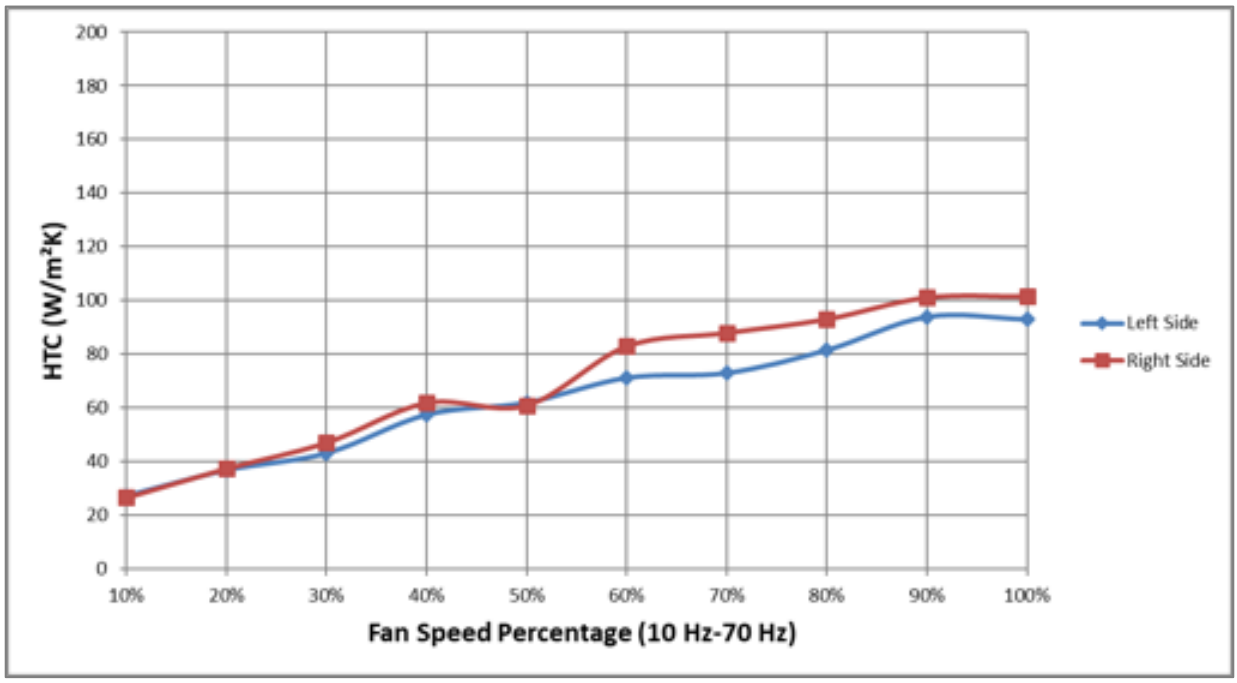

Figure 7-54: Heat Transfer Coefficient at -40°C

7.3.1.2 -50°C

The performance of heat transfer coefficients at -50°C is shown in Figure 7-55. The data highlights a similar trend presented in section 7.3.2.1 reflecting an increased convective heat transfer coefficient with an increase in fan rotations. The data highlights a level of variation which can be dependent on a number of factors including the positioning of the copper disc between left and right positions within the chamber. The discrepancy can highlight the velocity variation around the chamber space.

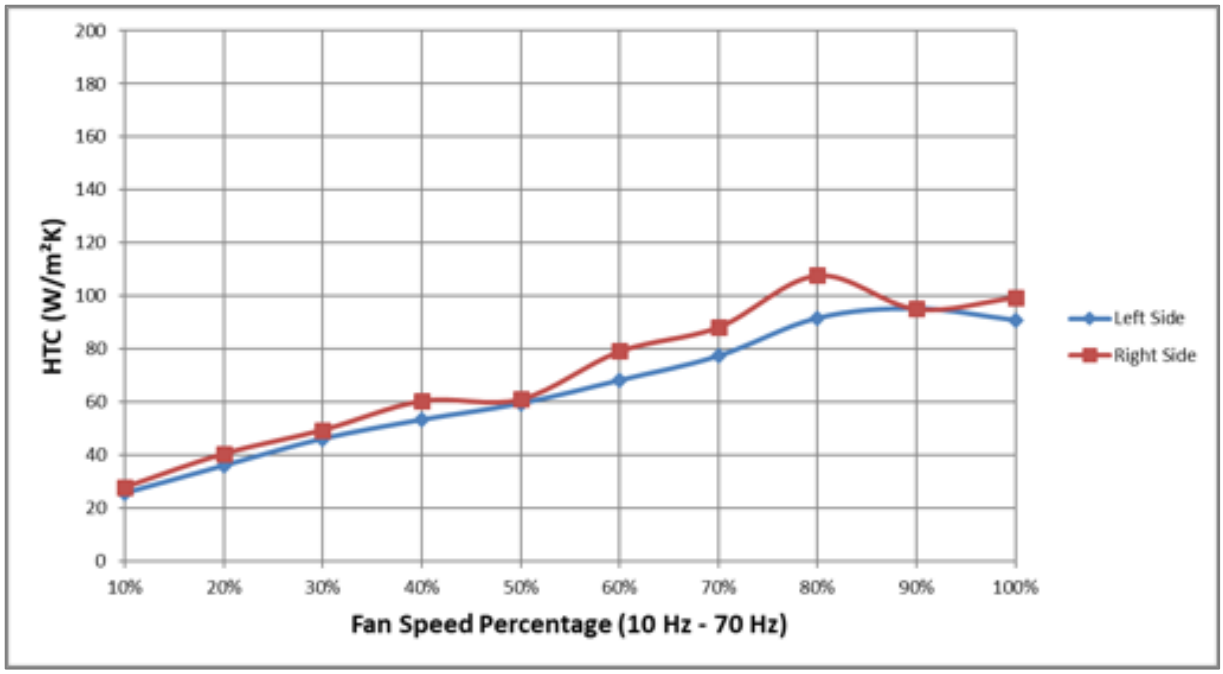

Figure 7-55: Heat Transfer Coefficient at -50°C

7.3.1.3 -60°C

Figure 7-56 presents the average convective heat transfer coefficients obtained with a -60°C set point, for a fan operation from 195RPM (10%) to 1995RPM (100%). The data shown highlights a positive trend with an increase in heat transfer coefficient as a result of increasing the level of forced convection. The averaged data reflects a discrepancy between both sides of the loading position which can potentially indicate uneven freezing chamber flow profile.

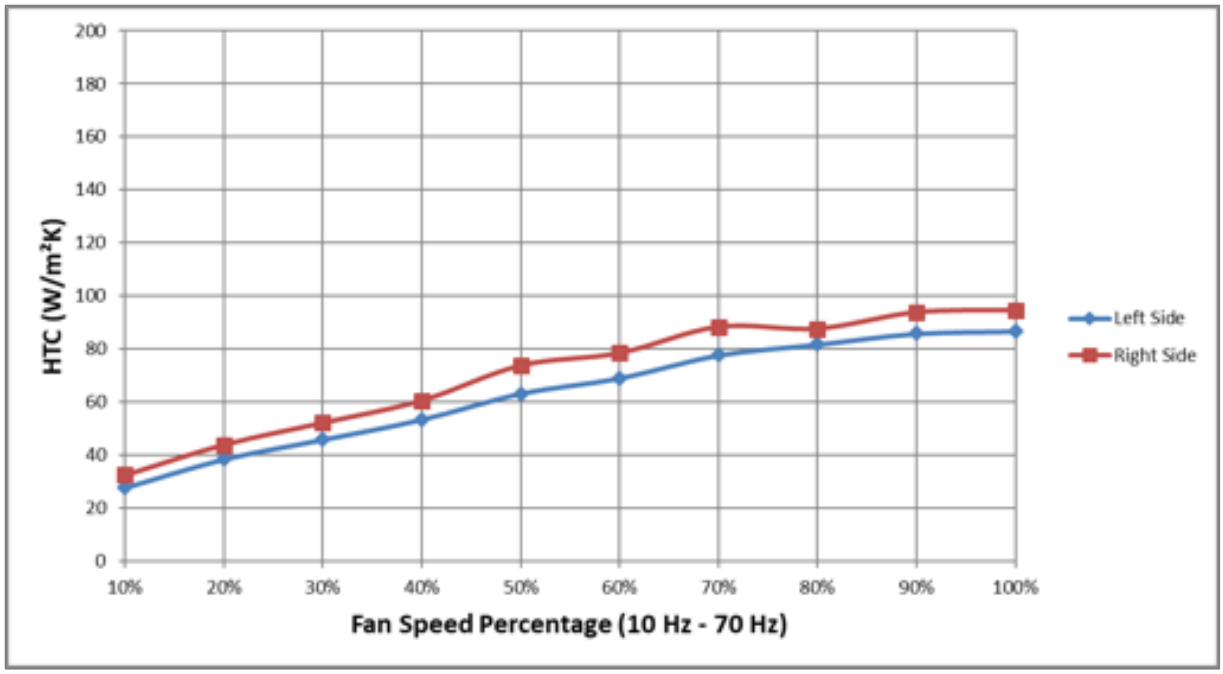

Figure 7-56: Heat Transfer Coefficient at -60°C

7.3.1.4 -70°C

Figure 7-57 shows the average convective heat transfer coefficient at a -70°C set point temperature, for a fan operating from 195RPM to 1995RPM.The data highlights an almost identical positive trend on both sides with minimal variation indicating a symmetrical load position.

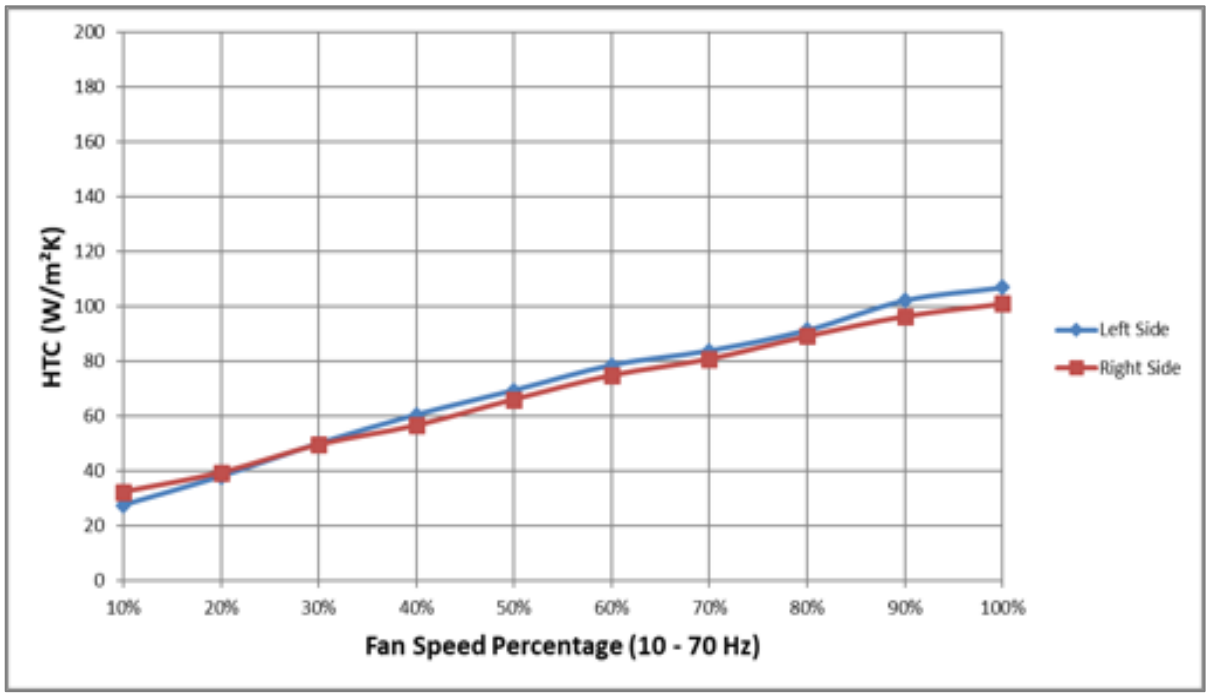

Figure 7-57: Heat Transfer Coefficient at -70°C

7.3.2 Heat Pipe Retrofitted Freezer

7.3.2.1 -40°C

7.3.2.1.1 285RPM

Figure 7-58 presents the steady state operation at -40°C at a 25% fan speed. The calculated heat transfer coefficient shows a similar trend as the injection-based system. Due to the increased temperature differential between the high temperature copper disc and the air temperature, resulting in a high heat transfer coefficient. This differential reduces due to the declining temperature of the copper disc to the equilibrium temperature, resulting in a decreasing heat transfer coefficient. The average heat transfer coefficient is: 31.2 W/m^{2}K

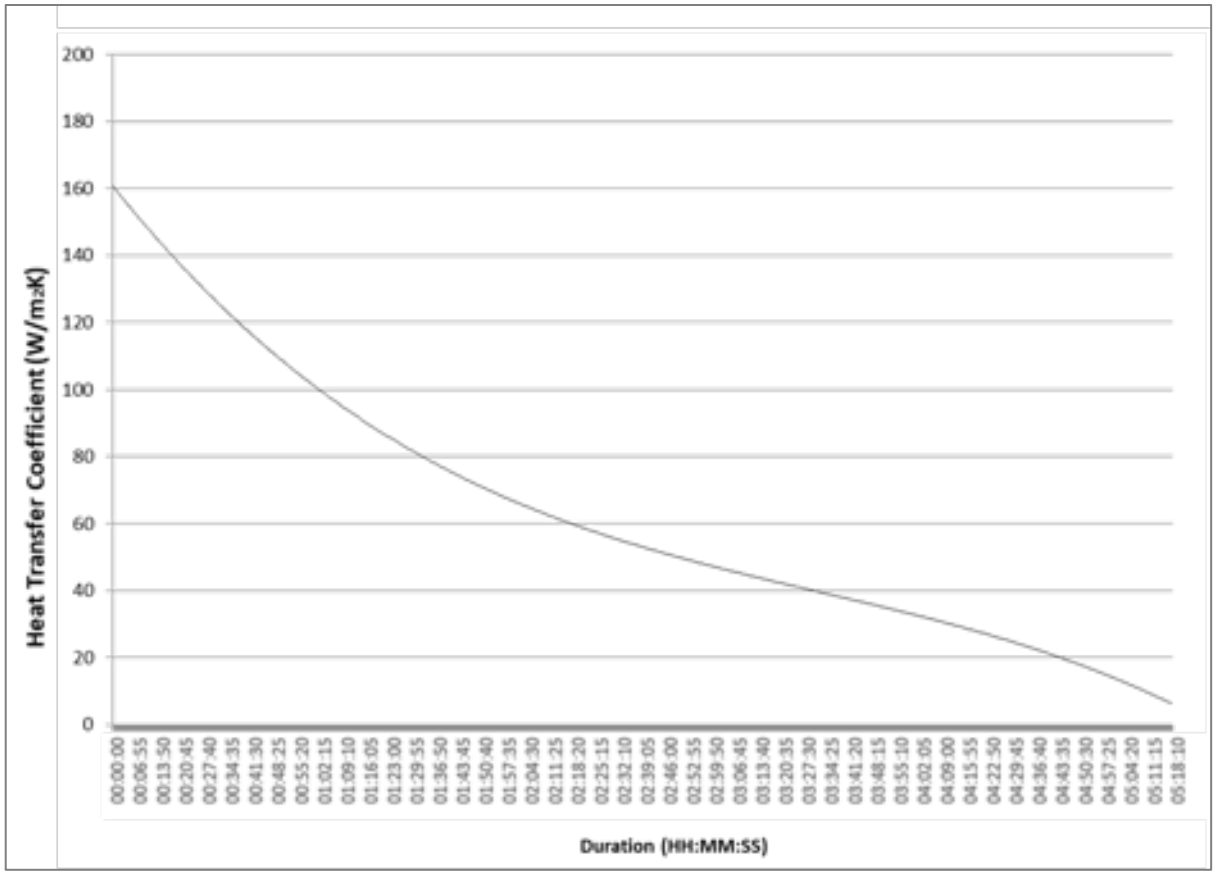

Figure 7-58: Heat Transfer Coefficient at -40°C at 285RPM

7.3.2.1.2 997RPM

The operation of the freezer at a higher fan speed results in a different profile in comparison to a 25% operation. Figure 7-59 shows the temperature profile in the general chamber space and the air temperature in the middle shelf. The temperature profile is jagged, to maintain the set point temperature during the cool down period of the hot copper disc. The variation during the steady state results in a slightly uneven profile shown in Figure 7-60. The associated heat transfer coefficient highlights a high heat transfer coefficient caused by the initial temperature differential but highlights a decline as the copper disc reaches equilibrium. The average heat transfer coefficient is: 49.11 W/m^{2}K

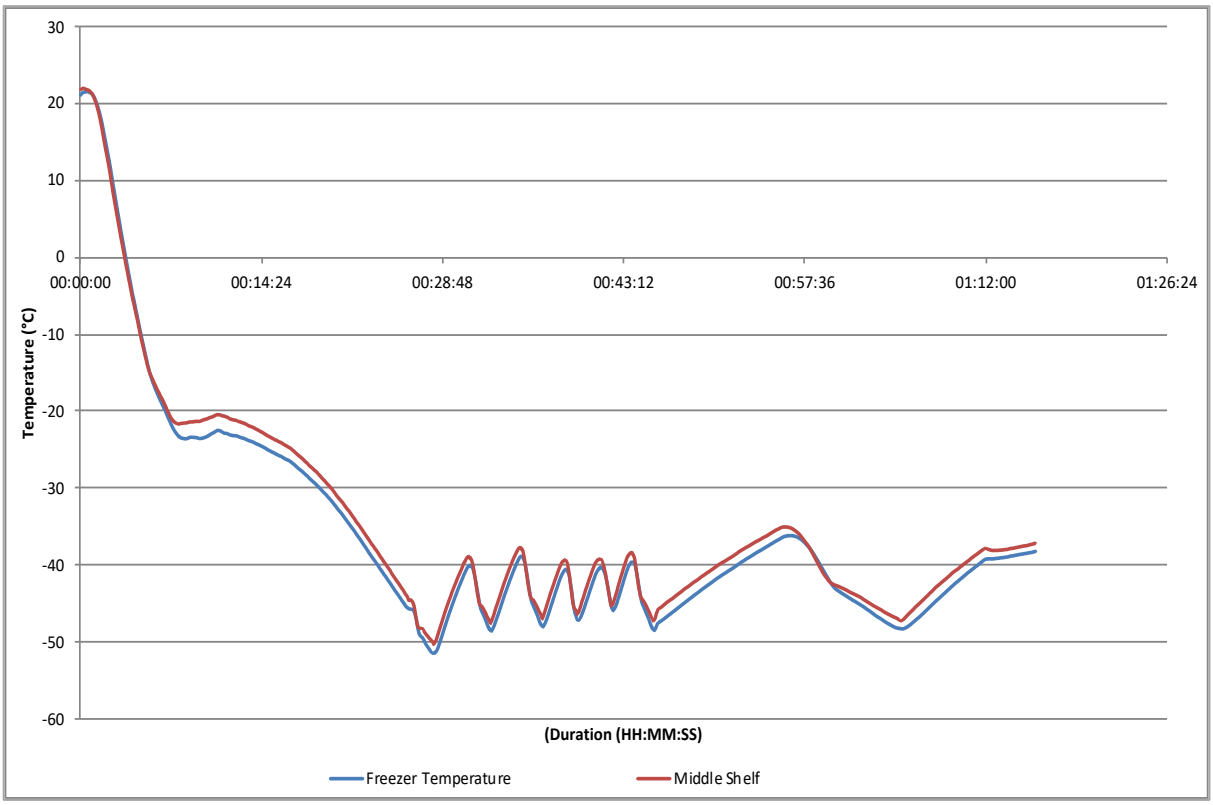

Figure 7-59: Temperature profile at -40°C Steady State

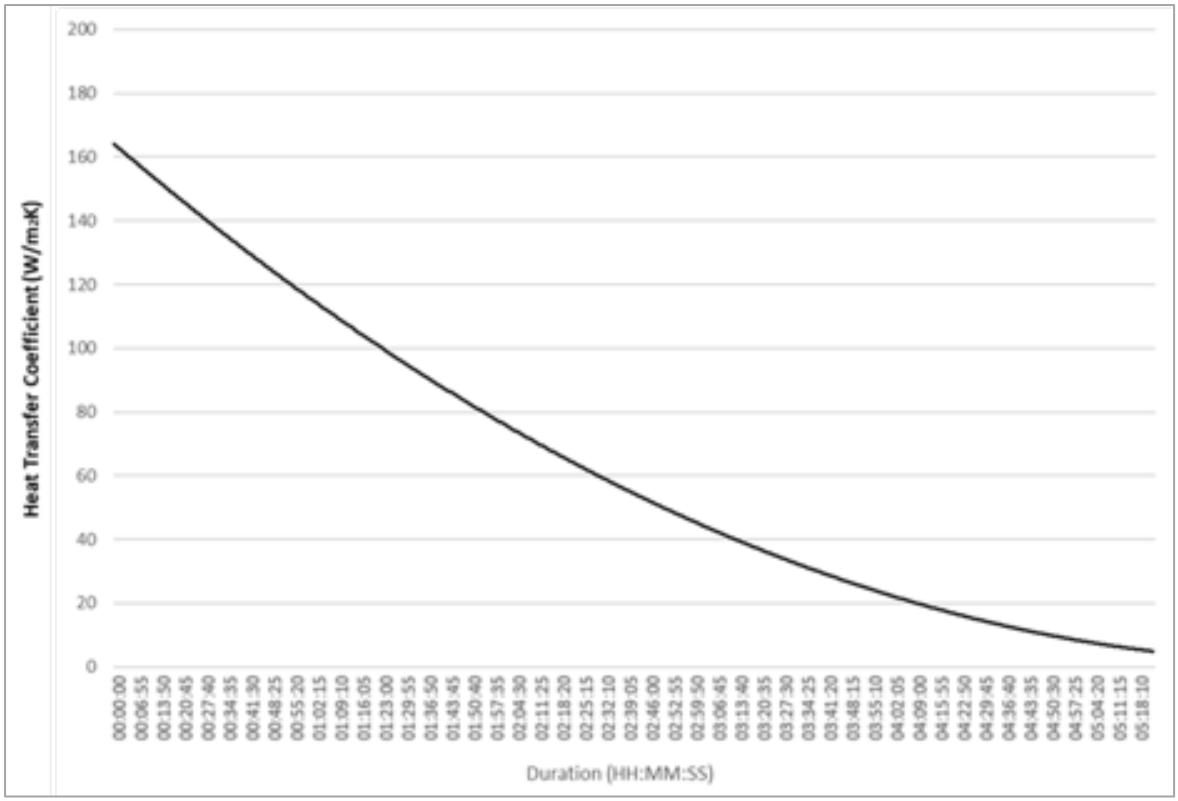

Figure 7-60: Heat Transfer Coefficient at -40°C and 997RPM

7.3.2.2 -50°C

7.3.2.2.1 285RPM

The operation at -50°C steady state at a 25% fan speed, is presented in Figure 7-61, highlighting the chamber temperature in relation to the air temperature measured in the middle shelf. The figure shows the decline to the set point temperature, with a slightly jagged profile due to maintenance of the chamber temperature. Figure 7-62 shows the corresponding heat transfer coefficient profile which indicates a significantly high heat transfer coefficient. at the initial conditions due to a large temperature differential. The trend is discussed in previous sections, and is related to the decline in heat transfer coefficient as the temperature difference decreases. The average heat transfer coefficient is: 48.11 W/m^2K

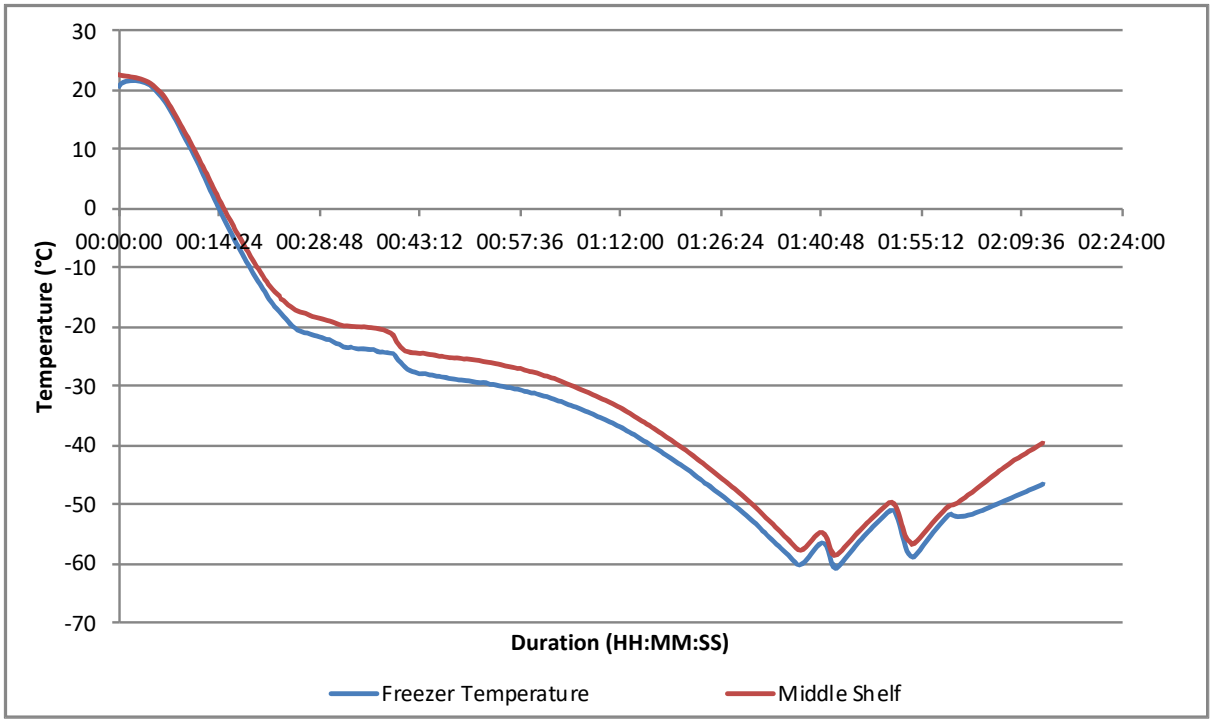

Figure 7-61: Temperature Profile at -50°C

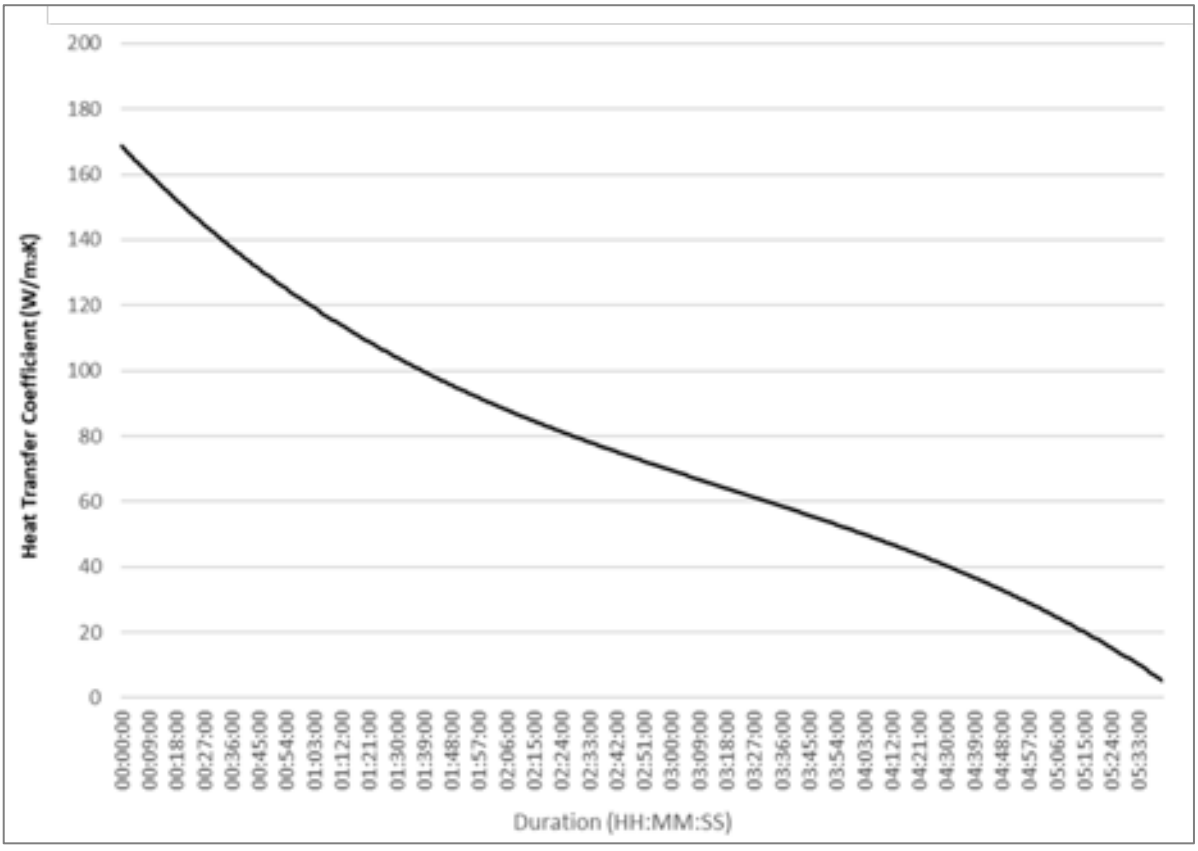

Figure 7-62: Heat Transfer Coefficient at -50°C and 285RPM

7.3.2.2.2 997RPM

The operation at a 50% fan speed shows a similar jagged profile shown in Figure 7-63 due to the control function of the liquid nitrogen feed. The result is a varying set point temperature related to a slight variation in the heat transfer coefficient during the decline to the equilibrium shown in Figure 7-64. The associated heat transfer coefficient data shows a similar trend to those previously presented with a high heat transfer coefficient due to a large temperature differential. The average heat transfer coefficient is: 58.6 W/m^{2}K

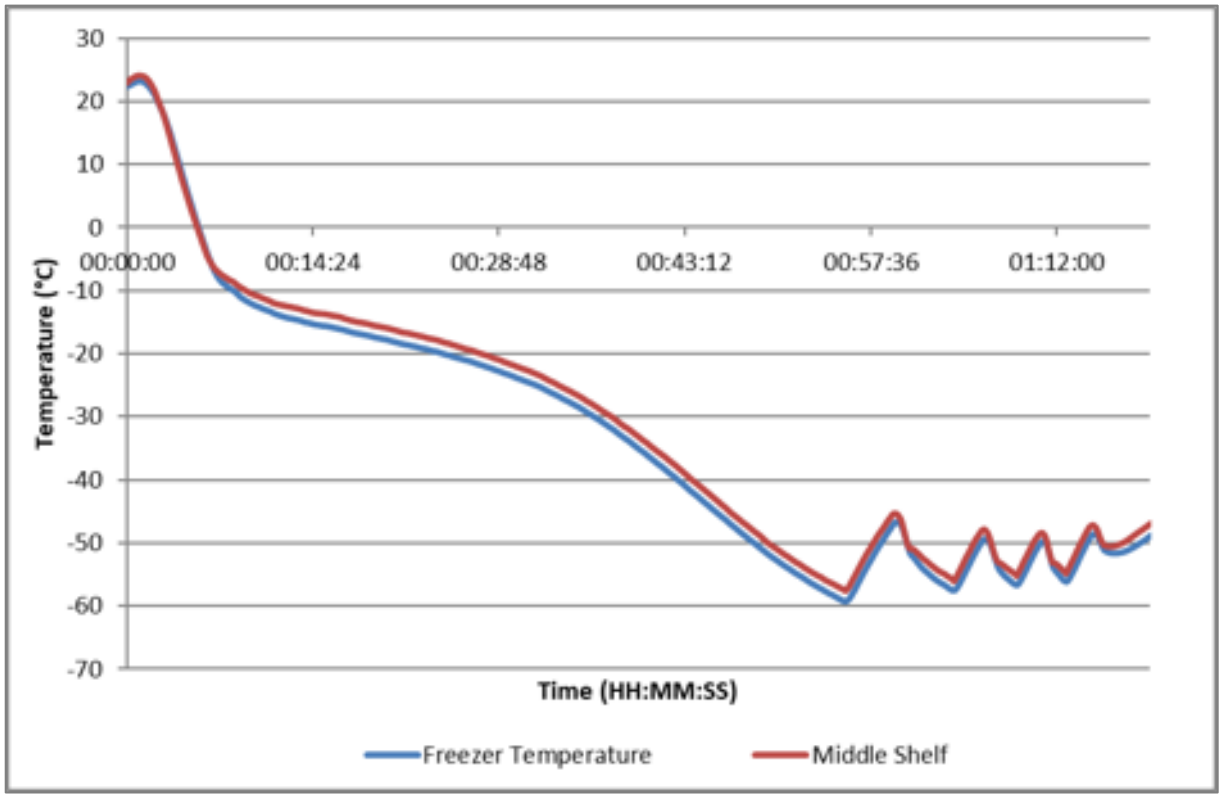

Figure 7-63: Temperature Profile of -50°C

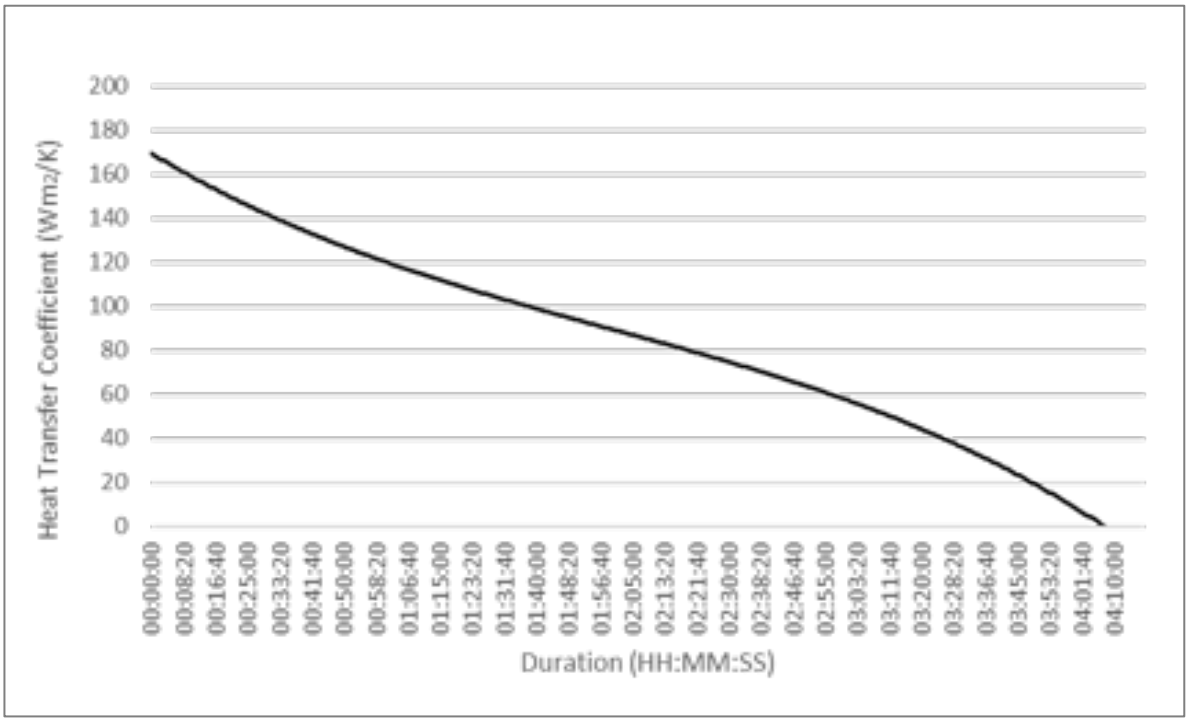

Figure 7-64: Heat Transfer Coefficient at -50°C and 997RPM

7.3.2.3 -60°C

7.3.2.3.1 285RPM

The calculated heat transfer coefficient shown in Figure 7-65 highlights an undisrupted profile indicating minimal thermal disruption. The data shows a recurring trend of an initially high heat transfer coefficient due to an initially high temperature differential. The subsequent decline in temperature reduces the differential, causing a lower heat transfer rate closer to the equilibrium. The average heat transfer coefficient is: 52.97 W/m^{2}K

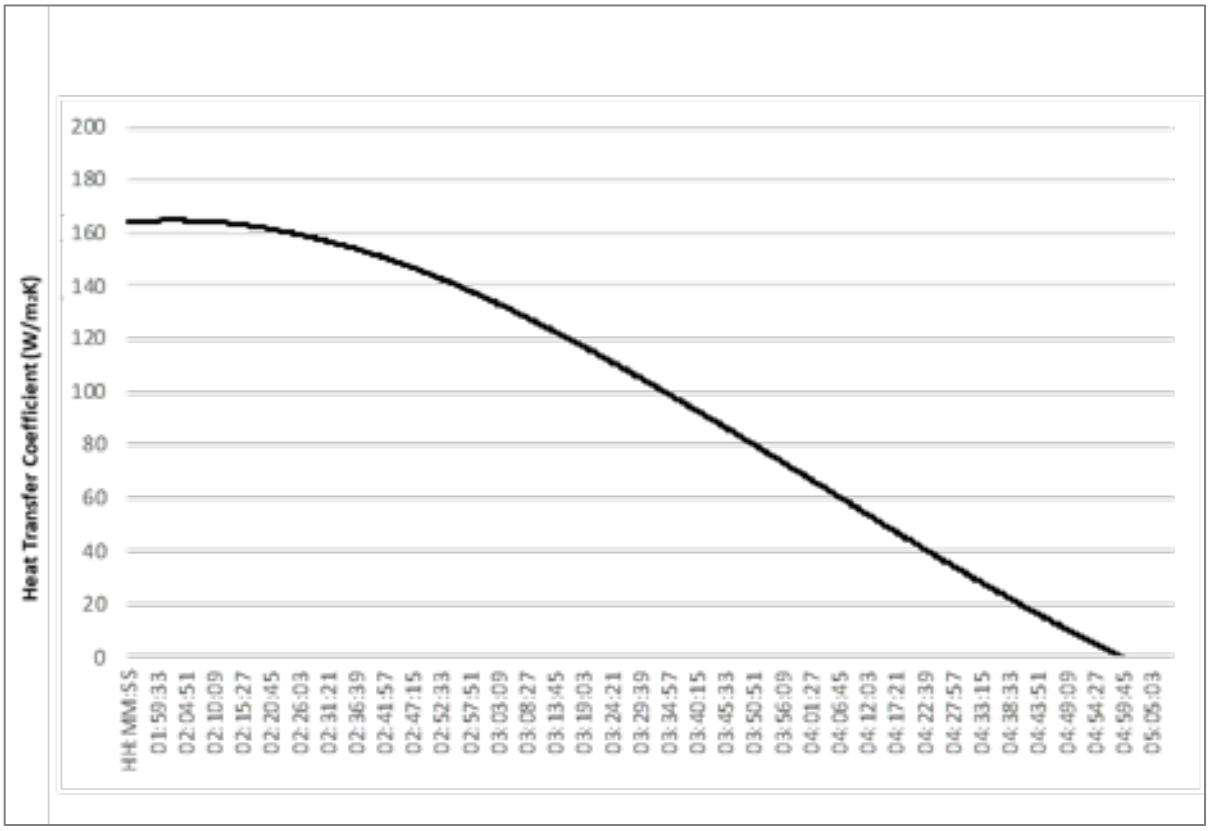

Figure 7-65: Heat transfer coefficient at -60°C at 285RPM

7.3.2.3.2 997RPM

Similarly to previous results, the operation at -60°C at a 50% fan speed shown in Figure 7-66 highlights a similar undisrupted regime, with minimal variation. The data shows a high heat transfer coefficient at the initial conditions due to the temperature difference between the copper disc and the chamber air temperature. The data then shows a decline due to the minimising differential between the copper disc and the chamber temperature. The average heat transfer coefficient is: 65.52 W/m^{2}K

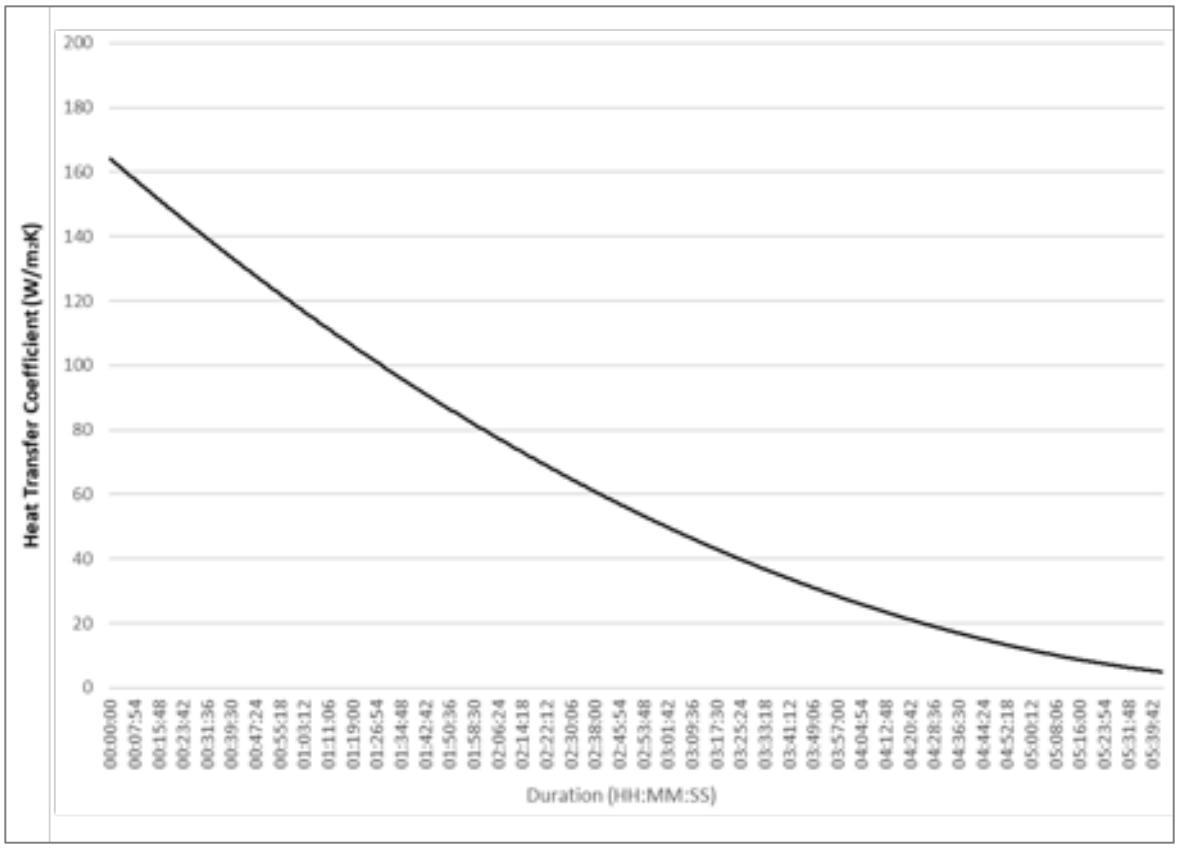

Figure 7-66: Heat transfer coefficient at -60°C at 997RPM

7.4: Chapter Conclusion

The chapter shows a direct comparison between a heat pipe based cryogenic freezer and an injection based cryogenic freezer. Both CFD and experimental results of the heat pipe model show an improved and homogeneous heat transfer in comparison to an injection based freezer. The data highlighted in Figure 7-67 shows the comparative performance characteristics to reach -40°C with a fan speed of 997RPM. The data reflecting the injection based freezer shows a rapid decline due to the high heat transfer coefficient of liquid nitrogen droplets. The data shows a level of stagnation to indicate the solidification process, the subsequent data shows a rapid decline to the set point temperature. The data reflecting the heat pipe freezer shows a significantly prolonged profile even with a cooler plasma bag load. The data shows the heat pipe to reach the set point temperature 40 minutes after the injection model. As this model exists as a proof of concept and an initial prototype, the data indicates the ability to freeze plasma bags using heat pipe technology.

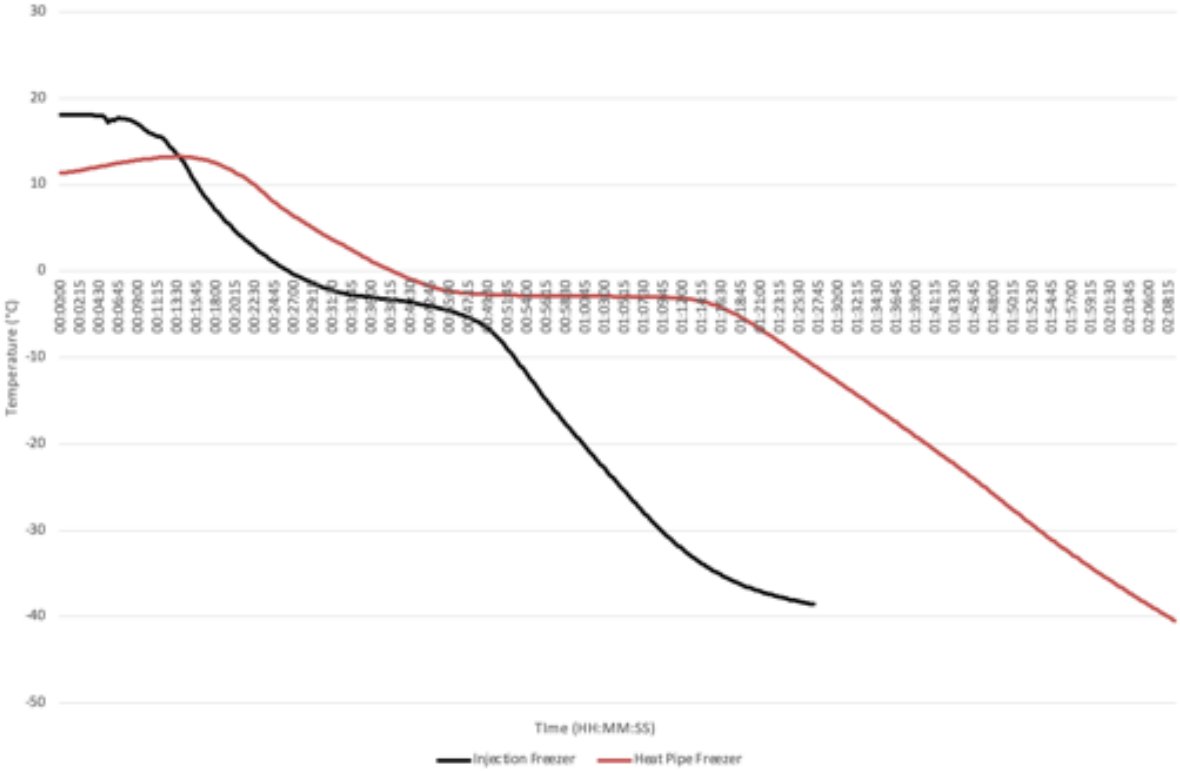

Figure 7-67: Freezer performance comparison

Chapter 8 :Conclusion and Recommendation for Future work

8.1 Conclusions

The outcomes from the research highlight the novel potential for passive cooling technologies allowing for a safer freezing regime. The heat pipe-based system maximises the benefits of heat pipe technology by allowing nearly continuous operation, with minimum downtime for repairs and maintenance. The simulation and validation of thermosyphon systems and multiphase modelling is increasing with the advances in technological developments. The research presented in this thesis highlights the development of a wickless heat pipe-based cryogenic freezer that allows a detailed view into the potentials and benefits of passive cooling technology. The retrofitting of an injection-based system to a heat pipe-based system in preservation technology allows for two identical systems to be mapped. The final result is an in-depth overview of their performance and changes in subsequent freezing patterns.

The numerical validation of the solidification process and the heat pipe-based cryogenic freezer was conducted by using ANSYS Fluent CFD. The software was used to define the chamber conditions investigated experimentally for different operational conditions, including set points and fan operation, highlighting the flexibility of the solver. Similarly, the simulations of solidification for the blood plasma simulant highlight the accuracy of the viscosity dependent UDF, given the lack of convection within the fluid. To improve the simulation accuracy, a user- defined function (UDF) was developed to account for the change in properties during the solidification process.

The work described in the thesis presents the following outcomes previously shown in Figure1-1.

Solidification of the blood plasma simulant:

- The first outcome highlights the study of the solidification of the blood plasma, in a three-dimensional geometry, with the consideration of forced convection and conduction surface boundary conditions. The study highlights a non-planar solidification process due to the change in boundary conditions throughout the plasma bag geometry. Given the assumptions made during the simulations, the results show good agreement with the experimental results whilst providing visualisation of the solidification process. The model highlights the solidification of the blood plasma simulant, with successful tracking of the

interface during the solidification process and definition of both liquid and solid phases. The results from the solidification investigation highlight the successful application of solidification outside the typical applications of the CFD model. With the nature of numerical models, a level of variance exists between simulated and experimental results due to omitted terms in the mathematical model which are evident. The definition of the solidification of the plasma simulant in chapter 5 highlighted the moving interface between the liquid and solid phases. The influence of external factors observed experimentally for a single load was validated to account for an additional resistance of a shelf. The external conditions affecting the solidification process observed were implemented as boundary conditions in the simulations, generating the favourable results shown in chapter 5

- Characterisation and development of a heat pipe based retrofitted freezer: The second outcome from the research developed in this thesis highlights the success of heat pipes within a retrofitted system, with the successful implementation of heat pipes for a cryogenic system, which has previously been unreported in the literature. The initial model was a baseline model where the main function was injection-based cryogenic freezing. The simulation is based on the freezing cycle to a defined set point (°C), and the results demonstrated a good agreement between the experimental plasma simulant temperature and the CFD model. The premise of the simulation is based on the change in temperature as a function of elapsed time. There is a level of variation in the physical experiment, which causes a high-level difference between the CFD model and the experimental results. As a comparison, the heat pipe was considered at identical conditions and a set value of thermal conductivity applied. The results of both systems reflect a temperature variation throughout the system, where the injection model shows a significantly high heat flux. The high heat flux is located towards the injectors, implying that a level of liquid nitrogen droplets impacts the shell of the plasma bag. This high heat flux creates a significant variation in the temperature distribution throughout the freezing chamber, where the loads located away from the injectors experience a significantly lower heat flux. In comparison, the heat pipe system shows a less extreme thermal progression, with a more coherent temperature distribution. The influence of the heat pipe is evident, leading to a more coherent freezing profile. The main difference in the operation between both is the freezing time. As the injection version is a fully commercialised unit, the freezing time is significantly quicker. In comparison, the retrofitted heat pipe model has a significantly slower freezing

time, but the system exists as a proof of concept prototype. The heat pipe model highlights the possibility to use remote cooling technologies for cryopreservation.

.

The collective results highlight the potentials of remote cooling, but both injection and heat pipe versions provided a visualisation within the chamber which would previously been unknown. The validation between both versions indicates that the CFD models are accurate and can be further used to investigate different operating conditions without the alteration of freezing chambers and experimental set ups.

8.2 Recommendations for Future Work

The research scope exists as a section of an overall design process as described in Appendix A. The development of the heat pipe-based cryogenic freezer has been expanded to the point of an almost commercially-ready system during the scope of this research. Throughout the progress of the research, potential areas for expansion have been identified for future work.

The following extensions to this research are recommended:

1. Further investigations should be carried out to identify the location in which solidification initially occurs. As the initial point of solidification is currently unknown, its identification can provide an insight into the crystallisation growth rate, which can affect the solidification pattern.
2. As the current solidification model only takes a single plasma bag into consideration, additional simulations would be recommended to investigate the change in solidification patterns as a result of series or parallel placed plasma bags.
3. The heat pipe heat exchanger installed within the freezing chamber exists as two tube bundles connected to an interlinked header, to eliminate dry out. The installed heat pipe is not finned, which is acceptable, but the heat pipe could be optimised to account for finned sections to maximise the effective thermal area. This recommendation can only be applied for the optimisation of the initial heat pipe system, and not for the expansion work listed in Appendix A.
4. The amount of applicable areas where passive cooling technologies are recommended is vastly expanding, where a controlled and non-reactive cooling technique is required. Although this remark is outside of the research scope of this thesis, recently a study was

conducted by Grandjean et al [98] regarding the potentials of cryogenic cooling to reduce the chemical reactivity within damaged lithium batteries during transportation. The application highlights the need for a passive but stable cooling technology, which could be to the advantage of the heat pipe technology.

References

[1] Dempsey P. The art of air blast freezing: Design and efficiency considerations. Appl Therm Eng 2012;41:71–83. doi:10.1016/J.APPLTHERMALENG.2011.12.013.

[2] Chourot JM, Macchi H, Fournaison L, Guilpart J. Technical and economical model for the freezing cost comparison of immersion, cryomechanical and air blast freezing processes. Energy Convers Manag 2003;44:559–71. doi:10.1016/S0196-8904(02)00071-7.

[3] Agnelli ME, Mascheroni RH. Cryomechanical freezing. A model for the heat transfer process. J Food Eng 2001;47:263–70. doi:10.1016/S0260-8774(00)00126-6.

[4] Pereira H, Haug F, Silva P, Wu J, Koettig T. Cryogenic loop heat pipes for the cooling of small particle detectors at cern. AIP Conf Proc 2010;1218:1039–46. doi:10.1063/1.3422264.

[5] Reay DA. Advances in Heat Pipe Technology. 1981.

[6] Preciado J, Rubinsky B. The effect of isochoric freezing on mammalian cells in an extracellular phosphate buffered solution. Cryobiology 2018;82:155–8. doi:10.1016/J.CRYOBIOL.2018.04.004.

[7] Liang D, Lin F, Yang G, Yue X, Zhang Q, Zhang Z, et al. Advantages of immersion freezing for quality preservation of litchi fruit during frozen storage. LWT - Food Sci Technol 2015;60:948–56. doi:10.1016/J.LWT.2014.10.034.

[8] Wan L, Powell-Palm MJ, Lee C, Gupta A, Weegman BP, Clemens MG, et al. Preservation of rat hearts in subfreezing temperature isochoric conditions to – 8 °C and 78 MPa. Biochem Biophys Res Commun 2018;496:852–7. doi:10.1016/J.BBRC.2018.01.140.

[9] Chauhan A, Trembley J, Wrobel LC, Jouhara H. Experimental and CFD validation of the thermal performance of a cryogenic batch freezer with the effect of loading. Energy 2019;171:77–94. doi:10.1016/J.ENERGY.2018.12.149.

[10] Mirade P-S, Kondjoyan A, Daudin J-D. Three-dimensional CFD calculations for designing large food chillers. Comput Electron Agric 2002;34:67–88. doi:10.1016/S0168-1699(01)00180-6.

[11] Alberto Dopazo J, Fernández-Seara J. Experimental evaluation of freezing processes in horizontal plate freezers using CO2 as refrigerant. Int J Refrig 2012;35:2093–101. doi:10.1016/J.IJREFRIG.2012.08.018.

[12] Fadhl B, Wrobel LC, Jouhara H. CFD modelling of a two-phase closed thermosyphon charged with R134a and R404a. Appl Therm Eng 2015;78:482–90. doi:10.1016/j.applthermaleng.2014.12.062.

[13] Jouhara H, Meskimmon R. An investigation into the use of water as a working fluid in wraparound loop heat pipe heat exchanger for applications in energy efficient HVAC systems. Energy 2018;156:597–605. doi:10.1016/J.ENERGY.2018.05.134.

[14] Xu D, Li L, Liu H. Experimental investigation on the thermal performance of helium based cryogenic pulsating heat pipe. Exp Therm Fluid Sci 2016;70:61–8. doi:10.1016/J.EXPTHERMFLUSCI.2015.08.024.

[15] Goyal M, Suleria H, Kirubanandan S. Technological Processes for Marine Foods, From Water to Fork: Bioactive Compounds, Industrial Applications, and Genomics (Innovations in Agricultural & Biological Engineering). 2019.

[16] CREED PG, JAMES SJ. Heat Transfer During the Freezing of Liver in a Plate Freezer. J Food Sci 1985;50:285–8. doi:10.1111/j.1365-2621.1985.tb13383.x.

[17] Alberto Dopazo J, Fernández-Seara J. Experimental evaluation of freezing processes in horizontal plate freezers using CO2 as refrigerant. Int J Refrig 2012;35:2093–101. doi:10.1016/j.ijrefrig.2012.08.018.

[18] Wang J, Yang X-H, Mujumdar AS, Wang D, Zhao J-H, Fang X-M, et al. Effects of various blanching methods on weight loss, enzymes inactivation, phytochemical contents, antioxidant capacity, ultrastructure and drying kinetics of red bell pepper (Capsicum annuum L.). LWT 2017;77:337–47. doi:10.1016/J.LWT.2016.11.070.
[19] Liang D, Lin F, Yang G, Yue X, Zhang Q, Zhang Z, et al. Advantages of immersion freezing for quality preservation of litchi fruit during frozen storage. LWT - Food Sci Technol 2015;60:948–56. doi:10.1016/J.LWT.2014.10.034.
[20] Galetto CD, Verdini RA, Zorrilla SE, Rubiolo AC. Freezing of strawberries by immersion in CaCl2 solutions. Food Chem 2010;123:243–8. doi:10.1016/J.FOODCHEM.2010.04.018.
[21] Alhamdan A, Hassan B, Alkahtani H, Abdelkarim D, Younis M. Cryogenic freezing of fresh date fruits for quality preservation during frozen storage. J Saudi Soc Agric Sci 2018;17:9–16. doi:10.1016/J.JSSAS.2015.12.001.
[22] Agnelli M., Mascheroni R. Quality evaluation of foodstuffs frozen in a cryomechanical freezer. J Food Eng 2002;52:257–63. doi:10.1016/S0260-8774(01)00113-3.
[23] Ribero GG, Rubiolo AC, Zorrilla SE. Microstructure of Mozzarella cheese as affected by the immersion freezing in NaCl solutions and by the frozen storage. J Food Eng 2009;91:516–20. doi:10.1016/J.JFOODENG.2008.09.029.
[24] Sun W, Zhong W, Zhang Y. LES-DPM simulation of turbulent gas-particle flow on opposed round jets. Powder Technol 2015;270:302–11. doi:10.1016/j.powtec.2014.10.039.
[25] Sun Q, Sun F, Xia X, Xu H, Kong B. The comparison of ultrasound-assisted immersion freezing, air freezing and immersion freezing on the muscle quality and physicochemical properties of common carp (Cyprinus carpio) during freezing storage. Ultrason Sonochem 2019;51:281–91. doi:10.1016/J.ULTSONCH.2018.10.006.
[26] Volkert M, Ananta E, Luscher C, Knorr D. Effect of air freezing, spray freezing, and pressure shift freezing on membrane integrity and viability of Lactobacillus rhamnosus GG. J Food Eng 2008;87:532–40. doi:10.1016/J.JFOODENG.2008.01.008.
[27] Gazda W. Application possibilities of the strategies of the air blast–cryogenic cooling process. Energy 2013;62:113–9. doi:10.1016/J.ENERGY.2013.06.054.
[28] Dima JB, Santos MV, Baron PJ, Califano A, Zaritzky NE. Experimental study and numerical modeling of the freezing process of marine products. Food Bioprod Process 2014;92:54–66. doi:10.1016/j.fbp.2013.07.012.
[29] Becker BR, Fricke BA. Heat transfer coefficients for forced-air cooling and freezing of selected foods. Int J Refrig 2004;27:540–51. doi:10.1016/J.IJREFRIG.2004.02.006.
[30] Reno MJ, Resende JV, Peres AP, Giarolla TMO, Prado MET. Heat transfer and energy consumption in the freezing of guava pulp in large containers. Appl Therm Eng 2011;31:545–55. doi:10.1016/J.APPLTHERMALENG.2010.10.015.
[31] Otero L, Pérez-Mateos M, Rodríguez AC, Sanz PD. Electromagnetic freezing: Effects of weak oscillating magnetic fields on crab sticks. J Food Eng 2017;200:87–94. doi:10.1016/J.JFOODENG.2016.12.018.
[32] Otero L, Pérez-Mateos M, Rodríguez AC, Sanz PD. Electromagnetic freezing: Effects of weak oscillating magnetic fields on crab sticks. J Food Eng 2017;200:87–94. doi:10.1016/J.JFOODENG.2016.12.018.
[33] Kobayashi A, Kirschvink JL. A ferromagnetic model for the action of electric and magnetic fields in cryopreservation. Cryobiology 2014;68:163–5. doi:10.1016/J.CRYOBIOL.2013.12.002.
[34] Dalvi-Isfahan M, Hamdami N, Xanthakis E, Le-Bail A. Review on the control of ice nucleation by ultrasound waves, electric and magnetic fields. J Food Eng 2017;195:222–34. doi:10.1016/J.JFOODENG.2016.10.001.
[35] Kaku M, Kamada H, Kawata T, Koseki H, Abedini S, Kojima S, et al. Cryopreservation of periodontal ligament cells with magnetic field for tooth banking. Cryobiology 2010;61:73–8. doi:10.1016/J.CRYOBIOL.2010.05.003.

[36] Lyu C, Nastase G, Ukpai G, Serban A, Rubinsky B. A comparison of freezing-damage during isochoric and isobaric freezing of the potato. PeerJ 2017;5:e3322.
[37] Bilbao-Sainz C, Sinrod A, Powell-Palm M, Dao L, Takeoka G, Williams T, et al. Preservation of sweet cherry by isochoric (constant volume) freezing. Innov Food Sci Emerg Technol 2018. doi:10.1016/J.IFSET.2018.10.016.
[38] Năstase G, Lyu C, Ukpai G, Şerban A, Rubinsky B. Isochoric and isobaric freezing of fish muscle. Biochem Biophys Res Commun 2017;485:279–83. doi:10.1016/J.BBRC.2017.02.091.
[39] Wan L, Powell-Palm MJ, Lee C, Gupta A, Weegman BP, Clemens MG, et al. Preservation of rat hearts in subfreezing temperature isochoric conditions to – 8 °C and 78 MPa. Biochem Biophys Res Commun 2018;496:852–7. doi:10.1016/J.BBRC.2018.01.140.
[40] Takahashi T, Kakita A, Takahashi Y, Yokoyama K, Sakamoto I, Yamashina S. Preservation of rat livers by supercooling under high pressure. Transplant Proc 2001;33:916–9. doi:10.1016/S0041-1345(00)02268-5.
[41] Kannan M, Senthil R, Baskaran R, Deepanraj B. An experimental study on heat transport capability of a two phase thermosyphon charged with different working fluids. Am J Appl Sci 2014;11:584–91. doi:10.3844/ajassp.2014.584.591.
[42] Sureshkumar R, Mohideen ST, Nethaji N. Heat transfer characteristics of nanofluids in heat pipes: A review. Renew Sustain Energy Rev 2013;20:397–410.
[43] Jouhara H. Heat Pipes (Gravity Assisted and Capillary-Driven), Heat Exchanger Design Handbook. Begell House 2019.
[44] Jouhara H, Meskimmon R. Experimental investigation of wraparound loop heat pipe heat exchanger used in energy efficient air handling units. Energy 2010. doi:10.1016/j.energy.2010.03.056.
[45] Jouhara H, Meskimmon R. An investigation into the use of water as a working fluid in wraparound loop heat pipe heat exchanger for applications in energy efficient HVAC systems. Energy 2018;156:597–605. doi:10.1016/J.ENERGY.2018.05.134.
[46] Aprea C, Greco A, Maiorino A, Masselli C. The drop-in of HFC134a with HFO1234ze in a household refrigerator. Int J Therm Sci 2018;127:117–25. doi:10.1016/J.IJTHERMALSCI.2018.01.026.
[47] Illán-Gómez F, García-Cascales JR. Experimental comparison of an air-to-water refrigeration system working with R134a and R1234yf. Int J Refrig 2019;97:124–31. doi:10.1016/J.IJREFRIG.2018.09.026.
[48] Jouhara H, Chauhan A, Nannou T, Almahmoud S, Delpech B, Wrobel LC. Heat pipe based systems - Advances and applications. Energy 2017;128:729–54. doi:10.1016/j.energy.2017.04.028.
[49] Barrak AS, Saleh AAM, Naji ZH. An experimental study of using water, methanol, and binary fluids in oscillating heat pipe heat exchanger. Eng Sci Technol an Int J 2019. doi:10.1016/J.JESTCH.2019.05.010.
[50] Jouhara H, Nannou T, Ghazal H, Kayyali R, Tassou SA, Lester S. Temperature and energy performance of open refrigerated display cabinets using heat pipe shelves. Energy Procedia 2017;123:273–80. doi:10.1016/J.EGYPRO.2017.07.240.
[51] Hao T, Ma H, Ma X. Heat transfer performance of polytetrafluoroethylene oscillating heat pipe with water, ethanol, and acetone as working fluids. Int J Heat Mass Transf 2019;131:109–20. doi:10.1016/J.IJHEATMASSTRANSFER.2018.08.133.
[52] Guo Y, Lin G, He J, Bai L, Sun Y, Zhang H, et al. Experimental analysis of operation failure for a neon cryogenic loop heat pipe. Int J Heat Mass Transf 2019;138:96–108. doi:10.1016/J.IJHEATMASSTRANSFER.2019.04.045.
[53] Guo Y, Lin G, Zhang H, Miao J. Investigation on thermal behaviours of a methane charged cryogenic loop heat pipe. Energy 2018;157:516–25. doi:10.1016/J.ENERGY.2018.05.133.
[54] Chen X, Lin Y, Shao S, Wu W. Study on heat transfer characteristics of ethane pulsating

heat pipe in middle-low temperature region. Appl Therm Eng 2019;152:697–705. doi:10.1016/J.APPLTHERMALENG.2019.02.125.
[55] Sarafraz MM, Hormozi F. Experimental study on the thermal performance and efficiency of a copper made thermosyphon heat pipe charged with alumina–glycol based nanofluids. Powder Technol 2014;266:378–87. doi:10.1016/j.powtec.2014.06.053.
[56] Gupta NK, Tiwari AK, Ghosh SK. Heat transfer mechanisms in heat pipes using nanofluids – A review. Exp Therm Fluid Sci 2018;90:84–100. doi:10.1016/J.EXPTHERMFLUSCI.2017.08.013.
[57] Long ZQ, Zhang P. Impact of cooling condition and filling ratio on heat transfer limit of cryogenic thermosyphon. Cryogenics (Guildf) 2012;52:66–76. doi:10.1016/J.CRYOGENICS.2011.11.004.
[58] Long ZQ, Zhang P. Experimental investigation of the heat transfer characteristics of a helium cryogenic thermosyphon. Cryogenics (Guildf) 2013;57:95–103. doi:10.1016/J.CRYOGENICS.2013.04.006.
[59] Bolozdynya AI, Dmitrenko VV, Efremenko YV, Khromov AV, Shafigullin RR, Shakirov AV, et al. The two-phase closed tubular cryogenic thermosyphon. Int J Heat Mass Transf 2015;80:159–62. doi:10.1016/J.IJHEATMASSTRANSFER.2014.09.001.
[60] Bai L, Lin G, Zhang H, Miao J, Wen D. Experimental study of a nitrogen-charged cryogenic loop heat pipe. Cryogenics (Guildf) 2012;52:557–63. doi:10.1016/J.CRYOGENICS.2012.07.005.
[61] Yan T, Zhao Y, Liang J, Liu F. Investigation on optimal working fluid inventory of a cryogenic loop heat pipe. Int J Heat Mass Transf 2013;66:334–7. doi:10.1016/J.IJHEATMASSTRANSFER.2013.07.043.
[62] Mottet L. Heat and Mass transfer in the porous wickof a capillary evaporator. 2014.
[63] Khandekar S. PULSATING HEAT PIPE BASED HEAT EXCHANGERS 2020.
[64] Liang Q, Li Y, Wang Q. Experimental investigation on the performance of a neon cryogenic oscillating heat pipe. Cryogenics (Guildf) 2017;84:7–12. doi:10.1016/J.CRYOGENICS.2017.03.004.
[65] Li Y, Wang Q, Chen S, Zhao B, Dai Y. Experimental investigation of the characteristics of cryogenic oscillating heat pipe. Int J Heat Mass Transf 2014;79:713–9. doi:10.1016/J.IJHEATMASSTRANSFER.2014.08.061.
[66] Kreith F, Manglik RM, Bohn MS. Principles of heat transfer. Cengage learning; 2012.
[67] Churchill SW, Bernstein M. A Correlating Equation for Forced Convection From Gases and Liquids to a Circular Cylinder in Crossflow. J Heat Transfer 1977;99:300–6. doi:10.1115/1.3450685.
[68] Dewey Jr CF. A correlation of convective heat transfer and recovery temperature data for cylinders in compressible flow. Int J Heat Mass Transf 1965;8:245–52.
[69] Krokida MK, Zogzas NP, Maroulis ZB. Heat transfer coefficient in food processing: compilation of literature data. Int J Food Prop 2002;5:435–50.
[70] Hasan MR, Vo TQ, Kim B. Manipulating thermal resistance at the solid–fluid interface through monolayer deposition. RSC Adv 2019;9:4948–56.
[71] Aamir M, Liao Q, Zhu X, Wang H. Study On Ultra-fast Cooling Behaviors of Water Spray Cooled Stainless Steel Plates 2015.
[72] Nishikawa K, Fujita Y, Ohta H, Hidaka S. Effect of the surface roughness on the nucleate boiling heat transfer over the wide range of pressure. Int. Heat Transf. Conf. Digit. Libr., Begel House Inc.; 1982.
[73] Stephan K, Abdelsalam M. Heat-transfer correlations for natural convection boiling. Int J Heat Mass Transf 1980;23:73–87. doi:http://dx.doi.org/10.1016/0017-9310(80)90140-4.
[74] Kutateladze SS. Fundamentals of Heat Transfer (2nd Edn.) Edward Arnold. New York 1963:247.
[75] Danilova GN. Correlation of boiling heat transfer data for Freons. Heat Transf Res

1970;2:73–8.
[76] Rohsenow WM. A method of correlating heat transfer data for surface boiling of liquids. Cambridge, Mass.: MIT Division of Industrial Cooporation,[1951]; 1951.
[77] Guichet V, Jouhara H. Condensation, evaporation and boiling of falling films in wickless heat pipes (two-phase closed thermosyphons): A critical review of correlations. Int J Thermofluids 2019:100001. doi:10.1016/J.IJFT.2019.100001.
[78] Nusselt W. The condensation of steam on cooled surfaces. VDI-Zs 1916;60:541.
[79] Rohsenow WM. Heat transfer and temperature distribution in laminar film condensation. Trans Asme 1956;78:1645–8.
[80] Jouhara H, Robinson AJ. Experimental investigation of small diameter two-phase closed thermosyphons charged with water, FC-84, FC-77 and FC-3283. Appl Therm Eng 2010;30:201–11. doi:10.1016/j.applthermaleng.2009.08.007.
[81] Estrada-Flores S. Cryogenic Freezing of Food. Ref Modul Food Sci 2016. doi:10.1016/B978-0-08-100596-5.03175-9.
[82] Smith TJ. Modelling the Flow and Solidification of Metals. vol. 1. 1987.
[83] Voller VR. A heat balance integral method based on an enthalpy formulation. Int J Heat Mass Transf 1987;30:604–7. doi:10.1016/0017-9310(87)90275-4.
[84] Lunardini VJ. Heat transfer with freezing and thawing. Elsevier; 1991.
[85] Davis SH. Theory of solidification. Cambridge University Press; 2001.
[86] Carslaw HS, Jaeger JC. Heat conduction in solids. Oxford Univ Pr 白 S 1959.
[87] Hill JM, Dewynne JN. Heat conduction. United States: Blackwell Scientific Publications, Inc; 1987.
[88] Zhaoa KXH, Power H, Wrobel LC. Numerical simulation of dendritic crystal growth in a channel. Eng Anal Bound Elem 1997;19:331–7. doi:10.1016/s0955-7997(97)00035-0.
[89] Zerroukat M, Wrobel LC. A boundary element method for multiple moving boundary problems. J Comput Phys 1997;138:501–19. doi:10.1006/jcph.1997.5829.
[90] DeLima-Silva W, Wrobel LC. A front-tracking BEM formulation for one-phase solidification/melting problems. Eng Anal Bound Elem 1995;16:171–82. doi:10.1016/0955-7997(95)00053-4.
[91] Moraga NO, Jauriat LA, Lemus-Mondaca RA. Heat and mass transfer in conjugate food freezing/air natural convection. Int J Refrig 2012;35:880–9. doi:10.1016/j.ijrefrig.2011.11.017.
[92] Moraga NO, Barraza HG. Predicting heat conduction during solidification of a food inside a freezer due to natural convection. J Food Eng 2003;56:17–26. doi:10.1016/S0260-8774(02)00135-8.
[93] Faghri A. Heat Pipe Science and Technology. Second edi. Global Digital Press; 2016.
[94] Ramos J, Chong A, Jouhara H. Experimental and numerical investigation of a cross flow air-to-water heat pipe-based heat exchanger used in waste heat recovery. Int J Heat Mass Transf 2016;102:1267–81. doi:10.1016/j.ijheatmasstransfer.2016.06.100.
[95] Karwa R. Empirical Relations for Forced Convection Heat Transfer. In: Karwa R, editor. Heat Mass Transf., Singapore: Springer Singapore; 2017, p. 539–622. doi:10.1007/978-981-10-1557-1_8.
[96] Žukauskas A. Heat Transfer from Tubes in Crossflow. Adv Heat Transf 1972;8:93–160. doi:10.1016/S0065-2717(08)70038-8.
[97] Functions AFU. Ansys Fluent Guide 2011:1–39.
[98] Grandjean TRB, Groenewald J, Marco J. The experimental evaluation of lithium ion batteries after flash cryogenic freezing. J Energy Storage 2019;21:202–15. doi:10.1016/J.EST.2018.11.027.